VECTOR AND TENSOR POLARIZATION MEASUREMENTS FOR dp AND dn QUASIFREE SCATTERING USING THE $\vec{d}+d \rightarrow d+p+n$ BREAKUP REACTION AT 12 MeV

by

Paul Daniel Felsher

Department of Physics
Duke University

Date: 24 July 1991

Approved:

Richard L. Walter, Supervisor

Calvin R. Howell

Russell Roberson

Seog Oh

Larry Evans

Dissertation submitted in partial fulfillment of the requirements for the degree of Doctor of Philosophy in the Department of Physics in the Graduate School of Duke University

1991

ABSTRACT

(Physics-Nuclear)

VECTOR AND TENSOR POLARIZATION MEASUREMENTS
FOR dp AND dn QUASIFREE SCATTERING
USING THE $\vec{d}+d \rightarrow d+p+n$ BREAKUP
REACTION AT 12 MeV

by

Paul Daniel Felsher

Department of Physics
Duke University

Date: 24 July 1991

Approved:

Richard L. Walter, Supervisor

Calvin R. Howell

Russell Roberson

Séog Oh

Larry Evans

An abstract of a dissertation submitted in partial
fulfillment of the requirements for the degree
of doctor of philosphy in the Department
of Physics in the Graduate School
of Duke University

1991

VECTOR AND TENSOR POLARIZATION MEASUREMENTS
FOR dp AND dn QUASIFREE SCATTERING
USING THE $\vec{d}+d \rightarrow d+p+n$ BREAKUP
REACTION AT 12 MeV

by

Paul Daniel Felsher

Measurements of vector and tensor analyzing powers A_y, A_{yy} and A_{zz} for dp and dn quasifree scattering (QFS) have been made using the $\vec{d}+d \rightarrow d+p+n$ breakup reaction at the Triangle Universities Nuclear Laboratory. The experiment was conducted with a 12-MeV tensor-polarized deuteron beam incident on a gas cell filled with one bar deuterium. The momenta of two (deuteron-neutron, deuteron-proton or proton-neutron) of the three outgoing particles were measured simultaneously, thereby completely defining the reaction kinematics. Deuteron-proton coincidence data were taken at five laboratory angle pairs: $(\theta_d,\theta_p)= (\pm 10.0°, \mp 10.0°)$, $(\pm 10.0°, \mp 41.2°)$, $(\pm 17.0°, \mp 17.0°)$, $(\pm 17.0°, \mp 34.5°)$ and $(\pm 19.4°, \mp 19.4°)$. Deuteron-neutron and proton-neutron coincidence data were taken at three laboratory angle pairs: $(\theta_d,\theta_n)= (\theta_p,\theta_n)=(\pm 17.0°, \mp 17.0°)$, $(\pm 17.0°, \mp 34.5°)$ and $(\pm 19.4°, \mp 28.9°)$. The angle pairs (θ_d,θ_n), (θ_p,θ_n) and (θ_d,θ_p) were chosen such that the reaction would be well-suited for observing dn and dp QFS. Deuteron-proton coincidence data were sorted into two-dimensional (2D) spectra of deuteron energy versus proton energy, while proton-neutron and deuteron-neutron data were sorted into 2D spectra of neutron time-of-flight versus proton energy and deuteron energy, respectively. Each 2D spectrum was projected onto the kinematically allowed locus. Analyzing powers were computed as a function of arc length S along the locus for A_y, A_{yy} and A_{zz}.

Since four-nucleon calculations involving polarization observables for the $\vec{d}+d \rightarrow d+p+n$ breakup reaction are not yet available, the data are compared to Impulse-Approximation (IA) calculations. The IA calculations included off-the-energy-shell deuteron-nucleon (dN) amplitudes as well as on-the-energy-shell dN amplitudes and also included the coherent addition of scattering amplitudes for both target breakup and projectile breakup. The IA calculations fail to reproduce many

of the details in the measured data, indicating that the $\vec{d}+d \rightarrow d+p+n$ breakup process is inherently more complicated at 12 MeV than the single scattering assumption which forms the basis for the IA.

The possibility of using the $\vec{d}+d \rightarrow d+p+n$ breakup reaction to examine charge symmetry breaking in the nucleon-nucleon interaction is also explored. Some differences in the analyzing powers for charge symmetric processes were observed. Detailed examination of the breakup process suggests that while some of the differences can be attributed to electromagnetic effects, other differences cannot. These unexplained differences could be a signature of charge-symmetry breaking.

The development of a computer code to conduct four-nucleon calculations using a realistic microscopic approach for the $\vec{d}+d \rightarrow d+p+n$ reaction has recently been initiated by A.C. Fonseca of Lisbon. The forthcoming calculations will form the basis for interpreting the present data and stimulating further studies of nucleon-nucleon interactions through this breakup process.

ACKNOWLEDGMENTS

This project would never have been possible without the assistance of numerous people. Thanks go, first and foremost to my adviser Professor Richard L. Walter. His confidence, patience and encouragement were essential for the completion of this work.

Another person without which this project would never have come to fruition is Dr. Calvin Howell whose expertise and assistance in all aspects of the data acquisition, data analysis, theoretical computations and interpretation of the data were indispensable. His generosity is greatly appreciated.

I am grateful to Dr. Werner Tornow for unselfishly sharing his expertise in all aspects of this work. His enthusiasm for physics made working with him extremely pleasant and even when busy he always found the time to help.

Data acquisition for nuclear physics experiments usually require the assistance of many individuals. This work is no exception and the following people are recognized for their assistance: Dr. Richard Walter, Dr. Calvin Howell, Dr. Werner Tornow, Dr. Ivo Šlaus, Dr. Mark Roberts, Dr. John Hanly, Dr. Gerulf Mertens, Dr. Jim Lambert, Dr. Paul Treado, Gary Weisel, and Mohammed Al Ohali.

I have also benefitted greatly by the unselfishness of many individuals from other institutions. Dr. Ivo Šlaus was a motivating factor behind this work from beginning to end and his expertise was essential in the interpretation of the results. Dr. Jim Lambert is to be thanked for his assistance with the kinematics needed for the development of our Impulse Approximation codes and for the interpretation of results. Dr. Paul Treado's expertise was very beneficial in the development of the few-nucleon program at TUNL. Dr. Gerulf Mertens' willingness to help in any way possible was a blessing during his many visits to TUNL. Dr. Yasuro Koike is to be thanked for his generosity in providing his nucleon-deuteron code which formed the backbone of our NMPWIA and NMPWIAOFF codes. Dr. Antonio Fonseca is also to be thanked for his generosity in providing nucleon-deuteron transition matrices that were used as inputs into our NMPWIA and NMPWIAOFF codes and for his theoretical input into the interpretation of our results.

Dr. Russell Roberson and Dr. Chris Gould are to be recognized for their contributions to the development of the data acquisition and analysis system. Dr. Thomas Clegg is to be commended for his dedication to the construction and maintenance of the polarized ion source.

Special thanks go to the technical support staff at TUNL for their hard work in building, repairing and replacing the equipment. The electronics were maintained by Sidney Edwards and Patrick Mulkey. The accelerator and associated hardware was maintained by Robert Rummel and Paul Carter. Repairs of broken accelerator parts and the building of new equipment was handled by Alton Lovette and his machine shop staff.

Finally, I would like to thank my parents, Albert and Rosemary, for their continued support and encouragement throughout my entire education and to my wife, Nena, for her love and encouragement.

This work supported in part by the U.S. Department of Energy, Office of High Energy and Nuclear Physics, under Contract No. DE-AC05-76ER01067, the state of North Carolina through the use of CPU time on the Cray Y-MP located at the North Carolina Supercomputing Center, the U.S.-Yugoslav Joint Board under Contract No. JF 682 and the Deutsche Forschungsgemeinschaft under Contract No. Me 544/8-1.

Contents

List of Figures

List of Tables

Chapter 1

Introduction

Nuclear physics as we know it today was born in 1932 with the discovery of the neutron by Chadwick which led Heisenberg to postulate that the nucleus was composed of nucleons (neutrons as well as protons). The nuclear or strong force was then proposed as the force acting between nucleons. Since then, one of the major goals of the nuclear physics community has been to understand the fundamental interaction between nucleons, i.e., the nucleon-nucleon (NN) force. Much has been learned about this force since 1932 and today the most successful models of the nuclear force are those based on field theory. The presently accepted model of the strong interaction is quantum chromodynamics (QCD) with the field quanta being gluons which are exchanged between quarks [Ynd83]. Although QCD has given tremendous conceptual insight on the fundamental constituents of nuclear matter, the mathematical complexity of this model means that it is not useful yet for calculating observables in the NN or few-nucleon systems. Since the quark substructure of nucleons comes into play only at very small distances, an effective description of the NN interaction is adequate at low energies. Such descriptions, which are based on the exchange of mesons between nucleons, have resulted in the development of semiphenomenological potentials [Mac89]. Polarization observables have only recently been calculated rigorously using these semiphenomenological NN potentials for the three-nucleon ($3N$) system [Wit88, Wit89a, How88]. The extension to the $4N$ system is considerably more complicated than the $3N$ problem and taxes even today's supercomputers to the limit of their speed and memory capacities. The rigorous solution to the $4N$ problem only recently has been initiated, therefore, the only $4N$ calculations available today are comparable (in terms of the complexity of the NN force and the number of $4N$ partial

waves used in the calculations) to $3N$ calculations of about 20 years ago.

Comparisons between data and calculations for few-body systems provide a sensitive tool for studying the basic NN force, including exotic features such as charge-symmetry breaking, and the so-called $3N$ force.[1] While differential cross sections depend strongly on the central force, polarization measurements are frequently favored as a testing ground for new models, since these observables are particularly sensitive to spin-dependent interactions. The d+d system in particular,[2] provides a very rich test of theoretical models of the NN interaction in the low-energy region, since the size of polarization observables for $4N$ systems was found to be one to two orders of magnitude greater than that found in NN scattering [Gru81]. In addition to learning about the dynamics of a $4N$ reaction using models based on the NN interaction, d+d reactions are interesting because of the special symmetry between the two interacting particles and because they possess nuclear structure related to excited states of ^{4}He. The dd system can also provide both vector and tensor polarization observables whereas the $2N$ system is limited to vector observables.

Advances in computational techniques and increased computing power permitted the first realistic microscopic calculations to be made a few years ago for the $3N$ system [Wit88, Wit89a, How88]. Calculations for the $4N$ system of the same caliber will not be available for some time. However, we are encouraged by the report of progress of A.C. Fonseca [Fon89, Fon90] who has recently begun to calculate polarization observables for $4N$ systems at energies below the deuteron breakup threshold. Calculations of polarization observables for the $\vec{d}$+$d \rightarrow d$+p+n breakup reaction are expected in the next couple of years [Fon90]. Part of the stimulation of Fonseca's work is a set of measurements that forms the basis of this thesis: the vector and tensor analyzing powers for the $\vec{d}$+$d \rightarrow d$+p+n breakup reaction at 12 MeV laboratory energy. These data were originally designed to examine a naive view of quasifree Nd scattering, but the data proved that the reaction was much richer (or complex) than expected. These data will provide the bench mark tests for the new generation of $4N$ calculations that will emerge soon.

For the present analysis, we have compared our data to calculations based on the impulse approximation (IA). In these calculations the three-body characteristics of the d+$d \rightarrow d$+p+n breakup reaction are considered to cause only second order

[1] A force that depends in an irreducible way upon the simultaneous coordinates of three nucleons when only nucleon degrees of freedom are taken into account.

[2] A recent review of $4N$ experiments is given in [Pae88].

effects on the primary two-body interaction between the deuteron and one of the free nucleons in the exit channel. If this approach is valid and the IA calculations resemble our data, details of the NN interaction can be extracted. On the other hand, if the calculations fail to reasonably resemble the data, little information can be obtained about details of the NN interaction. In any case, the kinematics of the IA is useful to identify regions of phase space sensitive to gross features of the NN interaction.

Charge-symmetry breaking[3] in the NN force, i.e., differences in the nn and pp forces not due to electromagnetic (em) effects, can be examined through a (somewhat) model-independent procedure by a thorough investigation of the inherent symmetry or lack thereof in the $\vec{d}+d \rightarrow d+p+n$ breakup reaction. A careful analysis of the kinematics of the reaction should allow for the identification of regions of phase space that may be sensitive to this symmetry breaking. Such an analysis is reported in the present work.

The organization of this dissertation is divided into 7 chapters.

Chapter 2 Details of the measurement and descriptions of the techniques and equipment.

Chapter 3 Method for sorting the data and extracting the polarization observables.

Chapter 4 Description of the Impulse Approximation Calculations.

Chapter 5 Presentation of the data and a comparison to the Impulse Approximation calculations.

Chapter 6 Discussion of possible charge-symmetry breaking in the nucleon-nucleon force using a subset of our data.

Chapter 7 Summary of the findings for this work.

Appendix A Tabulation of all the data obtained in the present work.

Appendix B Tabulation of relevant kinematic quantities useful in the interpretation of data.

Our belief has always been that the data obtained in this study will assist the development of a more complete understanding of the NN force and will also provide valuable comparisons for $4N$ calculations which are soon to emerge. In an extension

[3]On the quark level the breaking of charge symmetry is due to the interchange of u- and d-quarks.

of the experiment, we are currently collaborating at the local Cray facility with A.C. Fonseca [Fon90] to calculate the first polarization observables for the $\vec{d}+d \rightarrow d+p+n$ breakup reaction using a realistic representation of the NN interaction.

From an applied point of view, a better understanding of the NN interaction and the $4N$ system may someday help decrease the demand for fossil fuels by allowing physicists to further develop fusion reactors that are powered by a virtually inexhaustible supply of deuterium fuel obtainable from sea water. The harnessing of energy released by nuclear-fusion reactions ($d+d \rightarrow p+{}^3\mathrm{H}$ and $d+d \rightarrow n+{}^3\mathrm{He}$) as a power source is favored over nuclear fission due to the reduction of radioactive waste produced by the former process. A neutron-lean reactor may also be feasible by decreasing the reaction rate for the undesirable $\mathrm{D}(d,n)^3\mathrm{He}$ reaction as opposed to the desirable ${}^3\mathrm{He}(d,p)^4\mathrm{He}$. Some scientists even feel that polarized fusion in particular, may be used to choose preferential emission directions of reaction products such as neutrons that may damage the reactor vessel. Polarized fusion may also lower the ignition temperature necessary for a self-sustaining fusion reaction. Recent calculations examining the feasibility of various fusion processes are given in [Zha86, Hof84b, Lem90].

Chapter 2

Experimental Details

2.1 Introduction

Vector (A_y) and tensor (A_{yy}, A_{zz}) analyzing powers have been measured for deuteron-proton (dp) and deuteron-neutron (dn) quasifree scattering (QFS) in a kinematically complete experimental arrangement using the $\vec{d}+d \rightarrow d+p+n$ breakup reaction. All measurements were performed at the Triangle Universities Nuclear Laboratory (TUNL). A *dc* beam of tensor-polarized deuterons, produced by the TUNL Lamb-shift polarized ion source (PIS), was accelerated to an energy of 12.07 MeV and was incident on a deuterium filled gas cell placed inside a specially designed scattering chamber. The gas cell was filled with one bar of 99.6% pure deuterium. Silicon surface-barrier detectors and liquid organic scintillators were placed in the horizontal reaction plane and were used to detect charged particles and neutrons, respectively. Two of the three outgoing particles were detected in coincidence on opposite sides of the incident beam. Table 2.1 lists the angle pairs used in the present measurements. The scattering chamber[1] installed on the 38° beam leg was used to take the data for the first three rows of angles shown in table 2.1, whereas the scattering chamber[2] installed on the 52° beam leg was used to obtain the data at the angle pairs given in the last five rows of the table. Simultaneous measurement of the accidental background was made possible by delaying the signal of one of the detected particles and recording the resulting coincidences. Monitoring of the beam flux and detector electronics was aided by recording all events occurring in two of the charged-particle detectors

[1] Hereafter called 38° scattering chamber for brevity.
[2] Hereafter called 52° scattering chamber for brevity.

Deuteron-Proton		Deuteron-Neutron		Proton-Neutron	
θ_d(deg.)	θ_p(deg.)	θ_d(deg.)	θ_n(deg.)	θ_p(deg.)	θ_n(deg.)
± 17.0	∓ 17.0	± 17.0	∓ 17.0	± 17.0	∓ 17.0
± 19.4	∓ 19.4	± 17.0	∓ 34.5	± 17.0	∓ 34.5
		± 19.4	∓ 28.9	± 19.4	∓ 28.9
± 10.0	∓ 10.0				
± 10.0	∓ 41.2				
± 17.0	∓ 17.0				
± 17.0	∓ 34.5				
± 34.5	∓ 17.0				

Table 2.1: Angle pairs used in coincidence measurements. The + and − refer to left and right scattering respectively and the angle θ is defined in figure 2.1. Angle pairs shown in the first three rows were taken with the 38° scattering chamber while the angle pairs shown in the last five rows were taken with the 52° scattering chamber.

on opposite sides of the beam axis.

Charged-particle telescopes in the standard ΔE-E arrangement were used for particle identification to distinguish between protons, deuterons, tritons and ^{4}He. Neutrons were detected in liquid organic scintillators. Since such detectors are sensitive to both neutrons and γ-rays, pulse-shape discrimination (PSD) was used to discriminate against events caused by γ-rays. The energy of the neutrons was determined by the time-of-flight difference (TOFD) between the arrival of the charged particle in the ΔE detector and the corresponding event in the neutron detector. Two-dimensional spectra for deuteron-proton (dp), deuteron-neutron (dn) and proton-neutron (pn) coincidences were obtained by plotting the energy of one detected particle versus the energy (TOFD in the case of a neutron) of the other detected particle.

2.2 Review of Coordinate System

To describe experiments initiated by polarized beams, one must define a coordinate system that specifies the "reaction coordinate frame" and another coordinate system that specifies the spin quantization axis of the projectile. The reaction coordinate frame and the beam polarization description (see figure 2.1) introduced here will

follow the conventions adopted at the *Madison Convention* [Bar70]. Let the positive z-axis of the reaction coordinate frame coincide with the incident beam momentum direction $\hat{k}_{in}$ and let the positive y-axis be along the normal to the reaction plane, i.e., along $\hat{k}_{in} \times \hat{k}_{out}$ where $\hat{k}_{in}$ and $\hat{k}_{out}$ are unit vectors in the laboratory reference frame in the direction of the incoming and outgoing beam momenta. The x-axis points in the direction to make this an orthogonal right-handed coordinate system. The location of detectors in the reaction plane (xz-plane) can be described by the angle θ measured from the positive z-axis to the line connecting the target to the center of the detector or equivalently between $\hat{k}_{in}$ and $\hat{k}_{out}$. Thus,

$$\cos\theta = \hat{k}_{in} \cdot \hat{k}_{out} \quad . \tag{2.1}$$

An ensemble of particles is said to be *polarized* when the orientation of the nuclear spins of the individual particles is arranged in some nonrandom fashion. Most experiments requiring polarized beams of particles obtain the beams from a previous scattering or from a polarized ion source. The latter is usually preferred due to the greater flexibility in preparing the polarization state of the beam, as well as increased beam intensities and higher degrees of polarization. Beams of polarized ions emanating from polarized ion sources, such as the Lamb-shift source at TUNL, contain an axis of symmetry called the spin quantization axis, which is defined by cylindrically symmetric magnetic fields about the beam momentum in the regions of the ion source where the deuteron atoms are polarized and ionized (see section 2.10.1). While being transported to the scattering chamber the beam passes through various magnetic fields which deflect the beam. Such fields may precess the spin quantization axis so that its orientation in space is changed by the time it reaches the target. According to the *Madison Convention* this new direction of the spin quantization axis, referred to as $\hat{s}$ can be characterized by the polar angle β and the azimuthal angle ϕ with respect to the reaction coordinate frame of figure 2.1. As shown in the figure, β is the angle between $\hat{s}$ and $\hat{k}_{in}$. Thus,

$$\cos\beta = \hat{s} \cdot \hat{k}_{in} \tag{2.2}$$

with $0 \leq \beta \leq \pi$. The angle ϕ is the angle measured from the y-axis to the half plane containing $\hat{s}$ with $0 \leq \phi \leq 2\pi$. Another way of looking at it is that ϕ is the angle measured from the y-axis to the projection of $\hat{s}$ onto the xy-plane. Notationally this is:

$$\cos\phi = \hat{y} \cdot (\hat{s} \times \hat{k}_{in}) = (\hat{k}_{in} \times \hat{k}_{out}) \cdot (\hat{s} \times \hat{k}_{in}) \quad . \tag{2.3}$$

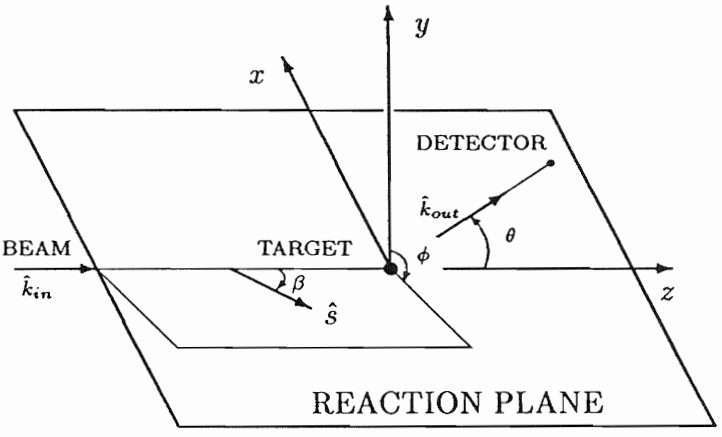

Figure 2.1: Coordinate system describing the spin quantization axis $\hat{s}$ relative to the reaction plane.

Thus, for scattering to the left side of the z-axis, $\phi = 0°$ when the projection of $\hat{s}$ on the xy-plane is parallel to the y-axis $\phi = 0°$; $\phi = 270°$ when parallel to the x-axis. Similarly, $\phi = 180°$ when antiparallel to the y-axis and $\phi = 90°$ when antiparallel to the x-axis. In our experiment the angles β and ϕ were set using a Wien filter which was located at the exit of the PIS.

2.3 Polarization Description of Spin-1 Particles

A spin-1 particle is characterized by a three-component spinor

$$\chi = \begin{pmatrix} a \\ b \\ c \end{pmatrix} \tag{2.4}$$

where the amplitudes a, b and c may be complex and satisfy the normalization requirement $|a|^2 + |b|^2 + |c|^2 = 1$. The polarization parameters describing an ensemble of spin-1 particles are certain expectation values of the spin-1 angular momentum

operator $\boldsymbol{S}$ with

$$S_X = \frac{1}{\sqrt{2}} \begin{pmatrix} 0 & 1 & 0 \\ 1 & 0 & 1 \\ 0 & 1 & 0 \end{pmatrix}$$

$$S_Y = \frac{1}{\sqrt{2}} \begin{pmatrix} 0 & -i & 0 \\ i & 0 & -i \\ 0 & i & 0 \end{pmatrix}$$

$$S_Z = \begin{pmatrix} 1 & 0 & 0 \\ 0 & 0 & 0 \\ 0 & 0 & -1 \end{pmatrix}. \tag{2.5}$$

In Cartesian notation these expectation values called spin moments are defined by

$$P_i \equiv \langle S_i \rangle \quad \text{for } i = X, Y, Z \tag{2.6}$$

for vector polarization and

$$P_{ij} \equiv \langle S_{ij} \rangle = \frac{3}{2} \langle S_i S_j + S_j S_i \rangle - 2\hbar\delta_{ij} \quad \text{for } i, j = X, Y, Z \tag{2.7}$$

for tensor polarization, with

$$\delta_{ij} = \begin{cases} 1 & \text{for } i = j \\ 0 & \text{for } i \neq j \end{cases}. \tag{2.8}$$

The expectation value of $\boldsymbol{S}^2$ given by

$$\langle \boldsymbol{S}^2 \rangle = S(S+1)\hbar = 2\hbar \tag{2.9}$$

implies that

$$\begin{aligned} P_{XX} + P_{YY} + P_{ZZ} &= 3\left(\langle S_X S_X \rangle + \langle S_Y S_Y \rangle + \langle S_Z S_Z \rangle\right) - 3 \times 2\hbar \\ &= 3\langle \boldsymbol{S}^2 \rangle - 6\hbar \\ &= 3 \times 2\hbar - 6\hbar \\ &= 0 \end{aligned} \tag{2.10}$$

since

$$\langle S^2 \rangle = \sum_{i=X,Y,Z} \langle S_i^2 \rangle \ . \tag{2.11}$$

Thus a deuteron beam, which is a collection of spin-1 particles, can be completely described by a second rank tensor with 8 independent parameters (3 vector and 5 tensor). In general for a particle with spin I (with I expressed in units of *Planck's constant* $\hbar$) the polarization state can be completely described by $(2I+1)^2 - 1$ independent parameters [Hae74].

As stated in section 2.2 beams produced by a polarized ion source usually contain an axis of symmetry $\hat{s}$. For a beam possessing this axial symmetry it is sufficient to choose a Z-axis along $\hat{s}$ and then the only non-zero expectation values can be expressed in terms of S_Z. The two significant expectation values of S_Z according to equations 2.6 and 2.7 are $P_Z = \langle S_Z \rangle$ and $P_{ZZ} = \langle 3S_Z^2 - 2 \rangle$.

The expectation values of a deuteron from a PIS can be considered to be in an eigenstate

$$\chi_+ = \begin{pmatrix} 1 \\ 0 \\ 0 \end{pmatrix}$$

$$\chi_0 = \begin{pmatrix} 0 \\ 1 \\ 0 \end{pmatrix}$$

$$\chi_- = \begin{pmatrix} 0 \\ 0 \\ 1 \end{pmatrix} \tag{2.12}$$

of S_Z where the spinors χ_+, χ_0 and χ_- represent the deuteron as being in one of the $m_I = +1, 0, -1$ magnetic substates.

Any axially symmetric polarization state can in general be expressed by an incoherent mixture of N_+ particles in the χ_+ eigenstate (spin along $+\hat{s}$), N_- particles in the χ_- eigenstate (spin along $-\hat{s}$) and N_0 particles in the χ_0 eigenstate (spin uniformly distributed in a plane perpendicular to $\hat{s}$). See figure 2.2 for a schematic

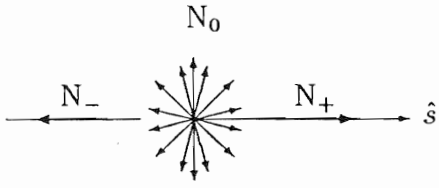

Figure 2.2: Schematic representation of axially symmetric polarized deuteron beam. The labels N_+, N_- and N_0 represent the fraction of particles with spin aligned, the fraction with spin anti-aligned and the fraction with spin uniformly distributed perpendicular to the axis of symmetry $\hat{s}$, respectively.

representation of an axially symmetric polarized deuteron beam. We adopt the normalization $N_+ + N_- + N_0 = 1$. Thus, since we have N_+ particles with $\langle S_Z \rangle = +1$, N_- particles with $\langle S_Z \rangle = -1$, and N_0 particles with $\langle S_Z \rangle = 0$, it follows that the value of $\langle S_Z \rangle = N_+ - N_-$. Thus, for vector polarization we obtain

$$P_Z = N_+ - N_- \ . \tag{2.13}$$

Furthermore, $\langle S_Z^2 \rangle = 1$ for $(N_+ + N_-)$ particles and $\langle S_Z^2 \rangle = 0$ for N_0 particles. Therefore, $3\langle S_Z^2 \rangle = 3\,(N_+ + N_-) = 3\,(1 - N_0)$ which shows that $\langle 3S_Z^2 - 2 \rangle = 1 - 3N_0$. Therefore, from the above equation for P_{ZZ} for the tensor polarization one obtains the simple expression

$$P_{ZZ} = 1 - 3N_0 \ . \tag{2.14}$$

From the definition of the spin moments (see equation 2.7) it is easy to see that $P_{XX} = P_{YY}$ for a beam that is axially symmetric about the Z-axis so that equation 2.10 implies that $P_{XX} = P_{YY} = -\frac{1}{2} P_{ZZ}$.

For reference, where practical, the relations will be given in both Cartesian and spherical coordinates. In spherical tensor notation equation 2.13 is

$$\tau_{10} = \sqrt{\frac{3}{2}}\,(N_+ - N_-) \tag{2.15}$$

and equation 2.14 becomes

$$\tau_{20} = \frac{1}{\sqrt{2}}\,(1 - 3N_0) \ . \tag{2.16}$$

A pure *vector polarized* beam can be obtained if all second rank moments vanish (i.e., if $N_0 = \frac{1}{3}$). The maximum vector polarization for such a case is then obtained when $N_+ = \frac{2}{3}$ and thus $P_Z = +\frac{2}{3}$ ($\tau_{10} = \sqrt{\frac{2}{3}}$). Pure tensor polarization occurs when $N_+ = N_-$. It is a maximum when $N_+ = N_- = \frac{1}{2}$ so that $P_{ZZ} = +1$ ($\tau_{20} = \frac{1}{\sqrt{2}}$) and is a minimum when $N_+ = N_- = 0$ so that $P_{ZZ} = -2$ ($\tau_{20} = -\sqrt{2}$). In the currently reported measurement various tensor and vector beam polarizations were used.

The vector and tensor beam moments can be expanded in terms of the angles β and ϕ, that $\hat{s}$ makes with the reaction coordinate frame as shown in figure 2.1. The vector beam moments in Cartesian notation are:

$$\begin{aligned} P_x &= -P_Z \sin\beta \sin\phi \\ P_y &= P_Z \sin\beta \cos\phi \\ P_z &= P_Z \cos\beta. \end{aligned} \tag{2.17}$$

while the tensor beam moments are:

$$\begin{aligned} P_{xx} &= P_{ZZ} \frac{1}{2}(3\sin^2\beta\sin^2\phi - 1) \\ P_{yy} &= P_{ZZ} \frac{1}{2}(3\sin^2\beta\cos^2\phi - 1) \\ P_{zz} &= P_{ZZ} \frac{1}{2}(3\cos^2\beta - 1) \\ P_{xy} &= -P_{ZZ} \frac{3}{2} \sin^2\beta\cos\phi\sin\phi \\ P_{xz} &= -P_{ZZ} \frac{3}{2} \sin\beta\cos\beta\sin\phi \\ P_{yz} &= P_{ZZ} \frac{3}{2} \sin\beta\cos\beta\cos\phi \ . \end{aligned} \tag{2.18}$$

The vector moments in spherical tensor notation are:

$$\begin{aligned} t_{10} &= \tau_{10}\cos\beta \\ it_{11} &= \tau_{10}\frac{1}{\sqrt{2}}\sin\beta(\cos\phi + i\sin\phi) \ . \end{aligned} \tag{2.19}$$

While the tensor moments are:

$$
\begin{aligned}
t_{20} &= \tau_{20}\frac{1}{2}\left(3\cos^2\beta - 1\right) \\
t_{21} &= -i\tau_{20}\sqrt{\frac{3}{2}}\sin\beta\cos\beta\left(\cos\phi + i\sin\phi\right) \\
t_{22} &= -\tau_{20}\sqrt{\frac{3}{8}}\sin^2\beta\left(\cos 2\phi + i\sin 2\phi\right) \ . \qquad (2.20)
\end{aligned}
$$

The beam moments P_i, P_{ij} and t_{kq} defined above will be used in section 3.4.

2.4 Acceleration & Beam Transport

A floor plan of the laboratory illustrating the layout of the PIS and the beam legs is shown in figure 2.3. For all of the present measurements a 50 keV *dc* beam of negatively ionized deuterium atoms was extracted from the PIS. The beam passed through the Wien filter and was bent by an inflection magnet onto the axis of the FN tandem Van de Graaff accelerator. The terminal voltage was set to about 6 MV, thereby accelerating the deuterons to an energy of about 12 MeV. The D^+ beam emerging from the tandem was deflected by the "20-70" analyzing magnet (see figure 2.3) through either 38° or 52° depending on which scattering chamber was to be used. The magnetic field of the analyzing magnet, regulated by an NMR gaussmeter, was set for a beam of 12.07 MeV deuterons. The difference signal from a set of horizontal slits at the exit of the magnet was sent to the tandem high-voltage control circuit to make minor adjustments to the terminal voltage. For maximum beam stability the input (object) slits to the "20-70" magnet were set to 1.5 cm wide by 1.5 cm high while the output (image) slits were set to 0.10 cm wide. The analyzed beam was then focused, collimated and transported to the scattering chamber where it was incident on the deuterium gas cell. Energy loss in the gas cell reduced the beam energy to 12.00 MeV at the center of the gas cell. The typical beam current on target was held to a low value ($\sim$ 25 nA) to keep the counting rates in the measurement at a reasonable level and to prevent rupture of the gas cell. The beam area at the target was relatively small, i.e., about 1 mm $\times$ 1 mm.

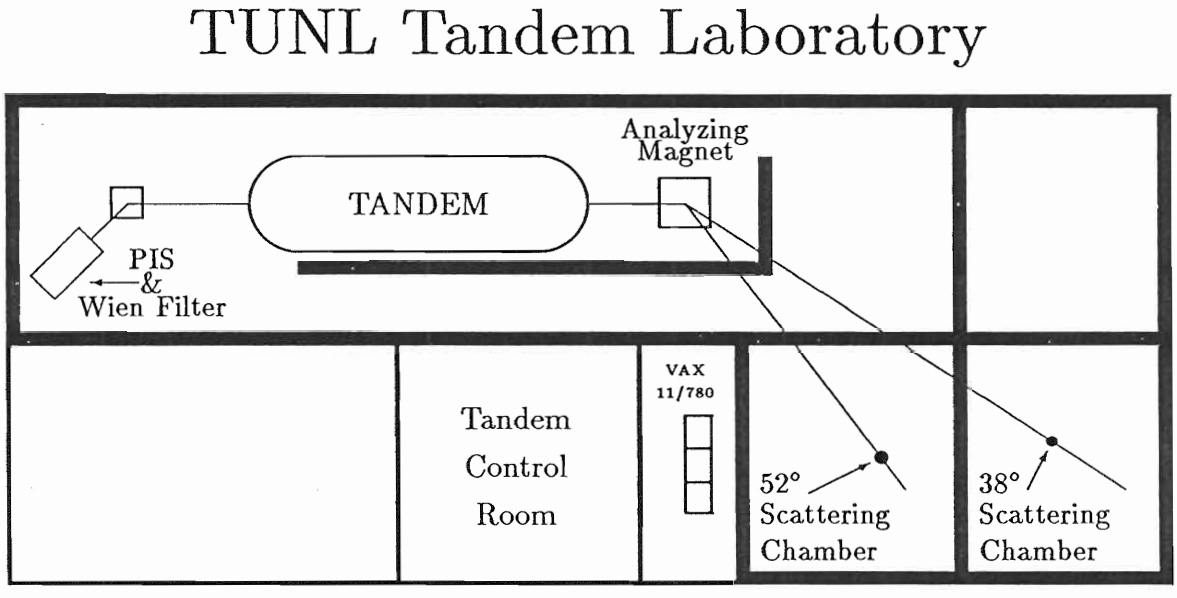

Figure 2.3: Floor plan of the Triangle Universities Nuclear Laboratory. Only the beam lines used in this work are shown. Drawing not to scale.

2.5 The 38° Beam Leg Modifications

For the past 20 years the 38° beam leg which ends in the neutron time-of-flight target room, has been used primarily for neutron scattering studies. In order to undertake the present measurements it was necessary to modify this beam leg to be suitable for performing charged-particle scattering experiments. A specially designed scattering chamber (described in section 2.6) was mounted at the end of the beam leg. To define the direction, diameter, and divergence of the incident beam, two sets of adjustable horizontal and vertical slits, separated by about one meter, were installed 40 cm upstream of the location of the scattering chamber. The upstream set of slits was set to 0.38 cm wide by 0.76 cm high, while the set closer to the chamber was set to 0.31 cm by 0.46 cm. With proper focusing this resulted in a beam spot on target of about 1 mm × 1 mm. To aid in beam tuning a remotely controlled beam stop and a permanent beam scanner were installed between the two sets of slits.

For the purposes of beam current integration (described in section 2.10.6) a beam dump in the form of a Faraday cup, consisting of a 2 m long, 15 cm diameter aluminum beam pipe and a tantalum beam stop, was located about 40 cm downstream of the scattering chamber. Since the neutron detectors themselves were unshielded and had no collimation it was deemed necessary to place the primary source of background radiation, i.e., the tantalum beam stop, a substantial distance away from the chamber. The 2 m length of the pipe permitted adequate shielding in the form of 50 cm of lithium-loaded paraffin stacked on both sides of the beam stop. The large diameter beam pipe used was required in order to minimize the amount of stray beam hitting the inside walls of the aluminum pipe. Secondary electron emission from the beam dump was suppressed by locating an electron suppression ring (biased to –300 V) at the entrance of the Faraday cup.

The addition of the chamber and the extra beam pipe required a supplemental diffusion pump and a liquid nitrogen cold trap just downstream of the chamber. Typical vacuum in the region of the scattering chamber during these measurements was $3\text{x}10^{-5}$ Torr.

2.6 The 38° Scattering Chamber

To have adequate neutron energy resolution in the *dn* and *pn* coincidence measurements the neutron detectors were placed at flight paths of 2.0–2.5 meters from the

center of the deuterium gas cell. The detection of low energy (0.5–12.0 MeV) charged particles on the other hand, necessitated that the silicon surface-barrier detectors be located in vacuum. We modified a scattering chamber that had been previously used at Duke University in the early 1960's to measure $^{13}C(p,p)^{13}C$ and $^{12}C(p,p)^{12}C$ cross sections [Ger63]. Along with a description of the relevant parameters of the original chamber, the major modifications will be detailed in this section. The chamber, made primarily of aluminum, has an internal diameter of 30.5 cm and a depth of 7.6 cm. The curved outer walls originally had a uniform thickness of 1.0 cm, but were modified by replacing portions of the wall in the angular region between 16° and 40° on both sides of the beam axis with two 0.064 cm thick stainless steel plates. These plates served as the *neutron* windows. A sketch of the chamber is shown in figure 2.4.

Two 30.2-cm diameter turn tables, one mounted on the bottom of the chamber and the other to the lid, were used to support the charged-particle detectors and their associated collimating systems inside the chamber. Each turn table had six equally spaced slots in which the detectors could be placed at flight paths from 5 cm to 12 cm. In addition to the slots, a number of holes were drilled in the plates to allow two detectors mounted on the same plate to be placed at different angles relative to each other. Shown in table 2.2 are the slit locations and dimensions used for the charged-particle detectors and the flight paths, detector sizes, angular spread and solid angles for both the charged particle and neutron detectors. Both turn tables were mounted on sliding vacuum seals so as to facilitate angle changes without breaking vacuum. Graduations on the rims of the turn tables, viewed through two glass windows on the side of the chamber, along with vernier indexes on the top and bottom of the chamber allowed the angles of the detectors relative to the chamber to be set to within $\pm$ 0.1°. The chamber itself was first aligned optically and then checked using the $D(d,dd)$ reaction by monitoring the coincidence count rates as the angles of the two detected deuterons were varied. From this it was determined that the optical alignment differed from the experimentally determined alignment by 0.6°. Angle settings during the QFS measurements were set according to the experimentally determined alignment.

The turn tables, which supported the solid-state detectors, were cooled with Freon to reduce electrical noise in the detectors and to increase the lifetime of the detectors. Due to problems in retrofitting the old chamber with cooling lines it was not possible to thermally isolate the cold turn tables from the rest of the chamber. This in turn meant that the entire chamber was cooled to some extent, causing excessive

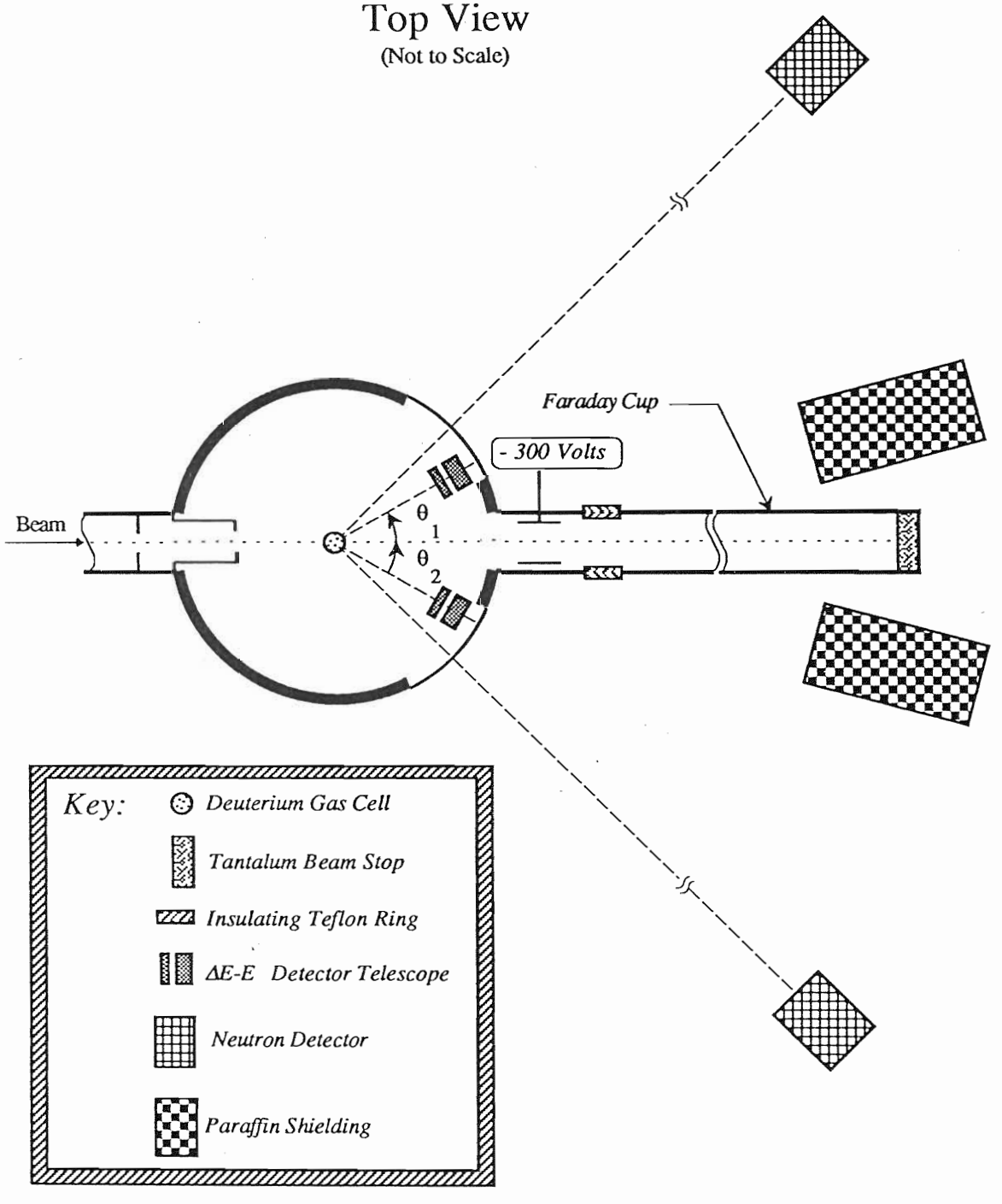

Figure 2.4: Top view of a schematic diagram of the 38° scattering chamber. Corresponding to the convention of a positive scattering angle for left scattering with a *spin up* incident beam, angles are recorded as positive for scattering to the left and negative for scattering to the right. Drawing not to scale.

Detector	Slit Locations		Slit Dimensions				Detector		Angular Spread	Solid Angle
			Width		Height					
	L_1 (cm)	L_2 (cm)	W_1 (cm)	W_2 (cm)	H_1 (cm)	H_2 (cm)	Location (cm)	Area (cm^2)	$\Delta\theta$ (deg)	$\Delta\Omega$ (msr)
ΔE-E	5.7	10.8	0.16	0.16	0.48	0.48	11.4	0.085	0.84	0.05
Neutron	N/A	265.0	N/A	7.62	N/A	15.24	265.0	116.1	1.65	0.13

Table 2.2: The 38° scattering chamber detector slit specifications. The slit locations are measured from the center of the gas cell to the slits with the slit closest to the gas cell being subscripted with the number "1" and the slit closest to the detector being subscripted with "2". The charged particle detectors are identified as ΔE-E since they were arranged in a ΔE-E telescope formation. Since no collimation was used for the neutron detectors, the values shown for slit location, width and height are the actual location, width and height of the detectors.

condensation on the exterior surfaces of the chamber. Plastic was used to wrap all electronic components attached to the exterior of the chamber in order to protect them from the excessive amounts of water dripping from the chamber.

The last major modification, designed to make the chamber a more flexible experimental apparatus, was the addition of a gas cell (see section 2.9). This allowed the experimenters to use either a gas-target or the original target rod capable of holding three thin-foil targets.

2.7 The 52° Scattering Chamber

A limitation of the 38° scattering chamber was that charged-particle detectors could not be placed forward of about 13° without their collimating systems being illuminated by the beam passing through the gas cell. The 63 cm diameter scattering chamber located on the 52° beam leg allowed the placement of the charged particle detectors at longer flight paths and thus more forward angles. The measurements given by the last five rows of angle pairs shown in table 2.1 were obtained in this chamber.

The entrance slits for this chamber were set to give a beam size on target equivalent to that used with the 38° chamber (1×1 mm^2). External condensation on the 52° scattering chamber was not a problem because the scattering tables inside the

Detector	Slit Locations		Slit Dimensions				Detector		Angular Spread	Solid Angle
			Width		Height					
	L_1 (cm)	L_2 (cm)	W_1 (cm)	W_2 (cm)	H_1 (cm)	H_2 (cm)	Location (cm)	Area (cm^2)	$\Delta\theta$ (deg)	$\Delta\Omega$ (msr)
ΔE-E	8.9	15.2	0.32	0.32	0.48	0.48	15.9	0.164	1.19	0.05
E	7.6	12.7	0.16	0.16	0.48	0.48	13.3	0.08	0.72	0.04

Table 2.3: The 52° scattering chamber detector slit specifications. The slit locations are measured from the center of the gas cell to the slits with the slit closest to the gas cell being subscripted with the number "1" and the slit closest to the detector being subscripted with "2". The telescope detector pair is labeled as ΔE-E while the other detector pair is labeled as E.

chamber, cooled by a Freon refrigeration system, were well insulated from the rest of the chamber. Typical vacuum in this chamber, maintained by a turbo molecular pump, was $3x10^{-6}$ Torr.

The primary disadvantage of using the 52° scattering chamber was that the thick (~2.5 cm) walls of the chamber would have significantly attenuated the low-energy neutrons of the deuteron-neutron or proton-neutron coincidence measurements. Furthermore, other beam lines and equipment in the vicinity of the chamber would have limited the location of the neutron detectors as well as prohibiting proper shielding of the neutron detectors. For these reasons only deuteron-proton coincidence data were taken with this chamber. Shown in table 2.3 are the slit locations and dimensions, detector flight paths, sizes, angular spread and solid angles for the charged-particle detectors used in the 52° scattering chamber. Two pairs of charged-particle detectors were used: pair one was a set of two ΔE-E telescopes and the other pair was a set of two E detectors.

2.8 CD_2 Foils

During some feasibility tests for the present measurements 350 $\mu g/cm^2$ thick carbon-backed deuterated polyethylene $(CD_2)_x$ foils were used. Not only are these foils expensive (~$100 each), but they also are very fragile. In our tests, holes developed in the foils after less than 1 h with 25 nA of beam incident on an area 1×1 mm^2. Thicker foils were not used since some of the outgoing charged particles of interest

would have been stopped in the foil. Thinner foils on the other hand would be extremely difficult to handle and would have provided an unacceptable counting rate.

Another problem experienced with the foils was that the experimentally observed dp coincidence count rate was extremely low (~30 counts/h). This count rate was a factor of 200 less than expected. It was eventually realized that in a coincidence experiment like this the active area of the target (defined by the area illuminated by the beam and viewed by both detectors) is critically dependent upon the alignment of the detector collimators and upon the beam position (when using narrow slit openings). The criticality of the beam position and the collimator alignment is significantly reduced when a gas target is used.

2.9 Deuterium Gas Target

All of the production runs for this experiment used a gas cell for the target. The cell itself consisted of a brass body with a window made of Kapton. The combination of brass and Kapton produced a gas cell which was essentially a right-circular cylinder with brass on the top and bottom, a small brass support post used to connect the upper and lower brass portions and Kapton covering the curved portions of the cylinder. This cylinder was then oriented perpendicular to the beam such that its axis was vertical and rotated so the beam entered the cell adjacent to the support post. This permitted the beam to enter through the Kapton and all reaction products in the horizontal plane to exit through the Kapton. A schematic diagram of the gas cell is shown in figure 2.5.

The choice of Kapton as a containment foil was based primarily on energy loss calculations of deuterons and protons in the 1-8 MeV energy range. This corresponds to the energies of the outgoing particles of interest in the $d+d \rightarrow d+p+n$ breakup reaction. Kapton, made by the Dupont company, comes in a variety of thicknesses and three different forms (uncoated or coated with different substances). For the present measurements, 8 μm (the thinnest size available) HN type Kapton foil, an all-purpose uncoated film, was used. Chemically it is a polymide polymer made of carbon, hydrogen, oxygen and nitrogen ($(C_{22}H_{18}O_5N_2)_x$).

The pressure in the gas cell was monitored with a model *PX 304-100A V* pressure transducer manufactured by OMEGA Engineering Inc. During data acquisition the signal from the pressure transducer was digitized and stored in the computer along with other data.

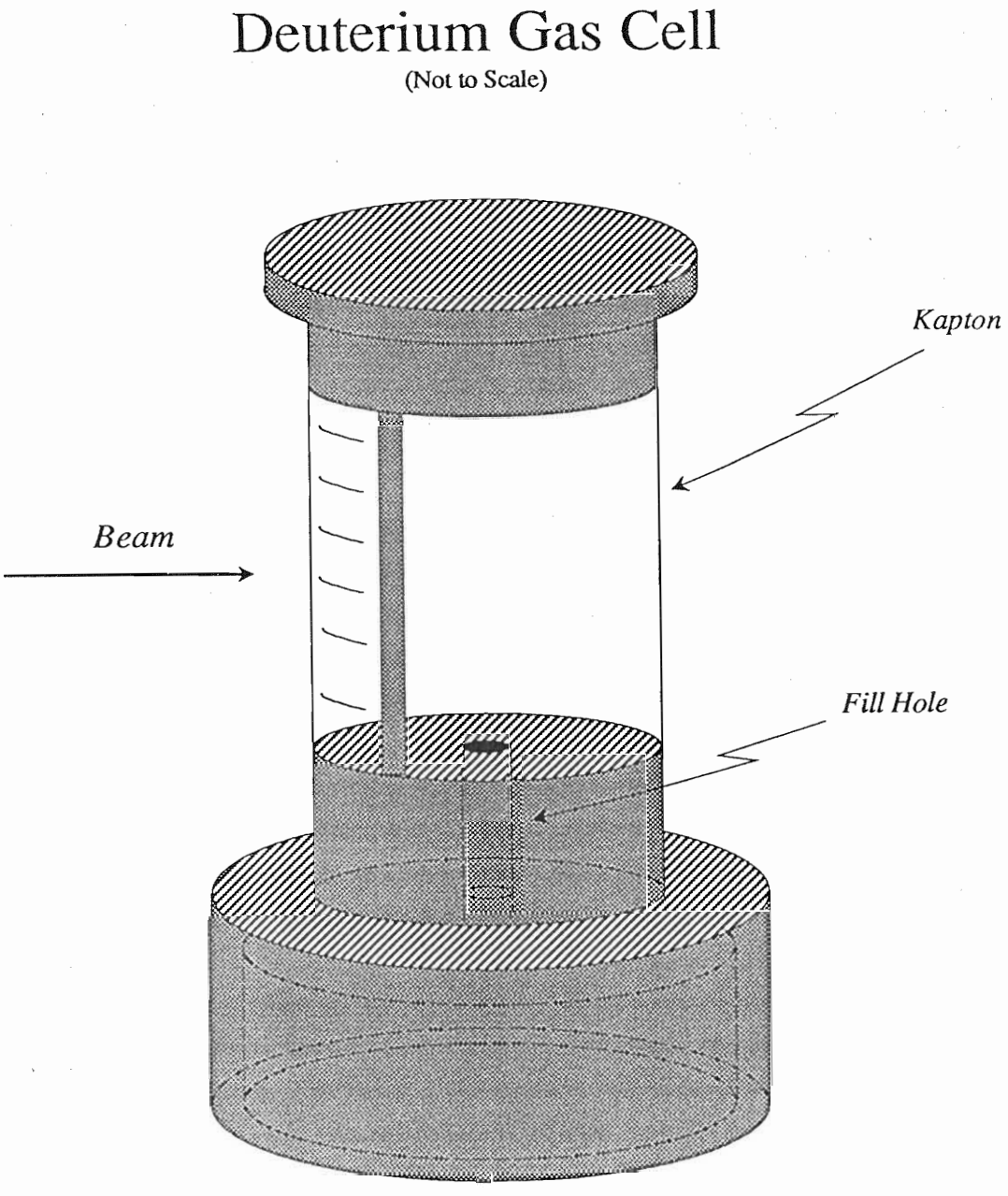

Figure 2.5: Schematic diagram of deuterium gas target. The body of the cell is made of brass while the deuterium containment foil is made of Kapton. Drawing not to scale.

During the preparation of the gas cell, which consisted of epoxying the Kapton foil to the brass body and then pressure testing, it was determined that the foil would rupture when pressurized between 1.5 and 2 bar positive gauge pressure. For the actual experiment the cell was filled with 1.0 bar of 99.6% pure deuterium. Kapton of the thickness used (8 μm) is somewhat porous to deuterium. With one bar absolute pressure of deuterium, a decrease in pressure (due to diffusion of deuterium through the Kapton) of about 2% per hour was observed while the gas cell was in vacuum. This was determined to be unacceptable during actual runs, therefore the gas cell was left open to the filling system and was regulated with the use of a regulator attached to the high pressure deuterium gas bottle of the filling system.

2.10 Data Acquisition

Data acquisition at TUNL was coordinated using a Digital Equipment Corporation VAX-11/780 mainframe computer. The hardware was controlled by a Microprogrammed Branch Driver MBD-11 connected to two daisy chained CAMAC crates. A more thorough description of the data acquisition hardware at TUNL is given by King *et al.* [Kin81] and Roberson *et al.* [Rob81].

The software system XSYS used to control data acquisition and analysis was developed at TUNL [Gou81] and contains a set of general purpose computer codes useful for all experiments performed at TUNL. Additional routines written in both FORTRAN and Digital Equipment's command language (DCL) were combined into an on-line data acquisition software package called DDND3 and an off-line data analysis software package called DDND3OFF.

The $A_y(\theta)$ and $A_{yy}(\theta)$ measurements were taken simultaneously while the $A_{zz}(\theta)$ measurements were taken separately since the beam polarization conditions required for the two sets of measurements differed. In both cases the data acquisition consisted of a four-step sequence where each step had the beam polarization prepared in a different way, i.e., rotation of the spin quantization axis $\hat{s}$ or a change in beam polarizations P_Z and P_{ZZ}. Data were accumulated by cycling through this four-step sequence until enough counts were obtained in the coincidence spectra to give analyzing powers at the QFS point to a statistical accuracy of $\pm 3\%$. In each step the same amount of beam charge was incident on the deuterium target. The charge was measured by integrating the current on the beam stop located downstream of the deuterium gas cell. The amount of charge chosen for each step took about 15 minutes

to accumulate. The short time per step insured adequate averaging over drifts in electronics, beam position on target and beam polarization during data accumulation for an angle pair. At the end of each four-step group the process was repeated, but in opposite order. This was done in order to help minimize experimental asymmetries due to drifts in the electronics or changes in gas pressure in the target cell. Data continued to be collected in this "forward-backward" step process for about 12 hours and then a new set of measurements was started and the process repeated. For data analysis each 12-h run for a given angle pair was analyzed and the results were combined statistically.

The approximate beam time used for each angle pair is given in table 2.4. This time included that for actual data acquisition along with time spent adjusting the electronics, beam tuning and computer down time (due to hardware induced crashes). On the average about 70% of this time was used for actual recording of data.

The signals from the various detectors, after passing certain hardware requirements (see section 2.10.4), were digitized by Analog to Digital converters (ADC's) and were processed by the on-line software package DDND3. Two-dimensional histograms were formed for the coincidence detection of two particles on opposite sides of the beam axis by plotting the energies of the detected charged particles (time-of-flight for detected neutrons) versus each other. Data were also stored in an unsorted form on magnetic storage tape in order to allow different software gates to be used in a replay of the data.

2.10.1 Lamb-Shift Polarized Ion Source & Wien Filter

The polarized deuteron beam for these measurements was obtained from the TUNL Lamb-shift polarized ion source (PIS). Only a brief description of the source will be given here since it has been described in much detail in other publications [Tra73, Cle74]. Deuterium ions (D^+) are produced in the duoplasmatron (see figure 2.6) and are accelerated to an energy of 1100 eV before entering the cesium canal where they interact with cesium vapor and capture a single electron. A small fraction of these neutral deuterium atoms exit the cesium canal in the $2S_{\frac{1}{2}}$ metastable state while most of the other remaining neutrals are in the $1S_{\frac{1}{2}}$ ground state. The neutral atoms then drift through the spin filter where the desired nuclear polarization is selected by causing certain hyperfine levels of the $2S_{\frac{1}{2}}$ states to mix with $2P_{\frac{1}{2}}$ states which quickly decay to the ground state. In order to be accelerated by the tandem Van de Graaff

Detected Particles	Angles	Time (h)	
		A_y & A_{yy}	A_{zz}
Deuteron, Proton	$\pm 10.0, \mp 10.0$	105	45
Deuteron, Proton	$\pm 10.0, \mp 41.2$	105	45
Deuteron, Proton	$\pm 17.0, \mp 17.0$	270	235
Deuteron, Proton	$\pm 17.0, \mp 34.5$	110	60
Deuteron, Proton	$\pm 19.4, \mp 19.4$	85	95
Deuteron, Proton	$\pm 34.5, \mp 17.0$	110	60
Deuteron, Neutron	$\pm 17.0, \mp 17.0$	70	105
Deuteron, Neutron	$\pm 17.0, \mp 34.5$	90	75
Deuteron, Neutron	$\pm 19.4, \mp 28.9$	85	95
Proton, Neutron	$\pm 17.0, \mp 17.0$	70	105
Proton, Neutron	$\pm 17.0, \mp 34.5$	90	75
Proton, Neutron	$\pm 19.4, \mp 28.9$	85	95

Table 2.4: Beam time used per angle pair.

the beam must be negatively ionized. This is accomplished in the Argon canal where the $2S_{\frac{1}{2}}$ metastable neutral atoms preferentially capture an electron and emerge from the Argon gas as a beam of nuclear-polarized D^- ions. The spin-quantization axis $\hat{s}$ is maintained by cylindrically symmetric magnetic fields in the spin-filter region and the Argon canal.

The negative ion beam is accelerated to an energy of 50 keV before passing through an ANAC Inc. model 2170 crossed-field spin precessor called a Wien filter. This device consists of a uniform magnetic field applied perpendicular to the polarized-beam velocity; the spin precesses by an amount dependent upon the strength of the field, and a compensating static electric field to prevent any net deflection of the beam. By adjusting the magnetic field strength and the angle of rotation of the Wien filter about the beam axis we are able to precess $\hat{s}$ to the desired orientation relative to the reaction coordinate frame depicted in figure 2.1.

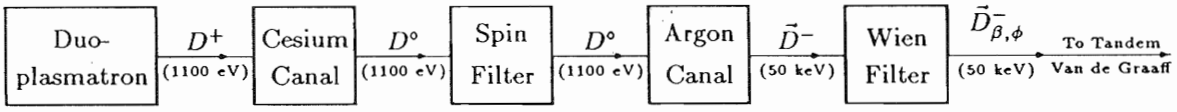

Figure 2.6: Schematic representation of the Lamb-shift polarized ion source and Wien filter. The deuteron beam is extracted from the duoplasmatron and exits the Wien filter. The numbers in parentheses indicate the energy of the deuteron beam at that location while the subscript β, ϕ indicates that the quantization axis of the polarized deuterons has been precessed to the desired orientation.

2.10.1-a Beam Conditions for the A_y and A_{yy} Measurements

Deuteron beam conditions necessary for measurements of A_y, A_{yy} and A_{zz} made it impractical to determine all three observables concurrently. As previously stated in section 2.10, the polarization observables for the $\vec{d}+d \rightarrow d+p+n$ breakup reaction were obtained in two successive measurements. The A_y and A_{yy} data were acquired simultaneously while the A_{zz} data was determined in a separate measurement.

With the use of both the spin filter and the Wien filter various deuteron beam conditions can be obtained. For the A_y and A_{yy} measurements a four-step sequence was used in which the beam was specially prepared for each step. Shown in table 2.5 are the angles β and ϕ along with the theoretical maximum values of the beam moments for each of the four steps. The angles β and ϕ are defined in section 2.3. Since this is a coincidence measurement between two particles on opposite sides of the beam axis, we specify which particle defines the coordinate frame of figure 2.1. In all our work the coordinate frame will be defined in reference to a deuteron scattered to the left for the *dp* and *dn* coincidences and to a proton scattered to the left for a *pn* coincidence. Note: a coordinate frame defined by a *right* scattering is a 180° rotation about the beam axis as compared to the coordinate frame defined by *left* scattering.

For all four steps the spin quantization axis $\hat{s}$ is perpendicular to the beam momentum. It points *up* for steps 1 and 4 and points *down* for steps 2 and 3. Inclusion of the beam moments $P_{Z_{max}}$ and $P_{ZZ_{max}}$ in our visualization leads to the deuteron spin vectors forming a *cigar* shape aligned along $\hat{y}$ for steps 1 and 2 and a *pancake* shape lying in the scattering plane for steps 3 and 4.

Data Step	β(deg.)	ϕ(deg.)	Cartesian		Spherical	
			$P_{Z_{max}}$	$P_{ZZ_{max}}$	$\tau 10_{max}$	$\tau 20_{max}$
1	90	0	1	1	$\sqrt{\frac{3}{2}}$	$\frac{1}{\sqrt{2}}$
2	90	180	1	1	$\sqrt{\frac{3}{2}}$	$\frac{1}{\sqrt{2}}$
3	90	180	0	-2	0	$-\sqrt{2}$
4	90	0	0	-2	0	$-\sqrt{2}$

Table 2.5: Beam conditions for the A_y and A_{yy} measurements. The angles β and ϕ are as defined in section 2.2.

2.10.1-b Beam Conditions for the A_{zz} Measurements

Like the A_y and A_{yy} measurements, the A_{zz} measurements also consisted of a four-step sequence (see table 2.6). The nuclear polarization of the deuteron beam was the same as in the A_y and A_{yy} measurements, however the Wien filter was adjusted to align the spin quantization axis $\hat{s}$ parallel to the beam momentum. Actually, steps 1 and 4 should be thought of as parallel and steps 2 and 3 as antiparallel to the beam momentum. Visually this would correspond with the deuteron spin vectors forming a *cigar* shape aligned along $\hat{z}$ for steps 1 and 2 and a *pancake* shape lying in the plane containing $\hat{x}$ and $\hat{y}$ for steps 3 and 4. Since the spin quantization axis is along the beam momentum, the angle ϕ is undefined for all four steps. Again we choose to define the reference coordinate frame by a left scattered deuteron for the *dp* and *dn*

Data Step	β(deg.)	ϕ(deg.)	Cartesian		Spherical	
			$P_{Z_{max}}$	$P_{ZZ_{max}}$	$\tau 10_{max}$	$\tau 20_{max}$
1	0	undefined	1	1	$\sqrt{\frac{3}{2}}$	$\frac{1}{\sqrt{2}}$
2	180	undefined	1	1	$\sqrt{\frac{3}{2}}$	$\frac{1}{\sqrt{2}}$
3	180	undefined	0	-2	0	$-\sqrt{2}$
4	0	undefined	0	-2	0	$-\sqrt{2}$

Table 2.6: Beam conditions for the A_{zz} measurements. The angles β and ϕ are defined in section 2.2.

coincidences and for a left scattered proton for the *pn* coincidences.

2.10.2 Neutron Detection

All of the measurements involving the detection of neutrons, i.e., deuteron-neutron and proton-neutron coincidences, were performed with the 38° chamber. Two identical neutron detectors (7.62Wx15.24Hx10.16D cm^3) were placed symmetrically about the beam axis 2.0–2.5 m from the center of the deuterium gas cell. They were unshielded except for the shielding located directly in the vicinity of the beam dump (see figure 2.4). Liquid organic scintillators, filled with Nuclear Enterprise scintillation fluid (NE-213) were used to permit pulse-shape-discrimination (PSD) against γ-rays. Since neutrons are typically not stopped in the detectors, only a fraction of the neutron energy is deposited in the detector, therefore it was necessary to use time-of-flight (TOF) techniques to determine the energy of the detected neutrons. The flight times were measured using the time-of-flight difference (TOFD) between a detected deuteron or proton on one side of the beam axis and the coincident neutron on the other side of the beam axis. The actual flight time of the neutron from the point of origin, i.e., the gas cell, is larger than that measured using this technique. This is due to the finite flight time of the charged particles (deuteron or proton) from the gas cell to the detector (typically a distance of 11 cm). In the analysis of the data this finite charged particle flight time was taken into account (see sections 3.3.2 and 3.3.3). A typical TOFD spectrum is shown in figure 2.7.

2.10.3 Charged-Particle Detection and Identification

The need for charged-particle identification is quite evident in an experiment of this type in which silicon surface-barrier detectors are used, since they have equal efficiency (unity) for detecting all the charged particles produced in d+d reactions, i.e., ^{3}He, tritons, deuterons and protons. Two arrangements were used. In both the 38° chamber and the 52° chamber two (a *left* and a *right*) ΔE-E telescopes, each consisting of a 50-μm and a 1500-μm thick detector were used. In addition to the two ΔE-E telescopes, the 52° chamber also had a pair (again a *left* and a *right*) of E detectors each consisting of a 1500-μm thick detector. All detector systems incorporated a collimating arrangement with two slits to define the direction of incoming particles. Electrons were prevented from hitting the detectors by placing small ferromagnets around the snouts holding the slits. Shown in figure 2.8 is a schematic of one of the

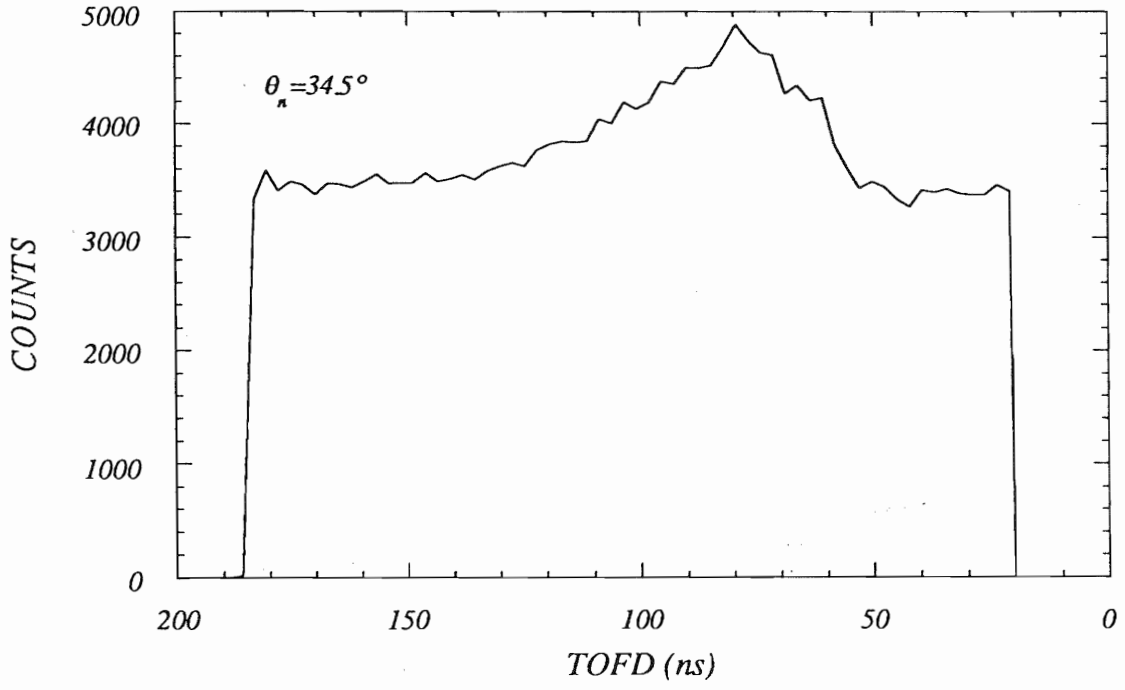

Figure 2.7: Neutron time-of-flight difference (TOFD) spectrum for neutrons detected at +34.5° in coincidence with charged particles detected at −17.0°. The TOFD of the "true + accidental" counts were measured as the time difference between the detected charged particle and the detected neutron. Note the cutoffs at both ends of the spectrum are due to the 170 ns TAC range used.

detector systems including its collimator arrangement. A typical spectrum showing counts versus energy for one of the ΔE-E telescopes is shown in figure 2.9. The kinematics of the various reactions in the d+d system permits the identification of some of the peaks in the spectrum. Notice the most intense peak is from deuteron-deuteron (dd) elastic scattering and that each well defined peak comes from a reaction in which two particles are in the final state. The deuterons and protons of interest (those from 3-body (3B) breakup) fall into a continuum of energies between 0.5 and 8 MeV.

In order to identify a particle as either a ^{3}He, a triton, a deuteron or a proton the detector system must measure independent functions of mass (M) and charge (Z). Fortunately, M in atomic mass units has near-integral values and Z in units of electron charge has integral values so that MZ^2 assumes unique values of 1, 2, 3 and 12 for protons, deuterons, tritons and ^{3}He, respectively. The quantity MZ^2 can be easily obtained from a detector telescope that measures the energy loss (ΔE) of a particle passing through a thin detector into a second detector where its residual energy (E_r) is deposited and measured. The thin transmission detector provides a direct measure of $\frac{dE}{dx}$ for the particle.

The rate at which a charged particle looses energy in a medium is described by the well known Bethe-Bloch equation [Mar69] and for nonrelativistic particles reduces to

$$\frac{dE}{dx} = C_1 \frac{MZ^2}{E} \ln\left(C_2 \frac{E}{M}\right). \tag{2.21}$$

where C_1 and C_2 are constants, E is the total kinetic energy of the particle. Since the logarithmic term varies only slowly with energy it can be neglected for our purpose. The resulting relationship is then

$$\frac{dE}{dx} \propto \frac{MZ^2}{E} \quad . \tag{2.22}$$

From this relationship we see that for different particles with a fixed energy E the rate of energy loss in the thin transmission detector is proportional to MZ^2, which has the discrete allowed values stated earlier (1, 2, 3 and 12). The total energy E can be obtained by summing the signals ΔE and E_r (assuming that the pulse heights from the two detectors have been matched for equal energy depositions). Therefore, if we plot $\frac{dE}{dx}$ *vs* E, we get bands of points corresponding to the different particles. In practice we do not know $\frac{dE}{dx}$, but we do know ΔE which is just $\frac{dE}{dx}\Delta x$, where Δx is the thickness of the transmission detector. Shown in figure 2.10 is a two-dimensional plot obtained from one of the detector telescopes. Here the total energy ($\Delta E + E_r$)

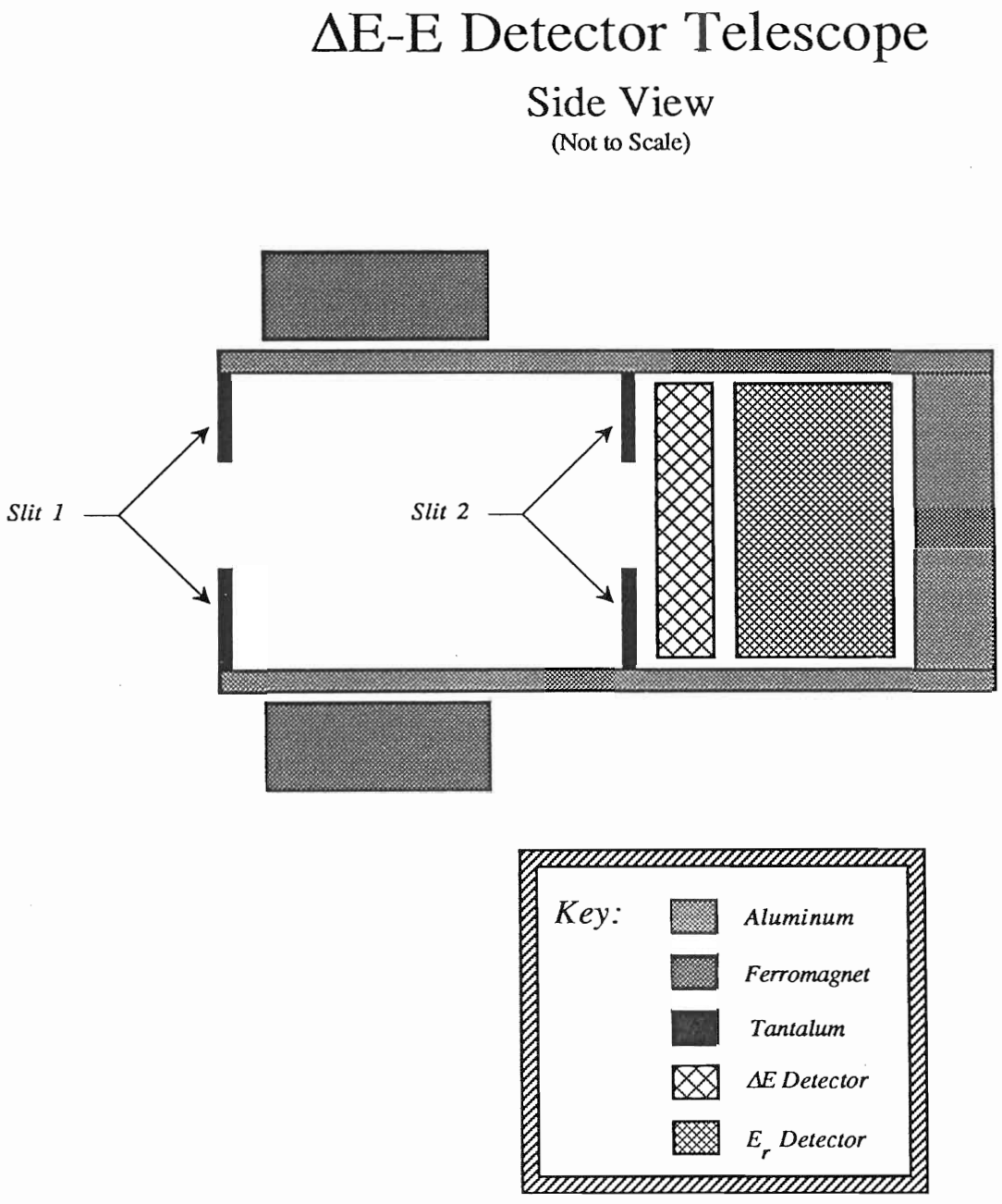

Figure 2.8: Schematic of a charged particle detector telescope including the collimating system. Charged particles enter from the left and are collimated by the tantalum slits. Ferromagnets are used to deflect forward going electrons emitted from slit 1 and from the region of the gas cell. The detectors labeled ΔE and E_r are the thin transmission detector and the residual energy detector, respectively.

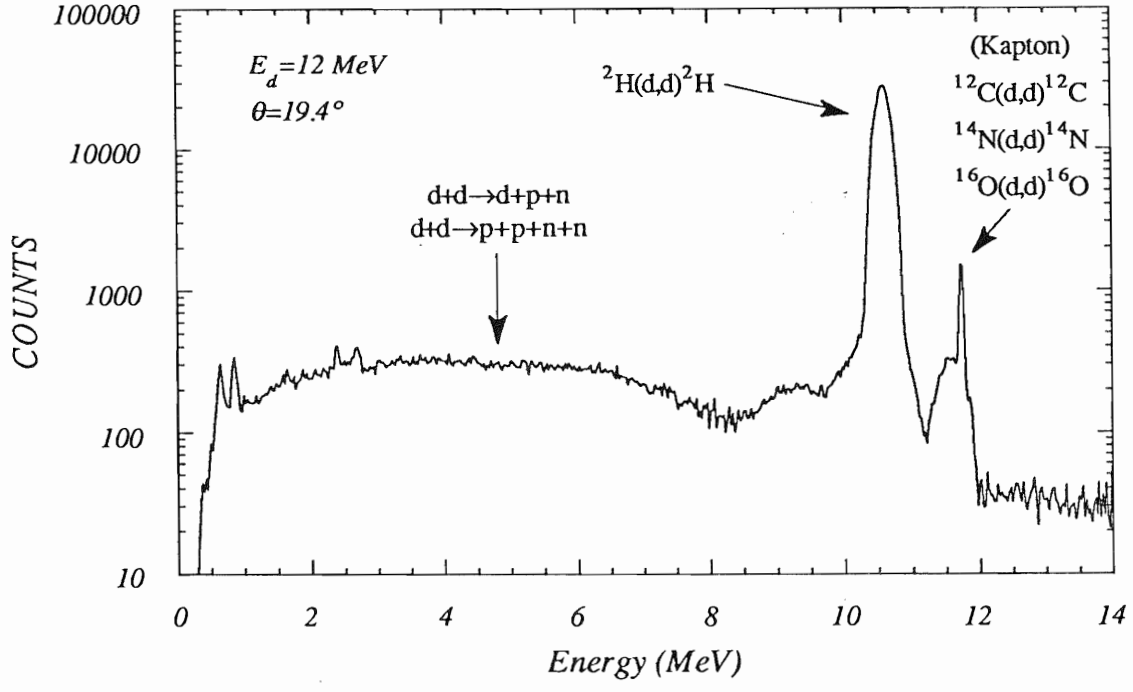

Figure 2.9: A one-dimensional spectrum showing counts *vs* detected energy for a charged-particle detector telescope at 19.4°. The peak at about 10.5 MeV is due to d+d elastic scattering and was used as a monitor of the incident deuteron beam and drifts in detector electronics. The peak at about 11.7 MeV is due to a small fraction of the incident beam scattered from the Kapton foil used to contain the deuterium gas. The charged particles from the breakup reaction of interest form a continuum in energy from about 0.5 to 8 MeV. The incident deuteron beam was 12 MeV.

is plotted versus the energy loss (ΔE) in the transmission detector. One immediate observation is that no particle identification is possible for low-energy particles that stop in the ΔE detector. Such low-energy particles fall along the straight line in figure 2.10 where $E = \Delta E$. Deuterons with energies less than ~2.5 MeV and protons with energies less than ~2.0 MeV were stopped in the transmission detector and thus deuterons and protons with energies less than 2.0 MeV were indistinguishable. Deuterons between 2.0 and 2.5 MeV were distinguishable from protons of the same energy but indistinguishable from tritons and ^{3}He.

Another problem occurs when a particle has sufficient energy to pass through the residual energy detector without depositing all of its energy. This was of no consequence for the present measurements since all of the outgoing deuterons and protons were stopped by the telescope arrangement.

During data acquisition and analysis a two-dimensional gate was drawn around the deuteron band and a second two-dimensional gate was drawn around the proton band (see figure 2.10). In both cases the gates included the linear region in which it is impossible to distinguish between a deuteron and a proton. A valid deuteron-proton coincidence is defined to be any coincidence in which one of the detected particles falls in the deuteron gate and the other detected particle falls in the proton gate. The lack of particle identification is not as bad as it may at first appear since a valid coincidence (dp or pd) between two charged particle detectors only requires the identification of one of the two particles. In our experiment, when the detected deuteron stops in the ΔE detector (thereby being indistinguishable from a proton) then, due to kinematics, the corresponding proton detected in the other telescope has sufficient energy to pass through the ΔE detector and deposit some energy in the residual energy detector, thereby being identifiable as a proton. The same argument applies to a low-energy proton and the corresponding higher energy deuteron. Omitted from the above discussion are valid pp coincidences coming from the four-body breakup reaction $d+d \rightarrow p+p+n+n$. Such events contribute only a very small background in the case when one or both protons is stopped in the ΔE detector.

2.10.4 Detection Electronics

Standard electronic modules are used to transform events in the detectors to pulses whose amplitudes are proportional to either the energy deposited by a charged particle in a solid-state detector or to the flight time of a neutron for the neutron detectors.

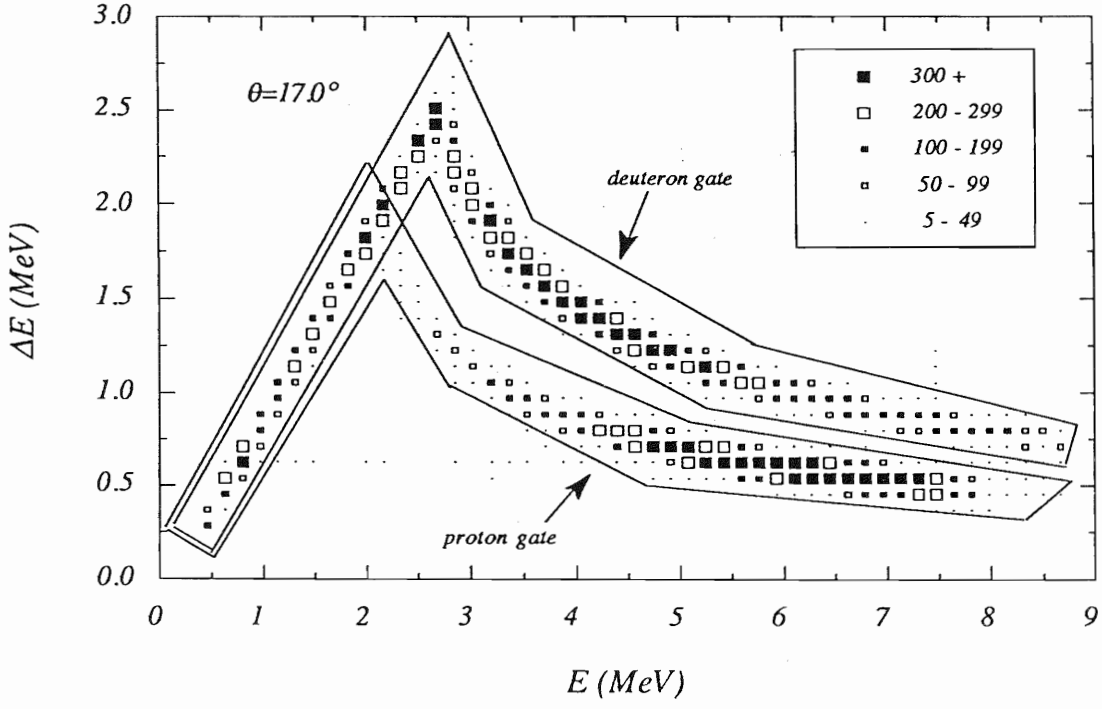

Figure 2.10: Two-dimensional histogram of ΔE *vs* E for a charged-particle detector telescope at $+17.0°$ in coincidence with either a charged-particle detector telescope at $-17.0°$ or a charged particle detector at $-34.5°$. The deuteron and proton gates used in sorting the data are shown.

These pulses are digitized by analog to digital converters (ADC's) and stored in a VAX 11/780 computer. The computer interface was CAMAC based with preprocessing done by a microprogrammable branch driver (MBD) connected to the VAX 11/780 via UNIBUS. All data were taken using the XSYS data acquisition software package.

Pulse-shape discrimination was used on the neutron detectors to reject γ-rays. Each event was tagged with the following router signals for storing and sorting the data in the computer: 1) detector pair involved in the event; 2) "true + accidental"/"accidental" event; 3) real/pulser event; 4) the data step number (see section 2.10); and 5) "pile-up" event rejection, that is the rejection of two events that occur within the gating time of the ADC's, thereby mixing the analog information from the two events.

2.10.4-a The 38° Chamber

For measurements utilizing the 38° scattering chamber, two ΔE-E detector telescopes and two neutron detectors were placed symmetrically about the beam axis with the ΔE-E telescopes located within the chamber and the neutron detectors located external to the chamber (see figure 2.4). A block diagram showing the electronics is depicted in figure 2.11. All four of the silicon detectors were connected to Ortec 142-A pre-amps which were located just outside of the scattering chamber. (Each detector along with its accompanying pre-amp is shown in figure 2.11 as one unit in the block diagram.) The pre-amps were used to generate a timing pulse and to amplify the energy pulses to sufficient amplitude for transport to the control room where the remainder of the signal processing was performed. The anode signals from the two neutron detectors and the energy signals from each of the four solid-state detectors (two from the ΔE's and two from the E_r's) were brought into the control room on 90Ω low-loss cables. The timing signals from the two ΔE detectors were brought into the control room on 50Ω cables.

Linear signals from the four charged-particle detectors were fed into spectroscopy amplifiers which produced unipolar outputs that were reshaped with linear gated stretchers (LGS's). Outputs from the LGS's for the ΔE detectors were fed into analog-to-digital converters (ADC's) at the computer interface (labeled $L_{\Delta E}$ and $R_{\Delta E}$) and also summed with the LGS's outputs from the E_r detectors. These summed pulses (L_E and R_E) were also fed into ADC's. Careful attention was paid to the spectroscopy amplifiers to insure gain matching between ΔE and E_r detectors in each

telescope.

A coincidence within 10 ns between events in the two ΔE-E telescopes provided the computer trigger for a breakup event. All time information for the ΔE-E telescopes was obtained from the ΔE detectors. The timing output of the 142-A preamp used for ΔE detectors was amplified with a timing filter amplifier (TFA) and passed into a constant-fraction discriminator (CFD). The threshold on the CFD was set just above the detector and amplifier noise. The outputs from the CFD's were sent to two coincidence units. The first coincidence module was used to measure the "true + accidental" events (hits in the ΔE detectors occurring within 50 ns). The output of the coincidence units were used for routing signals at the computer interface. The "accidental" events were measured by delaying one of the ΔE timing signals by 200 ns before forming the coincidence with the other ΔE detector. The output of this coincidence was used for routing the accidental signals. The router signals for the "true + accidental" and "accidental" coincidences are labeled $[L_{cp} + R_{cp}]$ and represent the coincidence between the left charged-particle detector and the right charged-particle detector. The square brackets are used to indicate that this is a routing signal and the parentheses within the square brackets indicate that the router is for an "accidental" event.

Any time a timing signal was above the threshold for a ΔE detector an "elastic" routing gate ($R_{elastic}$ or $L_{elastic}$) was generated for that detector. These gates informed the sorting software that an event was detected in one of the ΔE-E telescopes and that the total energy signal (L_E or R_E) for that detector should be processed and stored in the computer. These "elastic" events were useful for monitor gain shifts in the electronics as well as for monitoring beam intensity.

The circuit for neutron–charged-particle coincidences were identical for the two neutron detectors and very similar to that for coincidences between charged-particle detectors. For this reason, the discussion will only focus on the coincidence between a left charged particle and a right neutron.

The signals from the anode of each neutron detector were ORed with regenerated pulser signals and sent into the following circuits: 1) CFD to generate timing signals for the time-of-flight difference (TOFD) measurements; 2) a pulse-shape discriminator for γ-ray rejection; and 3) a shaping amplifier followed by a single-channel analyzer (SCA) to set the lower threshold on the energy of the neutrons involved in the neutron–charged-particle coincidence. The amplitude threshold was set by the lower level of the SCA to $\frac{1}{4}$ the light output produced by the maximum energy

Compton-recoil electrons for a ^{137}Cs γ-ray source. This threshold setting corresponds to a lower neutron energy of $\sim$ 500 keV. The above method of setting the neutron-energy threshold with a ^{137}Cs source is described in more detail in the Ph.D. thesis of Pedroni [Ped86].

Pulse-shape discrimination (PSD) was used to discriminate against γ-ray induced events. This method exploits the difference in the decay time of detector pulses produced by the electron recoils from γ-rays and pulses produced from recoil protons from neutrons. The CFD produces a fast pulse triggered on the leading edge of the detector pulse and serves as a "start" signal for a time-to-amplitude converter (TAC). From this point we shall refer to this TAC as the PSD-TAC to distinguish it from the TAC used in the TOFD measurements. The "stop" for the PSD-TAC comes from the PSD module which produces a fast signal triggered on the trailing edge of the detector pulse. The PSD-TAC spectrum contains a sharp peak due to γ-induced events followed by a broad mound due to neutron-induced events. The lower level of the SCA in the PSD-TAC was set just above the γ-ray peak to reject events involving the detection of a γ-ray in the neutron detector.

The time-of-flight difference (TOFD) between the arrival of a neutron at the neutron detector and the coincident arrival of a charged particle in the solid-state detector was measured by the TOFD-TAC. The TOFD-TAC range was set to 200 ns to measure the flight times of neutrons in the energy range from 0.5 MeV up to 8 MeV and still have some space in the TAC spectrum to monitor the accidental level. The "stop" signal to the TOFD-TAC was the associated ΔE timing signal delayed by 250 ns. A resolving time of 180 ns was defined for the neutron-charged particle coincidence by the regenerated ΔE timing signal at the input to the coincidence unit. Similar to the case of the charged-particle coincidences, the "accidental" coincidences were measured by delaying the ΔE timing signal by 300 ns before forming the coincidence with the neutron detector. The "start" signal for the TOFD-TAC came from the output of the "true + accidental" or "accidental" coincidence boxes. The reason for forming the neutron-charged particle coincidence prior to the TOFD-TAC was to minimize the dead time of the TAC by limiting the number of the "start" signals to the TAC and forcing a "stop" signal to be present within the TAC range for each start signal.

The SCA output from the TOFD-TAC was fed to a coincidence circuit. A wide gate coming from the CFD (which was set slightly lower than the SCA used to define the neutron-energy threshold) was used to gate the output of the SCA's set on the output of the pulse-height amplifier, the PSD-TAC and the TOFD-TAC. A

coincidence of all four signals defined a valid neutron event. The output from the coincidence unit was used as an input into two other coincidence units that were used to generate routing gates for either a "true + accidental" ($[R_n + L_{cp}]$) or an "accidental" event ($[R_n + L_{cp}]$).

The TOFD-TAC linear output signals from the left neutron detector were summed with those from the right neutron detector before being digitized by an ADC.

If any two of the six coincidence routers occurred within 2 μs of each other a pulse-pileup router was generated to be used by the sorting software to veto those events.

A pulser was used to measure the entire dead time (electronic plus computer) of the system. The pulser rate was triggered by every tenth pulse from the BCI unit which resulted in a pulser rate of about 5 Hz. The pulser signals were fed into the test inputs for the pre-amps used for charged-particle detectors and into a discriminator to be ORed with the signals from the neutron detectors. Care was taken to shape the signal entering the neutron-detector portion of the electronics to position the pulser signals slightly beyond the neutron mound in the PSD-TAC spectrum.

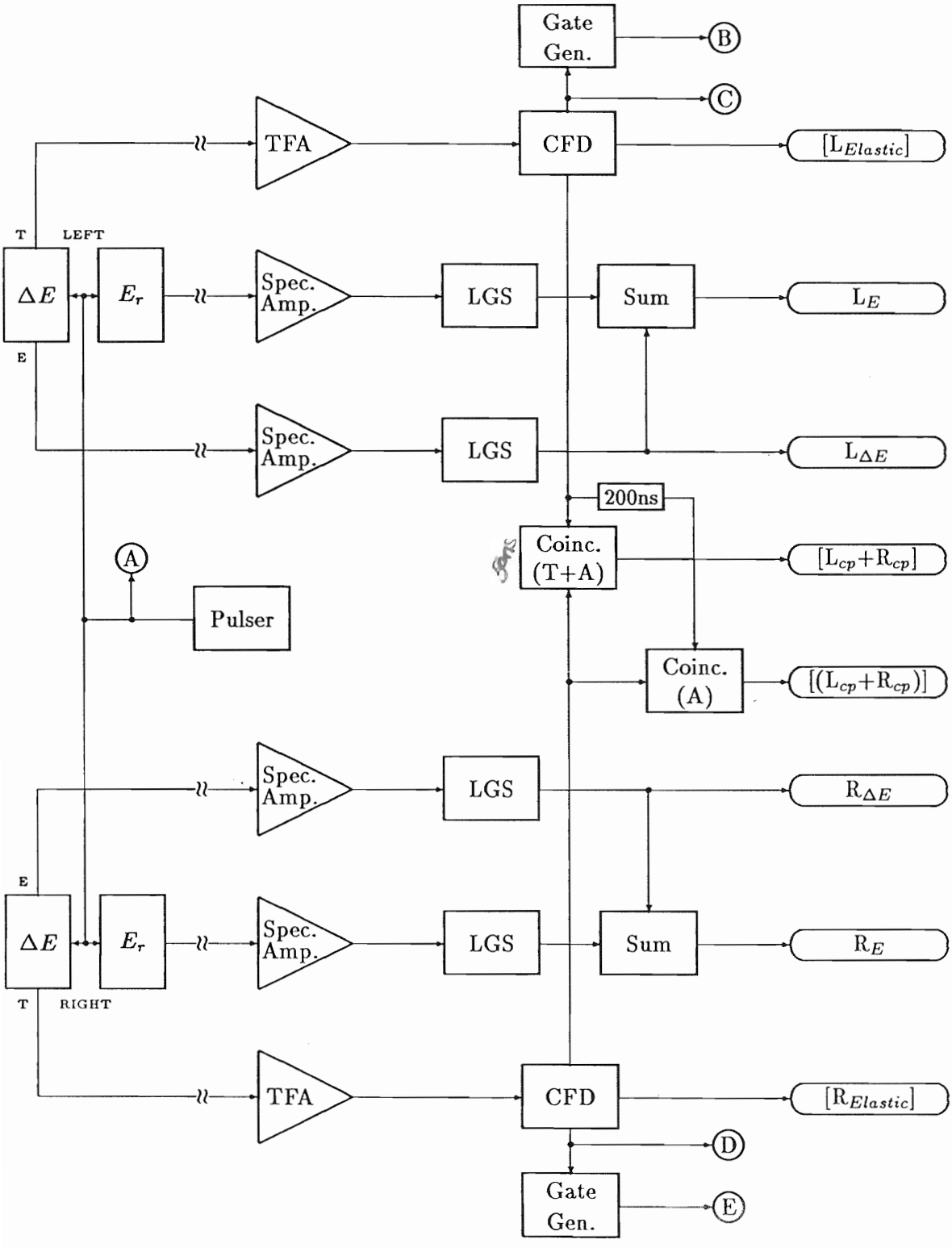

(Continued on next page.)

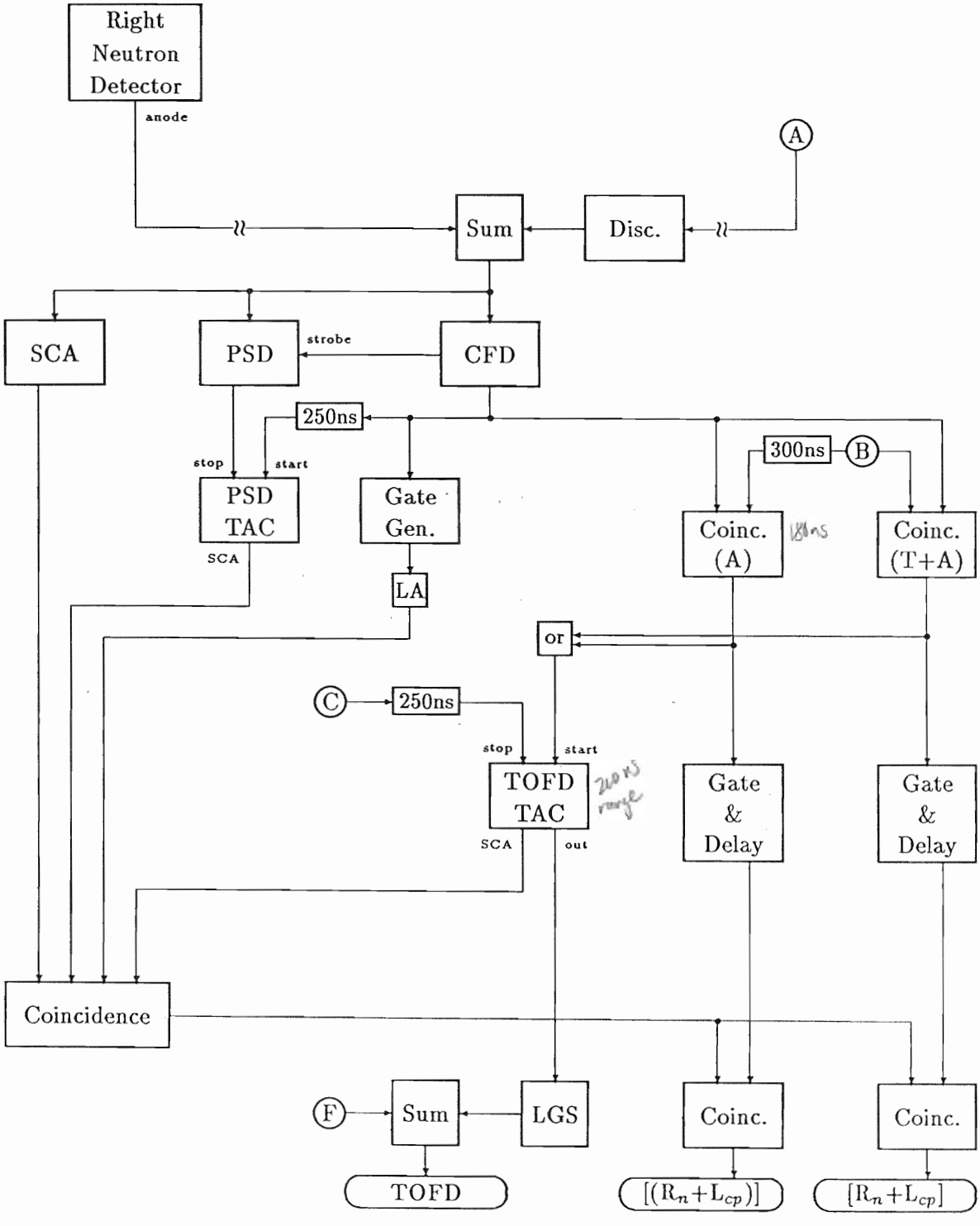

(Continued on next page)

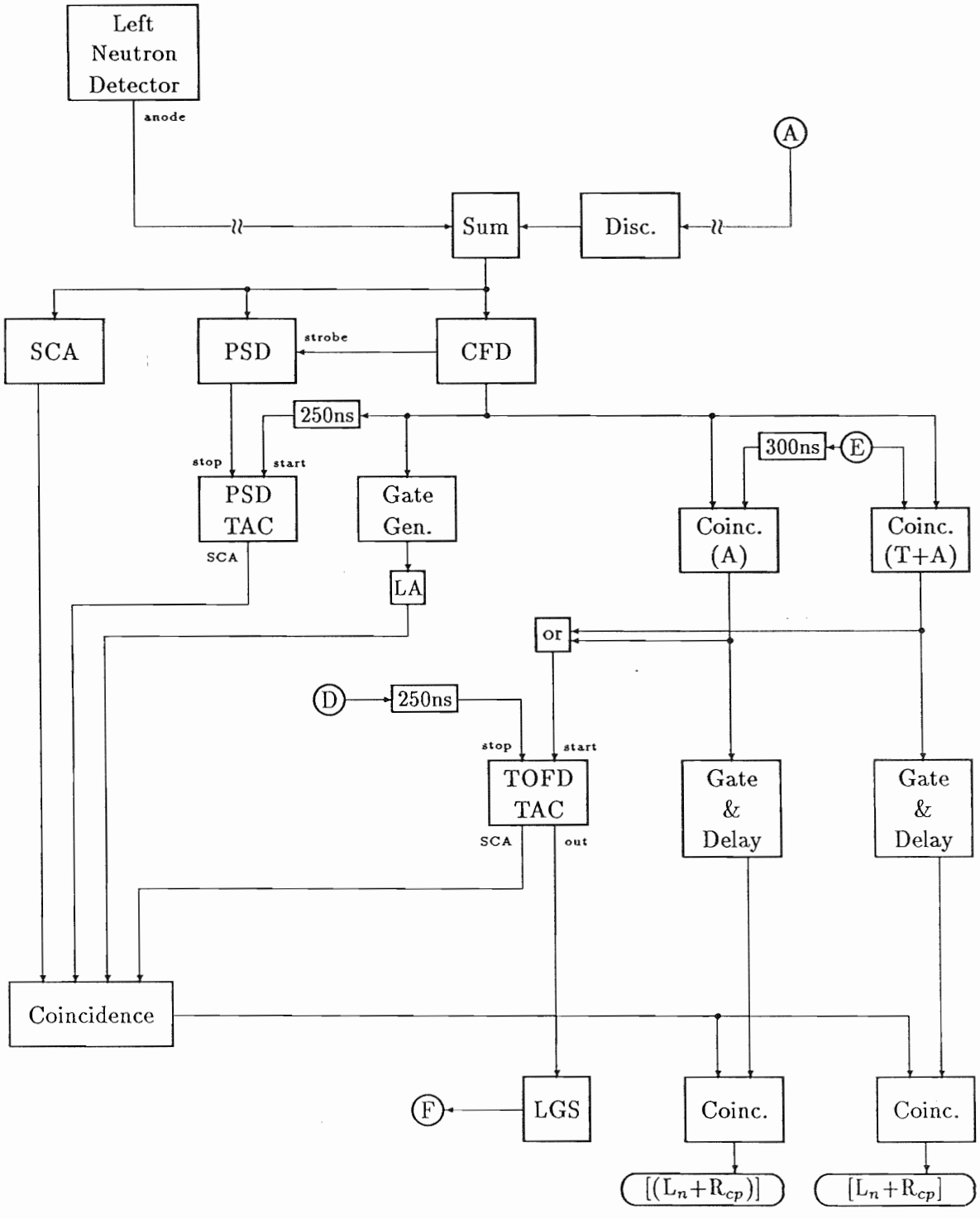

Figure 2.11: Block diagram of the electronics used with the 38° chamber. See text for discussion.

2.10.4-b The 52° Chamber

The detector arrangement for measurements utilizing the 52° scattering chamber was very similar to that used with the 38° scattering chamber. The primary difference between the two setups was the replacement of the neutron detectors with two additional E-detectors placed inside of the chamber. A block diagram showing the electronics is depicted in figure 2.12. Signal processing for the two setups was identical with the major exception that the energy information for the additional detectors was obtained from the pulse height generated by those detectors and not the TOFD. Furthermore, this energy information was digitized by two separate ADC's rather than being summed and digitized by the same ADC as was the case for the TOFD.

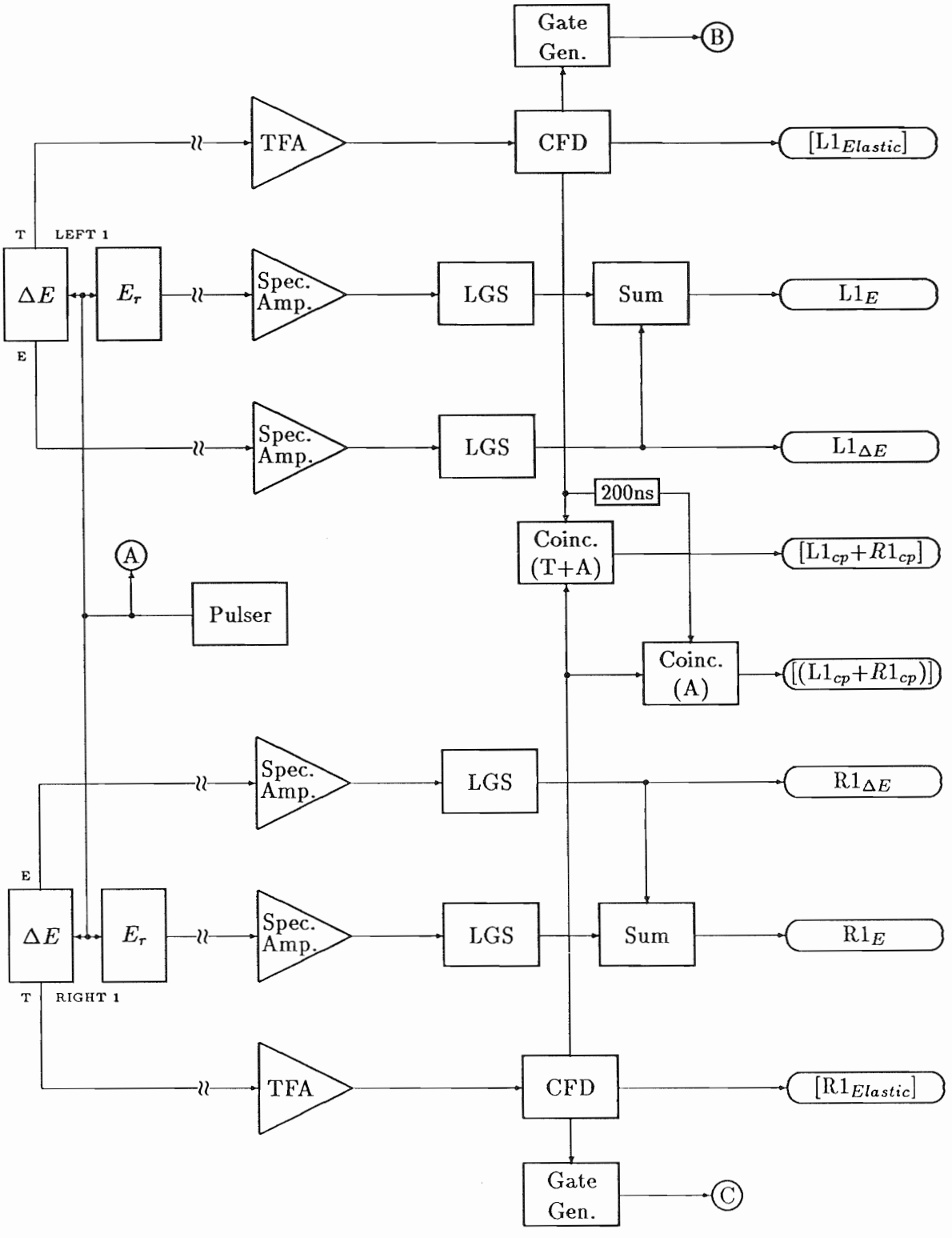

(Continued on next page.)

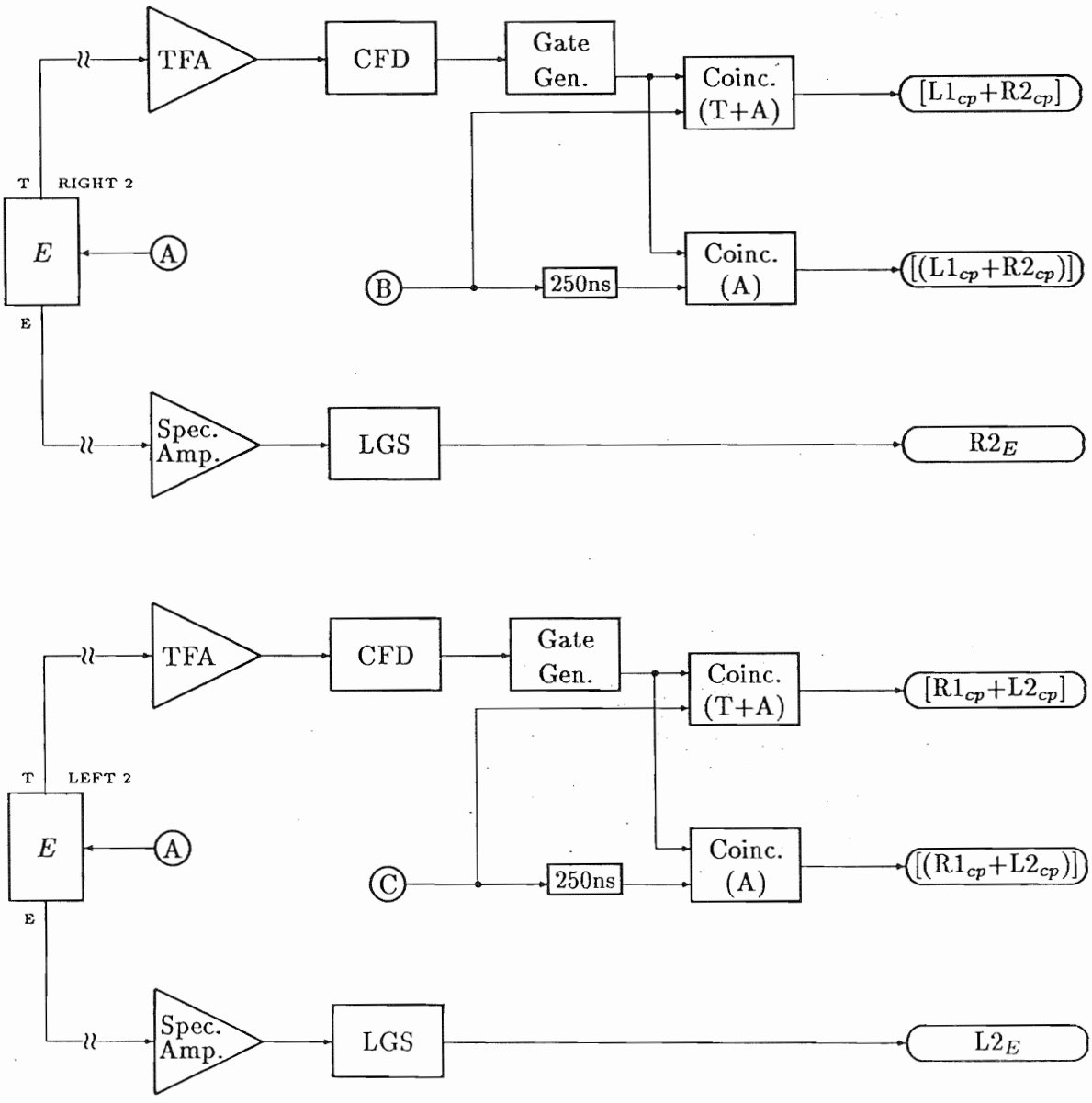

Figure 2.12: Block diagram of the electronics used with the 52° chamber. See text for discussion.

2.10.5 Beam Polarization Measurements

The application of any electromagnetic field that causes the metastable $2S_{\frac{1}{2}}$ atoms to mix with the $2P_{\frac{1}{2}}$ states and subsequently decay to the ground state is referred to as quenching. The spin filter is an example of a device that selectively quenches certain hyperfine states of the metastable atoms leaving the unquenched atoms in a preferred nuclear-spin state. The process of quenching the metastable atoms can also be used to determine the polarization of the deuteron beam. With the polarized ion source (PIS) at TUNL it is possible to quench the beam by applying 200 V dc to a pair of plates located shortly after the cesium canal. The metastable atoms that normally would survive the journey through the spin filter and get ionized in the argon canal to become the polarized component of the beam are quenched to the ground state by the applied electrostatic field. This quenchable beam which decays to the $1S_{\frac{1}{2}}$ ground state via the $1P_{\frac{1}{2}}$ state is not ionized in the argon canal.[3] A comparison of the beam current on a beam stop with and without the quench voltage applied gives a measure of the beam polarization P_b. The defining relationship for P_b is

$$P_b = 1 - \frac{I_Q}{I_0} \tag{2.23}$$

where I_Q is the quenched beam intensity and I_0 is the unquenched beam intensity. Generally the value of P_b is reported in percent and ranges from 0% to 100%; during our measurements P_b was usually in the neighborhood of 70%.

The quench ratio method may slightly underestimate or overestimate the beam polarization, usually by less than 2%. An overestimate is due to the so-called quenchable background, a term that is used to describe that portion of the unpolarized component of the beam that is removed from the beam when the quench voltage is applied, thus causing an overestimate of the beam polarization. During data acquisition the quenchable background was checked every few hours and was minimized by tuning the PIS. Under some circumstances it is also possible to get a slight increase in the unpolarized component of the beam during the quench process, this in turn underestimates the true beam polarization. A very thorough examination of the accuracy of various quenching methods for Lamb-Shift sources is presented by Ohlsen in a Los Alamos report [Ohl70].

[3] The ionization cross section, at 1100 eV, favors the $^2H(2S)+Ar \Rightarrow {}^2H^- + Ar^+$ reaction over the $^2H(1S)+Ar \Rightarrow {}^2H^- + Ar^+$ reaction because the potential energy of $^2H^- + Ar^+$ is only a few electron volts above that of $^2H(2S)+Ar$ for large internucleon separation [Hae67].

The beam polarization was measured at the end of each data step in the four-step sequence. The four-step sequence was repeated a sufficient number of times at each angle to insure that the beam polarization was measured at least 10 times for each step. For this work an error of 1.5% of the theoretical maximum beam polarization ($P_{Z_{max}}$ and $P_{ZZ_{max}}$) was assigned to P_b to cover the uncertainty in the quench-ratio technique (believed to be <1% [Ohl70]) and instabilities in the beam during the measurements. The quenchable background correction was applied to the average value of P_b for each of the steps. (For simplicity and since the correction was always small, from here on P_b will be understood to have the correction already applied.)

In order to obtain the actual deuteron vector and tensor beam polarizations P_Z and P_{ZZ}, one takes the product of P_b for each step and the theoretical maximum values for P_Z and P_{ZZ} for the corresponding step in tables 2.5 and 2.6. For simplicity, we define the beam polarizations $P_Z^{(i)}$ and $P_{ZZ}^{(i)}$ to be

$$\begin{aligned} P_Z^{(i)} &= P_b(i)\, P_{Z_{max}}(i) \\ P_{ZZ}^{(i)} &= P_b(i)\, P_{ZZ_{max}}(i) \end{aligned} \tag{2.24}$$

where i ranges from 1 to 4 and indicates the data step number.

2.10.6 Beam Current Integration

The deuteron beam dump located downstream of the chamber was electrically isolated so that the amount of charge deposited on the beam dump could be monitored by beam current integration techniques. The charge deposited on the beam dump was allowed to flow to ground through a Brookhaven Instruments Corporation model 1000 current integrator, also referred to as a beam current integrator (BCI). The BCI outputs one digital pulse per fixed amount of charge collected. These pulses were counted by a scaler and stored in the computer. A preset value was set by the experimenters and when the scaler reached the preset value the data acquisition was halted. Preset values were only changed after the completion of a full four-step sequence assuring that data were accumulated in each step for the same amount of integrated charge. Monitoring the beam using the BCI is preferred over a detector arrangement designed to measure the scattered beam intensity because the scattered intensity is sensitive to polarization changes and positional shifts in the incident beam. Furthermore, the BCI method contains a much less complicated assortment of electronics and software and therefore is easier to use.

Chapter 3

Data Sorting, Reduction and Analysis

3.1 Introduction

The processing of the data, including the sorting and calculations, was handled within the framework of the TUNL XSYStem data acquisition package. Before describing how XSYS processed the signals a number of terms need to be defined that will be used throughout this chapter:

Count Any event that passes all of the hardware requirements of the electronics setup and is sorted on-line as well as stored on magnetic tape.

Singles Any total energy count from either the left or right ΔE-E detector telescope. The routers for these signals have *Elastic* as a subscript. Note that the label *Elastic* is used simply because the majority of counts in these detectors come from *dd* elastic scattering.

Coincidences Any coincidence between a ΔE-E detector telescope on one side of the beam axis and any detector on the other side of the beam axis.

Conditional Only those coincidences which pass certain particle identification requirements of the ΔE-E telescope arrangement.

Unconditional Any coincidence. No requirements based on particle identification.

Accidental Any coincidence that came from two unrelated events, that is, the two detected particles did not come from the interaction of the same beam deuteron and target deuteron. Note that all counts passing the coincidence requirements of the "accidental" (A) coincidence box in figures 2.11 and 2.12 are represented by routers with a pair of parentheses.

True Any coincidence that came from the same two interacting deuterons. Note that routers generated by the "true + accidental" (T+A) coincidence box in figures 2.11 and 2.12 represent counts coming from both *true* and *accidental* counts.

A collection of XSYS command files and FORTRAN routines were combined to form the on-line software package DDND3 to handle data acquisition. All events that passed the hardware requirements of the electronics (see section 2.10.4) were sorted on-line by DDND3 into one-dimensional (1D) and two-dimensional (2D) histograms for viewing by the experimenters. The coincidence counts (i.e., breakup events) were sorted both on-line and stored on magnetic tape for playback later via the off-line software package DDND3OFF. In the off-line analysis the data could be resorted using different software gates and coincidence conditions than those used in the on-line sorting.

Both the on-line and off-line sorting of the coincidence events started with the 5 digitized linear signals (linears) coming from the ADC's for measurements made in the 38° scattering chamber and 6 linears for measurements made in the 52° scattering chamber (see table 3.1). Seven router bits were used to tell the sorting software which ADC's to read and how to sort the data (see table 3.2). The first bit was used to identify the count as a real event or one generated by the pulser, which was used to monitor gain shifts and measure dead-time corrections. The second bit was used to reject counts where pile-up of two coincidence events occurred simultaneously. The 3^{rd} and 4^{th} bit were used to identify which two detectors had counts in coincidence. Bits 5 and 6 identified the data step number and bit 7 was used to identify those counts due to accidental coincidences. As can be seen in table 3.2, three linears[1] ($E_\tau^{left}, \Delta E^{left}, TOFD$

[1]We do not distinguish between $TOFD^{left}$ and $TOFD^{right}$ because the TOFD from both detectors was fed into the same ADC. Hardware coincidence requirements passed signals coming only from coincidences on opposite sides of the beam axis. Furthermore, if both neutron detectors had valid coincidences at the same time then those counts would be rejected through the pile-up bit.

Scattering Chamber	Linear Signals					
38°	E_r^{left}	ΔE^{left}	E_r^{right}	ΔE^{right}	$TOFD$	
52°	E_r^{left}	ΔE^{left}	E_r^{right}	ΔE^{right}	E^{left}	E^{right}

Table 3.1: Linear signals generated by the ADC's. See text for discussion.

or $E_r^{right}, \Delta E^{right}, TOFD$) are needed for each ΔE-E detector telescope+neutron detector coincidence, four linears ($E_r^{left}, \Delta E^{left}, E_r^{right}, \Delta E^{right}$) for each ΔE-E detector telescope+ΔE-E detector telescope coincidence and three linears ($E_r^{left}, \Delta E^{left}, E^{right}$ or $E_r^{right}, \Delta E^{right}, E^{left}$) for each ΔE-E detector telescope+E detector coincidence.

A scalar was used to count the pulses generated by the 5 Hz pulser and a comparison between this value and the number of pulser-generated events that ended up in the coincidence spectra was used to determine the dead time corrections. These corrections were applied to the yields used in the calculation of observables (see section 3.4.1).

Since all data areas were duplicated in each of the four steps, it is only necessary to review the sorting process for one of the four steps. The first data step will be considered in the discussion of the sorting in the sections below.

A total of 15 2D (64-channel by 64-channel) data areas and two 1D (128-channel) data areas for each data step were used to store and display the data in various combinations. Both of the 1D data areas were used to store singles for the left and right ΔE-E detector telescopes. These data areas were useful for monitoring gain shifts or energy resolution changes and for identifying, through kinematics, any contaminants in the deuterium gas. A sample singles spectrum was shown in the previous chapter (see figure 2.9).

3.2 Raw 2D Coincidence Spectra

In addition to the 2D histograms of $\frac{dE}{dx}$ *vs* E used for particle identification (see figure 2.10), all of the coincidence counts were also sorted into 2D histograms. In the case of coincidences between events in two charged-particle detectors on opposite sides of the beam axis, the data were sorted into 2D histograms of the energy of one of the

Router	Bits	Meaning	
Pulser	0	Real count	
	1	Pulser count	
Pile-up	0	Good count	
	1	Bad count	
Detector Pair	00	ΔE-E^{left}–ΔE-E^{right}	(ΔE-E^{left}–ΔE-E^{right})
	01	ΔE-E^{right}–$TOFD$	(ΔE-E^{right}–E^{left})
	10	ΔE-E^{left}–$TOFD$	(ΔE-E^{left}–E^{right})
Data Step	00	Date step #1	
	01	Date step #2	
	10	Date step #3	
	11	Date step #4	
Accidental	0	"True + Accidental" count	
	1	"Accidental" count	

Table 3.2: Router bits used in the data sorting. The meaning of the router bits for the detector pairs is shown with parenthesis for the 52° scattering chamber and without parenthesis for the 38° scattering chamber.

detected particles versus that of the other detected particle. For the charged-particle–neutron coincidences, the data were sorted into 2D histograms of the energy of the detected charged particle versus the time-of-flight of the neutron, which was measured relative to the arrival of the charged particle at the solid-state detector. This time difference will be referred to as the TOFD (time-of-flight-difference) throughout this paper. See figure 3.1 for examples of these 2D coincidences.

Shown in figure 3.1-A is a 2D histogram of the coincidence counts for the energy deposited in a charged-particle ΔE-E telescope at $\theta_1 = +17.0°$ (horizontal axis) versus the energy deposited in a charged-particle detector at $\theta_2 = -34.5°$ (vertical axis). Here $\theta > 0$ implies that the detector is positioned on the left side according to the Madison convention. As shown in figure 3.1-A two loci result from the $d+d \rightarrow d+p+n$ breakup reaction. The upper locus is for the detection of a deuteron at $+17.0°$ in coincidence with a proton at $-34.5°$, and the lower locus is for a $+17.0°$ proton in coincidence with a $-34.5°$ deuteron.

Shown in figure 3.1-B is a 2D histogram of the coincidence counts for the energy deposited in a charged-particle ΔE-E telescope at $+17.0°$ (horizontal axis) versus the TOFD for a neutron detector at $-34.5°$ (vertical axis). Again kinematics allows for the easy identification of the two resulting loci. The upper locus is for a deuteron detected at $+17.0°$ in coincidence with a neutron detected at $-34.5°$ while the lower locus is for a proton detected at $+17.0°$ in coincidence with a neutron at $-34.5°$. Notice that the two loci merge together at low E_1 energies.

The particle identification information obtained from the ΔE-E telescopes was used to reduce backgrounds in the 2D histograms and to separate the two loci that result from the $d+d \rightarrow d+p+n$ breakup reaction. By imposing particle identification requirements on the charged particles detected using the ΔE-E telescopes, it was possible to select one locus over the other. For instance, in part (A) of figure 3.1 where we had a charged-particle ΔE-E telescope positioned at $\theta_1 = +17.0°$ and a charged-particle detector at $\theta_2 = -34.5°$, we required that the event in the $+17.0°$ detector fell within the proton gate set in the corresponding ΔE-E spectrum as shown in figure 2.10. Thus, sorting the data in this way results in a 2D histogram in which the particle detected at $+17.0°$ was identified as a proton and the type of particle at $\theta_2 = -34.5°$ was unidentified. Figure 3.2-A is an example of a 2D histogram after particle identification has been imposed.[2] By requiring that the particle detected

[2]The energies of the detected particles have been corrected for energy loss in the gas cell. See later in this section for further discussion.

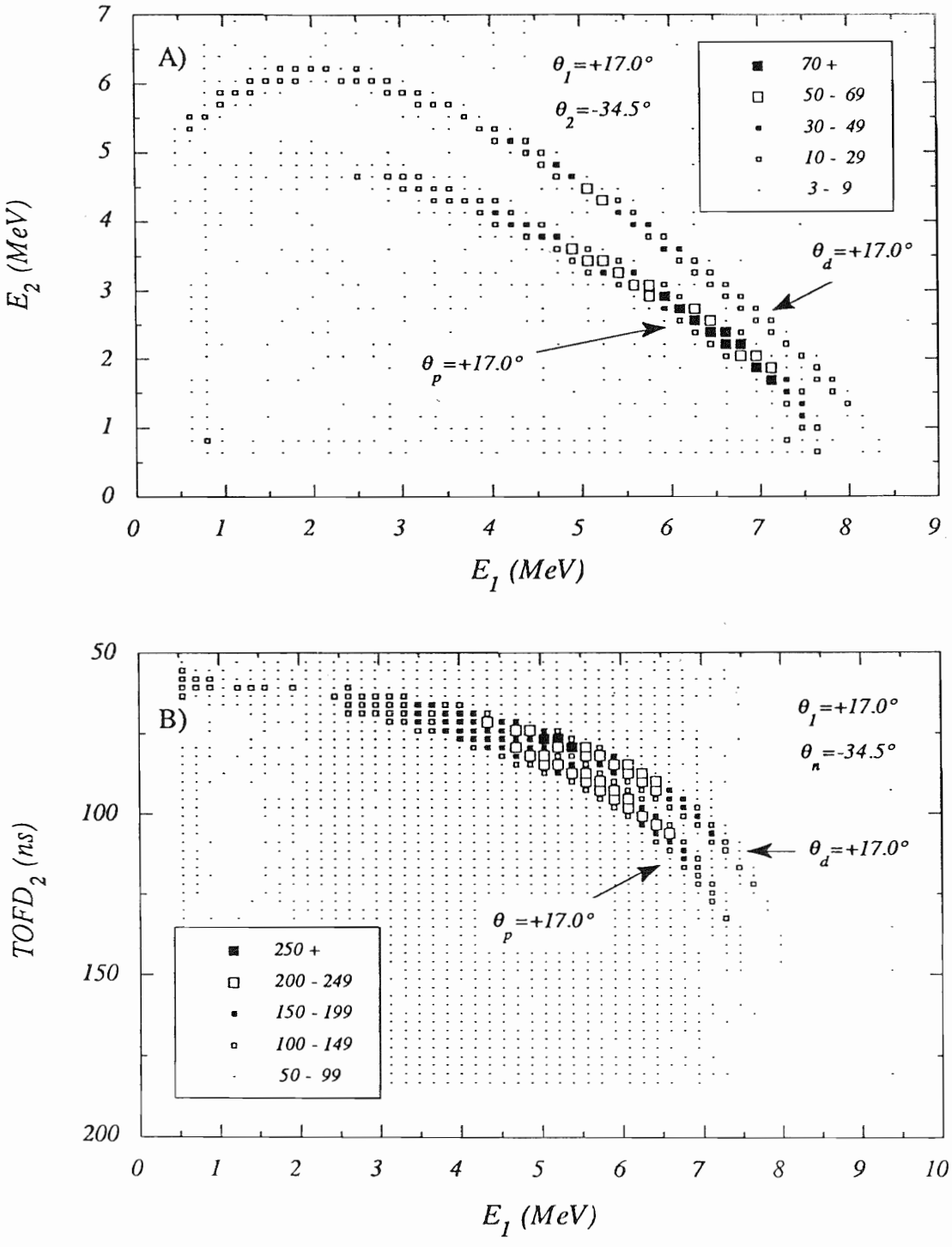

Figure 3.1: Ungated 2D histogram for "true + accidental" counts. Shown in the figure are the coincidence counts (A) as a function of the energy deposited in a ΔE-E telescope at +17.0° versus the energy deposited in a E detector at −34.5° and (B) as a function of the energy deposited in a ΔE-E telescope at +17.0° versus the TOFD for a neutron detector at −34.5°. See text for further details.

at $\theta_1 = +17°$ be a proton selects the lower of the two loci in figure 3.1-A and cleans up the spectrum considerably. Notice that in the upper left corner of figure 3.2-A a portion of the $\theta_d = +17.0°$ locus remains. This is because the 17.0° deuterons in this part of the locus do not have sufficient energy to completely pass through the ΔE detector and are consequently indistinguishable from low-energy protons which stop in the ΔE detector. In the cases where both charged-particle detectors were ΔE-E telescopes, this ambiguity was removed by imposing particle identification requirements on both particles. This was done at the following detector angle pairs: (+10.0°,−10.0°), (+17.0°,−17.0°) and (+19.4°, −19.4°).

For the coincidences between a neutron detector and a ΔE-E telescope we benefited from the fact that the particle detected by the neutron detector is already identified as a neutral particle (either a neutron or a γ-ray). The particle identification is done in the electronics for the neutron detector using PSD as described in section 2.10.2 and is available for the ΔE-E telescope in software as described above. Examples of 2D histograms, which are either unconstrained or constrained by particle identification of the detected charged particles, for a neutron detector in coincidence with a ΔE-E telescope are shown in figures 3.1-B, 3.3-A and 3.4-A. Again notice the degree to which particle identification aids in cleaning up the histogram.

In addition to the "true + accidental" 2D histograms mentioned above for *dp*, *dn* and *pn*, there were an equal number of "accidental" 2D histograms formed. Examples of these are shown in figures 3.2-B, 3.3-B and 3.4-B. Note the scale representing the number of counts is different for parts A and B of these figures.

The alert reader will have noticed that the loci of counts in the 2D "true + accidental" histograms gated by particle identification are slightly shifted to higher energies relative to those in the ungated histograms. This is because the energies plotted in the ungated 2D histograms are the energies of the detected particles while those in the conditional 2D histograms have been corrected for energy loss in the *Kapton* containment foil and the deuterium gas. These corrections range from ~40 keV to ~600 keV depending upon the type of particle (deuteron or proton) and energy. In the cases where the energy correction resulted in a fractional channel shift, the counts were proportioned between the two channels. (Corrections of this type cannot be made on the ungated histograms since the energy loss calculations require knowledge of the mass, charge and energy of the detected particle (see equation 2.21).) No correction was applied to the neutron TOFD since the flight time difference is not appreciably affected by the shift in the charged-particle energy due to the Kapton.

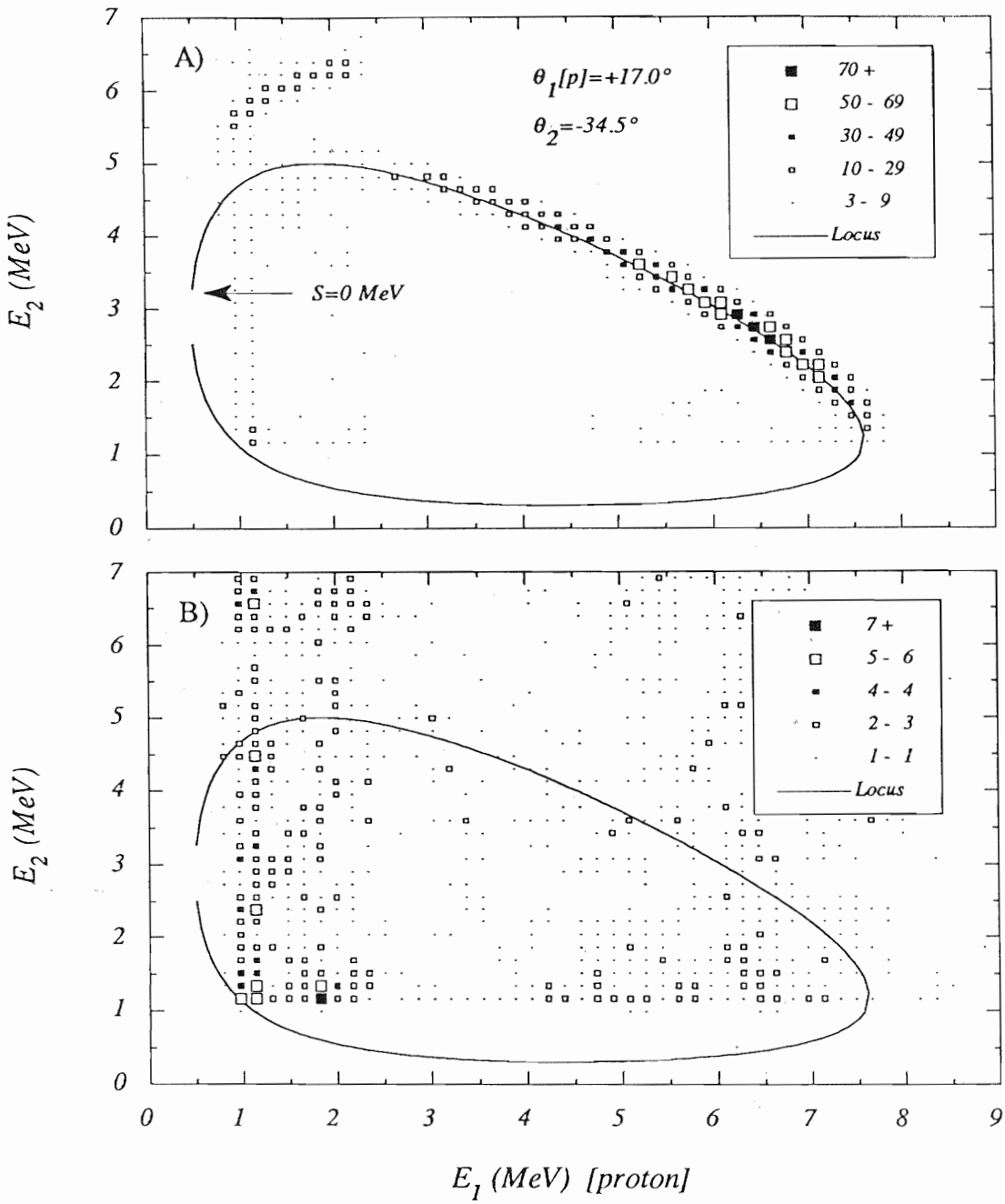

Figure 3.2: Gated 2D histogram for a coincidence between a ΔE-E telescope at +17.0° and a E detector at −34.5°. These spectra are gated by a window set on the protons in the E *vs* ΔE spectrum of the 17.0° ΔE-E telescope as shown in figure 2.10. The data displayed in part (A) are the same "true + accidental" counts as in figure 3.1-A except gated by the proton window in the 17.0° detector while the data in part (B) represent the "accidental" counts. Projection of the data onto the kinematically allowed locus (solid curve) started at the point labeled S=0 MeV and continued clockwise around the locus.

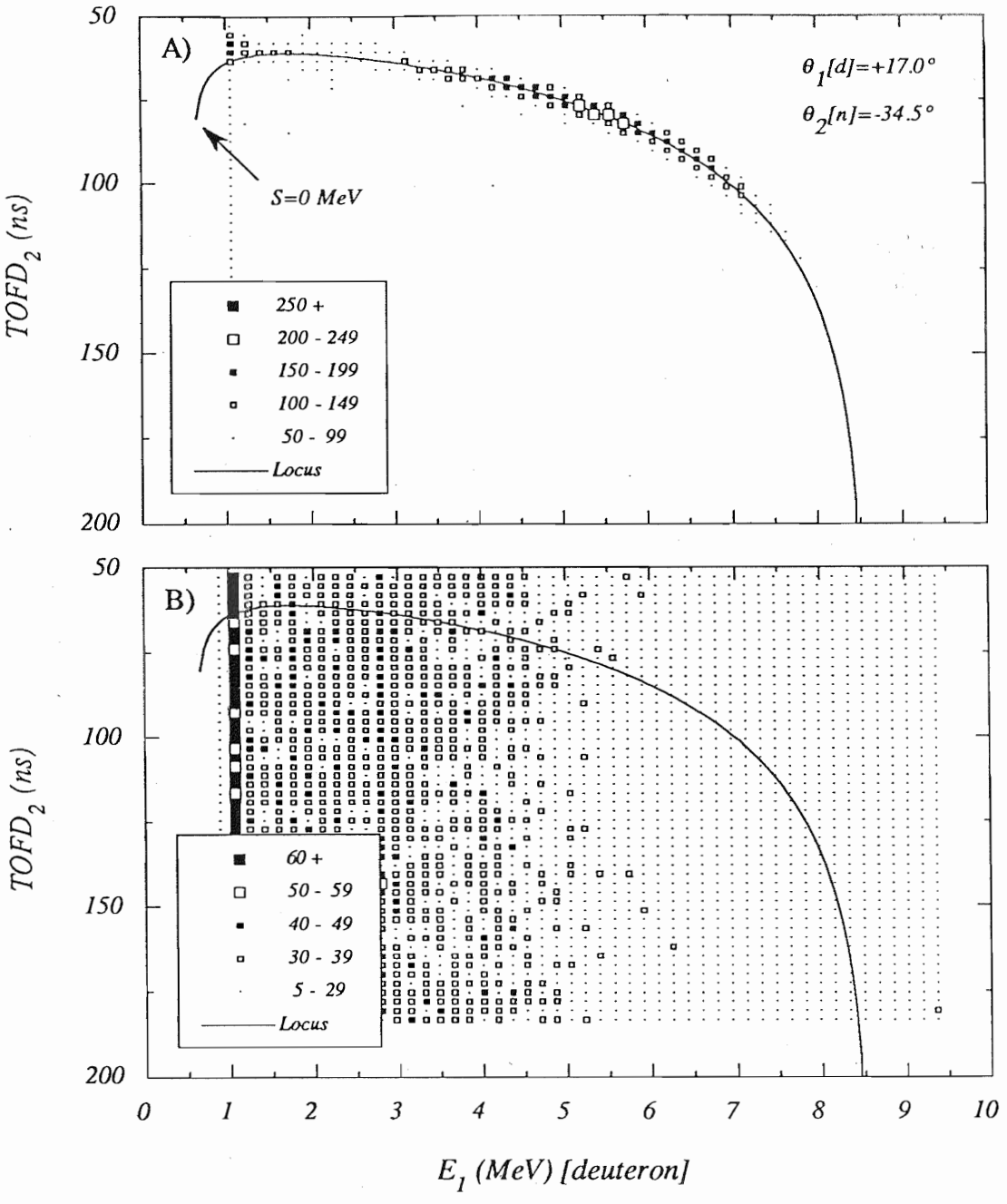

Figure 3.3: Gated 2D histogram for a coincidence between a ΔE-E telescope at $+17.0°$ and a neutron detector at $-34.5°$. These spectra are gated by a window set on the deuterons in the E *vs* ΔE spectra of the 17.0° ΔE-E telescope. The data displayed in part (A) are the same "true + accidental" counts as in figure 3.1-B except gated by the deuteron window in the 17.0° detector and corrected for energy loss in the gas cell, while the data in part (B) represent the "accidental" counts. Projection of the data onto the kinematically allowed locus (solid curve) started at the point labeled S=0 MeV and continued clockwise around the locus.

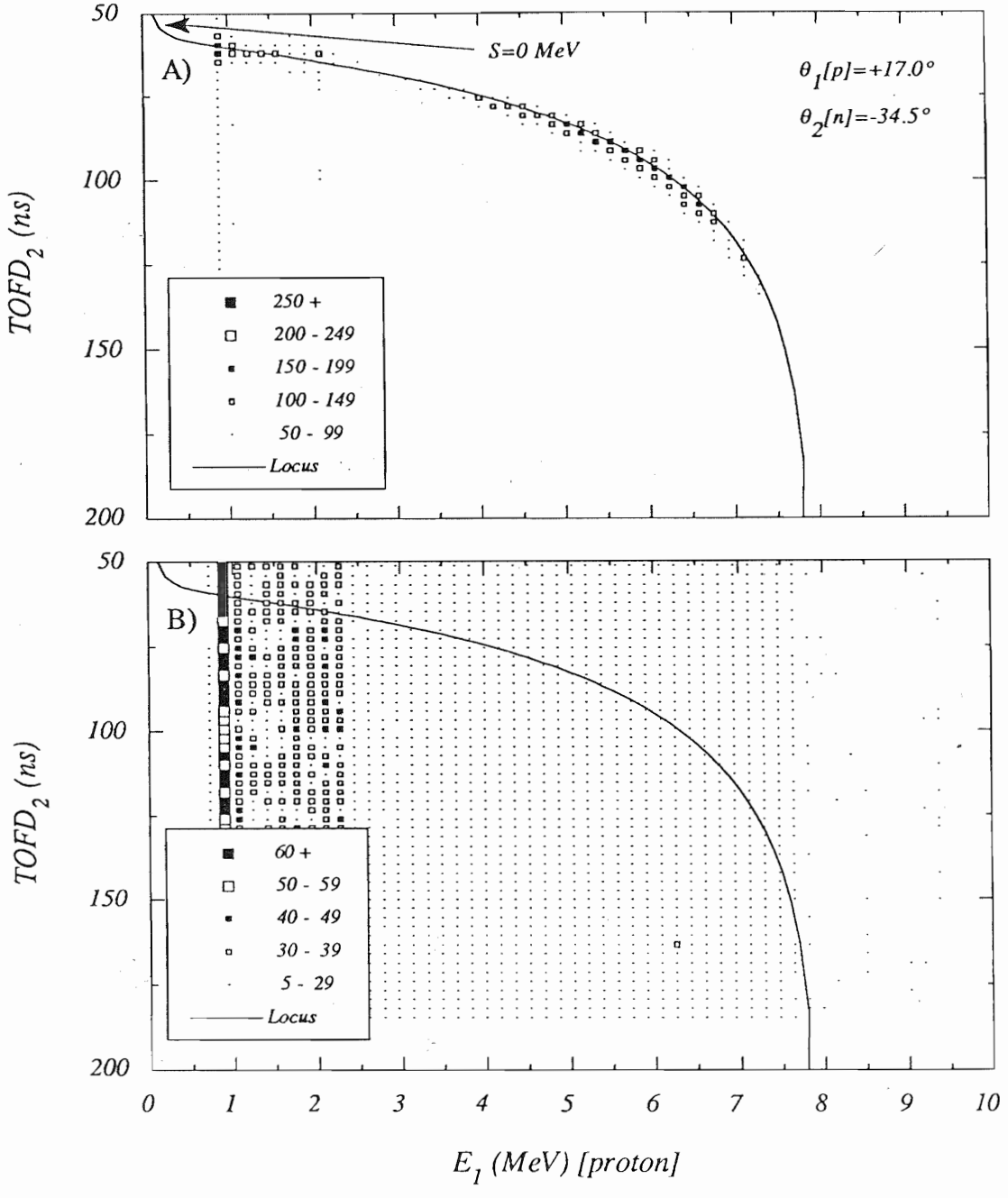

Figure 3.4: Gated 2D histogram for a coincidence between a ΔE-E telescope at $+17.0°$ and a neutron detector at $-34.5°$. These spectra are gated by a window set on the protons in the E *vs* ΔE spectra of the 17.0° ΔE-E telescope. The data displayed in part (A) are the same "true + accidental" counts as in figure 3.1-B except gated by the proton window in the 17.0° detector and corrected for energy loss in the gas cell, while the data in part (B) represent the "accidental" counts. Projection of the data onto the kinematically allowed locus (solid curve) started at the point labeled S=0 MeV and continued clockwise around the locus.

At this point the sorting of the data is complete and the analysis of the data begins. The separation between sorting and analysis is simply that the sorting is performed on an event-by-event basis while the analysis is performed on the histograms formed by the data sorting. Information on individual events is therefore lost.

3.3 Projection of Data onto Locus

Conservation laws of energy and momentum for each pair of angles measured give a well-defined kinematic locus S in the E_1 *vs* E_2 energy space along which all coincidence events from the d+$d \rightarrow d$+p+n breakup reaction must lie [Ohl81]. This locus is shown in figures 3.2, 3.3 and 3.4. Due to the finite geometry and the energy resolution the measured events do not necessarily lie exactly on the kinematic locus but instead lie within an area about the locus. The comparison of data for a breakup reaction to calculations is typically performed after the data has been projected onto the locus. The method of projection employed in the present analysis is the commonly used "minimum distance technique". The shortest distance from each point in a 2D histogram to the ideal locus was determined by minimizing the distance function D, which was defined as

$$D = \sqrt{(E_1^S - E_1)^2 + (E_2^S - E_2)^2} \tag{3.1}$$

where E_1 and E_2 are the energies of the two detected particles, and where E_1^S and E_2^S are the kinematically allowed energies along S for particles emitted at lab angles θ_1 and θ_2, respectively.

For all dp coincidence measurements any count that fell within 250 keV of the kinematically allowed locus was projected onto the locus (as described below). Because the energy resolution associated with the neutron TOFD measurements (dn and pn coincidences) was not as good, the minimum distance for projection onto the locus was increased to 500 keV for these cases.

Projection of the data onto S was performed in 250 keV steps along S. To reduce granularity of the projections due to the energy resolution per channel ($\sim$170 keV/channel) of the 2D histograms and due to the step size chosen for S, a smoothing function was built into the projection code. To obtain an understanding of how this smoothing was performed we will go through an example of the projection process for a coincidence between two charged particles.

The first step was to choose points along the kinematically allowed locus S in

step sizes of 50 keV starting at some arbitrary point on S labeled as S=0 MeV (see figure 3.5 for a close-up view of the projection process). Each breakup event is characterized by the energies of the two detected particles (E_1^{det}, E_2^{det}). The internal resolution of the data sorting software ($\pm$ ~85 keV for both E_1 and E_2) resulted in the energies being rounded off. The central point in each block in the 2D histogram is plotted at the available rounded off energies and represents all events with a given E_1^{det} and E_2^{det} that are contained within the borders of that block. The distance between the centroid of each block in the 2D histogram and the locus (shown as the open-headed arrow in the figure) was determined by using equation 3.1. If this distance was less than or equal to 250 keV then the range along S that was spanned by the block was determined. The counts associated with the particular block under consideration were then equally distributed among the points spanned along S. The two endpoints of the range were also determined by equation 3.1. They are indicated by the closed-headed arrows in the figure 3.5. After all blocks in the 2D histogram were processed, the projected counts along S were then added together in groups of five 50-keV bins, thereby resulting in a projection of 250 keV steps along S.

The projection procedures for *dn* and *pn* coincidences were the same as the *dp* coincidences, except that the TOFD for the neutron was first converted to a neutron energy.

3.3.1 Deuteron-Proton Coincidence Data

Following the procedures outlined above, the sample coincidence data for θ_1[p]=+17.0° and θ_2[d]=−34.5° shown in figure 3.2-A and 3.2-B were projected onto S. (Whenever the letters d, p or n appear inside square brackets, they simply indicate that the particle at that angle has been identified as a deuteron, proton or neutron, respectively.) These projected data are shown in figure 3.6-A where the solid curve represents the "true + accidental" counts of figure 3.2-A and the dashed curve represents the "accidental" counts of figure 3.2-B. Subtracting the "accidental" counts from the "true + accidental" counts results in the "true" counts shown in figure 3.6-B. Notice how clean the spectrum is when particle identification is imposed using a charged-particle ΔE-E telescope in coincidence with a charged-particle detector. If both coincidence detectors had particle identification capabilities the spectra would have been even cleaner and the small bump in the "accidental" counts between 0.5 and 2.5 MeV along S would have been eliminated.

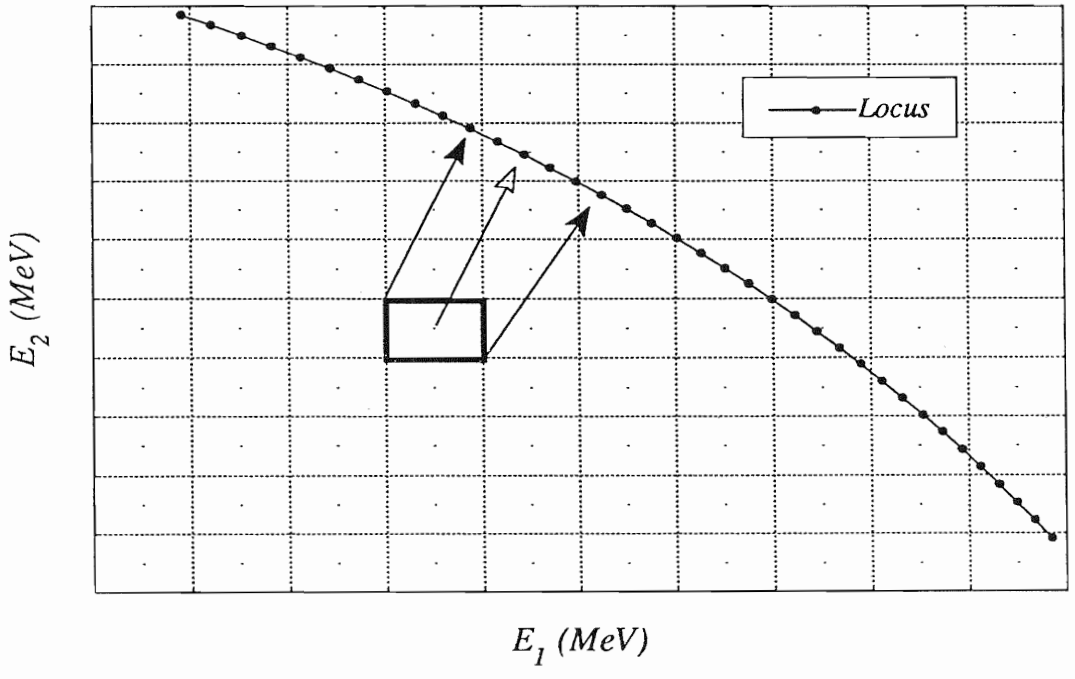

Figure 3.5: 2D projection example. The distance between the closest point on the curve and the center of the highlighted box was measured (indicated by the open-headed arrow). If this distance was within the projection limits then the portion of the locus spanned was determined by finding the closest points along the curve to the extreme edges of the block (indicated by the closed-headed arrows). The counts within the block were then equally divided among the points spanned along S.

As stated earlier in this chapter only step 1 of the 4-step sequence in the data acquisition is being shown here. As will be seen in section 3.4 the (small) differences in the shapes of the projected spectra for steps 1–4 will give rise to the analyzing powers.

3.3.2 Deuteron-Neutron Coincidence Data

The data shown in the sample coincidence histogram for θ_1[d]=+17.0° and θ_2[n]=−34.5° in figure 3.3-A and 3.3-B were projected in the same manner outlined above. The projected "true + accidental" counts of figure 3.3-A are shown as the solid curve in 3.7-A while the projected "accidental" counts of figure 3.3-B are shown as the dashed curve in figure 3.7-A. The "true" counts obtained by subtraction are shown in figure 3.7-B.

A problem with the data in figure 3.7-B is the bump between S=1.0 and 2.5 MeV. This bump is in the region where particle identification for the charged-particle ΔE-E telescope is inadequate. For this reason analyzing powers were only computed from 2.5 to 11 MeV along S. Similarly, analyzing powers for other deuteron-neutron coincidence measurements were computed only for regions along S where particle identification was unambiguous.

Also notice the relatively high background due to accidental counts in figure 3.7-A, especially in the region beyond S=9.0 MeV. This can easily be understood by referring to figure 3.3-B. The accidental background is quite flat in the TOFD space of the neutron, but heavily peaked in the low-energy region of the energy space of the deuteron. At first this seems inconsistent with the observation that the high background starts at about 7 MeV deuteron energy (9 MeV along S) and continues clockwise to about 8.5 MeV deuteron energy, where the spectrum ends because the deuterons did not have sufficient energy to exit the gas cell. However, in the TOFD between 50 and 100 ns a small time difference corresponds to a large neutron energy difference, while a small time difference in the region between 150 and 200 ns corresponds to a small neutron energy difference. This means that starting at S=0, the number of blocks within 500 keV of the locus projected onto each point on the locus S increases as one steps along S in even step sizes. Thus, in the deuteron energy range between 7 and 8.5 MeV, a large background results from projecting a large number of blocks, each with relatively few counts, onto each point along S. This is in contrast to the region between 2 and 3 MeV deuteron energy where very few blocks, each with

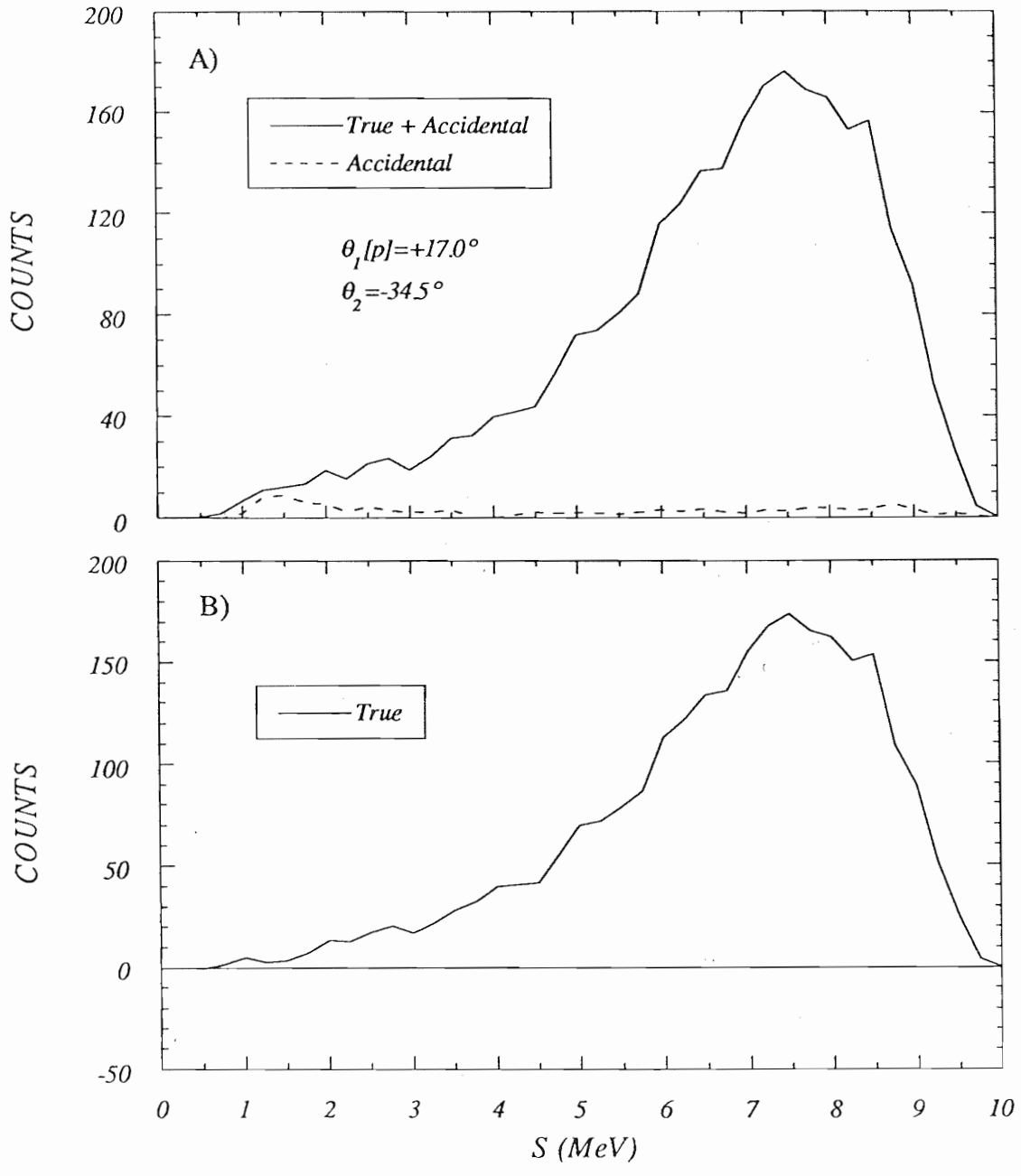

Figure 3.6: Projected data for (θ_d,θ_p)=(+34.5°, −17.0°). The solid and dashed curves in part (A) represent projection of "true + accidental" data of figure 3.2-A and "accidental" data of figure 3.2-B, respectively. The difference of the counts is represented in part (B).

many counts, are projected onto each point along S, resulting in a low background.

3.3.3 Proton-Neutron Coincidence Data

Again following the above described projection method, the data in the histogram for θ_1[p]=+17.0° and θ_2[n]=−34.5° (figure 3.4-A and 3.4-B) are transformed into the projected data of figure 3.8-A. The projected "true + accidental" counts of figure 3.4-A are shown as the solid curve in figure 3.8-A while the projected "accidental" counts of figure 3.4-B are shown as the dashed curve in figure 3.8-A. The "true" counts shown in figure 3.8-B are obtained by subtraction of the "accidental" counts from the "true + accidental" counts.

Particle identification in the charged-particle ΔE-E telescope is ambiguous for protons in the region below S=5 MeV; therefore analyzing powers were only computed between 5 and 12 MeV along S. Similarly, analyzing powers for other pairs of angles for proton-neutron coincidence measurements were computed only for regions along S where particle identification was unambiguous.

3.4 Polarization Observables

The effect that the incoming beam polarization and the reaction analyzing powers has on the cross section of any reaction induced by a polarized spin-1 projectile in Cartesian notation can be expressed by the following general expression [Ohl81]

$$\begin{aligned}\sigma(\xi) \;=\; \sigma_o(\xi)\Big\{1 &+ \frac{3}{2}\left[P_x A_x(\xi) + P_y A_y(\xi) + P_z A_z(\xi)\right] \\ &+ \frac{2}{3}\left[P_{xy} A_{xy}(\xi) + P_{yz} A_{yz}(\xi) + P_{zx} A_{zx}(\xi)\right] \\ &+ \frac{1}{3}\left[P_{xx} A_{xx}(\xi) + P_{yy} A_{yy}(\xi) + P_{zz} A_{zz}(\xi)\right]\Big\} \qquad (3.2)\end{aligned}$$

where the shorthand notation $\sigma(\xi)$ has been used for the differential cross section $\frac{d\sigma(\xi)}{d\xi}$; $\sigma_o(\xi)$ is the "unpolarized" differential cross section; P_i, P_{ij} are the beam polarization moments given in section 2.3; A_i, A_{ij} are the Cartesian analyzing power functions; and ξ represents any appropriate set of kinematic variables. For this work, in which there are three particles in the final state, the kinematic variables will be taken as E_1,

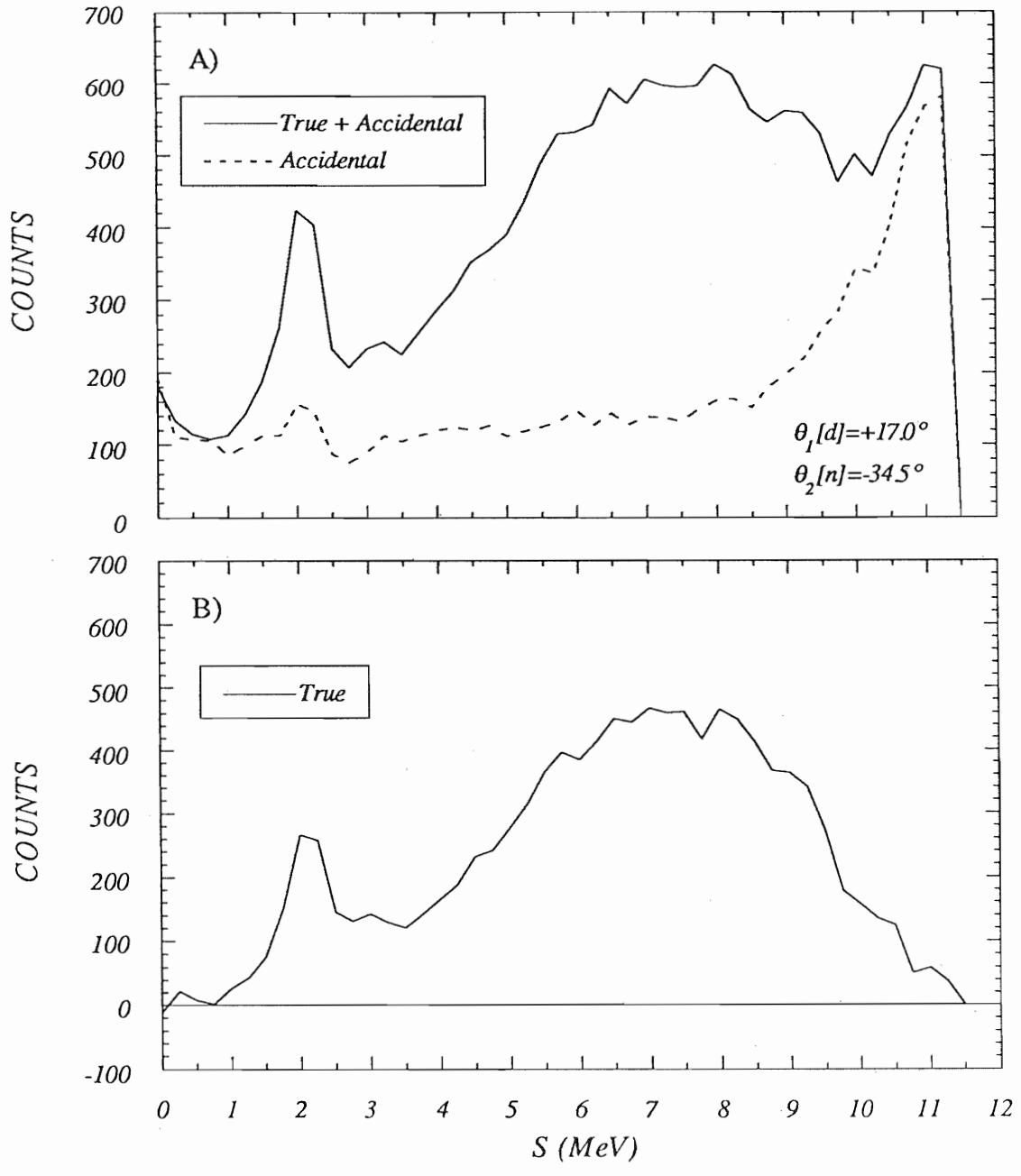

Figure 3.7: Projected data for (θ_d,θ_n)=(+17.0°, −34.5°). The solid and dashed curves in part (A) represent projection of "true + accidental" data of figure 3.3-A and "accidental" data of figure 3.3-B, respectively. The difference of the counts is represented in part (B).

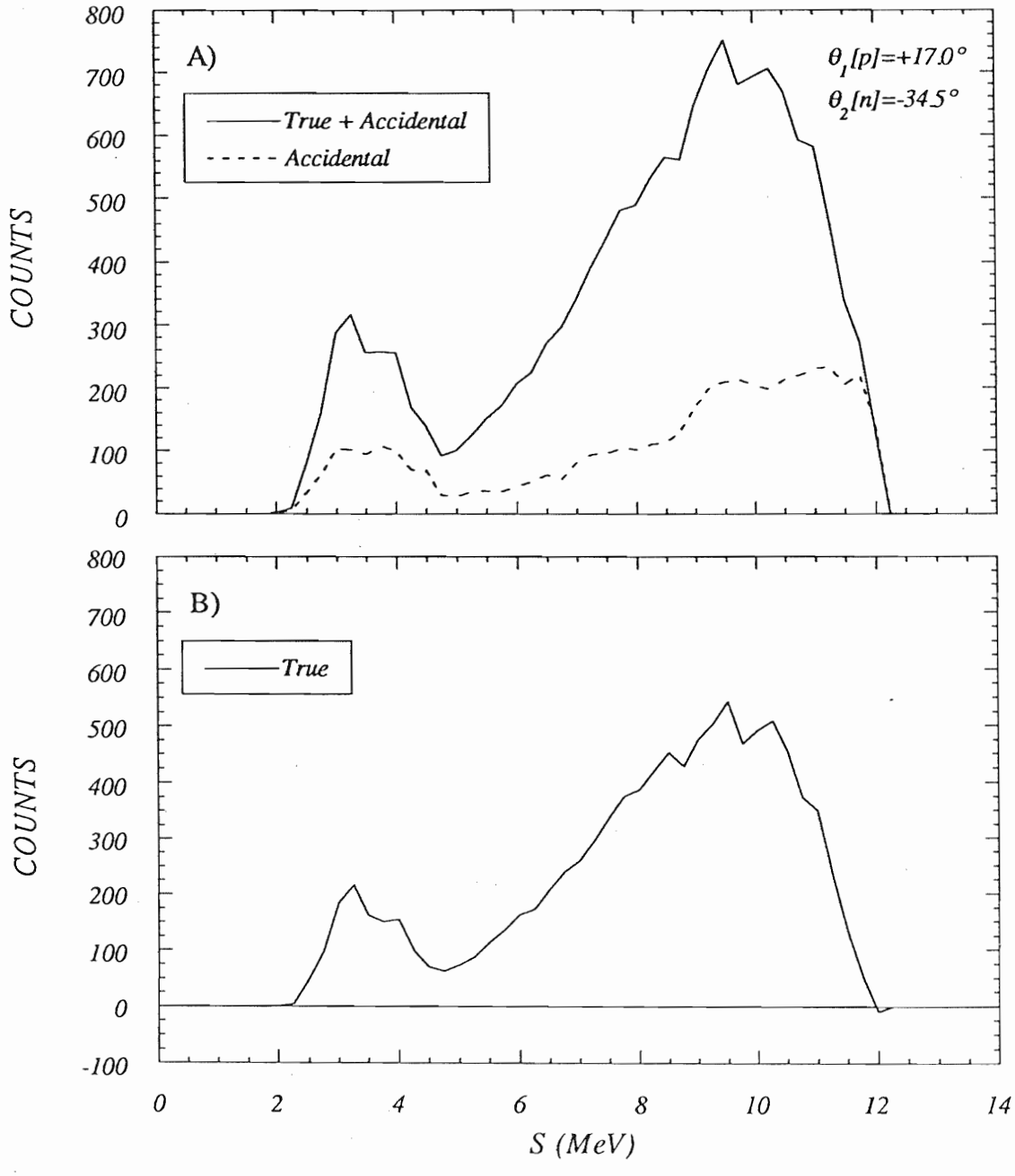

Figure 3.8: Projected data for (θ_p,θ_n)=(+17.0°, −34.5°). The solid and dashed curves in part (A) represent projection of "true + accidental" data of figure 3.4-A and "accidental" data of figure 3.4-B, respectively. The difference of the counts is represented in part (B).

E_2, θ_1, θ_2, ϕ_1 and ϕ_2 where particles "1" and "2" are detected in coincidence while particle "3" is left undetected. The actual values of ϕ_1 and ϕ_2 are unimportant in reporting the results of this work; only the difference between the two matters. For this reason we will set $\phi_1 \equiv \phi$ with ϕ defined in section 2.2. For simplicity ξ will be suppressed whenever possible. It is easy to see that in the case of an unpolarized incident beam ($P_i = P_{ij} = 0$) the differential cross section in equation 3.2 reduces to σ_o.

Substitution of equations 2.17 and 2.18 for the beam moments into equation 3.2 yields

$$\begin{aligned}\sigma &= \sigma_o \Big\{1 - \frac{3}{2} P_Z A_x \sin\beta \sin\phi - \frac{3}{2} P_Z A_y \sin\beta \cos\phi - \frac{3}{2} P_Z A_z \cos\beta \\ &\quad - P_{ZZ} A_{xy} \sin^2\beta \cos\phi \sin\phi - P_{ZZ} A_{yz} \sin\beta \cos\beta \cos\phi \\ &\quad - P_{ZZ} A_{xz} \sin\beta \cos\beta \sin\phi + \frac{1}{6} P_{ZZ} A_{xx} (3\sin^2\beta \sin^2\phi - 1) \\ &\quad + \frac{1}{6} P_{ZZ} A_{yy} (3\sin^2\beta \cos^2\phi - 1) + \frac{1}{6} P_{ZZ} A_{zz} (3\cos^2\beta - 1)\Big\}. \quad (3.3)\end{aligned}$$

For coplanar geometries, in which the projectile momentum and the momenta of all the outgoing particles lie in a single plane (this implies $|\phi_1 - \phi_2| = 0$ or π), parity conservation requires the A_x, A_z, A_{xy} and A_{yz} observables to vanish [Ohl81]. Taking this into account along with the relationship $A_{xx} + A_{yy} + A_{zz} = 0$ coming from the overcompleteness of the Cartesian tensors, we obtain:

$$\begin{aligned}\sigma &= \sigma_o \Big\{1 + \frac{3}{2} P_Z A_y \sin\beta \cos\phi \\ &\quad - P_{ZZ} A_{xz} \sin\beta \cos\beta \sin\phi \\ &\quad - \frac{1}{4} P_{ZZ} (A_{xx} - A_{yy}) \sin^2\beta \cos 2\phi \\ &\quad + \frac{1}{4} P_{ZZ} A_{zz} (3\cos^2\beta - 1)\Big\}. \quad (3.4)\end{aligned}$$

For reference, the general expression for the cross section of any reaction induced

by a polarized spin-1 projectile in spherical tensor notation is [Ohl72]:

$$\begin{aligned}\sigma &= \sigma_\circ \{1 + t_{10}T_{10} + 2Re(t_{11})Re(T_{11}) + 2Im(t_{11})Im(T_{11}) \\ &\quad + t_{20}T_{20} + 2Re(t_{21})Re(T_{21}) + 2Im(t_{21})Im(T_{21}) \\ &\quad +2Re(t_{22})Re(T_{22}) + 2Im(t_{22})Im(T_{22})\} \end{aligned} \tag{3.5}$$

where the spherical analyzing tensors T_{kq} are a function of the kinematic variables ξ. The terms involving T_{10}, $Re(T_{11})$, $Im(T_{21})$ and $Im(T_{22})$ vanish since parity conservation in the projectile helicity frame restricts each analyzing tensor to be pure real, pure imaginary or zero [Ohl72]. Substitution of the spherical beam moments t_{kq} from equations 2.19 and 2.20 into equation 3.5 yields

$$\begin{aligned}\sigma &= \sigma_\circ \Big\{1 + \sqrt{2}\,\tau_{10}\, iT_{11}\, \sin\beta\cos\phi \\ &\quad + \frac{1}{2}\,\tau_{20}\, T_{20}\, (3\cos^2\beta - 1) \\ &\quad + \sqrt{6}\,\tau_{20}\, T_{21}\, \sin\beta\cos\beta\sin\phi \\ &\quad - \sqrt{\frac{3}{2}}\,\tau_{20}\, T_{22}\, \sin^2\beta\cos 2\phi\Big\}. \end{aligned} \tag{3.6}$$

The conversion from Cartesian to spherical tensor analyzing powers is:

$$\begin{aligned} iT_{11} \equiv Re(iT_{11}) &= \frac{\sqrt{3}}{2}\, A_y \\ T_{20} \equiv Re(T_{20}) &= \frac{1}{\sqrt{2}}\, A_{zz} \\ T_{21} \equiv Re(T_{21}) &= -\frac{1}{\sqrt{3}}\, A_{xz} \\ T_{22} \equiv Re(T_{22}) &= \frac{1}{2\sqrt{3}}\,(A_{xx} - A_{yy}) = -\frac{1}{2\sqrt{3}}\,(2A_{yy} + A_{zz}) \end{aligned} \tag{3.7}$$

and from spherical to Cartesian notation:

$$\begin{aligned} A_y &= \frac{2}{\sqrt{3}} iT_{11} \\ A_{xx} &= \sqrt{3}\,T_{22} - \frac{1}{\sqrt{2}} T_{20} \\ A_{yy} &= -\sqrt{3}\,T_{22} - \frac{1}{\sqrt{2}} T_{20} \\ A_{zz} &= \sqrt{2}\,T_{20} \\ A_{xz} &= -\sqrt{3}\,T_{21} \ . \end{aligned} \tag{3.8}$$

3.4.1 Calculation of A_{yy}

As was stated earlier (see section 2.10) the A_y and A_{yy} data were taken simultaneously and involved a four-step sequence of runs. The differential cross section σ_i ($i = 1, 2, 3, 4$) for each step is obtained by substituting the beam polarization conditions for each of the four steps (see table 2.5) into equation 3.4 and replacing the beam polarization moments P_Z and P_{ZZ} with the actual beam moments according to equation 2.24. After simplifying we obtain

$$\begin{aligned} \sigma_1 &= \sigma_\circ \left\{ 1 + \frac{3}{2} P_Z^{(1)} A_y - \frac{1}{4} P_{ZZ}^{(1)} A_{zz} - \frac{1}{4} P_{ZZ}^{(1)} (A_{xx} - A_{yy}) \right\} \\ \sigma_2 &= \sigma_\circ \left\{ 1 - \frac{3}{2} P_Z^{(2)} A_y - \frac{1}{4} P_{ZZ}^{(2)} A_{zz} - \frac{1}{4} P_{ZZ}^{(2)} (A_{xx} - A_{yy}) \right\} \\ \sigma_3 &= \sigma_\circ \left\{ 1 - \frac{3}{2} P_Z^{(3)} A_y - \frac{1}{4} P_{ZZ}^{(3)} A_{zz} - \frac{1}{4} P_{ZZ}^{(3)} (A_{xx} - A_{yy}) \right\} \\ \sigma_4 &= \sigma_\circ \left\{ 1 + \frac{3}{2} P_Z^{(4)} A_y - \frac{1}{4} P_{ZZ}^{(4)} A_{zz} - \frac{1}{4} P_{ZZ}^{(4)} (A_{xx} - A_{yy}) \right\} . \end{aligned} \tag{3.9}$$

Assuming that the beam polarization moments do not change when the spin quantization axis $\hat{s}$ is rotated by 180° in the Wien filter, we can substitute the experimental

averages $P_Z^{(12)} \equiv \frac{1}{2}\left(P_Z^{(1)} + P_Z^{(2)}\right)$ and $P_{ZZ}^{(12)} \equiv \frac{1}{2}\left(P_{ZZ}^{(1)} + P_{ZZ}^{(2)}\right)$, for the beam moments in steps 1 and 2 and substitute $P_Z^{(34)} \equiv \frac{1}{2}\left(P_Z^{(3)} + P_Z^{(4)}\right)$ and $P_{ZZ}^{(34)} \equiv \frac{1}{2}\left(P_{ZZ}^{(3)} + P_{ZZ}^{(4)}\right)$ for steps 3 and 4. Also, since $A_{xx} + A_{yy} + A_{zz} = 0$ implies $-A_{zz} - A_{xx} + A_{yy} = 2A_{yy}$, we can further simplify the cross sections by factoring out $\frac{1}{4}P_{ZZ}$ in the last two terms in equation 3.9 and substituting for the quantity $-A_{zz} - A_{xx} + A_{yy}$ to give:

$$\begin{aligned}
\sigma_1 &= \sigma_\circ \left\{1 + \frac{3}{2}P_Z^{(12)}A_y + \frac{1}{2}P_{ZZ}^{(12)}A_{yy}\right\} \\
\sigma_2 &= \sigma_\circ \left\{1 - \frac{3}{2}P_Z^{(12)}A_y + \frac{1}{2}P_{ZZ}^{(12)}A_{yy}\right\} \\
\sigma_3 &= \sigma_\circ \left\{1 - \frac{3}{2}P_Z^{(34)}A_y + \frac{1}{2}P_{ZZ}^{(34)}A_{yy}\right\} \\
\sigma_4 &= \sigma_\circ \left\{1 + \frac{3}{2}P_Z^{(34)}A_y + \frac{1}{2}P_{ZZ}^{(34)}A_{yy}\right\}. \qquad (3.10)
\end{aligned}$$

Combining the cross sections for the first two steps and for the last two steps yields

$$\sigma_1 + \sigma_2 = \sigma_\circ \left\{2 + P_{ZZ}^{(12)}A_{yy}\right\} \qquad (3.11)$$

$$\sigma_3 + \sigma_4 = \sigma_\circ \left\{2 + P_{ZZ}^{(34)}A_{yy}\right\}. \qquad (3.12)$$

Using equation 3.12 and solving for $\sigma_\circ$ results in

$$\sigma_\circ = \frac{\sigma_3 + \sigma_4}{2 + P_{ZZ}^{(34)}A_{yy}} \quad . \qquad (3.13)$$

Substituting $\sigma_\circ$ into equation 3.11 and solving for A_{yy} gives

$$A_{yy} = \frac{2(\sigma_3 + \sigma_4) - 2(\sigma_1 + \sigma_2)}{(\sigma_1 + \sigma_2)P_{ZZ}^{(34)} - (\sigma_3 + \sigma_4)P_{ZZ}^{(12)}} \quad . \qquad (3.14)$$

After dead-time corrections have been applied and backgrounds subtracted, the number of true coincidence counts N for each 250 keV segment along S, recorded for a given set of kinematic variables ξ, is simply related to the differential cross section σ by $N = \epsilon I t \sigma$. Here ϵ is the product of the detector efficiencies for the coincidence, I is the beam flux in particles/cm^2, t is the target thickness in nuclei/cm^2. Noting

that the reaction plane has been defined for a *left* scattered deuteron in dp and dn coincidences and a *left* scattered proton for pn coincidences, we use the superscript "L" to rewrite the expression for A_{yy}:

$$A_{yy}^{(L)} = \frac{2(N_3^{(L)} + N_4^{(L)}) - 2(N_1^{(L)} + N_2^{(L)})}{(N_1^{(L)} + N_2^{(L)})P_{ZZ}^{(34)} - (N_3^{(L)} + N_4^{(L)})P_{ZZ}^{(12)}} \quad . \tag{3.15}$$

To help eliminate instrumental asymmetries, for every *left-right* detector pair there was an identical *right-left* detector pair used at the same time. Using the reaction plane defined above, a *right* scattered deuteron (for dp or dn) or proton (for pn) would have an azimuthal angle $\phi^{(R)} = \phi^{(L)} + \pi$ where $\phi^{(L)}$ and $\phi^{(R)}$ are the azimuthal angles for *left-right* and *right-left* scattering, respectively. Substituting into equation 3.4 and solving for $A_{yy}^{(R)}$ gives

$$A_{yy}^{(R)} = \frac{2(N_3^{(R)} + N_4^{(R)}) - 2(N_1^{(R)} + N_2^{(R)})}{(N_1^{(R)} + N_2^{(R)})P_{ZZ}^{(34)} - (N_3^{(R)} + N_4^{(R)})P_{ZZ}^{(12)}} \tag{3.16}$$

for a *right-left* coincidence with the obvious "R" superscript.

Taking the root-mean-square (RMS) of A_{yy}^{L} and A_{yy}^{R} gives

$$A_{yy}^{(RMS)} = \frac{2(N_{34} + N_{43}) - 2(N_{12} + N_{21})}{(N_{12} + N_{21})P_{ZZ}^{(34)} - (N_{34} + N_{43})P_{ZZ}^{(12)}} \tag{3.17}$$

where

$$\begin{aligned} N_{12} &\equiv \sqrt{N_1^{(L)}\, N_2^{(R)}} \\ N_{21} &\equiv \sqrt{N_2^{(L)}\, N_1^{(R)}} \\ N_{34} &\equiv \sqrt{N_3^{(L)}\, N_4^{(R)}} \\ N_{43} &\equiv \sqrt{N_4^{(L)}\, N_3^{(R)}} \quad . \end{aligned} \tag{3.18}$$

The RMS value above cancels all instrumental asymmetries to first order provided that the beam current integration and detector efficiencies are independent of the data accumulation step. The background-corrected coincidence yields have been corrected for computer and electronic dead time, insuring that the detector efficiencies for all

four steps are identical. To help cancel any false asymmetries due to slow drifts in electronics or gas loss in the deuterium target, the data taking order was reversed after each four-step sequence.

The error in the RMS value for A_{yy} is given by

$$\begin{aligned}\Delta A_{yy}^{(RMS)} &= \left\{ \left(\frac{\partial A_{yy}^{(RMS)}}{\partial N_{12}} \right)^2 (\Delta N_{12})^2 + \left(\frac{\partial A_{yy}^{(RMS)}}{\partial N_{21}} \right)^2 (\Delta N_{21})^2 \right. \\ &+ \left(\frac{\partial A_{yy}^{(RMS)}}{\partial N_{34}} \right)^2 (\Delta N_{34})^2 + \left(\frac{\partial A_{yy}^{(RMS)}}{\partial N_{43}} \right)^2 (\Delta N_{43})^2 \\ &+ \left. \left(\frac{\partial A_{yy}^{(RMS)}}{\partial P_{ZZ}^{(12)}} \right)^2 \left(\Delta P_{ZZ}^{(12)} \right)^2 + \left(\frac{\partial A_{yy}^{(RMS)}}{\partial P_{ZZ}^{(34)}} \right)^2 \left(\Delta P_{ZZ}^{(34)} \right)^2 \right\}^{\frac{1}{2}} \end{aligned} \tag{3.19}$$

where

$$\begin{aligned}\frac{\partial A_{yy}^{(RMS)}}{\partial N_{12}} &= -\frac{2 + P_{ZZ}^{(34)} A_{yy}^{(RMS)}}{(N_{12}+N_{21})P_{ZZ}^{(34)} - (N_{34}+N_{43})P_{ZZ}^{(12)}} \\ \frac{\partial A_{yy}^{(RMS)}}{\partial N_{21}} &= -\frac{2 + P_{ZZ}^{(34)} A_{yy}^{(RMS)}}{(N_{12}+N_{21})P_{ZZ}^{(34)} - (N_{34}+N_{43})P_{ZZ}^{(12)}} \\ \frac{\partial A_{yy}^{(RMS)}}{\partial N_{34}} &= \frac{2 + P_{ZZ}^{(12)} A_{yy}}{(N_{12}+N_{21})P_{ZZ}^{(34)} - (N_{34}+N_{43})P_{ZZ}^{(12)}} \\ \frac{\partial A_{yy}^{(RMS)}}{\partial N_{43}} &= \frac{2 + P_{ZZ}^{(12)} A_{yy}^{(RMS)}}{(N_{12}+N_{21})P_{ZZ}^{(34)} - (N_{34}+N_{43})P_{ZZ}^{(12)}} \\ \frac{\partial A_{yy}^{(RMS)}}{\partial P_{ZZ}^{(12)}} &= \frac{(N_{34}+N_{43})\, A_{yy}^{(RMS)}}{(N_{12}+N_{21})P_{ZZ}^{(34)} - (N_{34}+N_{43})P_{ZZ}^{(12)}} \\ \frac{\partial A_{yy}^{(RMS)}}{\partial P_{ZZ}^{(34)}} &= -\frac{(N_{12}+N_{21})\, A_{yy}^{(RMS)}}{(N_{12}+N_{21})P_{ZZ}^{(34)} - (N_{34}+N_{43})P_{ZZ}^{(12)}} \end{aligned} \tag{3.20}$$

and

$$\Delta N_{ij} = \sqrt{\frac{\left(N_i^{(L)}\right)^2 \left(\Delta N_j^{(R)}\right)^2 + \left(N_j^{(R)}\right)^2 \left(\Delta N_i^{(L)}\right)^2}{4\, N_i^{(L)}\, N_j^{(R)}}} \tag{3.21}$$

(for $ij = 12, 21, 34, 43$) with the uncertainty in the yields given by

$$\Delta N_i^{(L)} = \sqrt{\left(\Delta N_{i_{(T+A)}}^{(L)}\right)^2 + \left(\Delta N_{i_{(A)}}^{(L)}\right)^2}$$

$$\Delta N_i^{(R)} = \sqrt{\left(\Delta N_{i_{(T+A)}}^{(R)}\right)^2 + \left(\Delta N_{i_{(A)}}^{(R)}\right)^2} \tag{3.22}$$

(for $i = 1, 2, 3, 4$). Here $\Delta N_{1_{(T+A)}}^{(L)}$ and $\Delta N_{1_{(A)}}^{(L)}$ are the statistical errors for the "true + accidental" and "accidental" events, respectively for the *left-right* coincidences in step 1. The notation for steps 2, 3 and 4 as well as for *right-left* coincidences $\Delta N_i^{(R)}$ is similarly defined.

The quench ratio method of determining the beam polarization is believed to be accurate to within $\pm 1.5\%$ of the theoretical maximum (see section 2.10.5). Although our beam polarization is less than the theoretical maximum, we choose to take the values

$$\Delta P_{ZZ}^{(12)} \equiv 0.015 \left| P_{ZZ_{max}}^{(12)} \right| = 0.015$$

$$\Delta P_{ZZ}^{(34)} \equiv 0.015 \left| P_{ZZ_{max}}^{(34)} \right| = 0.030 \ . \tag{3.23}$$

3.4.2 Calculation of A_y

To obtain the expression for A_y we start with equation 3.10 and take the difference in the cross sections for the first two steps resulting in

$$\sigma_1 - \sigma_2 = \sigma_\circ \left(3\, P_Z^{(12)}\, A_y\right). \tag{3.24}$$

Substituting $\sigma_\circ$ from equation 3.13 into equation 3.24 and solving for A_y yields

$$A_y = \frac{\sigma_1 - \sigma_2}{\sigma_3 + \sigma_4} \left(\frac{2 + P_{ZZ}^{(34)}\, A_{yy}}{3\, P_Z^{(12)}}\right). \tag{3.25}$$

Converting to the RMS value simply involves the substitution of the yields from equation 3.18 for the cross sections, thus

$$A_y^{(RMS)} = \frac{N_{12} - N_{21}}{N_{34} + N_{43}} \left(\frac{2 + P_{ZZ}^{(34)}\, A_{yy}^{(RMS)}}{3\, P_Z^{(12)}}\right). \tag{3.26}$$

The error in $A_y^{(RMS)}$ is given by

$$\begin{aligned}\Delta A_y^{(RMS)} = \Bigg\{ & \left(\frac{\partial A_y^{(RMS)}}{\partial N_{12}}\right)^2 (\Delta N_{12})^2 + \left(\frac{\partial A_y^{(RMS)}}{\partial N_{21}}\right)^2 (\Delta N_{21})^2 \\ & + \left(\frac{\partial A_y^{(RMS)}}{\partial N_{34}}\right)^2 (\Delta N_{34})^2 + \left(\frac{\partial A_y^{(RMS)}}{\partial N_{43}}\right)^2 (\Delta N_{43})^2 \\ & + \left(\frac{\partial A_y^{(RMS)}}{\partial P_Z^{(12)}}\right)^2 \left(\Delta P_Z^{(12)}\right)^2 + \left(\frac{\partial A_y^{(RMS)}}{\partial P_{ZZ}^{(34)}}\right)^2 \left(\Delta P_{ZZ}^{(34)}\right)^2 \\ & + \left(\frac{\partial A_y^{(RMS)}}{\partial A_{yy}^{(RMS)}}\right)^2 \left(\Delta A_{yy}^{(RMS)}\right)^2 \Bigg\}^{\frac{1}{2}} \end{aligned} \tag{3.27}$$

with

$$\frac{\partial A_y^{(RMS)}}{\partial N_{12}} = \frac{2 + P_{ZZ}^{(34)} A_{yy}^{(RMS)}}{3\left(N_{34} + N_{43}\right) P_Z^{(12)}}$$

$$\frac{\partial A_y^{(RMS)}}{\partial N_{21}} = -\frac{2 + P_{ZZ}^{(34)} A_{yy}^{(RMS)}}{3\left(N_{34} + N_{43}\right) P_Z^{(12)}}$$

$$\frac{\partial A_y^{(RMS)}}{\partial N_{34}} = -\frac{A_y^{(RMS)}}{N_{34} + N_{43}}$$

$$\frac{\partial A_y^{(RMS)}}{\partial N_{43}} = -\frac{A_y^{(RMS)}}{N_{34} + N_{43}}$$

$$\frac{\partial A_y^{(RMS)}}{\partial P_Z^{(12)}} = -\frac{A_y^{(RMS)}}{P_Z^{(12)}}$$

$$\frac{\partial A_y^{(RMS)}}{\partial P_{ZZ}^{(34)}} = \frac{\left(N_{12} - N_{21}\right) A_{yy}^{(RMS)}}{3\left(N_{34} + N_{43}\right) P_Z^{(12)}}$$

$$\frac{\partial A_y^{(RMS)}}{\partial A_{yy}^{(RMS)}} = \frac{(N_{12} - N_{21})\, P_{ZZ}^{(34)}}{3\,(N_{34} + N_{43})\, P_Z^{(12)}} \quad . \tag{3.28}$$

The uncertainty in the yields is given by equations 3.21 and 3.22; the uncertainty in $A_{yy}^{(RMS)}$ is given by equation 3.19, while the uncertainty in the beam polarization is given similarly to equation 3.23 by

$$\begin{aligned} \Delta P_Z^{(12)} &\equiv 0.015 \left| P_{Z_{max}}^{(12)} \right| = 0.015 \\ \Delta P_Z^{(34)} &\equiv 0.015 \left| P_{ZZ_{max}}^{(34)} \right| = 0.030 \quad . \end{aligned} \tag{3.29}$$

3.4.3 Calculation of A_{zz}

The differential cross sections for the four steps in the A_{zz} measurements are obtained by substituting the polar and azimuthal angles ϕ and β from table 2.6 into equation 3.4 yielding

$$\begin{aligned} \sigma_1 &= \sigma_\circ \left\{ 1 + \frac{1}{2} P_{ZZ}^{(1)} A_{zz} \right\} \\ \sigma_2 &= \sigma_\circ \left\{ 1 + \frac{1}{2} P_{ZZ}^{(2)} A_{zz} \right\} \\ \sigma_3 &= \sigma_\circ \left\{ 1 + \frac{1}{2} P_{ZZ}^{(3)} A_{zz} \right\} \\ \sigma_4 &= \sigma_\circ \left\{ 1 + \frac{1}{2} P_{ZZ}^{(4)} A_{zz} \right\} . \end{aligned} \tag{3.30}$$

Combining the cross sections for the first two steps and for the last two steps yields

$$\sigma_1 + \sigma_2 = \sigma_\circ \left\{ 2 + P_{ZZ}^{(12)} A_{zz} \right\} \tag{3.31}$$

$$\sigma_3 + \sigma_4 = \sigma_\circ \left\{ 2 + P_{ZZ}^{(34)} A_{zz} \right\} \tag{3.32}$$

where the experimental beam polarization moments have been substituted for $P_{ZZ}^{(i)}$ $(i = 1, 2, 3, 4)$. Solving equation 3.31 for $\sigma_\circ$, substituting into equation 3.32 and

solving for A_{zz} yields

$$A_{zz} = \frac{2\{(\sigma_3+\sigma_4)-(\sigma_1+\sigma_2)\}}{(\sigma_1+\sigma_2)P_{ZZ}^{(34)}-(\sigma_3+\sigma_4)P_{ZZ}^{(12)}} \quad . \tag{3.33}$$

Converting to the RMS value simply involves the substitution of the yields from equation 3.18 for the cross sections. Thus, we obtain

$$A_{zz}^{(RMS)} = \frac{2\{(N_{34}+N_{43})-(N_{12}+N_{23})\}}{(N_{12}+N_{23})P_{ZZ}^{(34)}-(N_{34}+N_{43})P_{ZZ}^{(12)}} \quad . \tag{3.34}$$

The error in $A_{zz}^{(RMS)}$ is given by

$$\begin{aligned}\Delta A_{zz}^{(RMS)} = \Bigg\{ &\left(\frac{\partial A_{zz}^{(RMS)}}{\partial N_{12}}\right)^2 (\Delta N_{12})^2 + \left(\frac{\partial A_{zz}^{(RMS)}}{\partial N_{21}}\right)^2 (\Delta N_{21})^2 \\ &+ \left(\frac{\partial A_{zz}^{(RMS)}}{\partial N_{34}}\right)^2 (\Delta N_{34})^2 + \left(\frac{\partial A_{zz}^{(RMS)}}{\partial N_{43}}\right)^2 (\Delta N_{43})^2 \\ &+ \left(\frac{\partial A_{zz}^{(RMS)}}{\partial P_{ZZ}^{(12)}}\right)^2 \left(\Delta P_{ZZ}^{(12)}\right)^2 + \left(\frac{\partial A_{zz}^{(RMS)}}{\partial P_{ZZ}^{(34)}}\right)^2 \left(\Delta P_{ZZ}^{(34)}\right)^2 \Bigg\}^{\frac{1}{2}}\end{aligned} \tag{3.35}$$

where

$$\frac{\partial A_{zz}^{(RMS)}}{\partial N_{12}} = -\frac{2+P_{ZZ}^{(34)}A_{zz}^{(RMS)}}{(N_{12}+N_{21})P_{ZZ}^{(34)}-(N_{34}+N_{43})P_{ZZ}^{(12)}}$$

$$\frac{\partial A_{zz}^{(RMS)}}{\partial N_{21}} = -\frac{2+P_{ZZ}^{(34)}A_{zz}^{(RMS)}}{(N_{12}+N_{21})P_{ZZ}^{(34)}-(N_{34}+N_{43})P_{ZZ}^{(12)}}$$

$$\frac{\partial A_{zz}^{(RMS)}}{\partial N_{34}} = \frac{2+P_{ZZ}^{(34)}A_{zz}^{(RMS)}}{(N_{12}+N_{21})P_{ZZ}^{(34)}-(N_{34}+N_{43})P_{ZZ}^{(12)}}$$

$$\frac{\partial A_{zz}^{(RMS)}}{\partial N_{43}} = \frac{2+P_{ZZ}^{(34)}A_{zz}^{(RMS)}}{(N_{12}+N_{21})P_{ZZ}^{(34)}-(N_{34}+N_{43})P_{ZZ}^{(12)}}$$

$$\frac{\partial A_{zz}^{(RMS)}}{\partial P_{ZZ}^{(12)}} = \frac{(N_{34}+N_{43})A_{zz}}{(N_{12}+N_{21})P_{ZZ}^{(34)}-(N_{34}+N_{43})P_{ZZ}^{(12)}}$$

$$\frac{\partial A_{zz}^{(RMS)}}{\partial P_{ZZ}^{(34)}} = \frac{(N_{34} + N_{43})\, A_{zz}}{(N_{12} + N_{21})\, P_{ZZ}^{(34)} - (N_{34} + N_{43})\, P_{ZZ}^{(12)}} \tag{3.36}$$

with the uncertainty in the yields given by equations 3.21 and 3.22 and the beam polarization uncertainty given by

$$\Delta P_{ZZ}^{(12)} \equiv 0.015 \left| P_{ZZ_{max}}^{(12)} \right| = 0.030$$

$$\Delta P_{ZZ}^{(34)} \equiv 0.015 \left| P_{ZZ_{max}}^{(34)} \right| = 0.015 \ . \tag{3.37}$$

Chapter 4

Calculations

4.1 History and Introduction

In kinematically incomplete measurements of breakup reactions, the measurement integrates over a large portion of the available phase space. This integration can even mask prominent characteristics of contributing reaction mechanisms. On the other hand, kinematically complete measurements of these same breakup reactions allow a detailed exploration of selected regions of phase space to investigate specific reaction mechanisms. One such process that has received much attention in the past 20 years is quasifree scattering (QFS). The term QFS is used to refer to the direct knock-out reaction process in which a nucleon or light nucleus is ejected from the target by the projectile, which itself continues freely after the collision (see figure 4.1). In the QFS picture the projectile collides with the struck particle as though the latter is almost free (hence the term quasifree) and the rest of the target nucleus is simply a spectator. This notion that the residual nucleus is only a spectator to the scattering process is often referred to as the *spectator model.*

The weak binding of the deuteron suggests that the deuteron may be a good target nucleus for studying QFS from one of its constituent nucleons. When scattering from one of the constituent nucleons, the other nucleon (the spectator) is most likely left with zero momentum since the probability of finding the relative momentum of the two nucleons reaches a maximum at zero momentum value. This is precisely the kinematic condition that defines the QFS configuration. As the relative momentum between the nucleons deviates from zero, the spectator nucleon is left with a non-zero momentum and the process no longer fulfills the QFS condition.

Nucleon-deuteron (Nd) QFS using the $d+d \rightarrow d+p+n$ breakup reaction has been extensively studied in a quest for exploring details of the nucleon-nucleon (NN) interaction that cannot be observed in the simpler two-nucleon scattering experiments, e.g., off-the-energy shell. In the case of kinematically complete Nd experiments, the coincidence spectra show a broad enhancement in the cross section in regions of phase space favorable to QFS (i.e., regions where little or no momentum is transferred to the spectator) [And72, Bon73, Bur72, Dja76, Fuk89, Klu78, Val72a, Val72c, Wie71, Wit72]. Similar enhancements have been observed for other few-nucleon systems including: proton-deuteron (pd) QFS using the $p+{}^3\mathrm{He} \rightarrow d+p+p$ breakup reaction [Bun75, Eps71, Sla71b, Wie71]; proton-nucleon (pN) QFS using the $p+d \rightarrow p+p+n$ reaction [And72, Mar71, McI72, Pai70, Pet70]; and neutron-neutron (nn) QFS using the $n+d \rightarrow n+n+p$ reaction [Sla71a].

Until very recently, attempts to understand the basic NN interaction in systems consisting of four or more nucleons have been relegated to phenomenological nuclear models such as the resonating group theory of Hofmann [Hof84a], R-matrix analyses of Hale [Hal87] or Green Function Monte Carlo method of Carlson [Car89]. Emphasis is now being placed on understanding few-nucleon systems using a *microscopic* description in which the motions of individual nucleons and their interactions are studied. Even though we know a great deal about the NN potential, the influence that the surrounding nucleons have on the NN interaction cannot be treated in a perturbative method because the bare NN potential is too strong. However, the nuclear medium in which the nucleons move provides an effective potential which is weaker and more smoothly behaved than the free NN potential. Basing this effective interaction on the known NN force has resulted in *realistic* microscopic calculations.

The increased computing power available with supercomputers along with improved computational techniques has made parameter-free microscopic calculations based on realistic NN potentials feasible. Mdlalose *et al.* [Mdl86b, Mdl86a], following the procedure outlined by Sofianos *et al.* [Sof85],[1] used a S-wave[2] NN Yamaguchi potential and performed differential cross section calculations for the $p+{}^3\mathrm{He} \rightarrow d+p+p$

[1] Sofianos *et al.* used a procedure in which in the original operator equations obtained by the four-body theory of Alt, Grassberger and Sandhas [Alt70] are reduced to effective two-body Lippmann-Schwinger integral equations which contain boundary conditions corresponding to the initial and final state of the system and are equivalent to the Schrödinger equation.

[2] Both the ${}^3S_1$ and ${}^1S_0$ NN channels were included. The notation ${}^{2S+1}L_J$ used here is a compact way to represent the intrinsic nuclear spin S, the orbital angular momentum L and the total angular momentum J in the L-S coupling scheme.

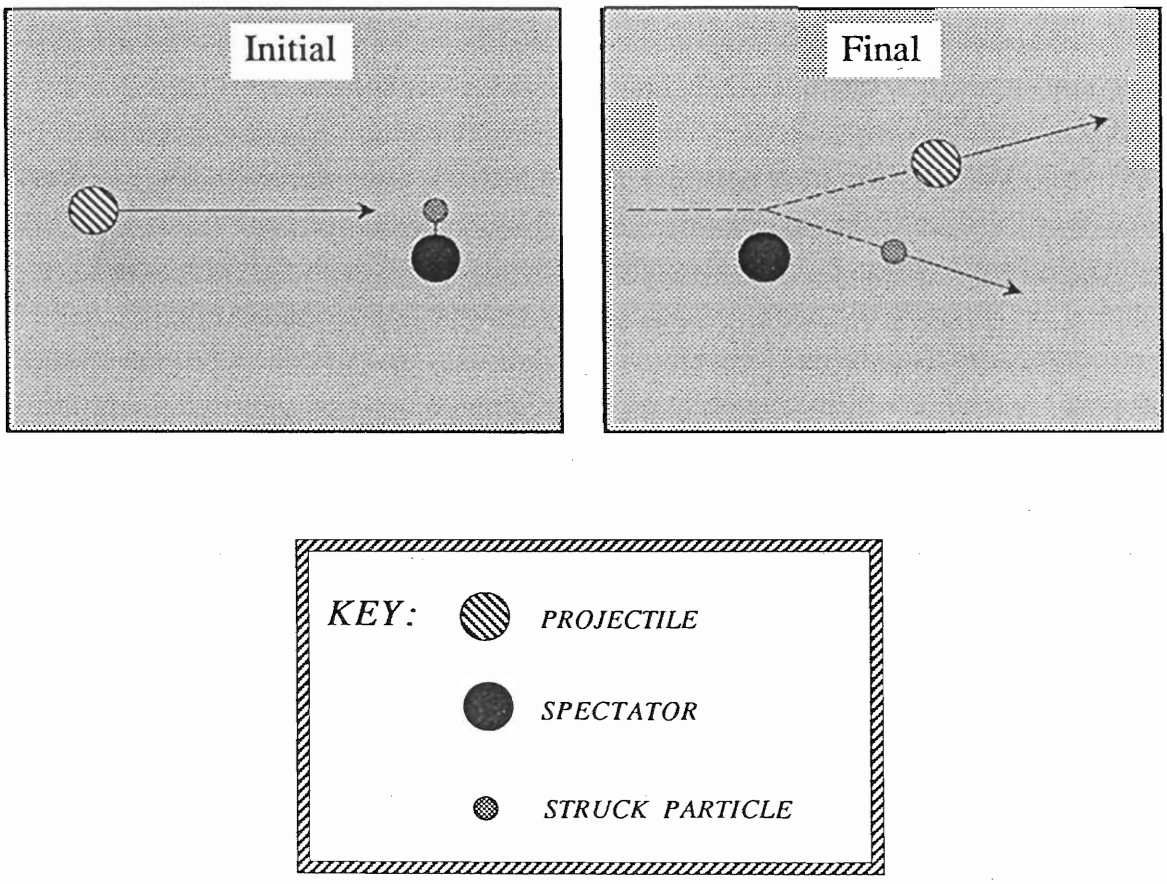

Figure 4.1: Schematic illustration of quasifree scattering shown in the rest frame of the nucleus that breaks up. The vectors represent the momenta of the respective particles.

[Mdl86b] and $d+d \rightarrow d+p+n$ [Mdl86a] breakup reactions with results that were encouraging when compared to experimentally obtained differential cross sections. For the first of these reactions, at incident proton laboratory energies of 35 and 45 MeV, they were able to reproduce the gross features of both the QFS enhancement and contributions from proton-proton (pp) final-state interactions (FSI).

Although their comparisons for the $d+d \rightarrow d+p+n$ breakup reaction were also encouraging, they were not quite as impressive as for $p+^3He$. For example, at an incident deuteron laboratory energy of 20.7 MeV and 27.5 MeV their calculations reproduced the shape of the QFS enhancement but failed to predict the proper magnitude. In fact, the calculations overpredicted the cross section by a factor of 2.0 at 20.7 MeV and 2.9 at 27.5 MeV. However, at an incident deuteron laboratory energy of 52.3 MeV they predicted the experimentally observed magnitude of the enhancement, but unfortunately failed in reproducing the shape of the enhancement. These discrepancies between the calculations and measured cross sections have been attributed to the fact that terms beyond the first-order K-matrix approximation were ignored. It should be pointed out that even though these calculations are based on a simple two-body interaction they still represent a microscopic approach without any free parameters.

Starting with the multiconfiguration resonating-group method, Kanada *et al.* [Kan91] calculated total reaction cross sections for $d+d \rightarrow p+^3H$ and $d+d \rightarrow n+^3He$ at 17.5 MeV and found agreement to within 6% of the experimental values. However, their cross-section calculations of the $d+d \rightarrow d+p+n$ and $d+d \rightarrow p+p+n+n$ breakup reactions, which included pseudoexcited states of the deuteron, were about a factor of 6 smaller than the experimentally observed cross sections. They suggest that the cluster-rearrangement configurations t^*+p and h^*+n, where t^* and h^* represent excited states of the three-nucleon ($3N$) $d+n$ and $d+p$ clusters, must be included to account for the missing cross section. They conclude that if their speculation is true, then at energies around 20 MeV the process of sequential decay through intermediate states ($d+d \rightarrow t^*+p \rightarrow d+n+p$ and $d+d \rightarrow h^*+n \rightarrow d+p+n$) is more important than the direct breakup process for dd breakup reactions. The notion of an intermediate state is reinforced by the phase-shift analysis by Arvieux [Arv74] of experimental pd scattering and reaction cross-section data that shows a resonance in the ^{3}He system at 14.2 MeV with a width of about 10 MeV. The inclusion of the intermediate states in the Kanada calculations is still a formidable task; furthermore they point out that their calculations lack noncentral forces which are essential for realistic calculations

of vector and tensor analyzing powers in the 3 and $4N$ scattering systems.

Yet another approach to the $4N$ problem has recently been attempted by Fonseca [Fon89], who started with four-body integral equations and calculated cross sections and analyzing powers for the $d+d \rightarrow d+d$ and $d+d \rightarrow p+^3\mathrm{H}$ reactions at 6 and 8 MeV incident deuteron laboratory energies. Using a single-term separable Yamaguchi potential which included both the $^1S_0$ and the $^3S_1$-$^3D_1$ channels for the NN interaction, he was able to predict the forward angle maxima in the cross sections, but underpredicted the cross sections at c.m. angles beyond 45° by as much as 60%. Furthermore, he was able to qualitatively predict the correct behavior of the analyzing powers (T_{20}, T_{21}, T_{22}, iT_{11}) for both scattering systems. (Although he was not able to reproduce both the magnitude and the sign of the tensor analyzing powers at all angles, he was able to predict the order of magnitude of the observables for both reactions without introducing any free parameters.) This is quite remarkable since the tensor analyzing powers for the $\vec{d}+d \rightarrow p+^3\mathrm{H}$ reaction are more than an order of magnitude greater than those for $\vec{d}d$ elastic scattering. Proper inclusion of the Coulomb distortion in the calculation should improve the predictions at forward angles. One difficultly Fonseca faced was the limitation of computer memory and time available on the Cray X-MP 48 used to perform the calculations. This forced him to severely limit the number of $3N$ subamplitudes in the calculations.

To date no realistic microscopic calculations for polarization observables for the $\vec{d}+d \rightarrow d+p+n$ breakup reaction are available. Our approach to describing the QFS process is based on the impulse approximation (IA). With the IA we are able to calculate polarization observables for the $\vec{d}+d \rightarrow d+p+n$ breakup reaction based on $3N$ calculations that include more physics than one can currently include in existing models for the $4N$ case.[3]

[3]A collaboration between Fonseca and our group at TUNL is currently underway. The calculations are being performed on the Cray Y-MP at the North Carolina Supercomputing Center which should eliminate many of these limitations. Our plan is to calculate polarization observables for the $\vec{d}+d \rightarrow d+p+n$ breakup reaction using the NN interaction given above. The inclusion of P-waves in the NN interaction will not be incorporated in his first-generation calculations. Since the vector analyzing powers A_y (which are of interest to us) come primarily from the P-waves in the NN interaction, his calculations of this observable will not be valid.

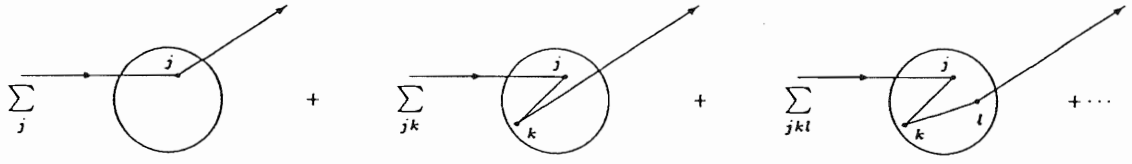

Figure 4.2: Schematic picture showing multiple scattering series (equation 4.4). The projectile successively scatters from one target nucleon, two target nucleons, three target nucleons, etc.

4.2 Impulse Approximation

To introduce the impulse approximation (IA) we first consider the scattering of a projectile by a collection of bound nucleons. The interaction is a sum of two-body interactions between projectile nucleons a and target nucleons A. That is, for the interaction between the projectile and an individual target nucleon j we have

$$V_j = \sum_{i \in a} V_{ij} \ . \tag{4.1}$$

So that, the total interaction V becomes

$$V = \sum_{j=1}^{A} V_j \ . \tag{4.2}$$

The two-body t-operator acting between the projectile and a target nucleon j is then

$$t_j = V_j + V_j G_o V_j + V_j G_o V_j G_o V_j + \cdots \ , \tag{4.3}$$

where G_o is the Green function propagator. According to formal scattering theory the transition operator T acting between the projectile and target can be expanded into a series of two-body t operators such that

$$T = \sum_{j=1}^{A} t_j + \sum_{j,k \neq j}^{A} t_j G_o t_k + \sum_{j,k \neq j, l \neq k}^{A} t_j G_o t_k G_o t_l + \cdots \ , \tag{4.4}$$

which is the well known Watson [Gle83] multiple scattering series. This can easily be pictured as a series of interactions like those indicated in figure 4.2 involving scattering from one target nucleon, two target nucleons, three target nucleons, etc.

We can obtain a *single-scattering* approximation by truncating the multiple scattering series (equation 4.4) after the first term. This approximation is not of much practical use unless one can calculate the two-body t operator t_j between the projectile and the j^{th} nucleon. Often a second approximation is employed by replacing t_j with τ_j, the two-body t operator describing the interaction between the projectile and a *free* nucleon. The individual scattering events described by t_j differ from that for scattering from a free nucleon because the scattering takes place in a medium of other nucleons which generates a mean field in the region where scattering occurs. In addition to the mean field, the other nucleons also influence the struck nucleon through the Pauli Exclusion Principle by preventing it from entering an occupied state. However, as the incident particle energy increases, $t_j \rightarrow \tau_j$ so t_j may be replaced by τ_j. The combination of truncating the multiple scattering series (equation 4.4) and substituting the free scattering interaction for the bound scattering is called the *impulse approximation*. It should be noted that this is not the first Born approximation[4] which results from retaining the full multiple scattering series (equation 4.4) and approximating the two-body t operator for the interaction with the j^{th} nucleon to first order in V_j.

The binding energy of the deuteron gives rise to the internal motion of the nucleons within the target which in turn causes the scattering between the projectile and target nucleons to differ from that of elastic scattering. Therefore, one must know the free T-operator ($T_{free} = \sum_{j=1}^{A} \tau_j$) *off-the-energy-shell.*[5] That is, one must know the transition matrix $\mathcal{T}_{free}$, where

$$\mathcal{T}_{free} = \langle \boldsymbol{k}', \boldsymbol{p}'_j | T_{free} | \boldsymbol{k}, \boldsymbol{p}_j \rangle \tag{4.5}$$

with $E' \neq E$ where E, $\boldsymbol{k}$ and $\boldsymbol{p}_j$ are the interaction energy, the momentum for the projectile and the momentum for the j^{th} nucleon, respectively. Here the primed quantities represent the final state and the unprimed the initial state. In practice one often extrapolates the off-shell value from the on-shell $\mathcal{T}_{free}$ for similar kinematics, for example, with the same final momenta $\boldsymbol{k}'$, $\boldsymbol{p}'_j$, and the same scattering angle. This approximation is called the post-collision prescription. Another approximation called the prior-collision prescription involves using similar kinematics for the entrance channel. In our calculations we will use the $\mathcal{T}_{free}$-matrices employing both the off-shell values and the post-collision prescription on-shell values.

[4]The first Born approximation is often referred to as the Born approximation.

[5]For brevity, off-the-energy-shell and on-the-energy-shell will be referred to as off-shell and on-shell, respectively.

The transition amplitude for scattering off the j^{th} nucleon is then given by the transition amplitude obtained by using $\mathcal{T}_{free}$ times the probability of striking the j^{th} nucleon. According to the spectator model, in the c.m. of the nucleus that breaks up, we have

$$\boldsymbol{q}_{struck\ nucleon} = -\boldsymbol{q}_{residual\ nucleus} \ . \tag{4.6}$$

Therefore, we are interested in the probability of striking the j^{th} nucleon when it has a momentum q ($q \equiv |\boldsymbol{q}_{struck\ nucleon}|$) relative to the c.m. of the nucleus within which it resides. Since the target nucleons are distributed over the nuclear volume with a probability given by their wave functions in configuration space, the corresponding momentum distributions are simply given by the Fourier transforms of the wave functions and the desired probability is just the square of the Fourier transform of the wave function of the j^{th} nucleon evaluated at a momentum q.

The IA was born from this notion that the many-body characteristics of a problem are sometimes only a secondary feature, and that the collision may be decomposed as a superposition of simple two-body collisions. Applied to the d+$d \rightarrow d$+p+n breakup reaction, the assumptions underlying the IA are [Che52]:

- The incident deuteron never interacts strongly with the two target nucleons at the same time.
- The amplitude of the incident wave falling on each constituent nucleon is nearly the same as if that nucleon were alone.
- The binding forces between the constituent nucleons are negligible during the decisive phase of the collision when the incident deuteron interacts strongly with the nucleons.
- Final state interactions between the outgoing particles are negligible.

The validity of the last point above was studied by Valković *et al.* [Val72a] and was found to be consistent with experimental data. No pn final-state interaction (FSI) peak has been observed in the d+$d \rightarrow d$+p+n breakup reaction. This is well understood since the pn $^1S_0$ FSI which normally gives a sharp enhancement, is isospin forbidden.[6] The broad enhancement from the $^3S_1$ pn FSI, which does not violate any

[6]The total parity of a system of nucleons is given by $P_r \cdot P_\sigma \cdot P_\tau = -1$ with $P_r = (-1)^L$, $P_\sigma = (-1)^S$ and $P_\tau = (-1)^T$ so that $L+S+T =$ odd where L, S and T are the angular momentum, spin and isospin, respectively. Since the ground state of the deuteron is a mixture of $^3S_1$ and $^3D_1$

selection rules, is expected to appear as a small uniform "background" [Klu78] in the $d+d \rightarrow d+p+n$ breakup spectrum.

Often the IA as applied to QFS is called either the *spectator model* or the *pole model*. In the case of the $d+d \rightarrow d+p+n$ breakup reaction, we will allow for breakup of either deuteron. Then the nucleon that we call the "struck nucleon" could be contained initially within either the projectile or the target. Thus, for this reaction we have the four *poles* shown graphically in figure 4.3. The labels n, p, d_t and d_p stand for neutron, proton, target deuteron and projectile deuteron, respectively. In QFS terminology the individual poles can unambiguously be referred to by the origin of the spectator nucleon (also called the residual nucleus). Thus, we adopt the notation Tn for spectator neutron in the target, Tp for spectator proton in the target, Pn for spectator neutron in the projectile and Pp for spectator proton in the projectile. In this description the QFS process can be viewed as proceeding in two steps:

1. Via a virtual decay; one of the deuterons dissociates into the residual nucleus (the spectator nucleon) and the struck nucleon with momentum $\boldsymbol{q}$ and $-\boldsymbol{q}$ with respect to the deuteron's c.m. motion.

2. The intact deuteron and the struck nucleon quasifree scatter.

The three-body breakup cross section using this pole description is then the coherent sum of the four terms obtained from the four poles Tn, Tp, Pn and Pp shown in figure 4.3. The probability of the first step occurring is determined by the Fourier transform of the wave function $\Phi_d(q)$ of the deuteron that breaks up; this is equivalent to the probability of striking a nucleon which has a momentum q within the deuteron. The second step is described by the dN free scattering amplitude. Therefore, the three-body breakup cross section is given by

$$\frac{d^3\sigma}{d\Omega_1\, d\Omega_2\, dS} = \kappa\, \rho \left(\frac{d\sigma}{d\Omega}\right)^{free}_{dN} |\Phi_d(q)|^2 \tag{4.7}$$

states we have $(-1)^{0 or 2} \cdot (-1)^1 \cdot (-1)^T = -1$, implying that T is even. With the isospin projection assignments of $T_3 = -\frac{1}{2}$ for a neutron and $T_3 = +\frac{1}{2}$ for a proton, we obtain $T = 0$ and $T_3 = 0$ for the ground state of the deuteron. Likewise for a neutron-proton pair in a $^1S_0$ state (denoted d^*) we have $T = 1$ and $T_3 = 0$, so that

	d	$+$	d	$\longrightarrow$	d	$+$	d^*
T	0		0		0		1
T_3	0		0		0		0 .

This however, is clearly forbidden by conservation of isospin.

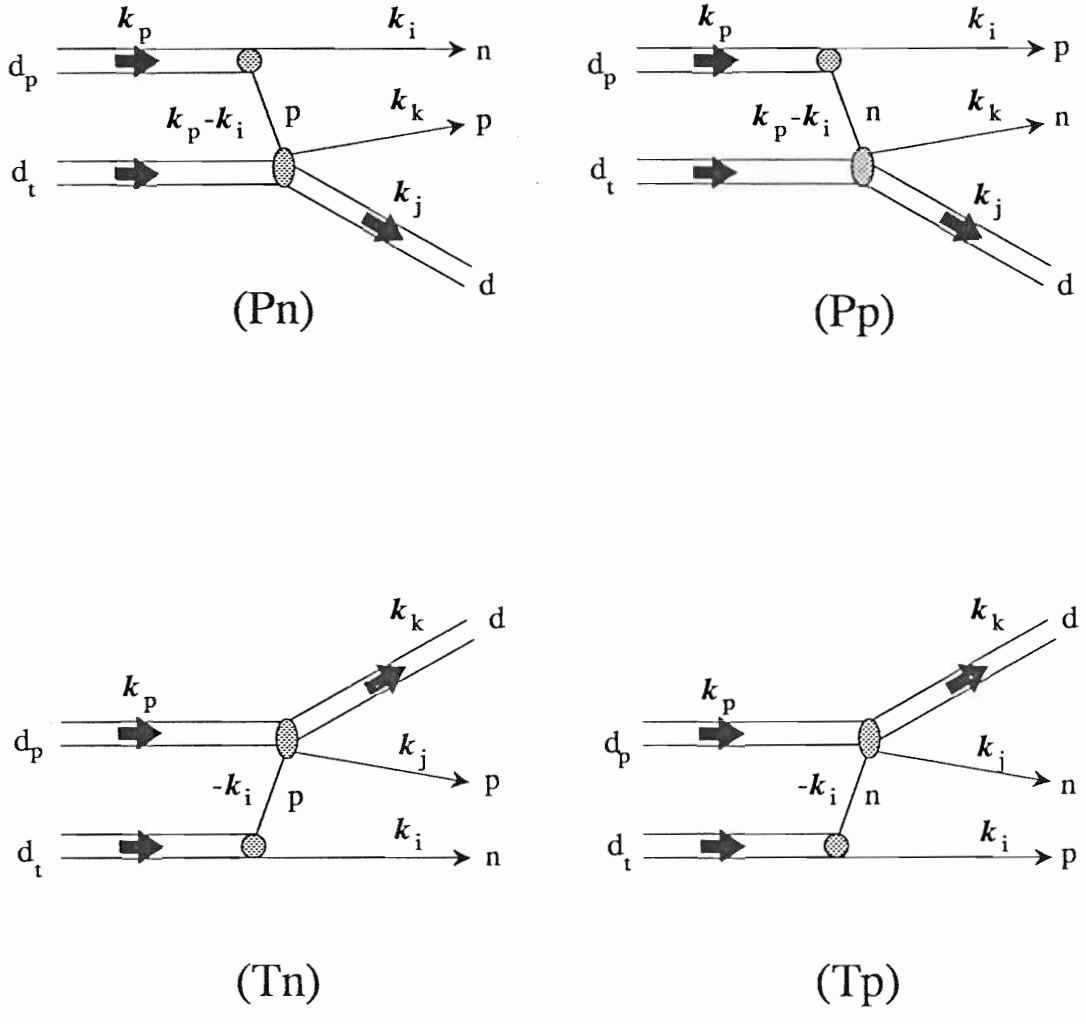

Figure 4.3: The four poles used in the unpolarized IA calculations. The letters d, n and p represent deuteron, neutron and proton while the subscripts p and t represent the incident and target particles, respectively. Particle momenta as defined in section 4.3 are denoted by $\boldsymbol{k}$. The four poles can be uniquely identified by the spectator particle: Tn, Tp, Pn and Pp for target-neutron, target-proton, projectile-neutron and projectile-proton, respectively.

where κ is a kinematic factor which depends upon the kinematics of the reaction; ρ is the phase space factor; $\left(\frac{d\sigma}{d\Omega}\right)_{dN}^{free}$ is the two-body free scattering cross section of the interacting dN pair evaluated at the appropriate c.m. energy and angle; and $\Phi_d(q)$ is the Fourier transform of the wave function of the deuteron which breaks up. The q in the deuteron wave function in equation 4.7 is the pre-collision momentum of the struck nucleon in the c.m. of the deuteron which breaks up.

Before realistic $3N$ calculations were available one often used measured elastic scattering data for $\left(\frac{d\sigma}{d\Omega}\right)_{dN}^{free}$ to predict the three-body breakup cross section with equation 4.7. However, a lack of data at the appropriate energies limited the calculations to specific energies. Furthermore, since the measured free-scattering data are on-shell, the calculations cannot properly take into account the off-shell behavior of the two-body reaction.[7] This problem is reduced at high energies where the off-shell behavior can be reasonably approximated by the on-shell interaction because the Q-value for the reaction is small compared to the interaction energy. Another problem inherent to using measured free-scattering data is that one cannot determine interference effects between different poles. Both of these problems can be avoided by calculating $\left(\frac{d\sigma}{d\Omega}\right)_{dN}^{free}$ instead of using data.

In order to allow for interference between poles, the amplitudes describing the dN vertex for each pole must be calculated and added coherently. This is accomplished by obtaining an effective transition matrix for the four-pole calculation ($\mathcal{T}_{4P}$) by weighting the scattering amplitudes for each pole by the Fourier transform of the deuteron wave function for that pole. The kinematic factor and phase space constants are the same for each pole and thus can be factored out. Therefore,

$$\mathcal{T}_{4P} = \mathcal{T}_{Tn}\Phi_d(q_{Tn}) + \mathcal{T}_{Tp}\Phi_d(q_{Tp}) + \mathcal{T}_{Pn}\Phi_d(q_{Pn}) + \mathcal{T}_{Pp}\Phi_d(q_{Pp}) \ . \tag{4.8}$$

The momentum q used in the deuteron wave function is determined from the kinematics as described in section 4.3. The subscripts on q refer to the different poles shown in figure 4.3.

The three-body breakup cross section becomes

$$\frac{d^3\sigma}{d\Omega_1\, d\Omega_2\, dS} = \kappa\,\rho\left(\frac{d\sigma}{d\Omega}\right)_{dN}^{\mathcal{T}_{4P}} \tag{4.9}$$

[7] Redish *et al.* [Red70] point out that using off-shell amplitudes in place of the on-shell amplitudes can change the calculated cross section significantly for $(p, 2p)$ reactions below 200 MeV. They further caution that extracting nuclear information from a QFS experiment is tenuous when using the on-shell approximation in the IA.

where $(\frac{d\sigma}{d\Omega})_{dN}^{\mathcal{T}_{4P}}$ is the deuteron-nucleon cross section obtained from using the effective four-pole transition matrix $\mathcal{T}_{4P}$. The dN cross section is calculated from the $\mathcal{T}_{4P}$ using the relationship

$$\left(\frac{d\sigma}{d\Omega}\right)_{dN}^{\mathcal{T}_{4P}} = b\,Tr\left(\mathcal{T}_{4P}\mathcal{T}_{4P}^{\dagger}\right) \quad , \tag{4.10}$$

where b is a normalization constant and Tr is the matrix trace operator.

In the case of polarization observables the analyzing power A for each pole is determined entirely by the corresponding analyzing power for dN free scattering evaluated at the appropriate c.m. energy and scattering angle, so that

$$A = \left(A_{dN}^{free}\right)_{pole} = c\,\frac{Tr\left(\mathcal{T}_{pole}^{\dagger}\mathcal{O}\mathcal{T}_{pole}\right)}{Tr\left(\mathcal{T}_{pole}\mathcal{T}_{pole}^{\dagger}\right)} \tag{4.11}$$

where *pole* indicates the applicable pole in figure 4.4, $\mathcal{O}$ is the operator for the analyzing power, c is a constant and $\mathcal{T}$ is the transition matrix for that pole (see section 4.8). A full four pole calculation of A would then be obtained by applying equation 4.11 to the effective transition matrix for all four poles $\mathcal{T}_{4P}$ (equation 4.8).

In our experiment the incident deuteron beam was polarized. Therefore, for target breakup processes (poles Tn and Tp) we made the assumption that the free dN vertex is described by a polarized deuteron interacting with an unpolarized nucleon ($\vec{d}N$). On the other hand, for projectile breakup (poles Pn and Pp) we assume that the process is described by the interaction between a polarized nucleon interacting with an unpolarized deuteron ($\vec{N}d$). This is shown graphically in the four pole figure 4.4.

Because the operator for calculating spin observables from the transition matrix differs for $\vec{d}N$ and $\vec{N}d$ scattering (see section 4.8), the analyzing powers for the target breakup (TB) poles must be calculated separately from the projectile breakup (PB) poles. To deal with this problem we calculated separately effective transition matrices for target breakup and projectile breakup. Analyzing powers are then calculated from each matrix assuming a $\vec{d}N$ or a $\vec{N}d$ interaction. The results are weighted by the cross sections and added incoherently. Accordingly, the expression for the analyzing powers is

$$A = \frac{A_{TB}\,\sigma_{TB} + A_{PB}\,\sigma_{PB}}{\sigma_{TB} + \sigma_{PB}} \tag{4.12}$$

with $\sigma_{PB} = (\frac{d\sigma}{d\Omega})_{dN}^{PB}$ and $\sigma_{TB} = (\frac{d\sigma}{d\Omega})_{dN}^{TB}$ being the differential cross sections calculated from the corresponding transition matrices. The expressions for the transition

matrices are given by[8]

$$\mathcal{T}_{TB} = \mathcal{T}_{Tn}\Phi_d(q_{Tn}) + \mathcal{T}_{Tp}\Phi_d(q_{Tp})$$

$$\mathcal{T}_{PB} = \mathcal{T}_{Pn}\Phi_d(q_{Pn}) + \mathcal{T}_{Pp}\Phi_d(q_{Pp}) \ . \tag{4.13}$$

For the calculation of the tensor analyzing powers, the contribution from the PB poles were set identically equal to zero ($A_{PB} \equiv 0$) since the tensor analyzing powers are undefined for a polarized spin $\frac{1}{2}$ particle interacting with an unpolarized particle.

The addition of transition matrices in this fashion allows for interference between the two PB poles and for interference between the two TB poles, but not between TB and PB poles. This is one of the inherent limitations of our implementation of the IA when calculating polarization observables. Our three-body breakup cross-section calculations using equation 4.9 used transition matrices which were produced by the coherent sum of the four poles. However, to maintain consistency with the analyzing power calculations, the cross section for the TB and PB poles (σ_{TB} and σ_{TB}, respectively) were calculated separately and combined incoherently to obtain the four-pole cross section. The cross section σ_{TB} and σ_{PB} were used to compute the analyzing powers in equation 4.12. Therefore, the cross-section calculations to be shown in the rest of this work do not allow for interference between the TB and PB poles; that is, the four-pole cross section is an incoherent sum of σ_{TB} and σ_{PB}.

Two computer codes NMPWIAOFF and NMPWIA have been developed at TUNL in order to calculate observables using the IA. The differences in the codes involve the way the transition matrix elements are calculated and will be explained further in section 4.7. In the sections that follow, a more detailed analysis of the terms entering the cross section and analyzing power expressions will be explored.

4.3 Kinematics

In this section we will explore various aspects of the three-body breakup reaction in a nonrelativistic formalism and derive several useful expressions. We will use the convention that the projectile particle is referred to as P, the target as T, the two detected particles as 1 and 2, and the undetected particle as 3. Thus, we write

$$P + T \rightarrow 1 + 2 + 3 \ .$$

[8] We have made the assumption that the probability for deuteron breakup is spin independent.

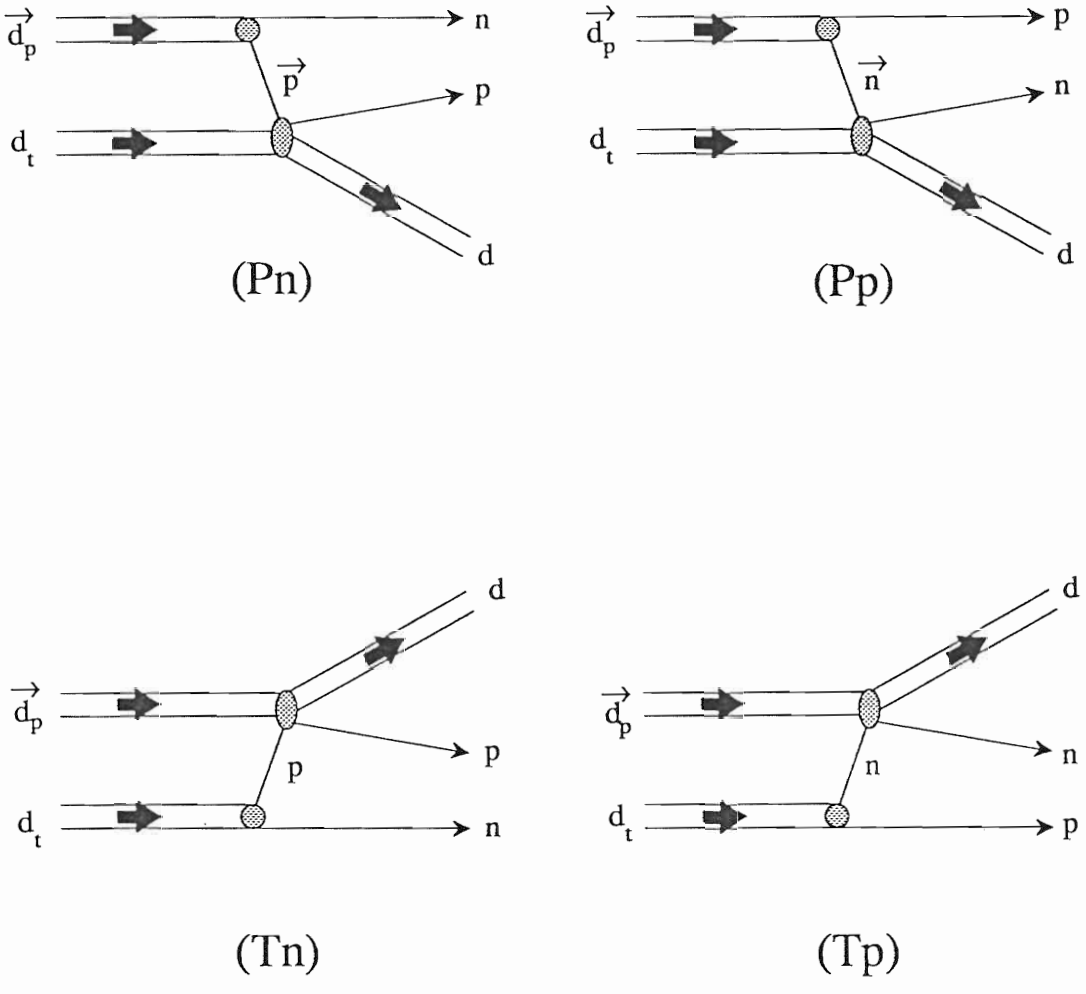

Figure 4.4: Same as figure 4.3 except that the projectile deuteron is polarized. In the case of a projectile breakup the interacting nucleon is assumed to be vector polarized.

Before proceeding further, it will be helpful to define a number of variables used in this section:

$$
\begin{aligned}
m &= \text{mass of particle} \\
E &= \text{laboratory kinetic energy} \\
\theta &= \text{laboratory polar angle measured relative to the } +z \text{ direction} \\
\phi &= \text{laboratory azimuthal angle measured up from the } +x \text{ axis} \\
\boldsymbol{k}_i &= \text{laboratory momentum after the collision of the } i^{th} \text{ particle} \\
\boldsymbol{k}_p &= \text{incident momentum of projectile in laboratory system} \\
Q &= \text{“Q value” for the reaction} \\
\theta_{ij} &= \text{angle between } \boldsymbol{k}_i \text{ and } \boldsymbol{k}_j. \qquad (4.14)
\end{aligned}
$$

Subscripts t, p, 1, 2 and 3 will be used as necessary to denote the appropriate particle. For convenience we use the convention that $c = 1$ so that masses and momenta can be expressed in MeV/c^2 and MeV/c, respectively. The coordinate frame will be defined as a right-handed-orthogonal system with the z-axis taken along $\boldsymbol{k}_p$ and the y-axis along $\boldsymbol{k}_p \times \boldsymbol{k}_1$. We will restrict ourselves to the case where the target is stationary in the laboratory reference frame and where the momenta of the detected particles ($\boldsymbol{k}_i$,$\boldsymbol{k}_j$) and the incident beam momentum ($\boldsymbol{k}_p$) are coplanar. Conservation of momentum in the $\hat{y}$ direction requires that $\boldsymbol{k}_3$ also lies in the xz-plane, therefore $\phi = 0°$ or $180°$.

In general, for a kinematically complete description of N particles in the final state, $3N - 4$ kinematic variables need to be determined (incident beam energy as well as the particle masses are assumed known); that is, for the three-body breakup reaction 5 quantities are necessary. Detecting the momenta of two of the three outgoing particles determines 6 variables, thus kinematically overdefining the reaction. This *overkill* aids in cleaning up the spectra by helping to eliminate accidental events. The 5 kinematic variables that we use in the derivations below are ϕ_1, ϕ_2, θ_1, θ_2 and E_1.

To simplify the kinematic equations we absorb the two possible values of $\phi = 0°$ or 180° into the sign of the polar angle θ. In our notation $\theta > 0°$ for $\phi = 0°$ and $\phi < 0°$ for $\theta = 180°$. Conservation of momentum and energy in the laboratory system require that

$$\boldsymbol{k}_p = \boldsymbol{k}_1 + \boldsymbol{k}_2 + \boldsymbol{k}_3 \tag{4.15}$$

and

$$E_p = E_1 + E_2 + E_3 + Q \ . \tag{4.16}$$

Solving equation 4.15 for $\boldsymbol{k}_3$ and squaring both sides yields

$$\begin{aligned} {k_3}^2 &= (\boldsymbol{k}_p - \boldsymbol{k}_1 - \boldsymbol{k}_2)^2 \\ &= {k_p}^2 + {k_1}^2 + {k_2}^2 - 2\boldsymbol{k}_p \cdot \boldsymbol{k}_1 - 2\boldsymbol{k}_p \cdot \boldsymbol{k}_2 + 2\boldsymbol{k}_1 \cdot \boldsymbol{k}_2 \\ &= {k_p}^2 + {k_1}^2 + {k_2}^2 + 2k_1 k_2 \cos\theta_{12} - 2k_p k_1 \cos\theta_1 - 2k_p k_2 \cos\theta_2 \ , \end{aligned} \tag{4.17}$$

where $\theta_{12} = (\theta_1 - \theta_2)$ is the angle between $\boldsymbol{k}_1$ and $\boldsymbol{k}_2$. Substituting $\frac{k^2}{2m}$ for E in equation 4.16 and solving for ${k_3}^2$ yields

$${k_3}^2 = \frac{m_3}{m_p}{k_p}^2 - \frac{m_3}{m_1}{k_1}^2 - \frac{m_3}{m_2}{k_2}^2 - 2m_3 Q \ . \tag{4.18}$$

Subtracting equation 4.18 from equation 4.17, and solving the resulting quadratic equation for k_2 yields,

$$k_2 = \frac{-B \pm \sqrt{B^2 - 4AC}}{2A} \ . \tag{4.19}$$

with

$$\begin{aligned} A &= 1 + \frac{m_3}{m_2} \\ B &= 2\left(\sqrt{2m_1 E_1}\cos\theta_{12} - \sqrt{2m_p E_p}\cos\theta_2\right) \\ C &= 2E_p(m_p - m_3) + 2E_1(m_1 + m_3) + 2m_3 Q - 4\sqrt{m_p m_1 E_p E_1}\cos\theta_1 \ . \end{aligned}$$

Setting ${k_2}^2 = 2m_2 E_2$ and simplifying yields

$$E_2 = \frac{B^2 - 2AC \mp B\sqrt{B^2 - 4AC}}{4m_2 A^2} \ . \tag{4.20}$$

Once E_2 is known we can use equation 4.16 to determine the energy of the undetected particle, so that

$$E_3 = E_p - E_1 - E_2 - Q \ . \tag{4.21}$$

Conservation of momentum along $\hat{x}$ gives

$$k_1 \sin\theta_1 + k_2 \sin\theta_2 + k_3 \sin\theta_3 = 0 \ . \tag{4.22}$$

Keep in mind that θ can have both positive ($\phi = 0°$) and negative ($\phi = 180°$) values. Solving for $\sin\theta_3$ using equation 4.22 and substituting $\sqrt{2mE} = k$ yields,

$$\sin\theta_3 = -\left(\frac{\sqrt{E_1 m_1}\sin\theta_1 + \sqrt{E_2 m_2}\sin\theta_2}{\sqrt{E_3 m_3}}\right) \ . \tag{4.23}$$

Likewise, conservation of momentum along $\hat{z}$ gives

$$\cos\theta_3 = -\left(\frac{\sqrt{E_1 m_1}\cos\theta_1 + \sqrt{E_2 m_2}\cos\theta_2 - \sqrt{E_p m_p}}{\sqrt{E_3 m_3}}\right) \ . \tag{4.24}$$

Once the energy and momenta of the outgoing particles are known, one can now calculate various quantities used in the evaluation of the matrix elements (see section 4.7). Let us call the spectator particle i, the struck particle j and the scattered particle k. The quantities of primary importance are:

k_{jk} = magnitude of the momentum of particle j relative to the j-k c.m. system after the collision

P_{jk} = magnitude of the momentum of particle j relative to the j-k c.m. system prior to the collision

$P_{k(jk)}$ = momentum of particle k in the j-k c.m. system before the collision

θ_{scat} = scattering angle of scattered particle k in the j-k c.m. system

q = momentum transferred to spectator particle i

e_{jk} = energy of particles j and k relative to the j-k c.m. system.

The momentum transferred to the spectator nucleon is defined to be the final momentum of that particle minus its initial momentum. That is,

$$\boldsymbol{q} = \begin{cases} \boldsymbol{k}_i & \text{for target breakup} \\ \boldsymbol{k}_i - \dfrac{m_i}{m_p}\boldsymbol{k}_p & \text{for projectile breakup.} \end{cases} \tag{4.25}$$

The above relationship between q and $\boldsymbol{k}$ assumes that before the collision the spectator nucleon is stationary in the case of target breakup and that it has equal momentum to the other nucleon in the incident deuteron in the case of projectile breakup.

In the context of the IA, it is assumed that the scattered particle collides with the struck particle that has a momentum, in the c.m. of the target, equal and opposite to the momentum transferred to the spectator particle. In this view, the momentum transferred to the spectator is actually due to the internal motion of the nucleons within the target at the time of the collision.

In the post-collision prescription the magnitude of the momentum of particle j relative to the j-k c.m. system is

$$k_{jk} = \left| \frac{m_j \boldsymbol{k}_k - m_k \boldsymbol{k}_j}{m_j + m_k} \right| \tag{4.26}$$

and the energy available in this c.m. is

$$e_{jk} = \frac{k_{jk}^2}{2\mu_{jk}} \tag{4.27}$$

with the reduced mass given by

$$\mu_{jk} = \frac{m_j m_k}{m_j + m_k} \quad . \tag{4.28}$$

In the pre-collision prescription the momentum of the struck particle is taken to be equal in magnitude to but opposite in direction to that of the spectator nucleon in the c.m. reference frame of the two particles after the collision. Therefore, the relative momentum between the scattered particle and the struck particle before the collision is

$$P_{jk} = \begin{cases} \left| \dfrac{m_p \boldsymbol{k}_i + m_j \boldsymbol{k}_p}{m_j + m_p} \right| & \text{for target breakup} \\ \left| \dfrac{m_t \left(\boldsymbol{k}_p - \boldsymbol{k}_i \right)}{m_j + m_t} \right| & \text{for projectile breakup.} \end{cases} \tag{4.29}$$

The energy available in this c.m. is

$$e_{jk} = \frac{P_{jk}^2}{2\mu_{jk}} \tag{4.30}$$

with the reduced mass given by

$$\mu_{jk} = \frac{m_j m_k}{m_j + m_k} \ . \tag{4.31}$$

To determine the scattering angle we first transform the initial laboratory momenta of the interacting particles to the c.m. of those particles after the collision. For target breakup the initial momentum of particle k in the j-k c.m. reference frame is

$$\boldsymbol{P}_{k(jk)} = m_k(\boldsymbol{u}_k - \boldsymbol{u}_{jk}) \tag{4.32}$$

where $\boldsymbol{u}_k$ is the laboratory velocity of particle k and $\boldsymbol{u}_{jk}$ is the laboratory velocity of the j-k c.m. The velocity of the j-k c.m. system is $\boldsymbol{u}_{jk} = \frac{\boldsymbol{k}_j + \boldsymbol{k}_k}{m_j + m_k}$. If particle k was initially the projectile then $\boldsymbol{u}_k = \frac{\boldsymbol{k}_p}{m_k}$ and $m_k = m_p$. If on the other hand, it was the target, then $\boldsymbol{u}_k = \boldsymbol{0}$ and $m_k = m_t$ so that

$$\boldsymbol{P}_{k(jk)} = \begin{cases} \dfrac{m_t}{m_j + m_k}(\boldsymbol{k}_j + \boldsymbol{k}_k) & \text{for target breakup} \\ m_k\left(\dfrac{\boldsymbol{k}_p}{m_p} - \dfrac{\boldsymbol{k}_j + \boldsymbol{k}_k}{m_j + m_k}\right) & \text{for projectile breakup.} \end{cases} \tag{4.33}$$

The final velocity of particle k is $\boldsymbol{u}_k{}' = \frac{\boldsymbol{k}_k}{m_k}$ so that the final momentum of particle k in the j-k c.m. is given by

$$\begin{aligned} \boldsymbol{P}'_{k(jk)} &= m_k(\boldsymbol{u}_k{}' - \boldsymbol{u}_{jk}) \\ &= m_k\left(\frac{\boldsymbol{k}_k}{m_k} - \frac{\boldsymbol{k}_j + \boldsymbol{k}_k}{m_j + m_k}\right) \\ &= \frac{m_j \boldsymbol{k}_k - m_k \boldsymbol{k}_j}{m_j + m_k} \end{aligned} \tag{4.34}$$

with $m_k = m_p$ for target breakup and $m_k = m_t$ for projectile breakup. The scattering angle is then

$$\theta_{scat} = \arccos\left(\frac{\boldsymbol{P}_{k(jk)} \cdot \boldsymbol{P}'_{k(jk)}}{P_{k(jk)} P'_{k(jk)}}\right). \tag{4.35}$$

4.4 Phase Space

The statistical distribution of final states in a system defines the phase space available to that system. The nonrelativistic expression for the available phase space for three particles in the final state is given by [Fur72]

$$\delta(E_p + Q - E_1 - E_2 - E_3)\delta(\boldsymbol{k}_p - \boldsymbol{k}_1 - \boldsymbol{k}_2 - \boldsymbol{k}_3)d\boldsymbol{k}_1 d\boldsymbol{k}_2 d\boldsymbol{k}_3 \tag{4.36}$$

where δ represents the conventional delta function.

For kinematically complete experiments it is convenient to consider the relative probability ρ_E that the energy of particle 1 in the coincident event lies between E_1^{low} and E_1^{high}. This is equivalent to projecting the available phase space onto the E_1 energy axis. Of greater use though is the knowledge of the relative probability ρ of finding E_1 and E_2 along a given element of the kinematically allowed arc S in the E_1 *vs* E_2 energy space. We will first present ρ_E and then ρ.

For projection onto the E_1 energy axis the expression for the available phase space (equation 4.36) needs to be integrated over $d\boldsymbol{k}_3$ and dE_2. After simplification this yields [Ohl65]

$$\rho_E(E_1)dE_1 d\Omega_1 d\Omega_2 = \frac{\eta\, m_1 m_2 m_3 k_1 k_2 h^{-6}}{(m_2 + m_3) + \frac{m_2(\boldsymbol{k}_1 - \boldsymbol{k}_p)\cdot\boldsymbol{k}_2}{k_2^2}} dE_1 d\Omega_1 d\Omega_2 \tag{4.37}$$

where η is a normalization factor. For our work, this factor was determined through a comparison to the Naval Research Laboratory's IA code [Lam91].

For projection onto the kinematically allowed curve S we start with ρ_E so that

$$\rho(E_1, E_2)dS d\Omega_1 d\Omega_2 = \frac{\rho_E}{\sqrt{1 + \left(\frac{dE_2}{dE_1}\right)^2}} \tag{4.38}$$

where

$$\frac{dE_2}{dE_1} = m_2\left(\alpha \pm \sqrt{\alpha^2 + \beta}\right)\left(\alpha' \pm \frac{\alpha\alpha' + \frac{\beta'}{2}}{\sqrt{\alpha^2 + \beta}}\right) \tag{4.39}$$

with

$$\alpha = \frac{\sqrt{2}\sin\theta_2 \sin\phi_2}{m_2 + m_3}\left(\sqrt{m_2 E_2}\sin\theta_2 + \sqrt{m_3 E_3}\sin\theta_3\right)$$

$$+\frac{\sqrt{2}\cos\theta_2}{m_2 + m_3}\left(\sqrt{m_2 E_2}\cos\theta_2 + \sqrt{m_3 E_3}\cos\theta_3\right)$$

$$\beta = \frac{2}{m_3(m_2+m_3)}\left[(m_2-m_3)E_3 - 2\sqrt{m_2 m_3 E_2 E_3}\cos\theta_{23}\right]$$

$$\alpha' = \frac{\sqrt{m_1}\,(\sin\theta_1\sin\theta_2\cos\phi_2 - \cos\theta_1\cos\theta_2)}{\sqrt{2E_1}(m_2+m_3)}$$

$$\begin{aligned}\beta' = {} & \frac{2m_3(m_1+m_2+m_3)}{m_2(m_2+m_3)^2}\left(\frac{\sqrt{m_1 m_p E_p}\cos\theta_1}{(m_p+m_t)\sqrt{E_1}} - 1\right) \\ & - \frac{2\sqrt{m_1}}{\sqrt{E_1}(m_2+m_3)^2}\left[\left(\sqrt{m_2 E_2}\sin\theta_2 + \sqrt{m_3 E_3}\sin\theta_3\right)\sin\theta_1\right. \\ & \left. - \left(\sqrt{m_2 E_2}\cos\theta_2 + \sqrt{m_3 E_3}\cos\theta_3\right)\cos\theta_1\right]. \end{aligned} \tag{4.40}$$

As can be seen by inspection of equations 4.37–4.40 the phase space factor is only a function of masses and of the final state momenta of the outgoing particles and therefore is identical for each of the four poles shown in figure 4.4.

4.5 Kinematic Factor

The kinematic factor κ is given by

$$\kappa = \frac{8({m_a}^2 + {m_b}^2 + m_a m_b)}{k_p} \tag{4.41}$$

where m_a and m_b are the masses of the interacting particles (scattered particle and struck particle, respectively) [Lam91]. Since the struck particle is either a proton or neutron and since their masses are approximately equal we set $m_b = 939.0$ MeV/c$^2 \equiv m_N$ so that

$$\kappa = \frac{8({m_d}^2 + {m_N}^2 + m_d m_N)}{k_p} \tag{4.42}$$

where $m_d = 1875.613$ MeV/c^2, the mass of the deuteron. With the above assumption that $m_a = m_N$ we see that κ is a constant for this reaction and also does not depend on the origin of the spectator particle (i.e., is the same for all four poles).

4.6 Deuteron Wave Function

The deuteron wave function can be approximated by a pure S-state[9] Hulthén wave function $\Psi(r)$ where

$$r\Psi(r) = C(e^{-ar} - e^{-br}) \tag{4.43}$$

with $a = 0.232$ fm^{-1}, $b = 1.202$ fm^{-1}, C a normalization constant and r the internucleon separation. The Fourier transform $\Phi(q)$ of $\Psi(r)$ in momentum space is [Bon73]

$$\Phi(q) = \frac{1}{\pi}\sqrt{\alpha\beta}\frac{(\alpha+\beta)^{\frac{3}{2}}}{(\alpha^2+q^2)(\beta^2+q^2)} \tag{4.44}$$

with $\alpha = a\hbar c = 45.78$ MeV/c, $\beta = b\hbar c = 237.18$ MeV/c and q is the magnitude of the momentum of each nucleon relative to the c.m. of the deuteron.

Using $\Phi(q)$ given above (equation 4.44), Valković *et al.* [Val72a, And72] showed that the IA predicts the general systematics of the shape of the cross section for the d+$d \rightarrow d$+p+n breakup reaction for incident deuterons in the 6–13 MeV laboratory energy range. To be more specific, the calculations predicted a structure that was somewhat broader than the measured spectra. Furthermore, it could not reproduce the magnitude; usually it overpredicts the cross section by an order of magnitude.

Similar discrepancies between data and IA calculations for the p+$d \rightarrow p$+p+n breakup reaction were observed (see for example [And72, Mar71, McI72]). Noting that the IA assumes that the spectator nucleon does not participate in the scattering process, it is easy to see that scattering events that occur when the two nucleons in the target deuteron are close to each other are more likely to violate this assumption. In this case, for low energy incident particles, the de Broglie wavelength is no longer small compared to the internucleon distance. However, at the QFS condition the internucleon distance of the particles in the target deuteron is at its greatest value and the assumptions leading to the IA are more likely to be valid. Using this observation, Paić *et al.* [Pai70] introduced a purely phenomenological approach to eliminate scattering events near the center of the deuteron. They used a cutoff radius R in the deuteron wave function so that the effective deuteron wave function $\Psi(r)$ became

$$\Psi(r) = \begin{cases} 0 & \text{for } r < R \\ \Psi(\text{Hulthén}) & \text{for } r > R \ . \end{cases} \tag{4.45}$$

[9]The assumption that the deuteron wave function is spherical is reasonable for small momentum transfers. As the momentum transfer increases the omission of the D-state becomes more serious.

This approach essentially excises the deuteron's center and leads to a reduction in the calculated cross section. The cutoff radius R then becomes an adjustable parameter in the IA. The value of R needed to reproduce the magnitude of the data decreases with increasing incident bombarding energy since the de Broglie wavelength decreases.

Although the introduction of the cutoff radius improved the agreement between the calculation and the magnitude of the cross section data, it caused the prediction to be narrower than the data. In other words, while in regions of small q (large internucleon separation) the agreement with data was good, but in regions of high momentum transfer (small internucleon distances) the IA underpredicted the cross sections. This led McIntyre *et al.* [McI72] to introduce a smooth cutoff procedure by adjusting β in equation 4.44. Their analysis showed that a smooth cutoff of the central part of the deuteron wave function can account for not only the magnitude of the QFS cross section but also for its shape as a function of momentum transfer.

A group at the Naval Research Laboratory [Bon73] studying the $d+d \rightarrow d+p+n$ breakup reaction at E_d=14–36 MeV followed the method of McIntyre of introducing a smooth cutoff in the deuteron wave function. Their modification to the deuteron wave function resulted in the Fourier transform being

$$\Phi(q) = \left[\frac{1}{\pi}\frac{\sqrt{\alpha\beta(\alpha+\beta)}}{\alpha-\beta}\right]\frac{(\alpha+\beta')(\alpha-\beta')}{(\alpha^2+q^2)(\beta'^2+q^2)} \tag{4.46}$$

where β' is an adjustable parameter. Using this approach they concluded that all QFS cross-section data for this reaction could be approximated by a single-pole (target breakup) IA calculation with only one adjustable parameter β' provided there is no interference from final-state interactions (FSI). They also point out that a sharp radial cutoff in the wave function introduces an oscillatory behavior in the tail of the wave function and therefore is not suitable for calculations involving interference between poles.

For our calculations $\beta' = 84.69$ MeV/c was chosen so that the cross section calculations using off-shell matrix elements reproduced the magnitude of the cross section reported by Valković [Val72a] for (θ_d, θ_n)=(+20.0°, −20.0°) at 12.0 MeV. Shown in figure 4.5 is the square of the fourier transform of the deuteron wave function as a function of nucleon momentum. The solid curve was obtained by using no cutoff radius (equation 4.44) while the dashed curve represents the smooth cutoff case (equation 4.46) with $\beta' = 84.69$ MeV/c.

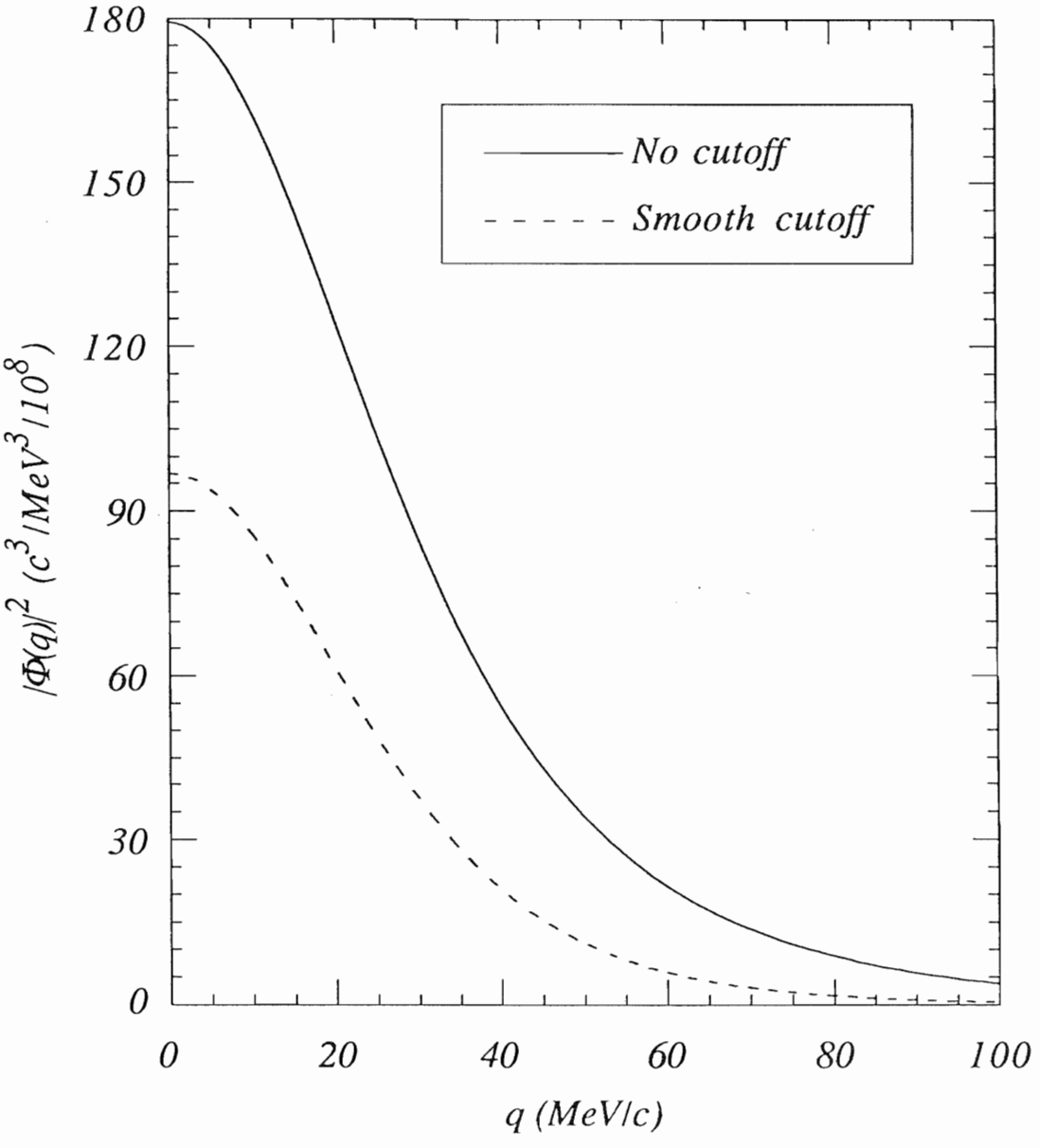

Figure 4.5: Square of the Fourier transform of the deuteron wave function as a function of nucleon momentum.

4.7 $\mathcal{T}$-Matrices for dn Free-Scattering

Two sets of dn transition matrices for use in the IA calculations were generated. The first set was computed at TUNL using the code of Y. Koike [Koi89, Koi86] and used a separable expansion of the Paris potential (PEST) for the NN interaction. The second set of transition matrices, computed on the Cray Y-MP at the North Carolina Supercomputing Center with the code of A.C. Fonseca [Fon90, Fon89], used a one-term separable Yamaguchi type NN potential. Both codes were run at a variety of interaction energies to cover the range of dn c.m. energies in the post-collision prescription appropriate for an incident energy of 12 MeV.

The primary differences in the two sets of matrices are listed in table 4.1. The calculations using the PEST potential contain nine NN partial waves while the Yamaguchi potential calculations included only two. The lack of P-waves in the Yamaguchi potential severely hinders the A_y calculations since the vector analyzing powers come primarily from P-waves in the NN interaction [How87]. Both potentials, however, included the tensor coupling ($^3S_1$–$^3D_1$) which strongly influences the tensor analyzing powers. On the other hand, sensitivity studies performed at TUNL indicate that the slight difference in the tensor forces in these potentials (the PEST and Yamaguchi potentials give a D-state probability for the deuteron of 5.5 and 5.0%, respectively) has little effect on our polarization observables. Nuclear matrix elements were computed for three-nucleon total angular momentum states up to $J^\pi = \frac{27}{2}^\pm$ and $\frac{15}{2}^\pm$ for the PEST and Yamaguchi potentials, respectively. At the low interaction energies (0–4 MeV in the c.m.) in our calculations convergence in the observables was obtained with $J^\pi \leq \frac{11}{2}^\pm$. The big advantage of Fonseca's code was that it allowed for the calculation of matrix elements both on- and off-the-energy-shell. However, neither code had the ability to treat the Coulomb force correctly[10] in the context of

[10]Kok and van Haeringen [Kok81] as well as Valković [Val72b] and Bajzer [Baj87] have introduced Coulomb corrections in the IA by means of a Coulomb distortion. It mainly affects the magnitude of the calculated cross section and to a lesser extent the shape of the QFS enhancement. Future improvements to our IA codes may include this correction though it is unlikely that the calculated polarization observables will be affected significantly.

Koonin and Mukerjee [Koo90], following the pioneering work of Oppenheimer and Phillips [Opp35] in which it was noted that the Coulomb field of the target nucleus acts only on the proton in the deuteron and not on the deuteron's c.m., have studied the effect of the Coulomb distortion of the deuteron on the relative cross sections for (d,p) and (d,n) reactions at $E_d \leq 3.5$ MeV. Their conclusion that the effect modifies the relative cross sections by only a few percent suggest that the effect on the d+$d \rightarrow d$+p+n cross section is also small. No conclusion was made on the effect the distortion has on polarization observables since they were not investigated.

Characteristics	Koike	Fonseca
NN potential	PEST	Yamaguchi
NN partial waves	${}^1S_0$, ${}^3S_1 - {}^3D_1$, ${}^1P_1$, ${}^3P_{0,1,2}$, ${}^1D_2$, ${}^3D_{2,3}$	${}^1S_0$, ${}^3S_1 - {}^3D_1$
D-state probability	5%	5.5%
$3N$ J^π	$\frac{1}{2}^\pm, \frac{3}{2}^\pm, \ldots, \frac{27}{2}^\pm$	$\frac{1}{2}^\pm, \frac{3}{2}^\pm, \ldots, \frac{15}{2}^\pm$
On-shell	Yes	Yes
Off-shell	No	Yes
Coulomb	No	No

Table 4.1: Characteristics of $\mathcal{T}$-matrices used in the IA calculations. See text for a complete discussion of the table.

the IA, so *dn* matrix elements were used in calculating observables for both *dn* and *dp* vertices.

The two IA codes developed at TUNL (NMPWIA and NMPWIAOFF) differ only in the manner that they handle the $\mathcal{T}$-matrices. The code NMPWIA used the matrix elements from Koike's code as an input and interpolated between the discrete interaction energies in the input to obtain matrix elements at the appropriate energy. Fonseca's matrix elements were used as inputs into NMPWIAOFF and had to be interpolated between energies for both the pre- and post-collision prescriptions. Consequently the code NMPWIAOFF ran several orders of magnitude slower than NMPWIA but it did correctly handle the *dn* off-shell interaction.

4.8 Extraction of Observables from $\mathcal{T}$-Matrix

The elements of the $\mathcal{T}$-matrices represent transitions from states with quantum numbers $m_n m_d$ to states with $m'_n m'_d$ where m_n and m_d are the spin projections of the neutron and deuteron, respectively onto the quantization axis (taken to be in the direction of the momentum of the neutron).

The nucleon-deuteron differential cross section can easily be extracted from the $\mathcal{T}$-matrix by simply taking the trace of $\mathcal{T}\mathcal{T}^\dagger$, where $\mathcal{T}^\dagger$ represents the complex conjugate

of $\mathcal{T}$, and multiplying by the appropriate constants:

$$\left(\frac{d\sigma}{d\Omega}\right)_{dn} = \frac{2}{27}(2\pi)^4\left(\frac{m}{\hbar^2}\right)Tr(\mathcal{T}\mathcal{T}^\dagger)$$

$$= \frac{2}{27}(2\pi)^4\left(\frac{m}{\hbar^2}\right)\sum_{m'_n m'_d m_n m_d}|\mathcal{T}(m'_n,m'_d;m_n,m_d)|^2 \quad . \qquad (4.47)$$

For a four-pole calculation of the three-body breakup cross section the appropriate $\mathcal{T}$-matrix (equation 4.13) needs to be substituted into equation 4.47 and the result then substituted into

$$\frac{d^3\sigma}{d\Omega_1 d\Omega_2 dS} \equiv \sigma_{4P} = \sigma_{TB} + \sigma_{PB}$$

$$= \kappa\,\rho\left(\left(\frac{d\sigma}{d\Omega}\right)_{dN}^{\mathcal{T}_{TB}} + \left(\frac{d\sigma}{d\Omega}\right)_{dN}^{\mathcal{T}_{PB}}\right). \qquad (4.48)$$

The polarization observables can be calculated as in equation 4.11. For target breakup processes the $\vec{d}n$ vector analyzing powers are given by

$$(A_y)_{\vec{d}n} = \frac{2\sqrt{2}\sum_{m'_n m_n m_d} Im(\mathcal{T}^*(m'_n,1;m_n,m_d)\mathcal{T}(m_n,0;m_n,m_d))}{\sum_{m'_n m'_d m_n m_d}|\mathcal{T}(m'_n,m'_d;m_n,m_d)|^2} \quad . \qquad (4.49)$$

For projectile breakup processes the $\vec{n}d$ vector analyzing powers are given by

$$(A_y)_{\vec{n}d} = \frac{2\sum_{m'_d m_n m_d} Im(\mathcal{T}^*(\frac{1}{2},m'_d;m_n,m_d)\mathcal{T}(-\frac{1}{2},m'_d;m_n,m_d))}{\sum_{m'_n m'_d m_n m_d}|\mathcal{T}(m'_n,m'_d;m_n,m_d)|^2} \quad . \qquad (4.50)$$

The $\vec{d}n$ tensor analyzing powers (used only for TB poles) in spherical notation are

$$(T_{20})_{\vec{d}n} = \frac{\sqrt{2}\sum_{m'_n m_n m_d}(|\mathcal{T}^*(m'_n,1;m_n,m_d)|^2 - |\mathcal{T}(m'_n,0;m_n,m_d)|^2)}{\sum_{m'_n m'_d m_n m_d}|\mathcal{T}(m'_n,m'_d;m_n,m_d)|^2} \qquad (4.51)$$

$$(T_{21})_{\vec{d}n} = \frac{-\sqrt{6}\sum_{m'_n m_n m_d}(Re(\mathcal{T}^*(m'_n,1;m_n,m_d)\mathcal{T}(m'_n,0;m_n,m_d)))}{\sum_{m'_n m'_d m_n m_d}|\mathcal{T}(m'_n,m'_d;m_n,m_d)|^2} \qquad (4.52)$$

$$(T_{22})_{\vec{d}n} = \frac{\sqrt{3}\sum_{m'_n m_n m_d}(Re(\mathcal{T}^*(m'_n,1;m_n,m_d)\mathcal{T}(m'_n,-1;m_n,m_d)))}{\sum_{m'_n m'_d m_n m_d}|\mathcal{T}(m'_n,m'_d;m_n,m_d)|^2} \quad . \qquad (4.53)$$

Conversion to Cartesian notation (see equation 3.8) is given by

$$A_{yy} = -\sqrt{3}\,T_{22} - \frac{1}{\sqrt{2}}\,T_{20}$$

$$A_{zz} = \sqrt{2}\,T_{20}\ . \tag{4.54}$$

4.9 Four-Pole Cross Section Example

In this section we illustrate the role of the various contributions to the three-body breakup cross section. The experimental data (points) obtained for (θ_d, θ_p)=(+17.0°, −17.0°) are shown in figures 4.6-A–E as a function of S along with a variety of kinematic quantities and theoretical calculations. The cross-section data was corrected for accidental background and the displayed error bars in the figures indicate the statistical uncertainties in the measurement. In figures 4.6-A the curves represent the q for each of the four poles, where q is the pre-collision momentum of the struck nucleon in the c.m. of the deuteron that broke up. Notice that q is relatively large for two of the poles (Tp and Pn) while somewhat flat at 35 MeV/c for pole Pp and dips to zero for the Tn pole (at the point along the locus that satisfies the QFS condition). The square of the Fourier transform of the deuteron wave function $|\Phi(q)|^2$ as a function of q is shown in figure 4.6-B for each pole. While the $|\Phi(q)|^2$ is relatively flat for the Pp pole and is practically zero for the Tp and Pn poles because of the large values of q for the latter two poles, it varies strongly as a function of S for the Tn pole and reaches a maximum near the peak in the cross section.

The kinematic factor (κ) and phase space factor (ρ) are identical for all four poles; their product is shown in figure 4.6-C. The dN cross sections, calculated using off-shell matrix elements produced with the Yamaguchi potential, are larger for the Pp pole than for the Tn pole as shown in figure 4.6-D. This somewhat compensates for the smaller Fourier transform of the Pp pole. The three-body breakup cross sections obtained from the product of κ, ρ, $|\Phi_d(q)|^2$ and $(\frac{d\sigma}{d\Omega})_{dN}$ are shown in figure 4.6-E. Here it can easily be seen that even though q is relatively large for the Pp pole, the dN cross section keeps the three-body cross section comparable to that of the Tn pole. Notice that both poles peak at approximately the maximum in the experimental cross section. Also shown is the four-pole cross section (solid curve) obtained from equation 4.48.

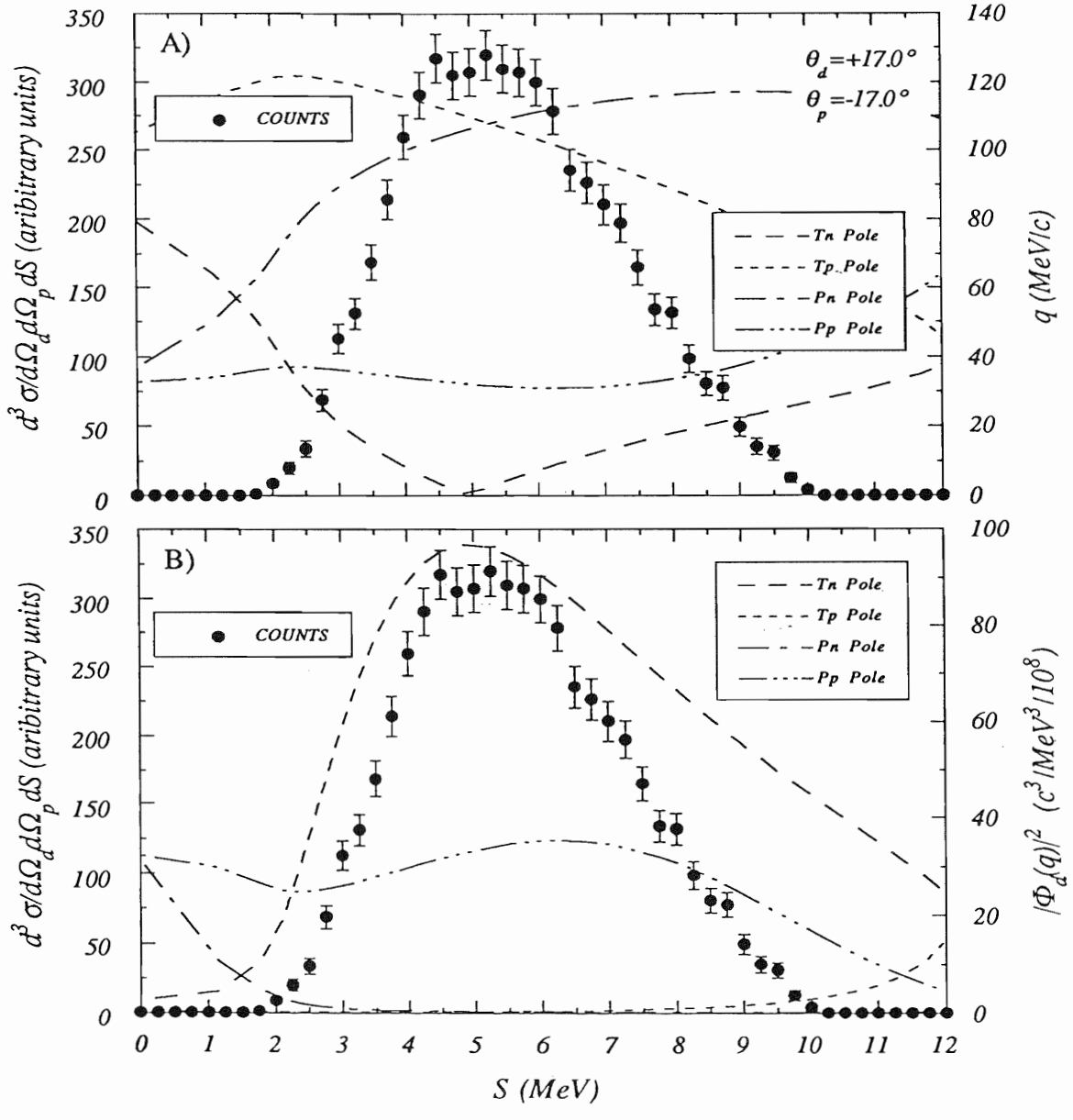

(Continued on next page.)

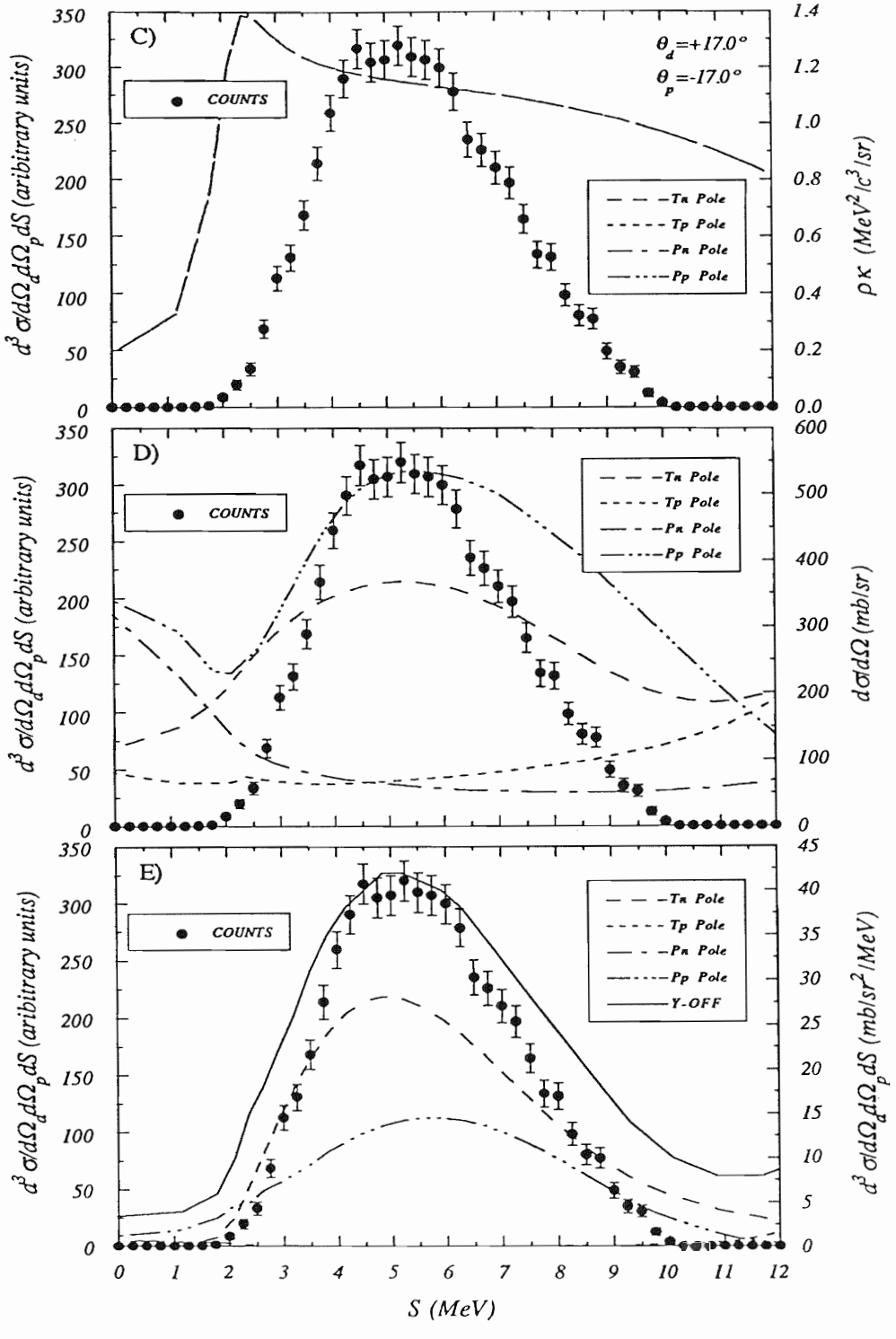

Figure 4.6: Cross section calculated from the IA as a function of S. The measured yields are displayed as the points (left scale) and q, $|\Phi_d(q)|^2$, $\rho\kappa$, $(\frac{d\sigma}{d\Omega})_{dN}$, and $\frac{d^3\sigma}{d\Omega_d d\Omega_p dS}$ for each of the poles are displayed as the curves (right scale) in parts A, B, C, D and E, respectively. See text for further discussion.

In most of the cases studied in this work the cross section was dominated by two poles, one TB and one PB. The exceptions were in the cases of the *pn* coincidence measurements where the two dominant poles were both PB. Shown in table 4.2 is a calculation of the relative contributions of the four poles at the peak in the cross section. The calculations for table 4.2 assumed an incoherent addition of the four poles. These calculations were done using both on- and off-shell matrix elements, as shown in table 4.2. It should be pointed out that the values in the table are quite model dependent in that using a different value for the adjustable parameter β' in the Fourier transform changes the relative weights of the cross sections.

In most cases going from on-shell to off-shell increased the dominance of the strongest pole. This is just a consequence of a feature of breakup reactions that was recognized by Redish [Red70]. He found that the cross section for $(p, 2p)$ knockout reactions roughly scales inversely with the degree to which the two-particle vertex is off-shell. Because in our case the secondary poles were always further off-shell than the primary pole, their calculated cross sections dropped more than that of the primary pole when switching from on-shell to off-shell matrix elements.

Detected Particles	Angles	On-Shell				Off-Shell			
		Tn	*Tp*	*Pn*	*Pp*	*Tn*	*Tp*	*Pn*	*Pp*
Deuteron-Proton	±10.0, ∓10.0	**53%**			47%	**56%**			44%
Deuteron-Proton	±10.0, ∓41.2	**59%**	39%	1%	1%	**62%**	38%		
Deuteron-Proton	±17.0, ∓17.0	**55%**			45%	**67%**			33%
Deuteron-Proton	±17.0, ∓34.5	**82%**	3%		14%	**93%**	1%		6%
Deuteron-Proton	±19.4, ∓19.4	**55%**			15%	**71%**			29%
Deuteron-Proton	±34.5, ∓17.0	40%		2%	**58%**	**53%**		1%	46%
Deuteron-Neutron	±17.0, ∓17.0		**55%**	45%			**67%**	33%	
Deuteron-Neutron	±17.0, ∓34.5	3%	**83%**	14%		1%	**93%**	6%	
Deuteron-Neutron	±19.4, ∓28.9	1%	**68%**	31%			**83%**	17%	
Proton-Neutron	±17.0, ∓17.0	1%	1%	**49%**	**49%**			**50%**	**50%**
Proton-Neutron	±17.0, ∓34.5	4%	1%	14%	**81%**	2%		9%	**89%**
Proton-Neutron	±19.4, ∓28.9	3%	1%	27%	**70%**	1%		22%	**77%**

Table 4.2: Relative contributions of poles to the cross section (assuming an incoherent sum of all four poles) evaluated at the peak in the cross section for the 4-pole off-shell calculation. The primary pole for each calculation is indicated in bold-faced font while blank spaces indicate <0.5% contribution.

Chapter 5

Presentation of Data and Calculations

5.1 Introduction

Previous attempts to use the phenomenological approach of the Impulse Approximation (IA) to calculate the cross section of the $d+d \rightarrow d+p+n$ breakup reaction had only a limited success (see chapter 4). Without modifying the deuteron's wave function, the calculations usually predict a quasifree scattering (QFS) enhancement that is both broader and greater in magnitude (often by a factor of 10 or more) than the measured values. At energies greater than 100 MeV the IA has been used with better success[1] for the $p+d \rightarrow p+p+n$ breakup reaction [McC71]. At energies below 100 MeV the failure of the IA is often attributed to the lack of inclusion of multiple scattering terms in the formulation of the theory. Cahill *et al.* [Cah74] point out that for the $n+d \rightarrow n+n+p$ breakup reaction at $E_{lab} = 14$ MeV that all multiple scattering terms peak at the same point as the single scattering term for QFS. These rescattering terms were investigated by Witała *et al.* [Wit89b] for the $n+d \rightarrow n+n+p$ and $p+d \rightarrow p+p+n$ breakup reactions under QFS conditions at E_{lab}=22.7 MeV. They

[1] Impulse approximation calculations for the $p+d \rightarrow p+p+n$ and $n+d \rightarrow n+n+p$ breakup reactions are in general simpler than for the $d+d \rightarrow d+p+n$ breakup reaction. This stems from the fact that in the first two cases there are only two poles (both target breakup) involved whereas the later case involves two loosely bound deuterons resulting in four poles (two target breakup and two projectile breakup). With fewer poles involved, the calculation is less complicated since interference effects between the poles is reduced due to their distribution in phase space. Furthermore, the problem associated with breakup of a polarized particle is eliminated if in the first two cases polarization measurement are performed with polarized nucleons interacting with an unpolarized deuteron.

found that the addition of the rescattering terms to the single scattering term, which is the only term in the IA, strongly reduced their calculated cross section and put it in agreement with the measured data. Furthermore, they claim that the influence of the interference between the rescattering terms on scattering observables is angle dependent. This explains why the IA seems to work better in certain angular regions than others.

Our aim in this chapter is to take the IA one step further in the investigation of the $\vec{d}+d \rightarrow d+p+n$ breakup reaction by using it to calculate polarization observables. Usually the multiple scattering terms discussed above are taken into account in the IA by either the introduction of a cutoff radius in the wave function of the particle that breaks up or as an overall normalization in the calculation of the three-body breakup cross section. If the scaling factor due to rescattering is independent of the relative spin orientation of the interacting particles, then the IA should give a good description of spin observables since they depend on relative, rather than absolute cross sections.

To date, there is only one published measurement of analyzing powers for the $\vec{d}+d \rightarrow d+p+n$ breakup reaction [Fuk89]. Fukunaga *et al.* measured cross sections and vector analyzing powers A_y at an incident deuteron energy of 60 MeV and compared their data to IA calculations. In their IA they introduced a multiple scattering correction factor η that was calculated in a manner that is independent of the spin-direction of the interacting particles. Because η is spin-direction independent it cancels in the calculations of spin observables, since ratios of cross sections are taken. They claim that η, at the energy of their experiment, accounts for the majority of the effects due to rescattering. Their claim is evidenced by their ability to correctly predict the proper magnitude of the QFS enhancement without the introduction of a cutoff radius in the deuteron wave function. However, it should be pointed out that they make no claim about the effect of η on the shape of the QFS enhancement and admit that as the detector angle pairs are changed their calculations fail to reproduce the structure found in the angular distribution of their QFS cross-section data.

They were able to pick deuteron+proton angle pairs corresponding to essentially a pure single pole process since the four poles are well separated in phase space at an incident energy of 60 MeV. In one set of measurements they concentrated on target breakup (TB) with the single dominant pole being Tn and for another set of measurements they concentrated on projectile breakup (PB) with the Pn pole being dominant. They compared their A_y measurements to published A_y data for free

scattering. Using a variant of the pre-collision-prescription to compute the interaction energy in the IA, they compared their TB data to ^{1}H$(\vec{d},d)^1$H data at E_d=60 MeV and their PB to D$(\vec{p},p)$D data at E_p=30 MeV. The comparison between QFS data and free scattering (FS) data is valid, within the context of the IA, if the process is essentially a single pole process and if off-shell effects are neglected. At these energies the off-shell effects are small when the comparison is made at the peak of the QFS enhancement rather than in the tails of the enhancement. The respectable agreement between their QFS data and the FS data support the contention that when an unpolarized deuteron quasifree scatters off a nucleon contained within a vector polarized deuteron, that interaction can be viewed as a deuteron interacting with a polarized nucleon that has the same direction and magnitude of polarization as the vector polarization of the deuteron in which it resided. However, since $\vec{d}p$ FS and $\vec{p}d$ FS A_y show similar energy and angular dependences [Fuk89], their results do not really distinguish between $\vec{d}p$ QFS and $\vec{p}d$ QFS. Therefore, the use of a vector polarized deuteron does not adequately distinguish between a $\vec{d}p$ and a $\vec{p}d$ interaction. Our work, on the other hand, includes tensor observables which are different for the two interactions. In fact, the tensor observables are undefined for a $\vec{p}d$ interaction, thereby making the distinction between the $\vec{d}p$ and $\vec{p}d$ interaction trivial.

In the sections that follow, our data will be compared to three different IA calculations which include contributions from all four poles as outlined in chapter 4. They will be referred to as P-ON, Y-ON and Y-OFF and are defined below.

P-ON Impulse approximation calculation using the PEST NN potential evaluated at the on-shell interaction energy given by the post-collision-prescription.

Y-ON Impulse approximation calculation using the Yamaguchi type NN potential evaluated at the on-shell interaction energy given by the post-collision-prescription.

Y-OFF Impulse approximation calculation using the Yamaguchi type NN potential evaluated at the off-shell interaction energy which is given by a combination of the pre- and post-collision-prescriptions.

The three calculations in addition to being compared with the data, will be compared to each other in an attempt to further understand the dynamics of the $\vec{d}+d \rightarrow d+p+n$ breakup reaction.

The analyzing powers for each of our angle pairs were computed in 250 keV bins along the locus S as described in chapter 3 and are presented in tabular form in appendix A.1. To reduce the uncertainty in the displayed data the binning size was increased to 750 keV (see appendix A.2 for tabulated data). This was accomplished by the statistical addition of the points from the 250 keV bins in groups of three. The effective centroid for each 750 keV bin was determined by weighting the centroids of the 250 keV bins by the uncertainty in the A_{zz} data. In the plots that follow, the vertical error bars represent the uncertainty in the measurement as defined in sections 3.4.1–3.4.3 and the horizontal bars indicate the arc segment along S which that point spans.

5.2 Off-Shell IA Calculations Compared to Data

Shown in figures 5.1–5.12 are the measured data along with our Y-OFF calculations. For the A_y measurements the calculated analyzing powers are displayed for each of the four poles (identified by the origin of the spectator particle; Tn, Tp, Pn and Pp) and are shown as the dashed curves in the figures. For A_{yy} and A_{zz} only the calculations for the TB poles are shown, since tensor analyzing powers for the PB poles are undefined in our model. In the weighted average (see equation 4.12) for calculating the four-pole tensor analyzing powers, the PB poles were treated as unpolarized contributions by setting the values of A_{yy} and A_{zz} identically equal to zero for these poles. The full calculation which incorporates all four poles is shown as the solid curve in the figures and is labeled as Y-OFF.

For comparison purposes the vertical scales in the figures were fixed to the same values for all angle pairs and in several cases the A_{zz} calculations for one or both of the TB poles were entirely above the upper scale limit and therefore were not plotted. In all of these cases the TB poles that were not plotted contributed <2% of the cross section and therefore played a minor role in the calculation of the polarization observables (see table 4.2 for a listing of the various strengths of the different poles).

In the sections that follow, we will make several observations about the calculations in comparison to the data and discuss some of their implications. However, the lack of P-waves in the NN potential renders the comparison of measured data with the A_y calculations somewhat fruitless, since it is known that the vector analyzing powers in $\vec{N}d$ and $\vec{d}N$ free scattering come primarily from the ^3P NN interaction. Therefore, the data and calculations for A_y, A_{yy} and A_{zz} will be presented in this section, but

the discussion of the A_y data and calculations will be delayed until section 5.3.

5.2.1 Deuteron-Nucleon Coincidence Data

The dp and dn coincidence data along with the Y-OFF calculations are presented in figures 5.1–5.6 and 5.7–5.9, respectively. By examining the quality of agreement between the calculations for the individual poles and the data, we can determine the extent to which the breakup process is dominated by a single pole. At higher energies the kinematics clearly suggest that the individual poles occupy a smaller region of phase space and consequently are better separated. Examination[2] of the figures for the dp coincidence reveals that the calculations for the Tn pole, which is the dominant pole (see tables 4.2 and B.1–B.9) and has the smallest spectator momentum of all the poles, always gives a better description of the A_{yy} and A_{zz} observables than the Tp pole calculation. This is expected since the Tp pole contributes less than 1% of the cross section at the peak of the enhancement for all angle pairs except for $(\theta_d,\theta_p)=(+10.0°,-41.2°)$, where it contributes 38% of the cross section. Since the values of A_{yy} and A_{zz} for the PB poles are set to zero, these poles have been neglected in the comparisons. For the dn data the dominant pole is Tp and the calculation for this pole always gives the better prediction of the data. This indicates that the analyzing powers in the $\vec{d}+d \rightarrow d+p+n$ breakup process are dominated by the same single pole as indicated by cross-section calculations.

Since our IA model does not have a prescription for calculating tensor polarization observables for PB with the incident deuteron polarized, we have set the tensor analyzing powers to zero. The validity of this approach can be examined by comparing the analyzing powers for the dominant pole to the full four-pole calculation.[3] In each of the cases where the PB poles contribute 20% or more of the cross section, setting the analyzing powers equal to zero for the PB poles improves the agreement with the data. This is evident in the comparison of the Tn (Tp) pole to the Y-OFF calculations for the dp (dn) coincidence data. However, there are three cases where this trend is violated. For the angle pairs $(\theta_d,\theta_p)=(+17.0°,-34.5°)$, $(\theta_d,\theta_n)=(+17.0°,-34.5°)$ and

[2]The quality of the agreement between data and calculations was determined by visual inspection only.

[3]Actually one would like to examine the effects of adding the four poles in as many combinations as possible, but this would require 15 different combinations per angle pair and would be prohibitively time consuming. In reality, a two-pole calculation involving the two major poles is essentially a four-pole calculation since in all cases studied the two major poles accounted for 98% or more of the cross section.

$(\theta_d,\theta_n)=(+19.4°,-28.9°)$, in which the PB poles contribute 6%, 6% and 17% of the cross section, respectively, the deterioration of the agreement between the IA calculations and the data when PB poles are included in the calculations does not support the notion of zero tensor analyzing powers for PB. Furthermore, for these three cases we find in the kinematic tables in appendix B that the spectator momentum q relative to the c.m. of the breakup deuteron is always equal to or greater than 55 MeV/c, while for angle pairs which support the conjecture that the analyzing powers for the PB poles are zero, have $q \leq$38 MeV/c. In the remaining case, $(\theta_d,\theta_p)=(+10.0°,-41.2°)$, the influence of the PB poles is not felt (PB poles contribute less than 0.5% of the cross section), however the agreement with the data is still poor. From these observations we can conclude that when a PB pole contribution to the cross section is greater than ~20%, which also corresponds to the q for that pole being less than 38 MeV/c, the calculations tend to favor the addition of a zero for the analyzing powers of that PB pole. This notion of setting the tensor analyzing powers to zero for PB poles will be explored further with the *pn* coincidence data. Since kinematics suggest that the *pn* coincidence processes are virtually pure PB, one should observe a tensor analyzing power of zero.

The problem associated with calculating tensor analyzing powers for PB poles is not a factor when examining the *dp* coincidence data for $(\theta_d,\theta_p)=(+10.0°,-41.2°)$, since the breakup reaction at this angle pair is practically pure TB. Also the difficulty in our calculations of properly treating the interference between the four poles (see section 4.2) is avoided. The four-pole calculations agree better with the data than the major pole Tn, but they still fail to accurately reproduce the structure along the locus, even predicting the wrong sign for A_{zz}. Furthermore, the secondary pole (the Tp pole) contributes 38% of the cross section and has a spectator momentum equal to or greater than 60 MeV/c.

While the four-pole calculations Y-OFF show some resemblance to the data for both *dp* and *dn* coincidences, one would be hard pressed to suggest that the calculations accurately describe the data. However, the calculations tend to have the best qualitative agreement with the data for cases in which the detectors in the pair were placed at symmetric angles. In the symmetric angle arrangements, the spectator momentum in the secondary poles was always less than 38 MeV/c. An interesting feature of the data for symmetric angle measurements is that they all follow the same trend; the A_{yy} makes small undulations around zero along S and the A_{zz} starts positive at low values of S and decreases with increasing S eventually turning negative. The

calculations seem to describe the A_{zz} data at small S and to reproduce the negative slope of the data, but they fail to change sign as does the data at larger values of S.

5.2.2 Proton-Neutron Coincidence Data

To further test the notion that the tensor analyzing powers should be zero for PB, we measured analyzing power data for the *pn* coincidences (see figures 5.10–5.12). The kinematics of these reactions indicate that the processes are essentially pure PB ($\leq$2% TB). With this in mind we would expect the measured tensor analyzing powers to be almost zero in figures 5.10–5.12. In fact, this is not observed for A_{yy}. The values of A_{yy} are almost always about +0.05, while the values of A_{zz} are nearly zero or slightly negative. The calculations for A_{zz} are in good agreement with the data except at the extreme values of S. An additional observation based on the kinematics of the reactions (see tables in appendix B) is that the spectator momentum never drops below 30 MeV/c for any of the poles, indicating that each of the four poles is far from the QFS condition.

It is possible that the two PB poles interfere in such a way to produce a non-zero analyzing power. Unfortunately, our calculations do not contain the sophistication necessary to support or refute that suggestion.

One interesting feature of the (θ_p,θ_n)=(+17.0°,−17.0°) data is the inherent symmetry in the system which will be used in our test of charge-symmetry breaking presented in chapter 6.

5.2.3 Conclusions

The lack of consistent agreement between our data and our IA calculations presented in sections 5.2.1–5.2.2 indicate that the IA at low energies cannot reliably be used to calculate spin observables for the $\vec{d}+d \rightarrow d+p+n$ breakup reaction. The primary deficiency inherent in the IA is the lack of inclusion of multiple scattering terms. While the IA, which assumes single scattering, is sufficient to approximate the shape and location of the enhancements in the cross section, it does not predict the correct magnitude of the cross section nor does it give a detailed description of the analyzing powers. The importance of the multiple scattering terms is reinforced by the observation of non-zero tensor analyzing powers associated with the breakup of the polarized (i.e., projectile) deuteron. Ignoring multiple scattering terms also excludes

the possibility of the formation of a compound nucleus which can decay through excited states of ^{3}H or ^{3}He as proposed by Kanada *et al.* [Kan91]. Furthermore, the relatively large analyzing powers observed in some of our measurements suggest that the breakup process goes through an intermediate state with n-^{3}He or p-^{3}H scattering, since it is well known that these two scattering systems can generate analyzing powers significantly larger than either $\vec{d}d$ or $\vec{d}N$ scattering at low energies [Gru81].

The failure of the IA to accurately describe our data is not surprising since most of our observables were measured for configurations with a sizeable spectator momentum in one of the major poles. The IA is expected to be most valid for configurations closest to the QFS condition, which corresponds to zero spectator momenta relative to the c.m. of the breakup deuteron (i.e., the nucleons in the breakup deuteron are at their largest separation distance). Therefore, a deterioration in the agreement between the data and the IA is expected for increasing distances along the locus from the point which corresponds to QFS.

While not violating the basic assumptions of the IA, there are a number of deficiencies in our calculations: 1) The Coulomb force between the protons has been neglected. At small relative energies and small scattering angles (see tables B.1–B.12) it is well known that the Coulomb force can dominate the scattering process. 2) Interference effects between the PB and TB poles are not handled properly. 3) The $^3S_1$ neutron-proton final state interaction, which was shown by Kluge *et al.* [Klu78] to be an important contribution to the breakup spectrum in the region of the QFS enhancement, was ignored in our IA calculations.

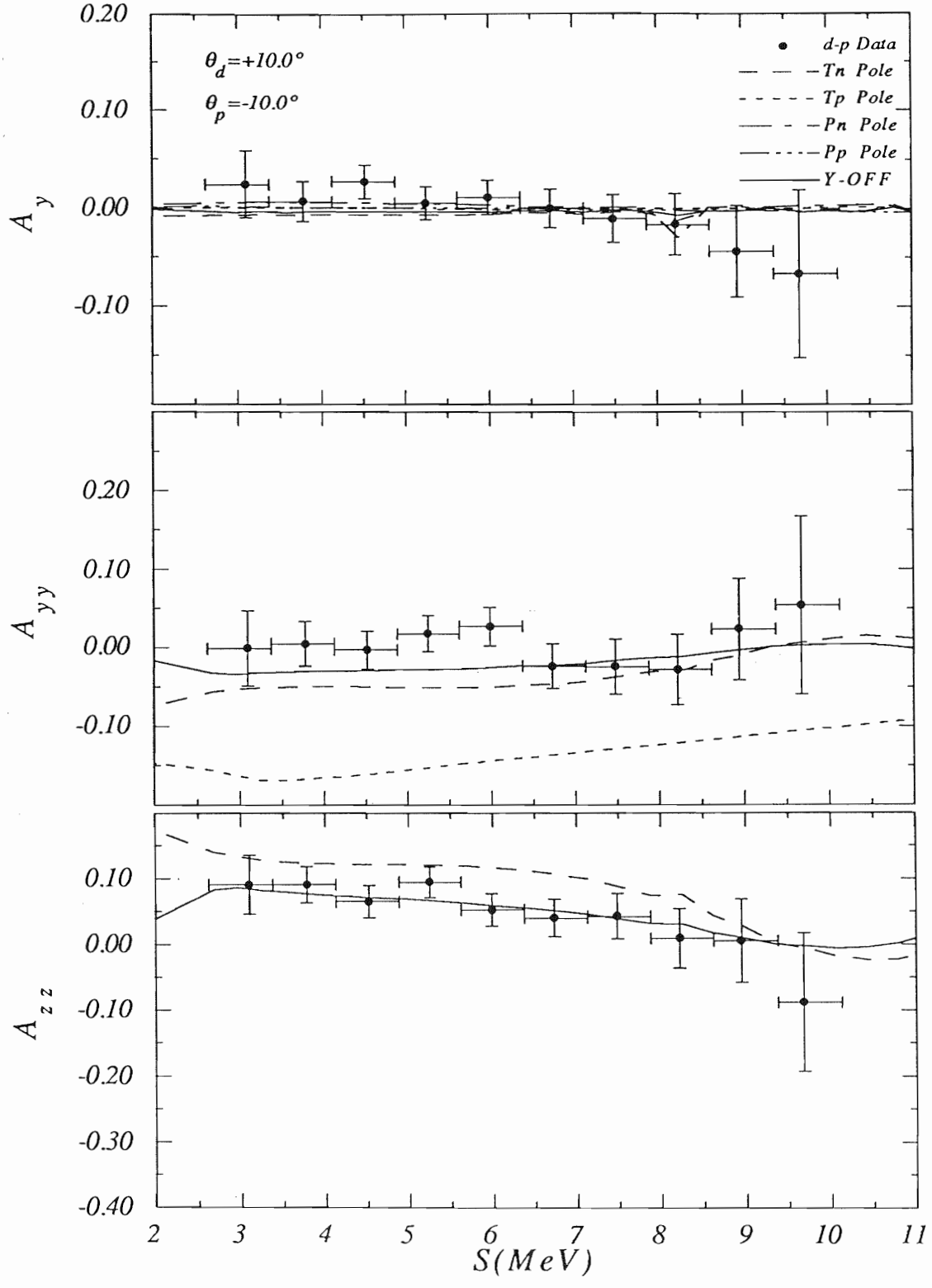

Figure 5.1: Comparison of off-shell IA calculations to D$(\vec{d}, dp)n$ data with (θ_d, θ_p)=(+10.0°, −10.0°).

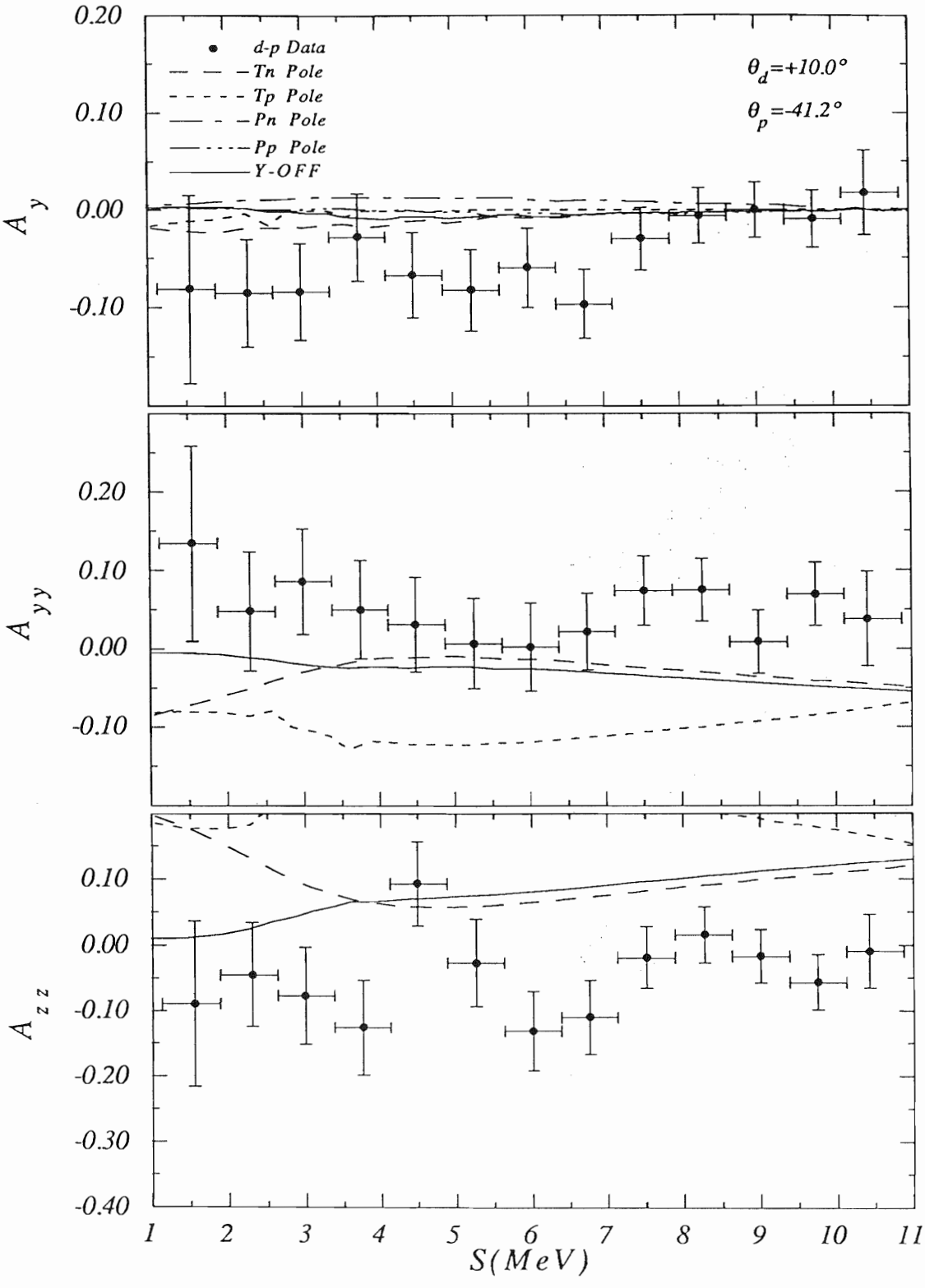

Figure 5.2: Comparison of off-shell IA calculations to $D(\vec{d}, dp)n$ data with $(\theta_d, \theta_p)=(+10.0°, -41.2°)$.

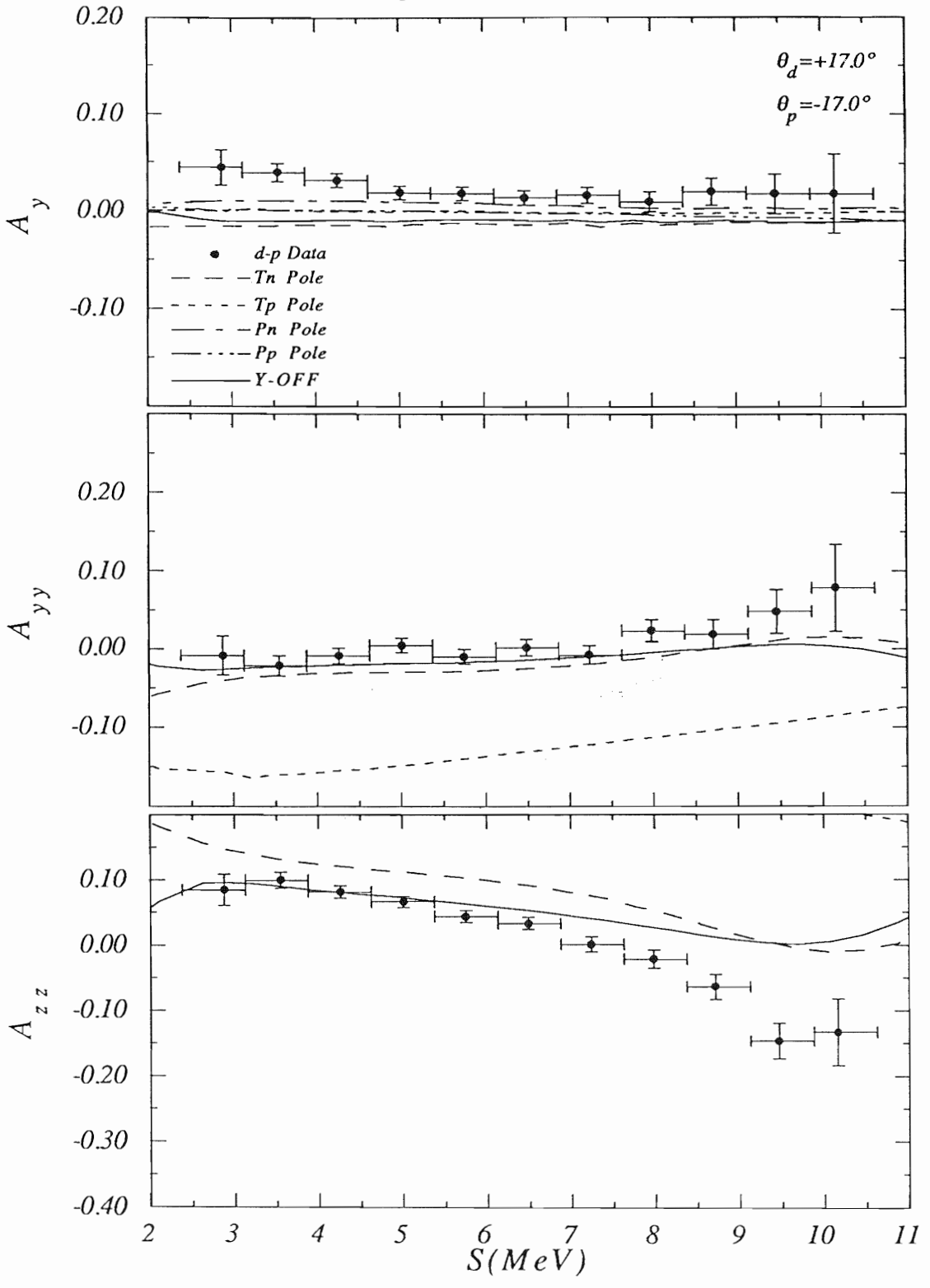

Figure 5.3: Comparison of off-shell IA calculations to D$(\vec{d}, dp)n$ data with (θ_d, θ_p)=(+17.0°, −17.0°).

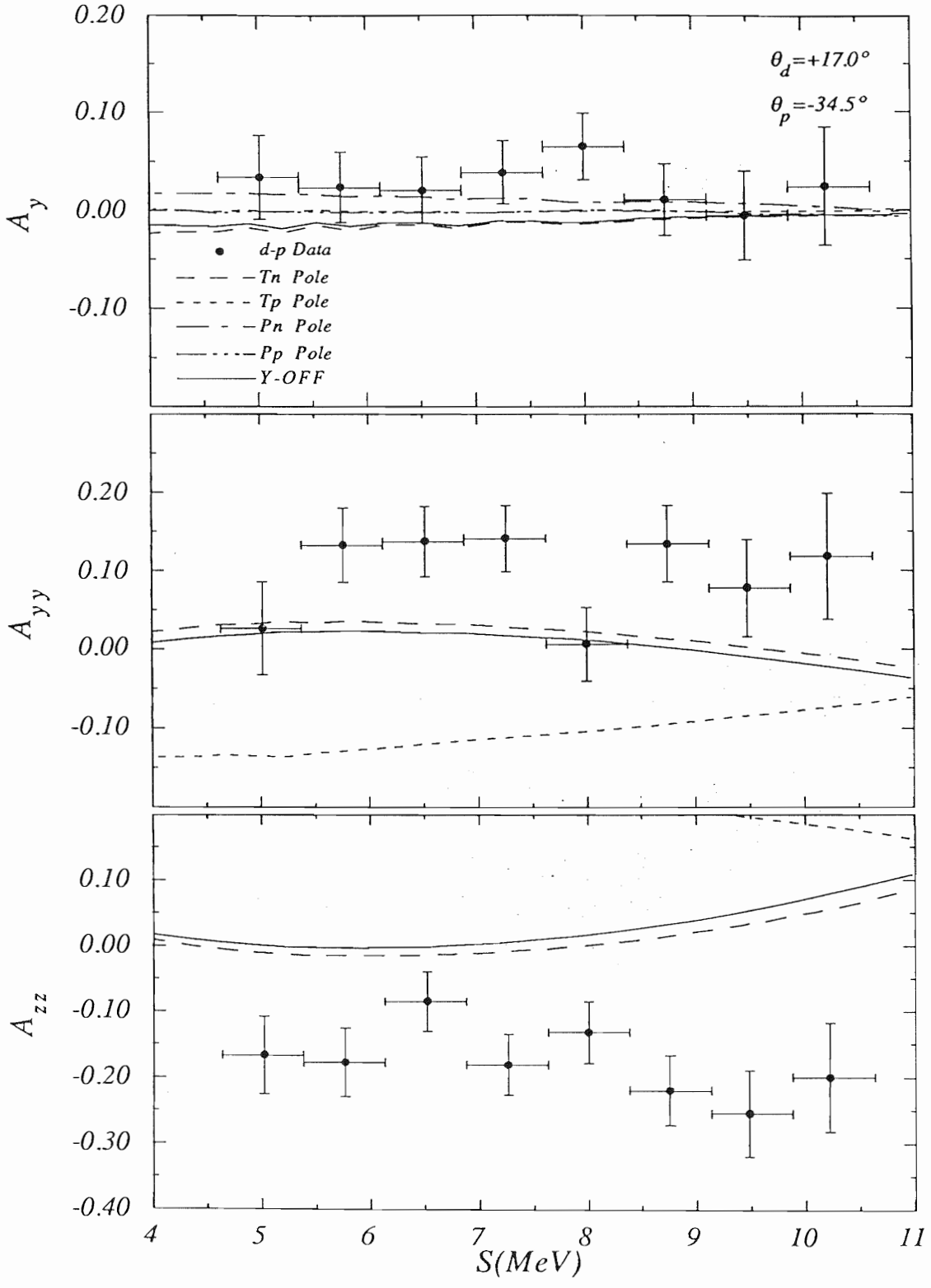

Figure 5.4: Comparison of off-shell IA calculations to $D(\vec{d}, dp)n$ data with (θ_d, θ_p)=(+17.0°, −34.5°).

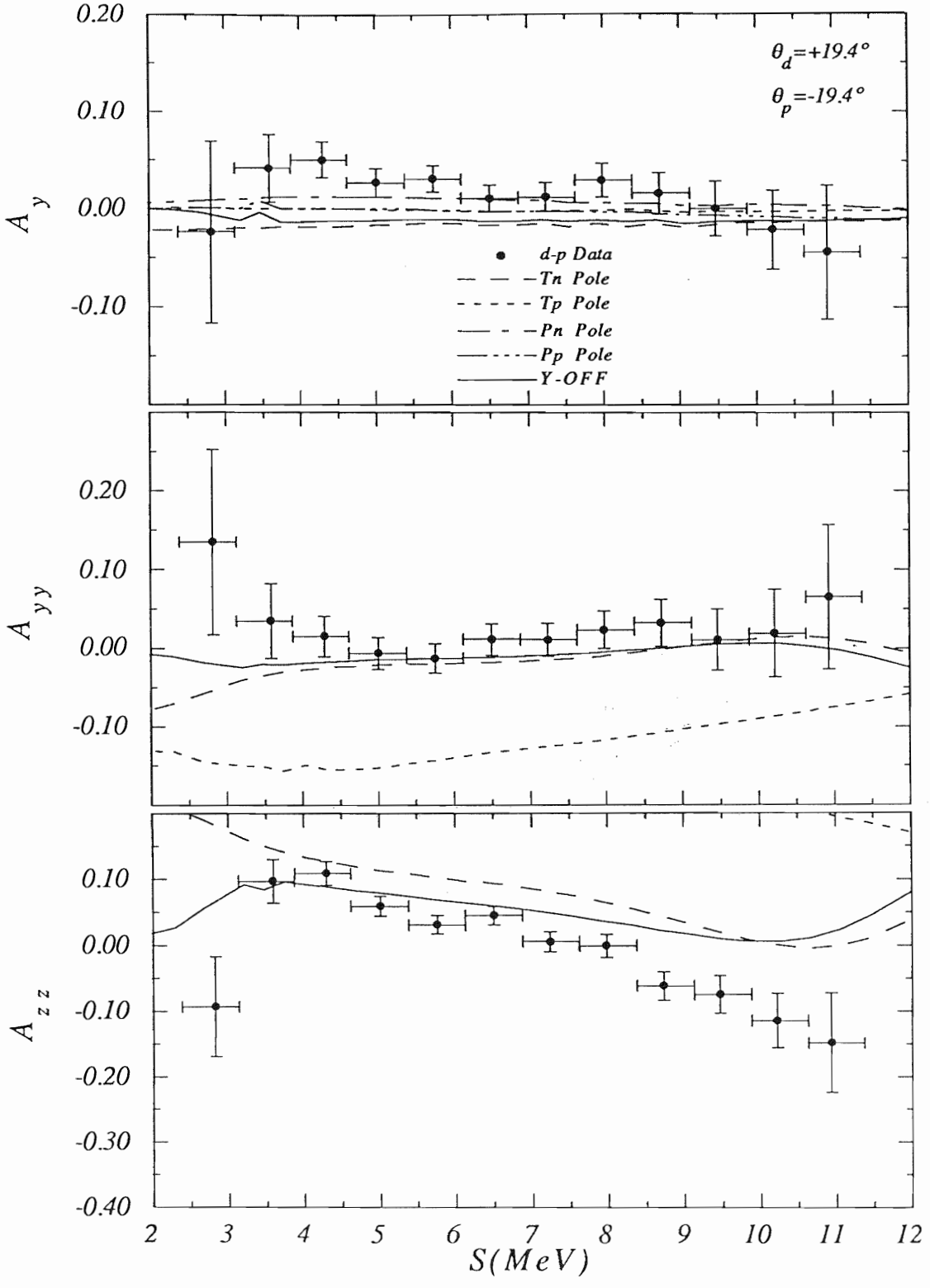

Figure 5.5: Comparison of off-shell IA calculations to D$(\vec{d}, dp)n$ data with (θ_d, θ_p)=(+19.4°, −19.4°).

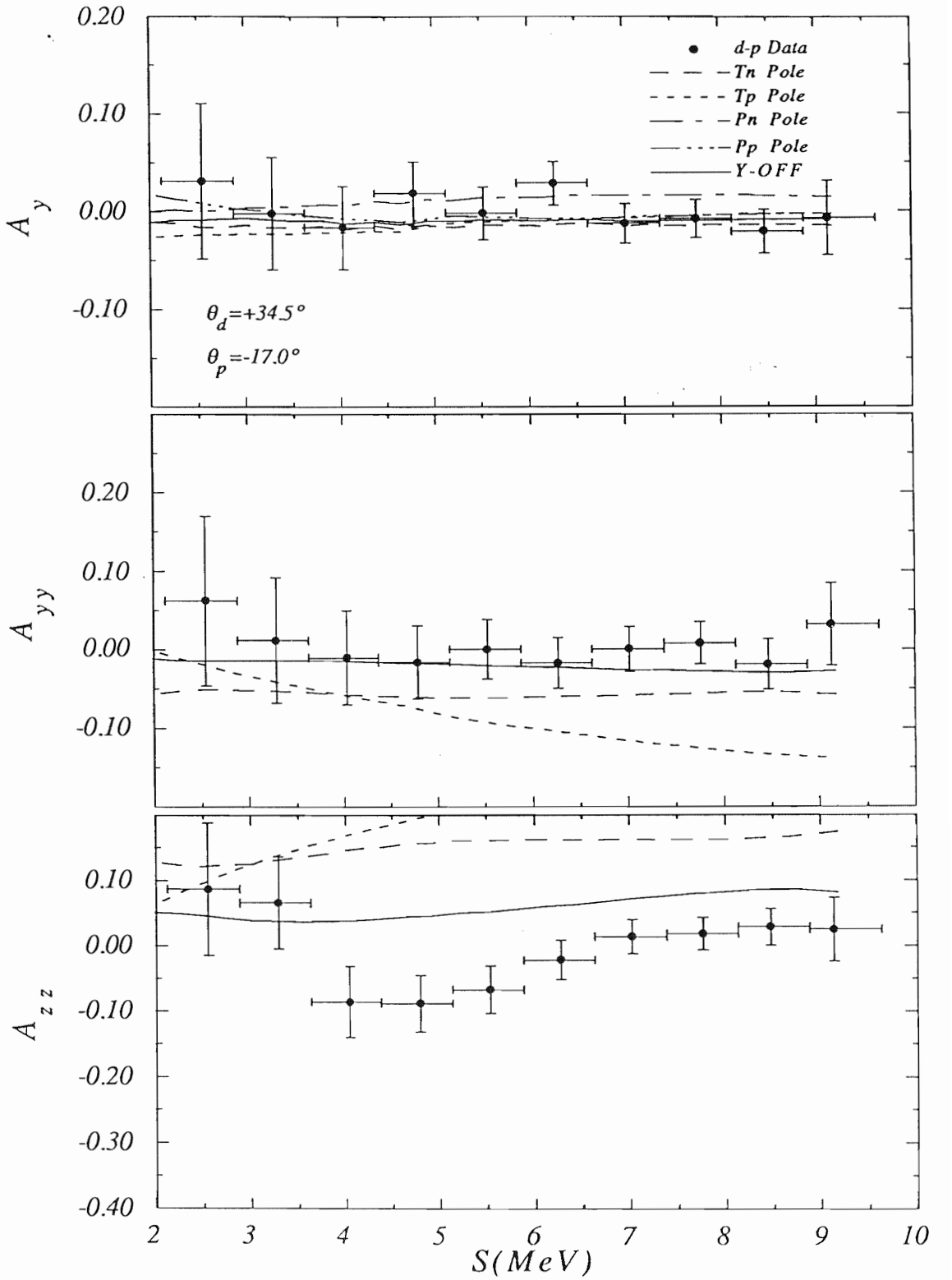

Figure 5.6: Comparison of off-shell IA calculations to D($\vec{d}, dp$)n data with (θ_d,θ_p)=(+34.5°, −17.0°).

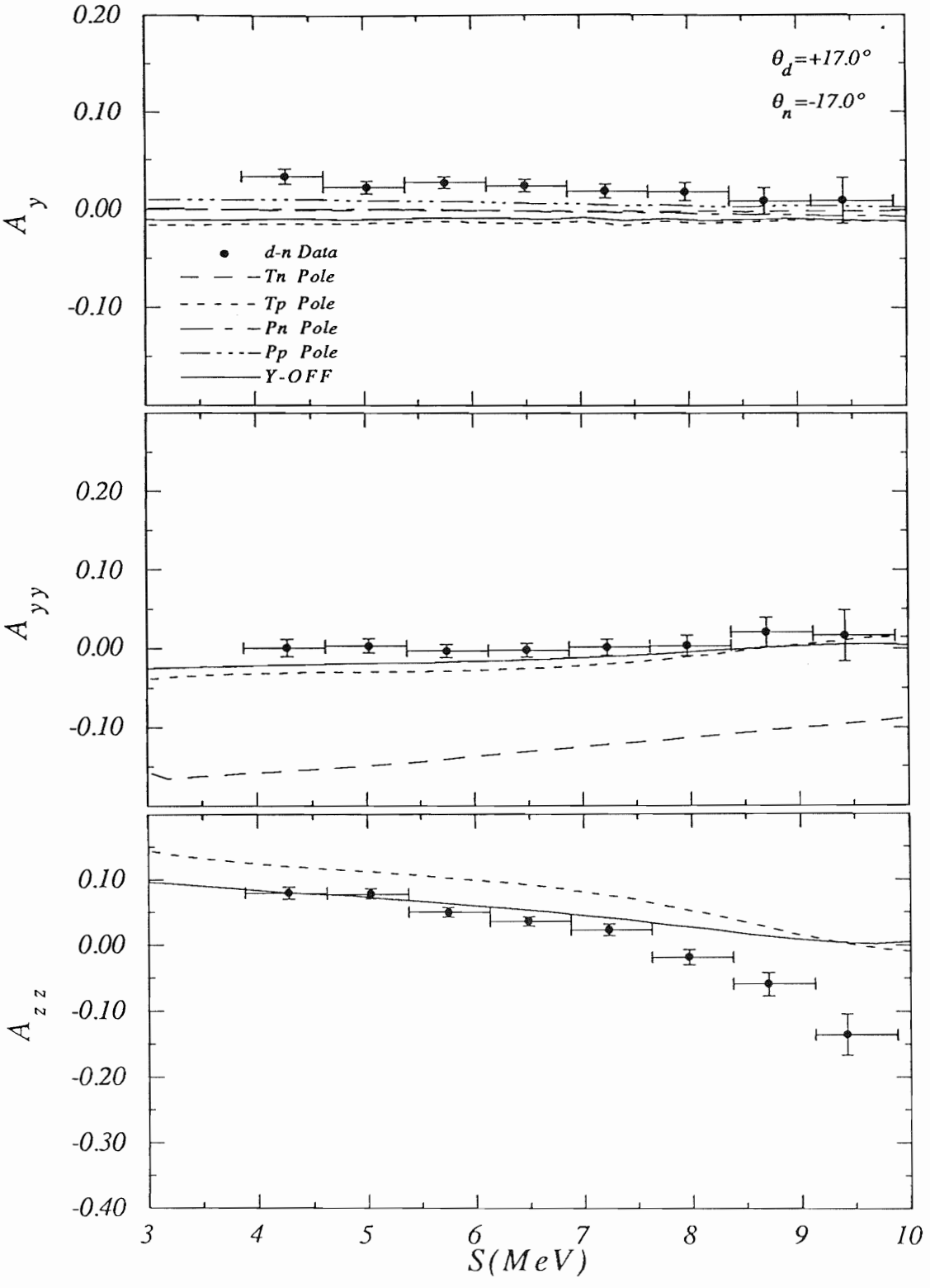

Figure 5.7: Comparison of off-shell IA calculations to $D(\vec{d}, dn)^1H$ data with (θ_d, θ_n)=(+17.0°, −17.0°).

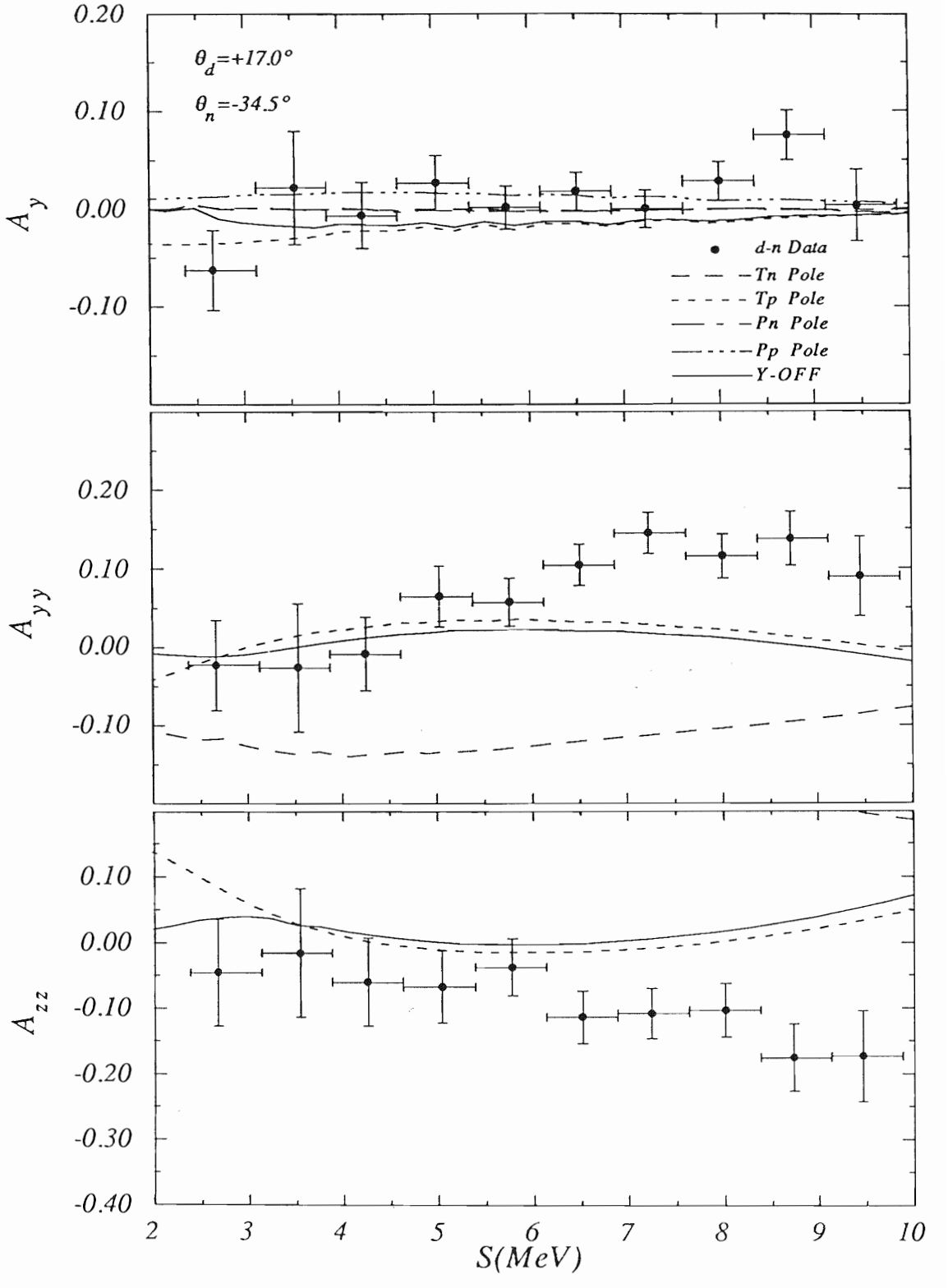

Figure 5.8: Comparison of off-shell IA calculations to $D(\vec{d}, dn)^1H$ data with $(\theta_d, \theta_n)=(+17.0°, -34.5°)$.

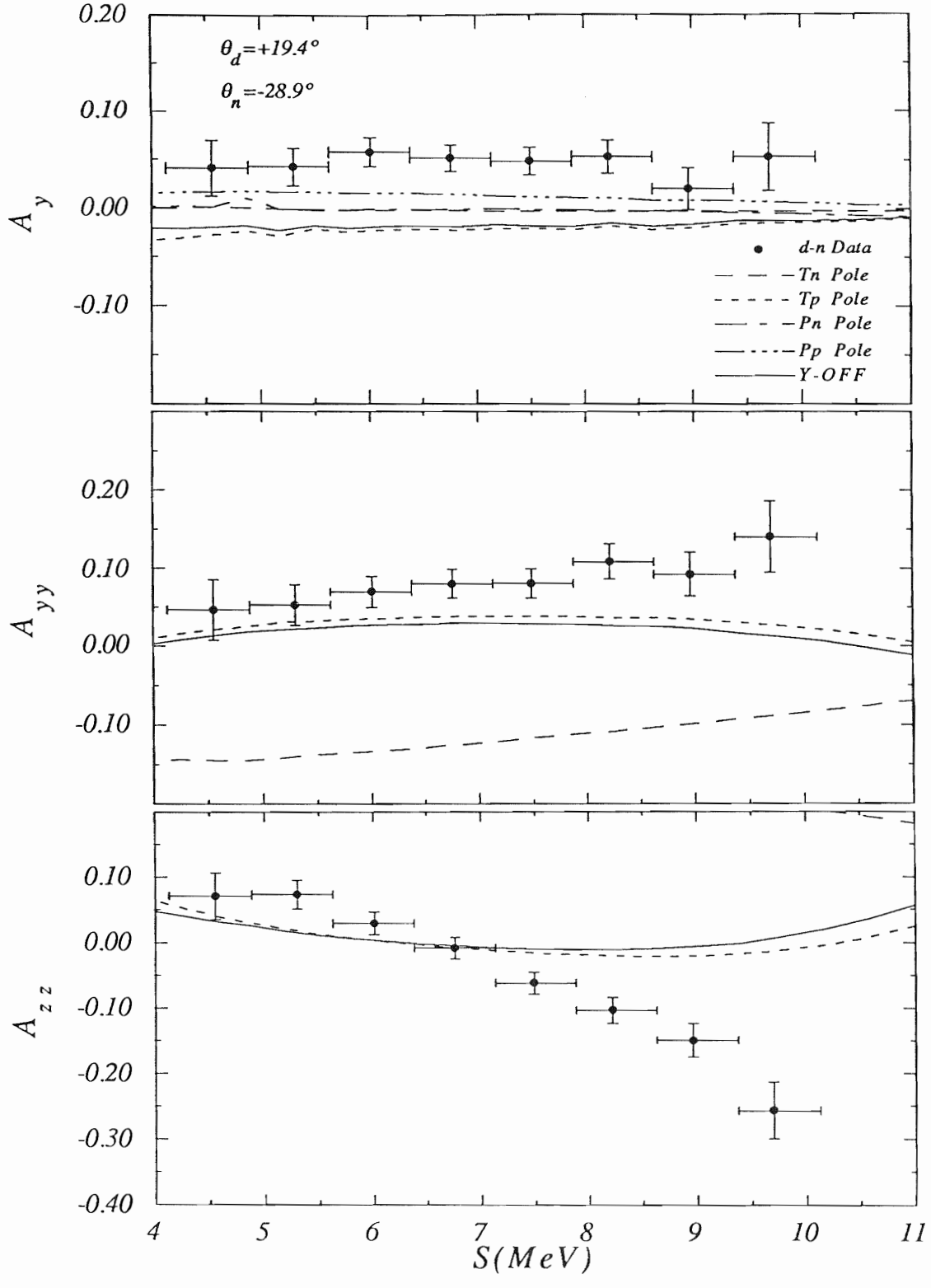

Figure 5.9: Comparison of off-shell IA calculations to $D(\vec{d}, dn)^1H$ data with (θ_d, θ_n)=(+19.4°, −28.9°).

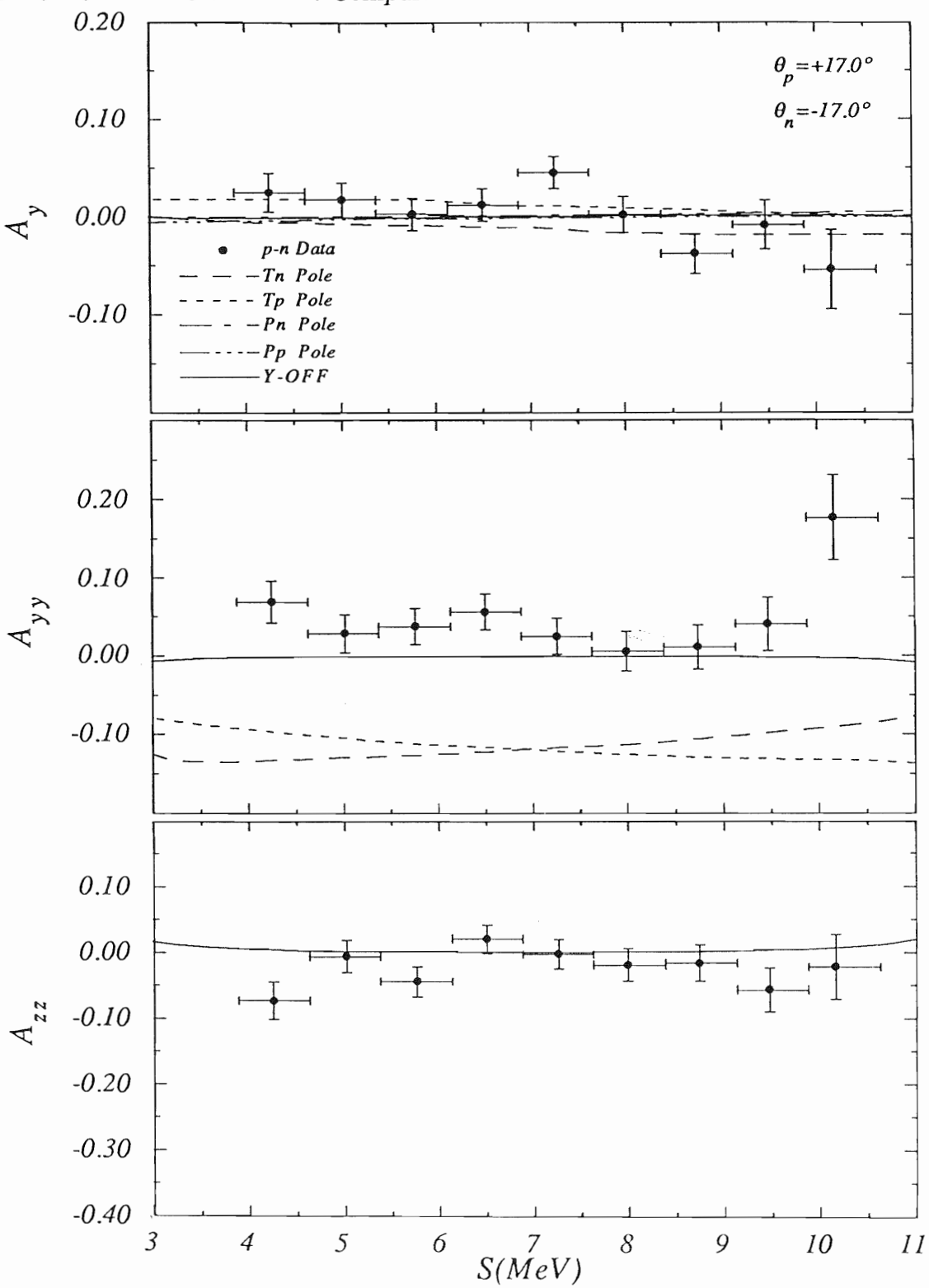

Figure 5.10: Comparison of off-shell IA calculations to D($\vec{d}, pn$)D data with (θ_p,θ_n)=(+17.0°, −17.0°).

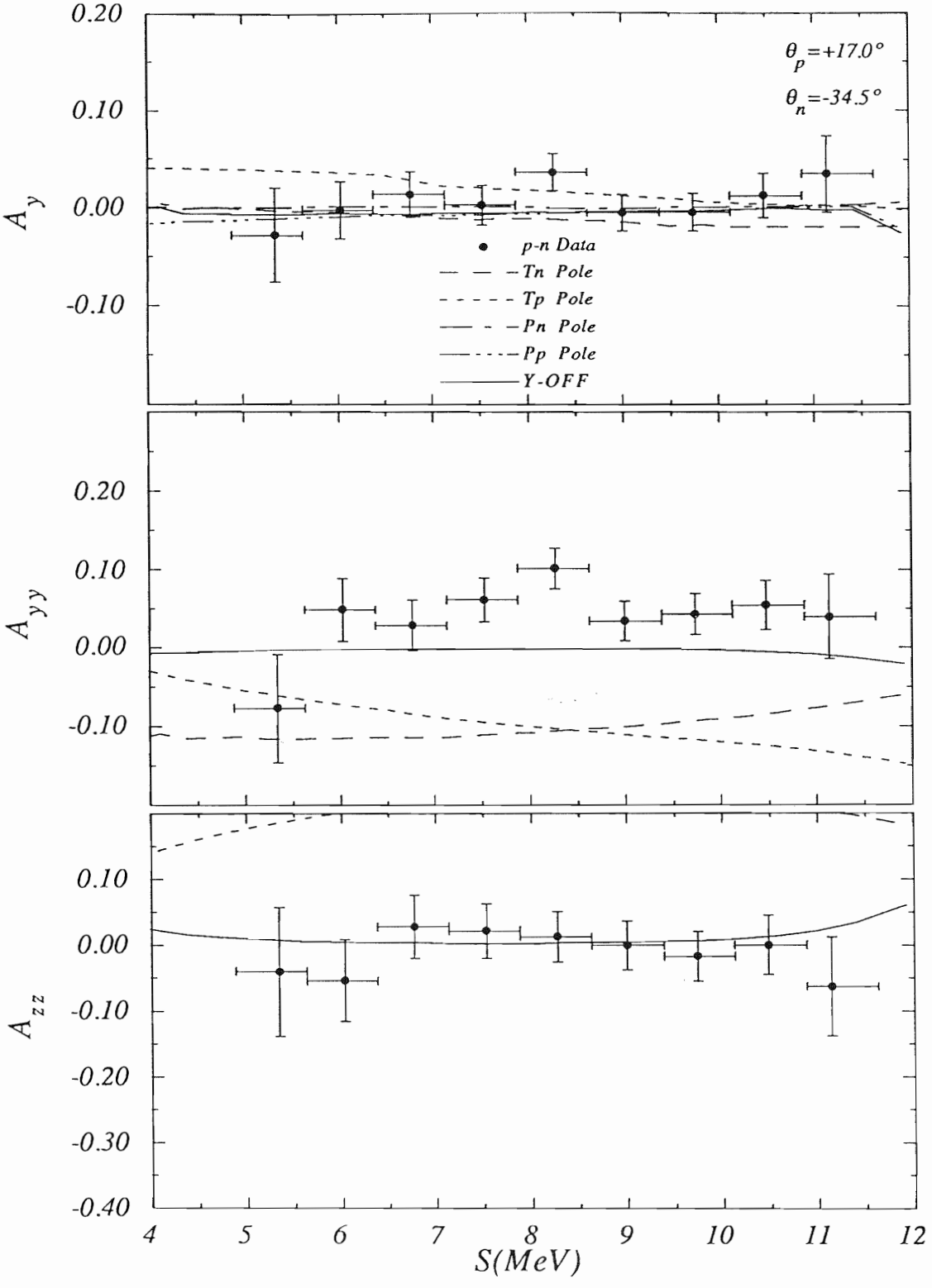

Figure 5.11: Comparison of off-shell IA calculations to D($\vec{d}, pn$)D data with (θ_p,θ_n)=(+17.0°, −34.5°).

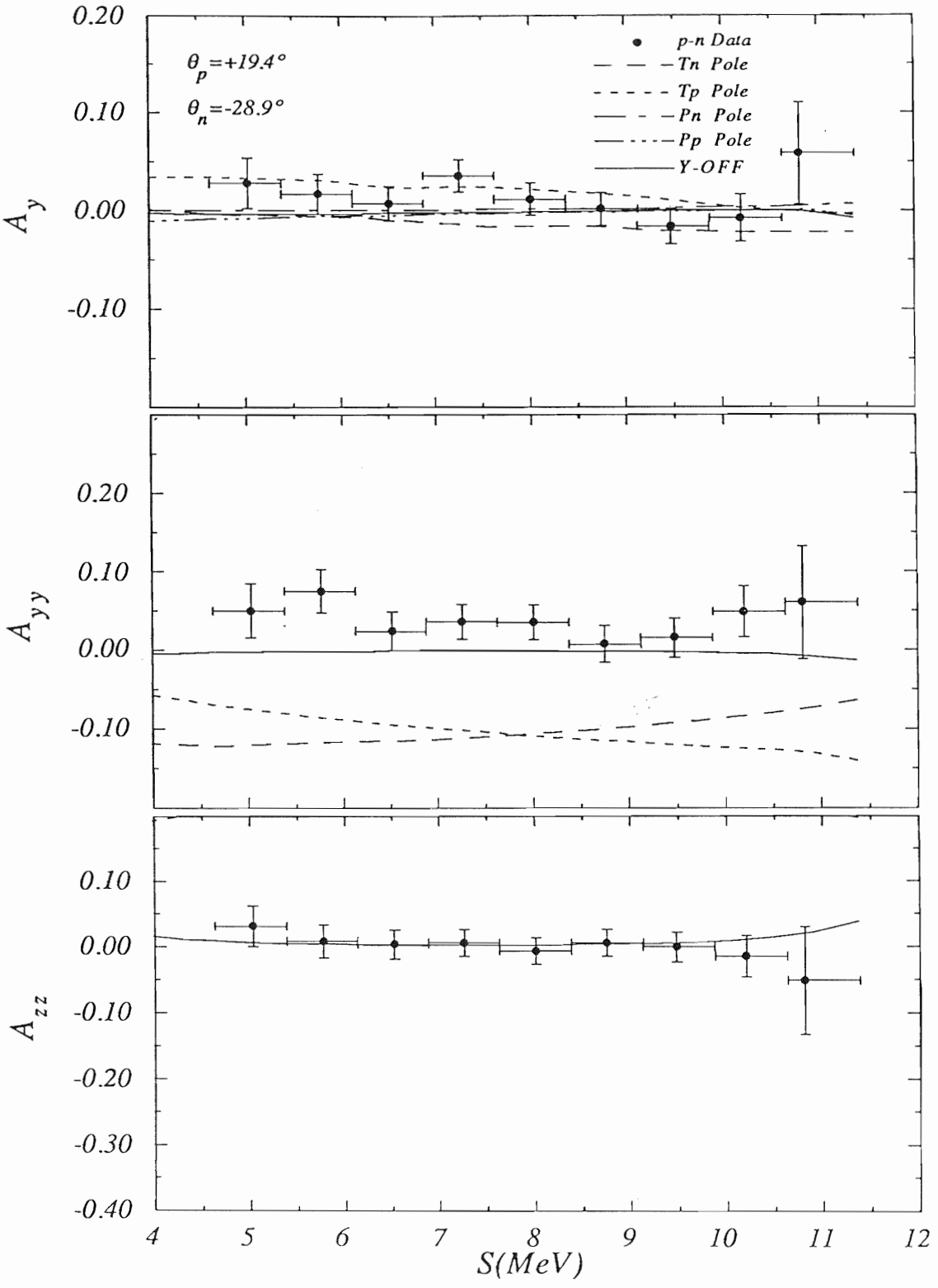

Figure 5.12: Comparison of off-shell IA calculations to D($\vec{d}, pn$)D data with (θ_p,θ_n)=(+19.4°, −28.9°).

5.3 On- and Off-Shell IA Calculations Compared to Data

Keeping in mind the limitations of the IA, we again present the data in an attempt to identify regions of phase space that may be sensitive to the reaction dynamics of $d+d \rightarrow d+p+n$ breakup. Shown in figures 5.13–5.24 are the analyzing powers as a function of the arc length S along with three IA calculations P-ON, Y-ON and Y-OFF represented by the curves. In section 5.3.1 we investigate the effect of calculating the dN vertex on-the-energy-shell versus off-the-energy-shell by comparing Y-ON to Y-OFF, and in section 5.3.2 the effects of the various partial waves in the NN interaction on the scattering observables are studied by comparing the Y-ON to P-ON calculations. In the sections that follow, we will concentrate on the dp and dn coincidence data, since no significant differences in the P-ON, Y-ON and Y-OFF calculations were found in the case of the pn coincidence (see figures 5.22–5.24). For the tensor observables, this is a consequence of setting the analyzing powers equal to zero for PB poles, which are the dominant poles in the reaction. The vector analyzing powers show little difference in the three calculations since the major poles correspond to forward angle scattering ($< 40°$) in the dN c.m. system where the calculated magnitude of the $\vec{n}d$ vector analyzing powers are less than 0.03.

5.3.1 Comparison of Y-ON to Y-OFF

The vast amount of NN data available today provides a rich arena for testing only the on-shell behavior of the NN interaction, of course with exception of NN bremsstrahlung data [Bro90]. Potentials which give a good description of NN data can differ considerably in their off-shell behavior [Zan84]. The validity of the off-shell behavior of NN potentials can be tested with few-nucleon systems. Although the bound states of few-nucleon systems provide some information about the off-shell behavior of the NN force, the kinematic freedom of nuclear reactions make them attractive for studying off-shell effects over large regions of NN phase space. In light of the fact that both our on-shell and off-shell IA calculations fail to reproduce the data in a reasonable manner we are unable to make specific conclusions about details of the NN interaction with the present calculational approach. However, we will attempt to identify regions of phase space in the $\vec{d}+d \rightarrow d+p+n$ breakup reaction for which the polarization observables are sensitive to off-shell effects in the dN interaction. Our

findings will provide a good starting point for more complete $4N$ calculations.

For the vector analyzing powers A_y, little difference between the on- and off-shell calculations is observed (see figures 5.13–5.24). This is almost certainly due to the lack of P-waves in the NN interaction, which will be addressed further in the section 5.3.2.

The off-shell calculations for the tensor analyzing powers always show more structure than the on-shell calculations. This increased structure is qualitatively supported by the present data, at least for the Nd angle pairs with θ_d=θ_N (see figures 5.13, 5.15, 5.17, 5.19). For non-symmetric angle pairs, the on-shell calculations generally give a better description of the data than the off-shell calculations (see figures 5.14, 5.16, 5.18, 5.20, 5.21). The increased structure in the calculations obtained when one switches from on-shell to off-shell dN matrix elements is a clear indication that our tensor analyzing power calculations are very sensitive to the off-shell behavior of the Nd subsystem. The regions along S of greatest sensitivity usually occur away from the point where the primary pole comes closest to satisfying the QFS condition. This is not surprising, since as one deviates from the QFS condition (increasing spectator momentum) the degree to which the dN subsystem is off-shell increases. We assume that these sensitivities to off-shell effects in the dN are present in our data.

The differences between on- and off-shell calculations stem from two sources: 1) the calculated analyzing powers for each pole differ for on- and off-shell Nd matrix elements, and 2) the calculated cross sections for each pole differ for on- and off-shell matrix elements, thereby changing the weighting of the poles in the four-pole calculations. The difference in the relative magnitude of the contributing poles when calculating with on-shell versus off-shell Nd matrix elements is shown in table 4.2. In general, the pole that is identified as being the primary pole when using on-shell amplitudes becomes even more dominant when using off-shell amplitudes.

Previously, off-shell effects in the dN vertex have been introduced in the IA by including a separable form factor based on the relative momenta of the interacting particles and a parameter dictated by the deuteron radius [Duc72]. This phenomenological approach produced a reduction in and a narrowing of the calculated reaction cross sections, thus improving the agreement with data [Duc72]. While our unmodified IA calculation (i.e., no cutoff radius) using on-shell dN matrix elements produced an enhancement in the cross section associated with dN QFS which was broader than the data, we were able to obtain better agreement with the data by switching to off-shell matrix elements. However, a further narrowing of the calculated cross section

was needed. Since we did not measure an absolute cross section, we compared only the shape of the calculated enhancement to our measured spectra. A first attempt at reproducing the shape of our enhancement by the addition of a smooth cutoff radius in the deuteron wave function resulted in a cross section of about 5 mb/sr^2/MeV, whereas previously reported measurements by Valković *et al.* [Val72a] indicated a value of around 40 mb/sr^2/MeV. When the cutoff radius parameter in the wave function in our calculations was adjusted to give an QFS enhancement in the cross section of 40 mb/sr^2/MeV, the shape of the enhancement broadened considerably. The sensitivity of our IA calculations[4] to the value of the cutoff radius reinforces the importance of including off-shell effects in $4N$ calculations of observables for the $d+d \rightarrow d+p+n$ breakup reaction.

5.3.2 Comparison of Y-ON to P-ON

The comparison of our two on-shell calculations gives us a tool for identifying regions of phase space in which our data show sensitivity to different NN partial waves. The characteristics of the PEST and Yamaguchi potentials are listed in table 4.1. Sensitivity studies indicated that the addition of $3N$ angular momentum states with $J^\pi \geq \frac{13}{2}^\pm$ in the calculations using the PEST potential made very little difference, suggesting thereby that convergence was reached with $J^\pi = \frac{11}{2}^\pm$. Also, the small difference in the tensor force of the PEST and Yamaguchi potentials, as indicated by their prediction of the D-state probability of the deuteron, was found to be of negligible significance.[5] Therefore, a comparison between calculations using the two potentials should test the sensitivity of the observables to the additional NN partial waves included in the PEST potential (see table 4.2).

Examination of figures 5.13–5.24 reveals only slight differences between Y-ON and P-ON in the A_{yy} and A_{zz} observables, but rather large differences in the A_y. The slight differences observed in the tensor analyzing powers are probably due to differences in the relative strengths of the various poles and not to differences in the analyzing powers of the poles. The observed differences in A_y are most likely due

[4] Adding all four poles together coherently resulted in a cross section that was between two and four times larger than that obtained by the current procedure of only adding coherently those poles originating from the same breakup deuteron. In general, all four poles were in phase so that they constructively interfered whenever they were added coherently.

[5] This was determined by performing two calculations using two identical Yamaguchi potentials that differed only in their D-state probability. One had a D-state contribution of 4% while the other had a 5.5% contribution.

to the higher partial waves included in the P-ON calculation. This conclusion is reinforced by an analysis of A_y data for $\vec{n}$-d elastic scattering at 10–14 MeV which showed extreme sensitivity to ${}^3P_{0,1,2}$-waves [How87]. The fact that the A_y data agree with the P-ON calculations better than the Y-ON calculations indicates that inclusion of ${}^3P_{0,1,2}$-waves and possibly ${}^3D_{2,3}$-waves and ${}^1D_2$-waves in the NN interaction is necessary for a proper description of A_y for the $\vec{d}$+$d \rightarrow d$+p+n breakup reaction.

5.3.3 Conclusions

Our calculations suggest that ${}^3P_{0,1,2}$-waves must be included in the NN interaction for a meaningful calculation of A_y. Since our off-shell calculations lacked these ${}^3P$-waves no conclusion on the sensitivity of A_y to off-shell effects in the dN subsystem can be made. However, A_{yy} and A_{zz} show little sensitivity to these partial waves, but show great sensitivity to off-shell effects in the dN subsystem. Specifically, regions along S furthest from the QFS point for the primary pole showed the greatest sensitivity to off-shell effects.

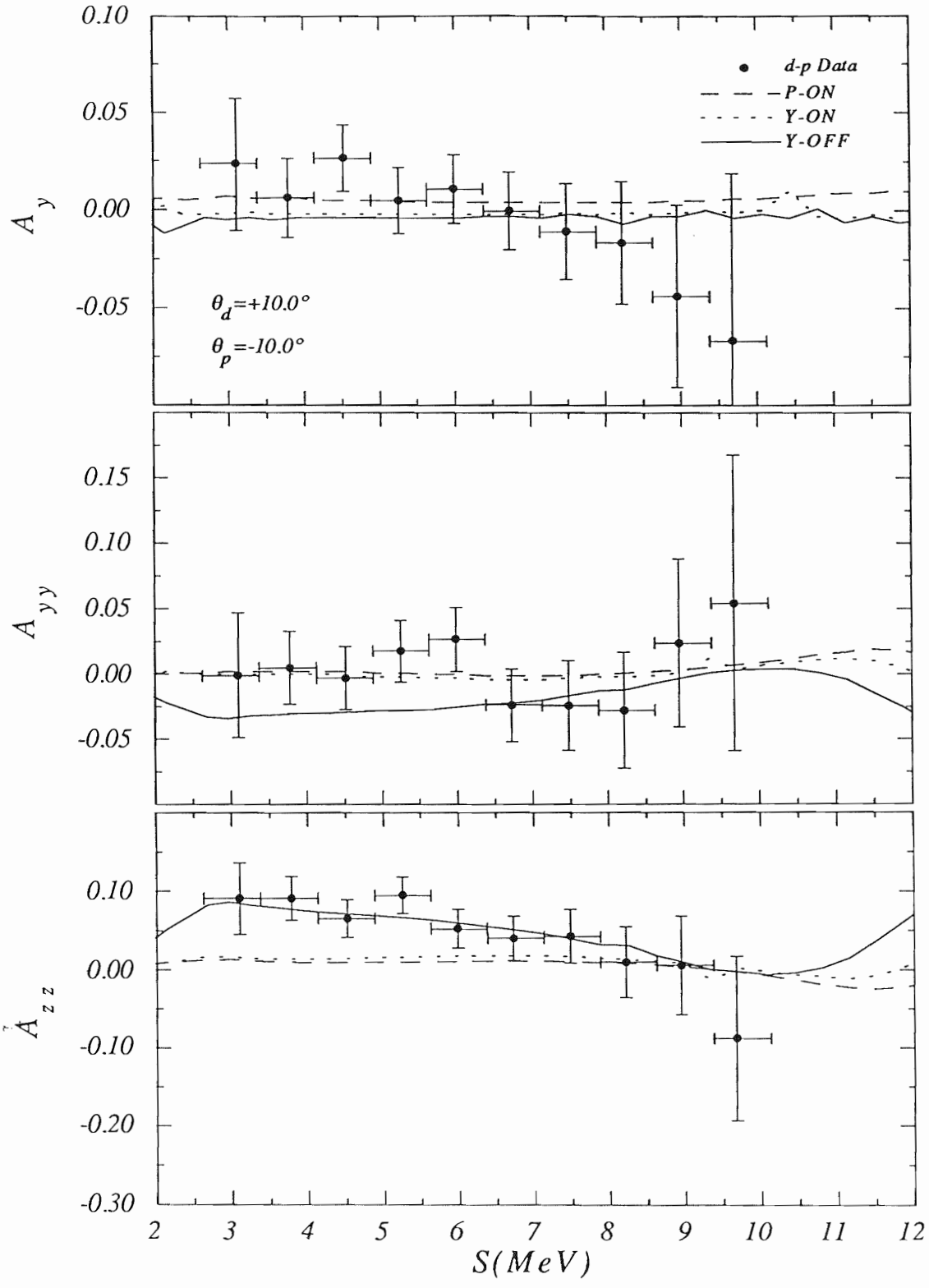

Figure 5.13: Comparison of on-shell and off-shell IA calculations to D($\vec{d}, dp$)n data with (θ_d,θ_p)=(+10.0°, −10.0°).

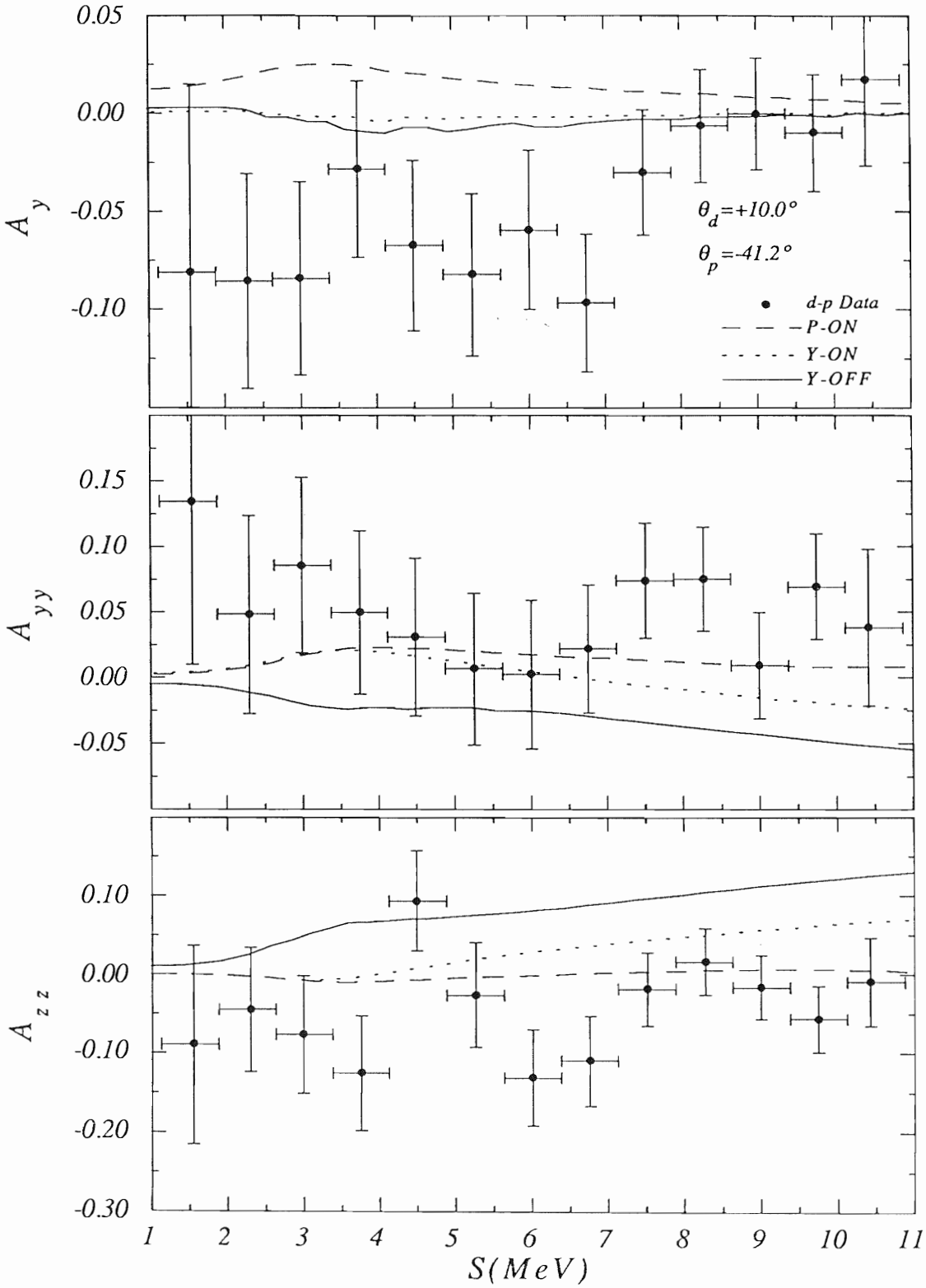

Figure 5.14: Comparison of on-shell and off-shell IA calculations to D($\vec{d}, dp$)n data with (θ_d,θ_p)=(+10.0°, −41.2°).

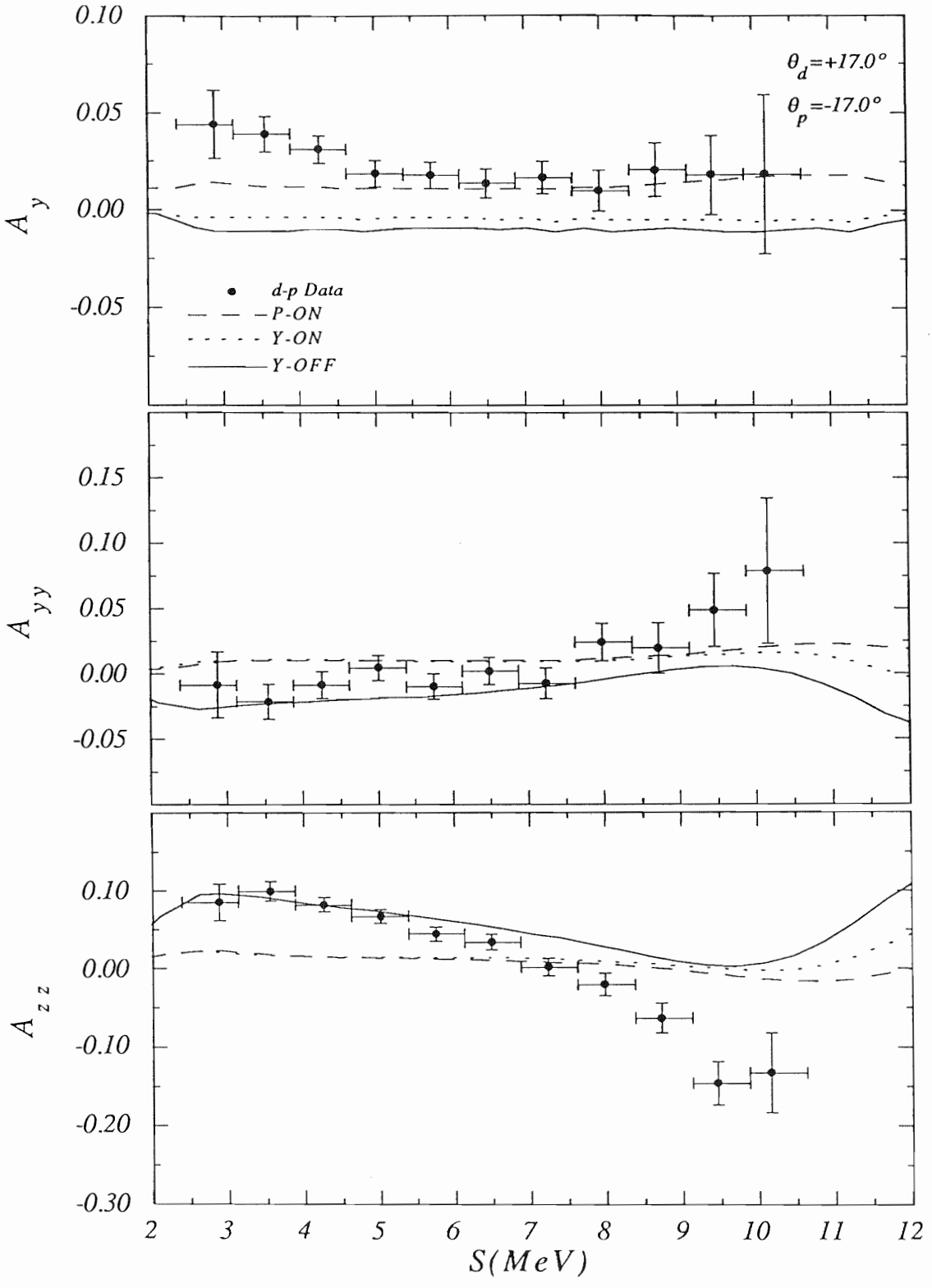

Figure 5.15: Comparison of on-shell and off-shell IA calculations to D($\vec{d}, dp$)n data with (θ_d,θ_p)=(+17.0°, −17.0°).

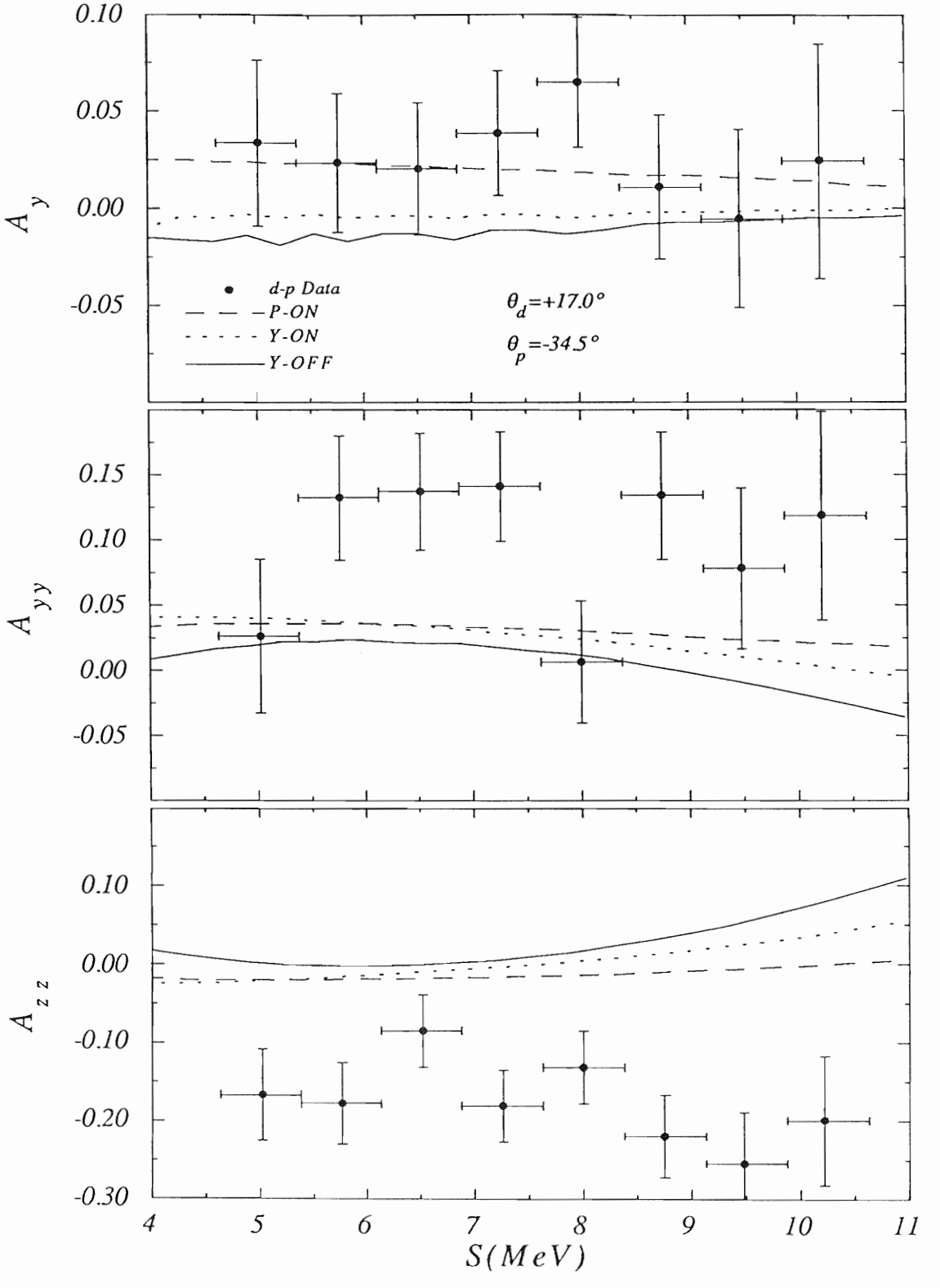

Figure 5.16: Comparison of on-shell and off-shell IA calculations to D($\vec{d}, dp$)n data with (θ_d,θ_p)=(+17.0°, −34.5°).

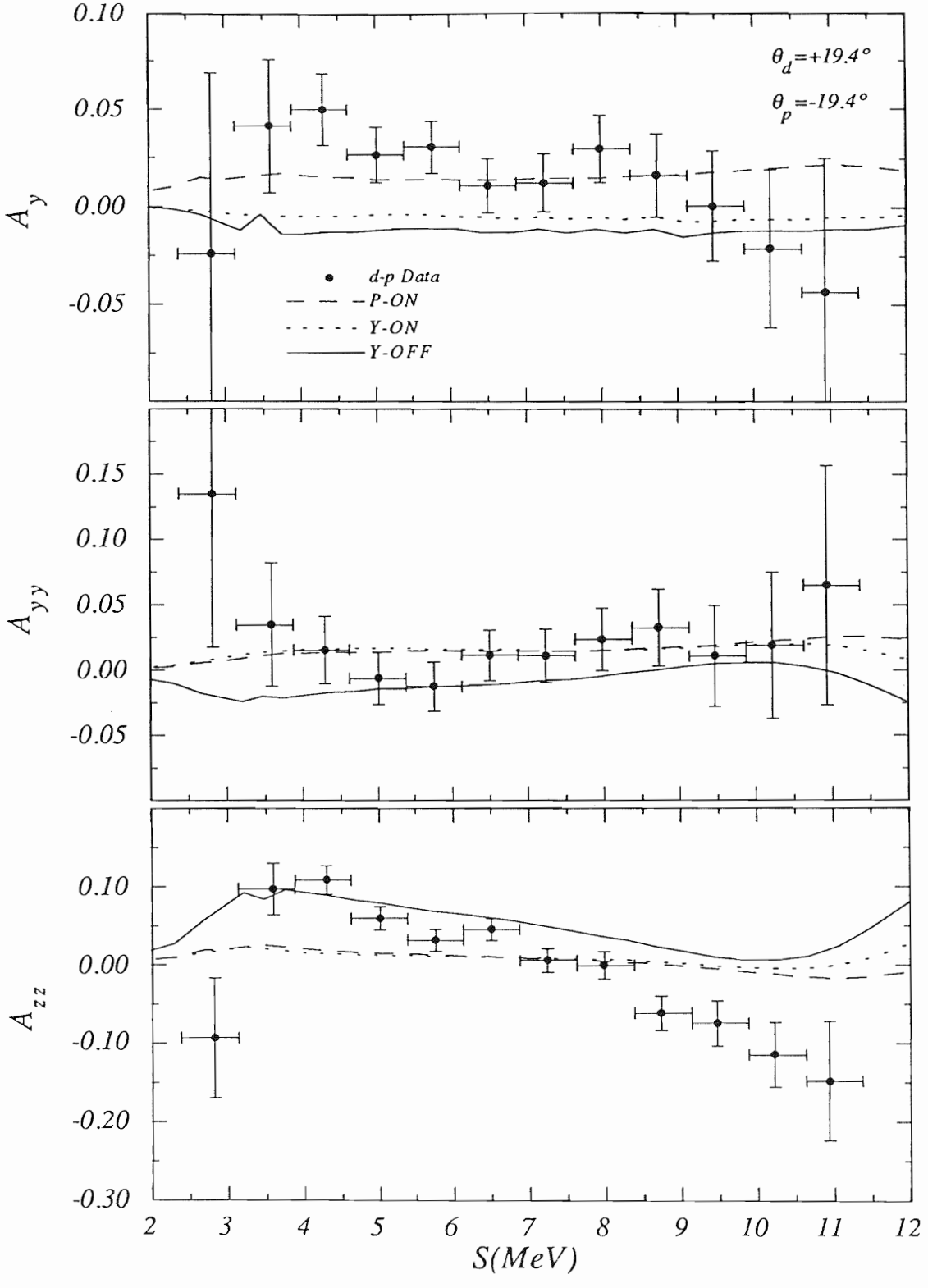

Figure 5.17: Comparison of on-shell and off-shell IA calculations to D($\vec{d}, dp$)n data with (θ_d,θ_p)=(+19.4°, −19.4°).

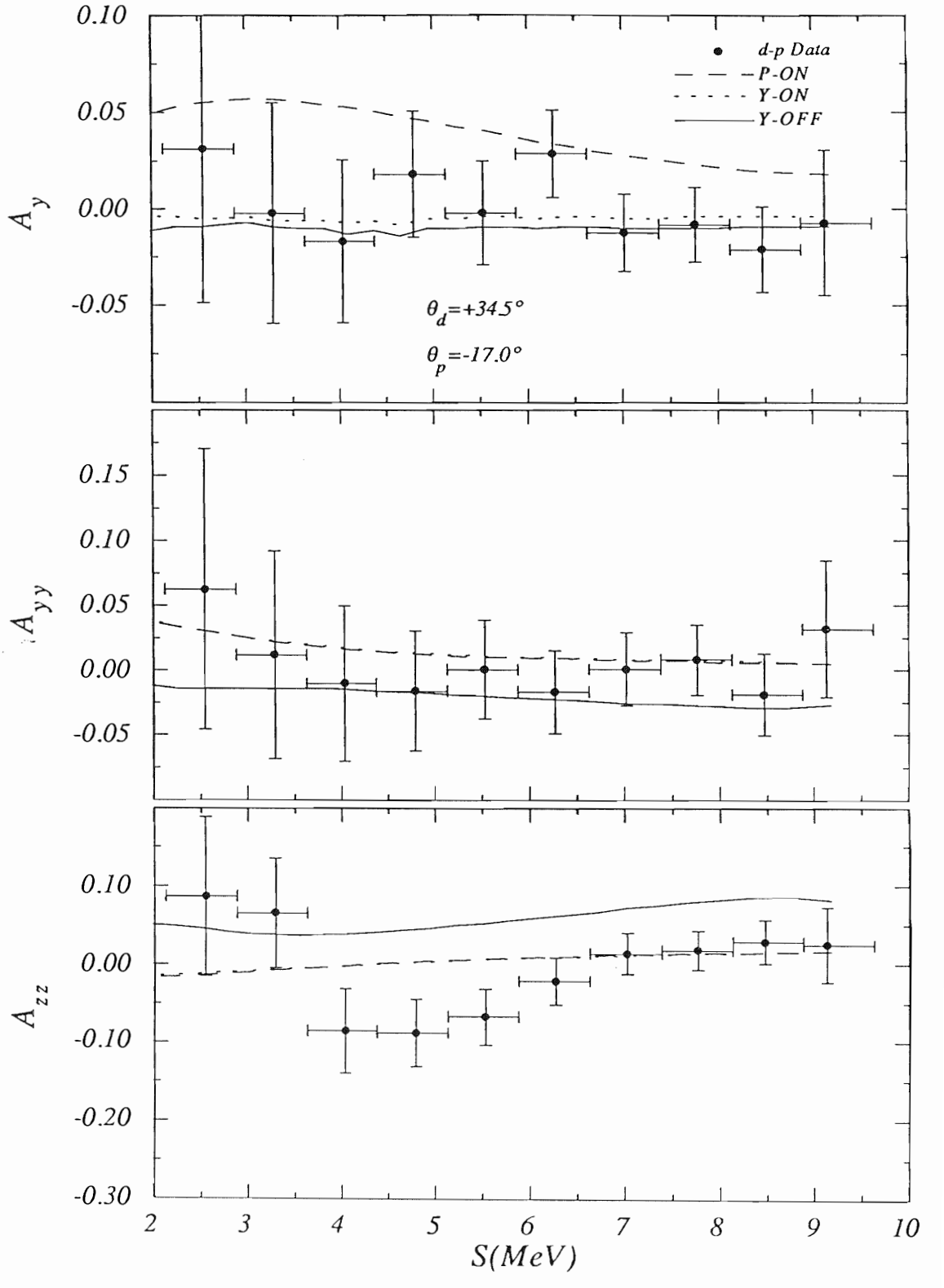

Figure 5.18: Comparison of on-shell and off-shell IA calculations to D($\vec{d}, dp$)n data with (θ_d,θ_p)=(+34.5°, −17.0°).

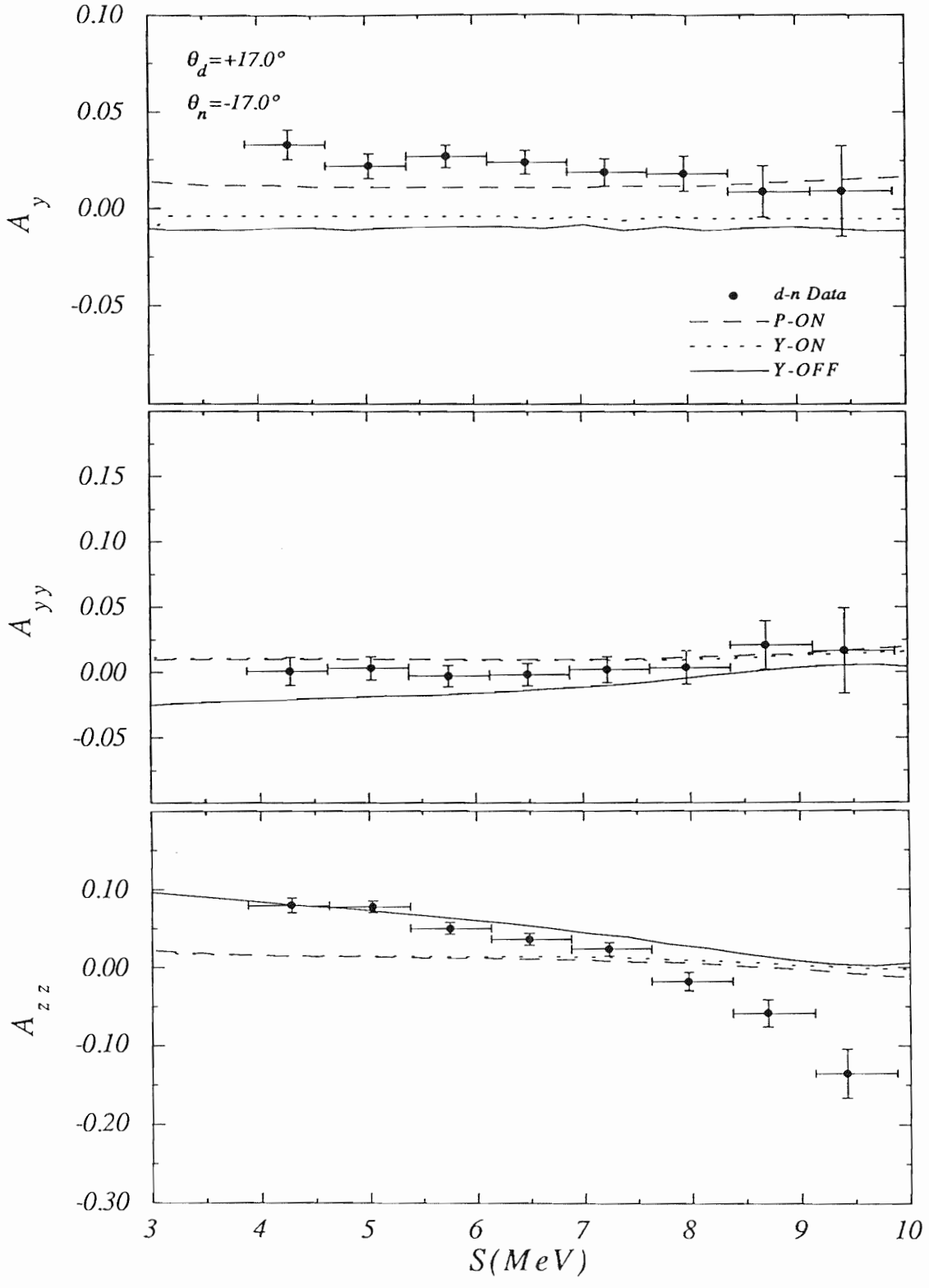

Figure 5.19: Comparison of on-shell and off-shell IA calculations to $D(\vec{d}, dn)^1H$ data with (θ_d,θ_n)=(+17.0°, −17.0°).

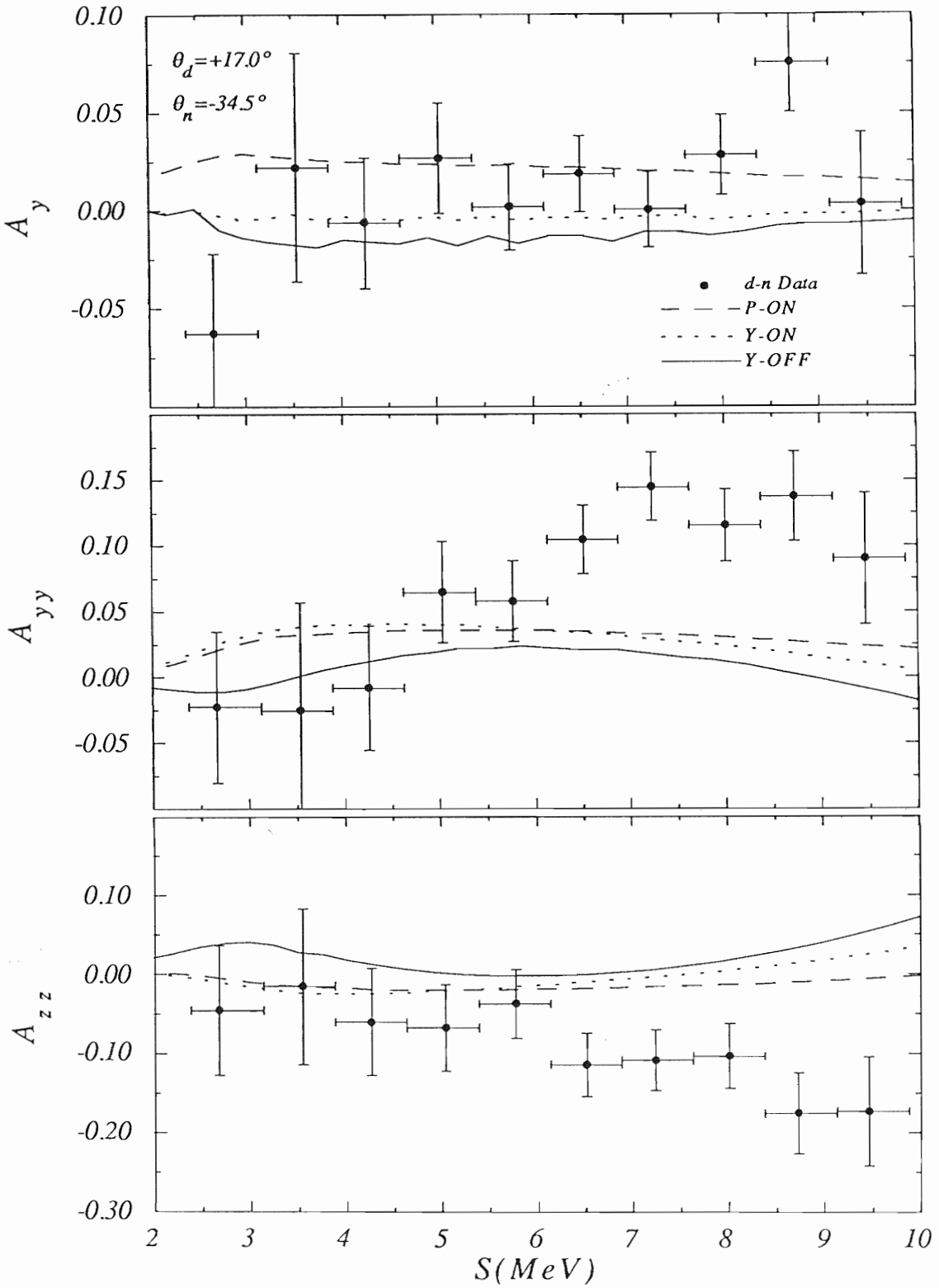

Figure 5.20: Comparison of on-shell and off-shell IA calculations to $D(\vec{d}, dn)^1H$ data with (θ_d,θ_n)=(+17.0°, −34.5°).

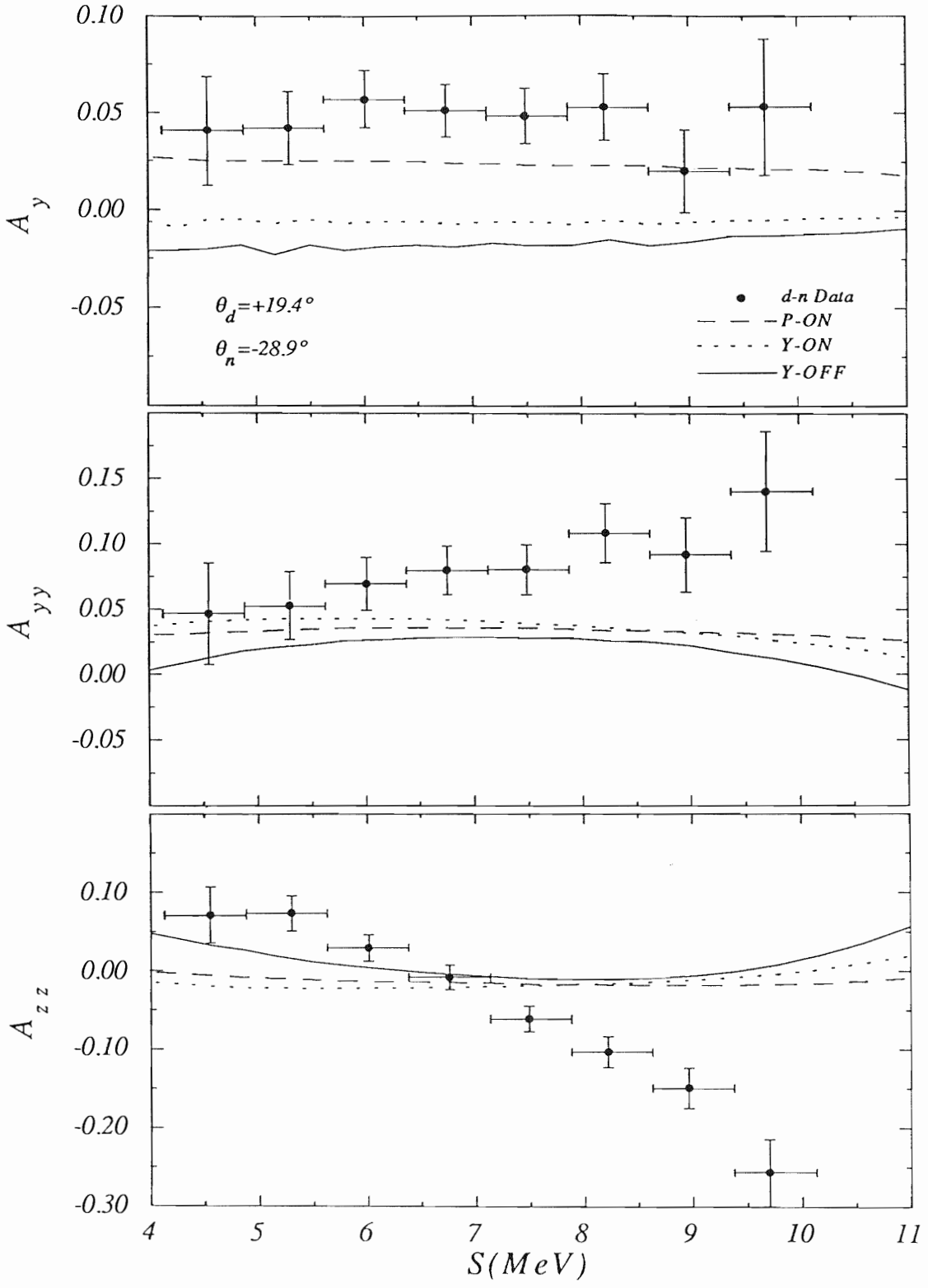

Figure 5.21: Comparison of on-shell and off-shell IA calculations to $D(\vec{d}, dn)^1H$ data with $(\theta_d,\theta_n)=(+19.4°, -28.9°)$.

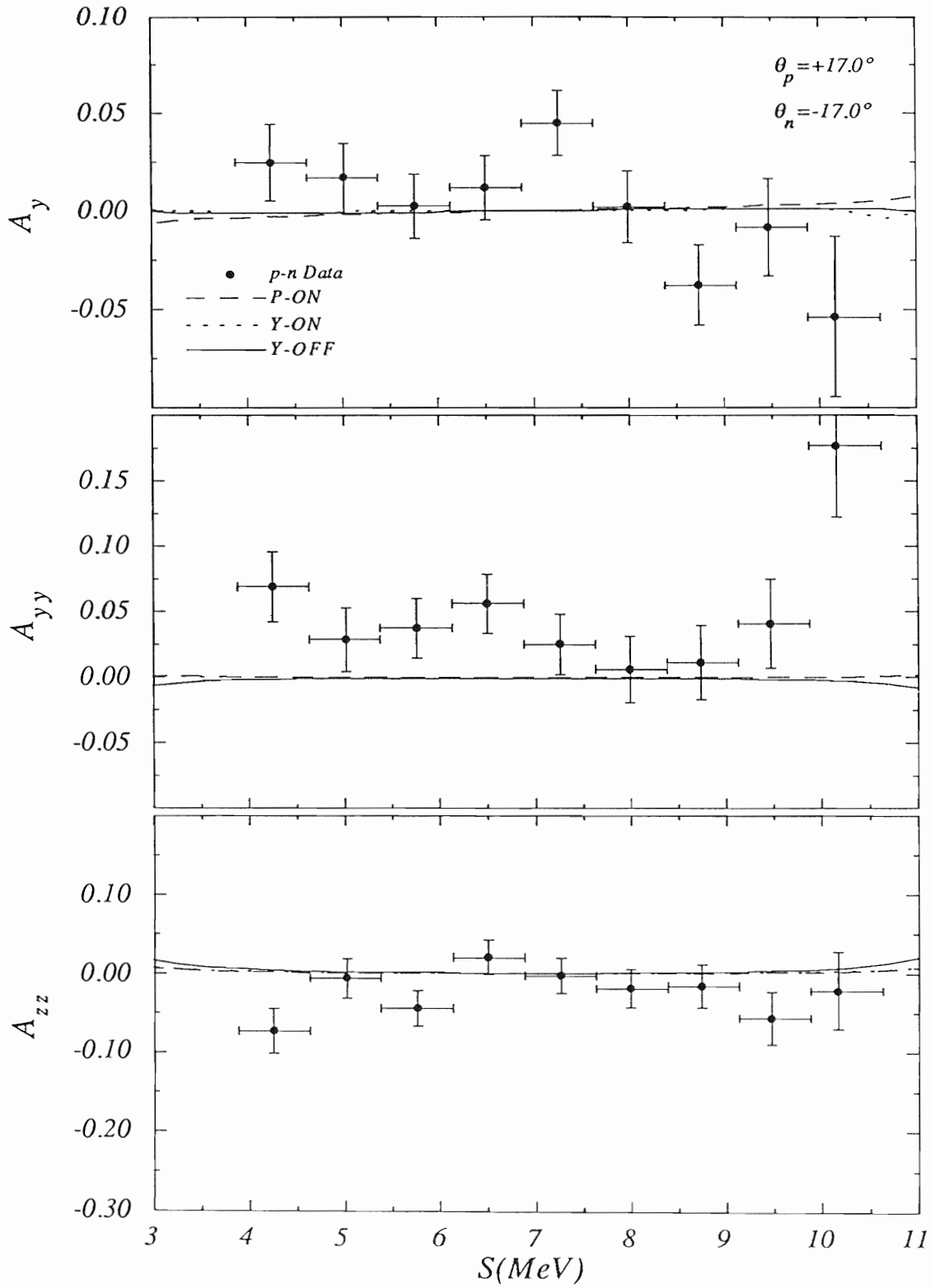

Figure 5.22: Comparison of on-shell and off-shell IA calculations to D($\vec{d}, pn$)D data with (θ_p,θ_n)=(+17.0°, −17.0°).

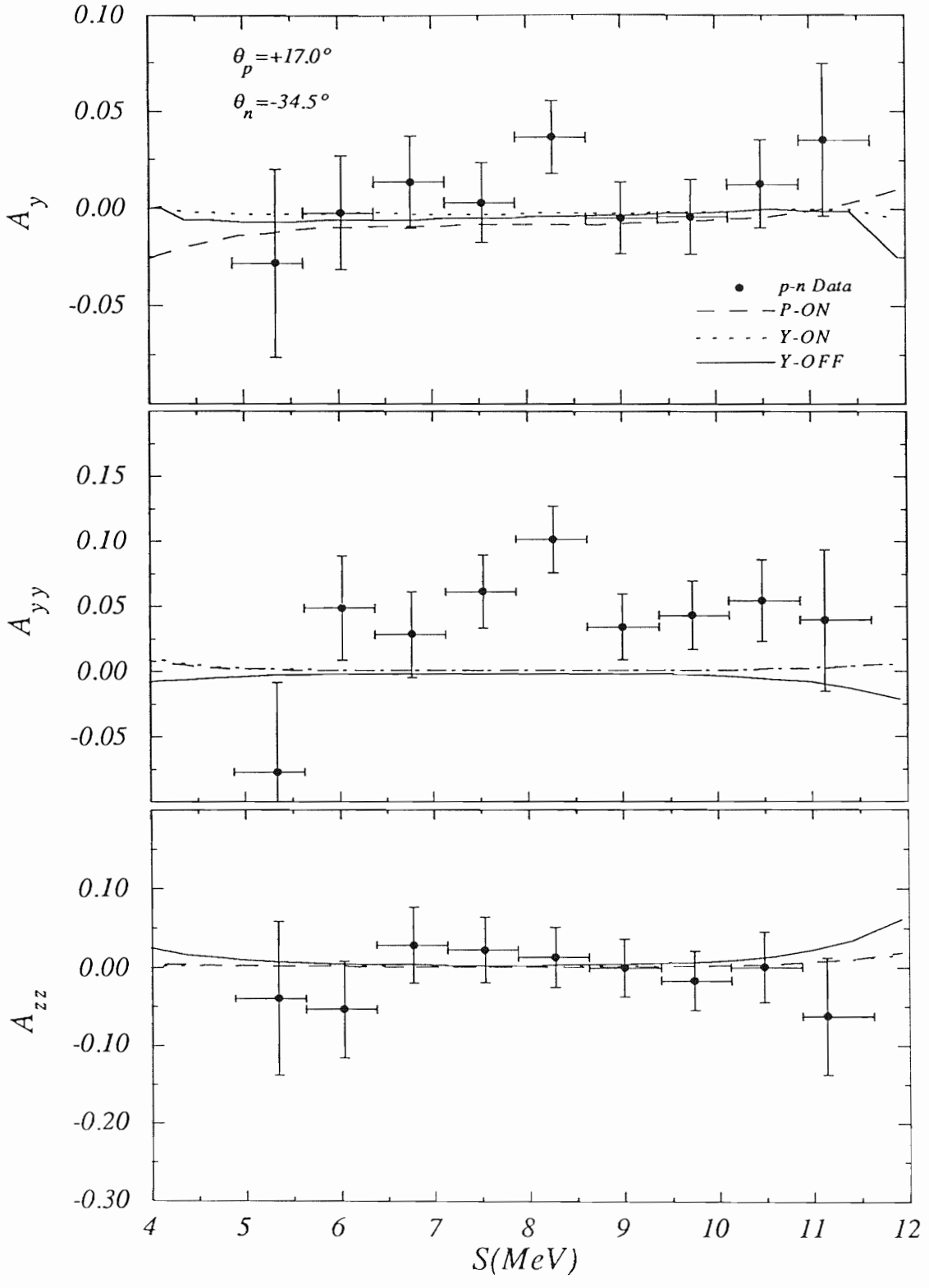

Figure 5.23: Comparison of on-shell and off-shell IA calculations to D($\vec{d}, pn$)D data with (θ_p, θ_n)=(+17.0°, −34.5°).

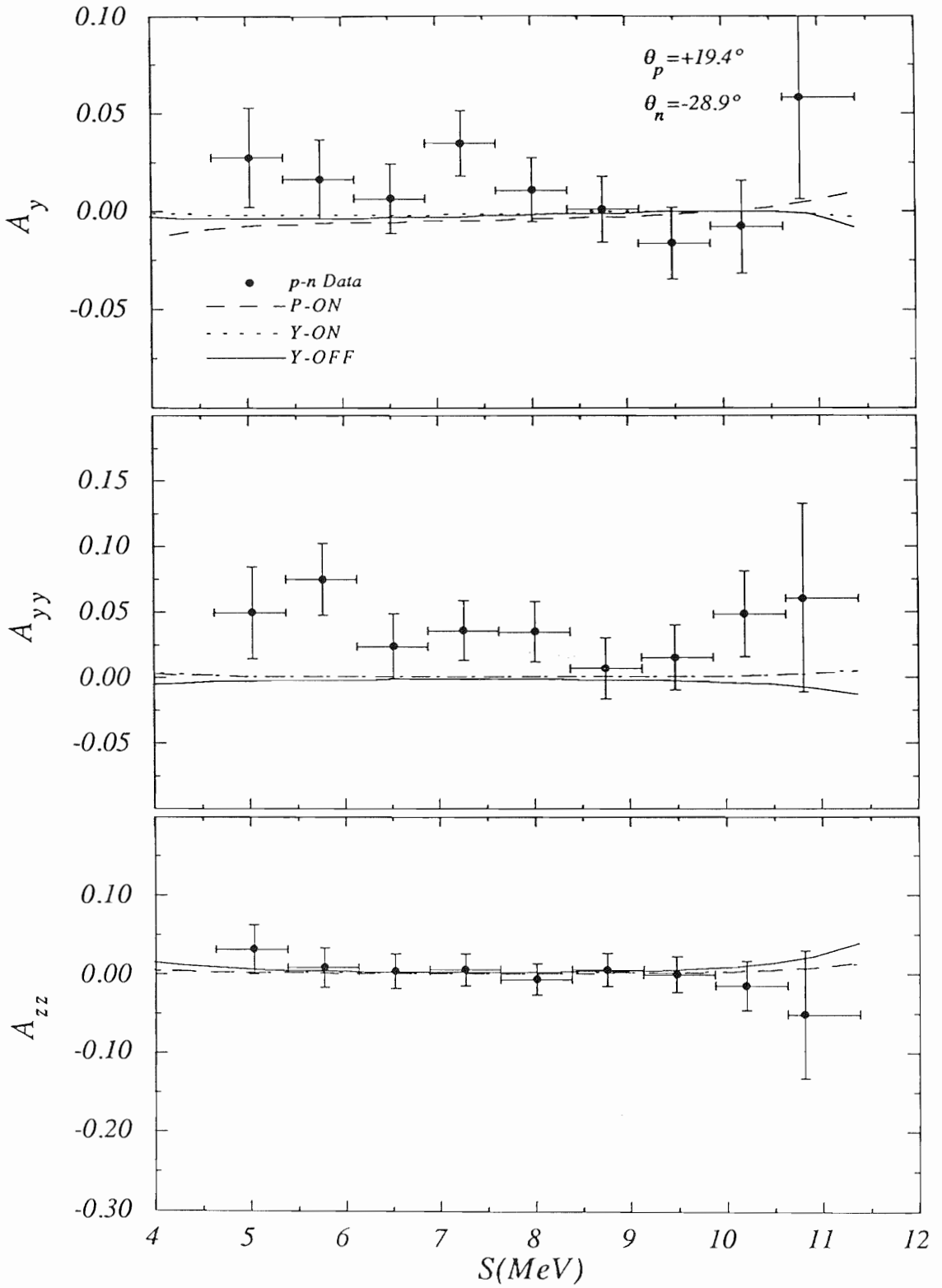

Figure 5.24: Comparison of on-shell and off-shell IA calculations to D($\vec{d}, pn$)D data with (θ_p,θ_n)=(+19.4°, −28.9°).

5.4 Summary

Our IA calculations of the $\vec{d}+d \rightarrow d+p+n$ breakup reaction confirm earlier observations that the IA at low energies does not contain the necessary sophistication needed to reliably calculate vector and tensor analyzing powers. The calculations can however be used to study the reaction dynamics by identifying the location of enhancements in the cross section and regions of phase space sensitive to certain aspects of the NN and dN interactions. Clearly our data and calculations suggest a sizeable sensitivity of A_{yy} and A_{zz} to off-shell effects in the dN interaction and A_y to ^3P-waves in the NN interaction. The importance of multiple scattering processes in the $\vec{d}+d \rightarrow d+p+n$ breakup reaction is also unquestionably reinforced by the observation of non-zero tensor analyzing powers in the pn coincidence data.

Chapter 6

Charge-Symmetry Breaking

6.1 Introduction

Note: the majority of the text in this chapter comes directly from a brief letter which is being readied for rapid publication [Fel91].

Fundamental symmetries in physics play an important role in the understanding of the interaction of matter. From a theoretical point of view these symmetries are desirable because they lead to a tremendous simplification in the physical laws governing the interaction. One such symmetry often studied in nuclear physics is the symmetry associated with isospin space. In this representation the neutron (n) and proton (p) are treated as two states of the nucleon and the nuclear Hamiltonian is independent of arbitrary rotations in isospin space. Therefore, the nn, pp and np forces must be identical. This equivalence of nuclear forces is known as charge independence. A special form of symmetry occurs under a 180° rotation about the T_2 axis which reverses the sign of T_3, the isotopic spin projection. For nucleons this rotation, called the charge-symmetry (CS) operation, changes protons into neutrons and vice versa. At the quark level the CS operation interchanges u and d quarks. Clearly at the hadron level, charge symmetry is broken by the electromagnetic (em) interaction and the n-p mass difference. A precise determination of any deviation from CS is necessary to determine if it can be explained on the basis of em interactions and mass differences or if there is a fundamental breaking in the nuclear part of the interaction.

Consistent information now exists to verify that the nuclear part of the pp and nn interactions are not identical, or in other words, that charge symmetry is broken

[Mil90]. This information, obtained from a variety of observables and systems, is also leading to an understanding of the fundamental causes of the breaking of this elementary symmetry [Mil90]. In particular, the difference between the $^1S_0$ nn and pp scattering lengths [Sla89], and the observed ^{3}H-^{3}He mass difference [Wu90, Fri87, Bra88] are fully explained by symmetry breaking in the S-wave part of the nucleon-nucleon (NN) force.[1] However, very little is known about charge-symmetry breaking (CSB) in the NN angular momentum states for $\ell \geq 1$.

In addition to using NN systems to investigate CSB [Knu91], information on CSB can be obtained by comparing data from charge-symmetric reactions such as neutron and proton elastic scattering from T=0 nuclei (i.e., nuclei with an equal number of protons and neutrons) [Win86] and neutron and proton stripping reactions on the same nucleus, such as the (d,n) and (d,p) reactions [Gru89]. However, since an exact treatment of the reaction dynamics does not exist for nuclear stripping reactions for many-body systems, it is difficult to relate observations from studies of many-body systems and stripping reactions to the NN force. Therefore, recent experimental studies have concentrated on the A=3 system, where rigorous Faddeev-type calculations are available [Wit88, Wit89c, How88] and on the A=4 system, for which microscopic calculations are beginning to appear in the literature [Fon90, Fon89, Mdl86b, Mdl86a]. (The rigorous inclusion of the Coulomb force in both the three-nucleon ($3N$) and $4N$ scattering systems still remains formidable.) Both the progress in these realistic calculations and the recognition that at low energies ($E_{cm} < 20$ MeV) there is a strong sensitivity of A_y in the A=3 and 4 scattering systems to the P-wave part of the NN force [Fon90, How87] makes these few-nucleon systems attractive for studying CSB in the NN P-waves. The large size of the deuteron, in particular, implies large impact parameters for scattering from individual nucleons and therefore, increases the contribution of P-waves at low energies.

In the A=3 system, both bound and scattering states can be used to study CSB. The difference in the ^{3}H and ^{3}He binding energies as well as differences between data for neutron-deuteron (nd) and proton-deuteron (pd) elastic scattering provide a measure of CSB. The main difficulty in interpreting the results in these studies is discerning between differences that are due to CSB and those that are due to the em force, which is generally the dominant cause of the measured differences in A=3

[1] According to the classification scheme of Henley and Miller [Hen79], nn and pp forces are sensitive to class III charge-symmetry-breaking potentials and np forces are sensitive to class IV charge-symmety-breaking potentials.

charge-symmetric systems. For instance, a recent study concluded that only about 75 keV of the observed 764 keV ^{3}H–^{3}He binding energy difference is due to CSB, the remainder being due to em effects [Wu90]. Similarly, in a comparison between data for $\vec{n}d$ and $\vec{p}d$ elastic scattering, a 10% difference in $A_y(\theta)$ near the minimum in the differential cross section was concluded to be mainly due to the static Coulomb force in the entrance channel [Tor91]. The Coulomb repulsion of the incident proton in pd scattering causes the effective interaction energy to be less than that of a neutron at the same incident energy. This Coulomb energy shift in pd scattering at 10 MeV is -640 keV, however with a relatively large uncertainty of ± 200 keV, which is mainly due to the diffuseness of the deuteron surface. The 30% uncertainty of this shift gives an indication of the difficulty one faces in attempts to extract a measure of CSB from comparisons of pd and nd elastic scattering.

In the A=4 system, attempts have been made to observe CSB by comparing polarization data for the mirror reactions D$(\vec{d},p)^3$H and D$(\vec{d},n)^3$He [Gru89]. Although the Coulomb force in the entrance channel is identical, there are difficulties in interpreting the results. First, because of the differences in the Q-values, for equal incident energy the kinematics of the particles in the exit channel cannot be matched in order to make these reactions perfectly charge symmetric. Second, the effect of the Coulomb force in the exit channels is clearly different, since in one case two charged particles are emitted and in the other a charged particle and a neutral particle are emitted. Therefore, the observed differences for the D$(\vec{d},p)^3$H and D$(\vec{d},n)^3$He reactions cannot be reliably attributed to CSB without the completion of rigorous theoretical calculations.

In this part of the thesis we investigate the use of spin observables from the $\vec{d}$+$d \rightarrow d$+p+n breakup reaction as a probe of CSB. The D$(\vec{d},dp)n$ and D$(\vec{d},dn)^1$H are charge symmetric processes, assuming of course that the comparison is made at the same reaction angles and at the same point on the kinematically allowed locus. Even though rigorous calculations do not exist for these reactions, we favor this probe because of the following advantages over the comparisons of nd and pd elastic scattering data and of D$(\vec{d},p)^3$H and D$(\vec{d},n)^3$He data:

1. Since the entrance channels are identical, the ambiguity of the Coulomb energy shift in the entrance channel in pd scattering is avoided.
2. Because of the kinematic flexibility of the d+$d \rightarrow d$+p+n breakup reaction, the Coulomb force in the exit channel of the D$(\vec{d},dp)n$ and D$(\vec{d},dn)^1$H reactions can be made very similar by a judicious choice of the particle

emission angles.

3. The complication due to differences of the Q-value in mirror reactions such as D$(d,p)^3$H and D$(d,n)^3$He is not present.

4. The use of tensor polarized deuteron beams allows measurements of several spin observables, rather than of only A_y as in the case of $\vec{N}d$ elastic scattering.

5. Unlike the A_y data for the *nd–pd* comparisons, the D$(\vec{d},dp)n$ and D$(\vec{d},dn)^1$H data can be measured simultaneously, thereby cancelling most instrumental asymmetries and all uncertainties in the incident beam polarization.

6.2 The Evidence

Of the 12 angle pairs measured in this work, those most relevant to CSB studies were the *dp* and *dn* coincidence data at angle pairs (θ_d,θ_N)=(+17.0°,−17.0°) and (+17.0°,−34.5°) and the *pn* coincidence data at (θ_p,θ_n)=(+17.0°, −17.0°). If CS is valid, then the observables for D$(\vec{d},dp)n$ and D$(\vec{d},dn)^1$H should be equal.[2] Furthermore, for the *pn* coincidence data the tensor analyzing powers along the kinematic locus in a plot of E_p versus E_n should be symmetric (A_y is antisymmetric) with respect to the E_p=E_n point. This latter feature can be seen as follows: since A_{yy} and A_{zz} are invariant under a 180° rotation about the z-axis (see equation 3.4 and let $\phi \rightarrow \phi + 180°$),

$$A_{ii}(\theta_p=+\theta,\theta_n=-\theta,E_p=E_1,E_n=E_2) = A_{ii}(\theta_p=-\theta,\theta_n=+\theta,E_p=E_1,E_n=E_2) \quad (6.1)$$

where the particle angles and energies are specified above. If charge symmetry holds then

$$A_{ii}(\theta_p=-\theta,\theta_n=+\theta,E_p=E_1,E_n=E_2) = A_{ii}(\theta_p=+\theta,\theta_n=-\theta,E_p=E_2,E_n=E_1). \quad (6.2)$$

Therefore, we obtain the symmetric relationship

$$A_{ii}(\theta_p=+\theta,\theta_n=-\theta,E_p=E_1,E_n=E_2) = A_{ii}(\theta_p=+\theta,\theta_n=-\theta,E_p=E_2,E_n=E_1). \quad (6.3)$$

[2]The 0.1% mass difference between the n and p influences the kinematics, but since our energy bins along S were 250 keV wide, this effect is negligible.

Det. Part.	(θ_1,θ_2)	S_l–S_u	θ_{pole1}	θ_{pole2}	$A_y \pm \Delta A_y$	$A_{yy} \pm \Delta A_{yy}$	$A_{zz} \pm \Delta A_{zz}$
dn	(+17.0°, −17.0°)	3.9–7.4	124°–141°	169°–180°	0.026 ± 0.003	−0.001 ± 0.004	0.055 ± 0.004
dp	(+17.0°, −17.0°)	3.9–7.4	124°–141°	169°–180°	0.020 ± 0.003	−0.003 ± 0.005	0.051 ± 0.004
dn	(+17.0°, −17.0°)	3.9–9.9	97°–141°	160°–180°	0.023 ± 0.003	0.002 ± 0.004	0.040 ± 0.003
dp	(+17.0°, −17.0°)	3.9–9.9	97°–141°	160°–180°	0.019 ± 0.003	0.001 ± 0.004	0.034 ± 0.004
dn	(+17.0°, −34.5°)	4.6–9.9	71°–99°	147°–179°	0.021 ± 0.009	0.107 ± 0.012	**−0.105±0.017**
dp	(+17.0°, −34.5°)	4.6–9.9	71°–99°	147°–179°	0.029 ± 0.014	0.100 ± 0.019	**−0.165±0.019**
pn	(+17.0°, −17.0°)	3.9–6.4	0°–6°	9°–16°	0.011 ± 0.010	0.044 ± 0.013	−0.032 ± 0.013
pn	(+17.0°, −17.0°)	7.6–10.1	9°–16°	0°–6°	−0.016 ± 0.012	0.021 ± 0.016	−0.027 ± 0.016
pn	(+17.0°, −17.0°)	6.4–7.9	6°–9°	6°–9°	**0.031±0.012**	0.036 ± 0.016	0.009 ± 0.016

Table 6.1: Comparison of data for charge-symmetric observables. The A_y, A_{yy} and A_{zz} summed over the arc from S_l(lower) to S_u(upper) and the two-body c.m. angles of the two QFS particles for the two dominant poles. (See appendix B for additional kinematic information.) Det. Part. stands for the particles detected in coincidence at (θ_1,θ_2). The three analyzing powers indicated in bold-faced type are those that show a significant difference between CS observables.

This simply means that if CS holds, the tensor analyzing powers A_{yy} and A_{zz} must be symmetric about the E_p=E_n point along the locus of E_p *vs.* E_n. On the other hand, since A_y is antisymmetric under a 180° rotation about the z-axis (see equation 3.4), the A_y for the breakup reaction must be antisymmetric about the E_p=E_n point.

Figure 6.1 shows the A_y, A_{yy} and A_{zz} data for (θ_d,θ_N)=(+17.0°,−17.0°) plotted as a function of arc length along the kinematically allowed curve S. The data for the two reactions are indistinguishable within statistical uncertainties, except for the A_y data around S=6 MeV where the observable for the *dn* data systematically runs higher than the *dp* data. To more closely investigate this latter difference, the uncertainties were reduced by summing all the data between S=3.9–7.4 MeV (this region is roughly centered about the maxima in the cross section). Table 6.1 shows that there is a slight difference of 0.006 ± 0.004 in A_y for these two processes and that A_{yy} and A_{zz} for the two reactions agree within ±0.006. Summing the data from S=3.9–9.9 MeV yields differences in A_y, A_{yy} and A_{zz} between the two processes of 0.004 ± 0.004, 0.001 ± 0.006 and 0.006 ± 0.005, respectively. In summary, there is no convincing evidence for differences in the data for (θ_d,θ_N)=(+17.0°,−17.0°).

The data for (θ_d,θ_N)=(+17.0°,−34.5°) are shown in figure 6.2 and table 6.1. Because of the relatively large uncertainties in the observables the data were summed over the interval S=4.6–9.9 MeV. The A_y and A_{yy} for the two processes, in this interval, agree within their statistical errors of ±0.017 and ±0.022, respectively. However, there is a significant difference of 0.060 ± 0.025 between the A_{zz} data.

The A_y, A_{yy} and A_{zz} data for the reaction D$(\vec{d},pn)$D with (θ_p,θ_n)=(+17.0°,−17.0°) are shown in figure 6.3 and are compared in the two regions S=3.9–6.6 and 7.6–10.4 MeV in table 6.1. These regions are symmetric in energy with respect to the E_p=E_n point (S=7 MeV). The A_{yy} and A_{zz} data are symmetric to within the statistical errors of ±0.02 and the A_y data are antisymmetric to within their statistical errors of ±0.016 (see table 6.1). If CS is valid, A_y should be zero at the E_p=E_n point (S=7 MeV) due to the antisymmetric nature of $A_y(S)$. However, in the interval S=6.4–7.9 MeV around this E_p=E_n point, the value of A_y is 0.031 ± 0.012.

Summarizing all these results, we find that our study has found excellent agreement, i.e., between CS observables to within an absolute uncertainty of ±0.004 to ±0.02, with two exceptions. These exceptions are the A_{zz} data with (θ_d,θ_N)= (+17.0°,−34.5°) at S=4.6–9.9 MeV and the A_y data with (θ_p,θ_n)=(+17.0°,−17.0°) at S=6.4–7.9 MeV. The question to be addressed next is: *Are these differences true CSB or merely electromagnetic effects?*

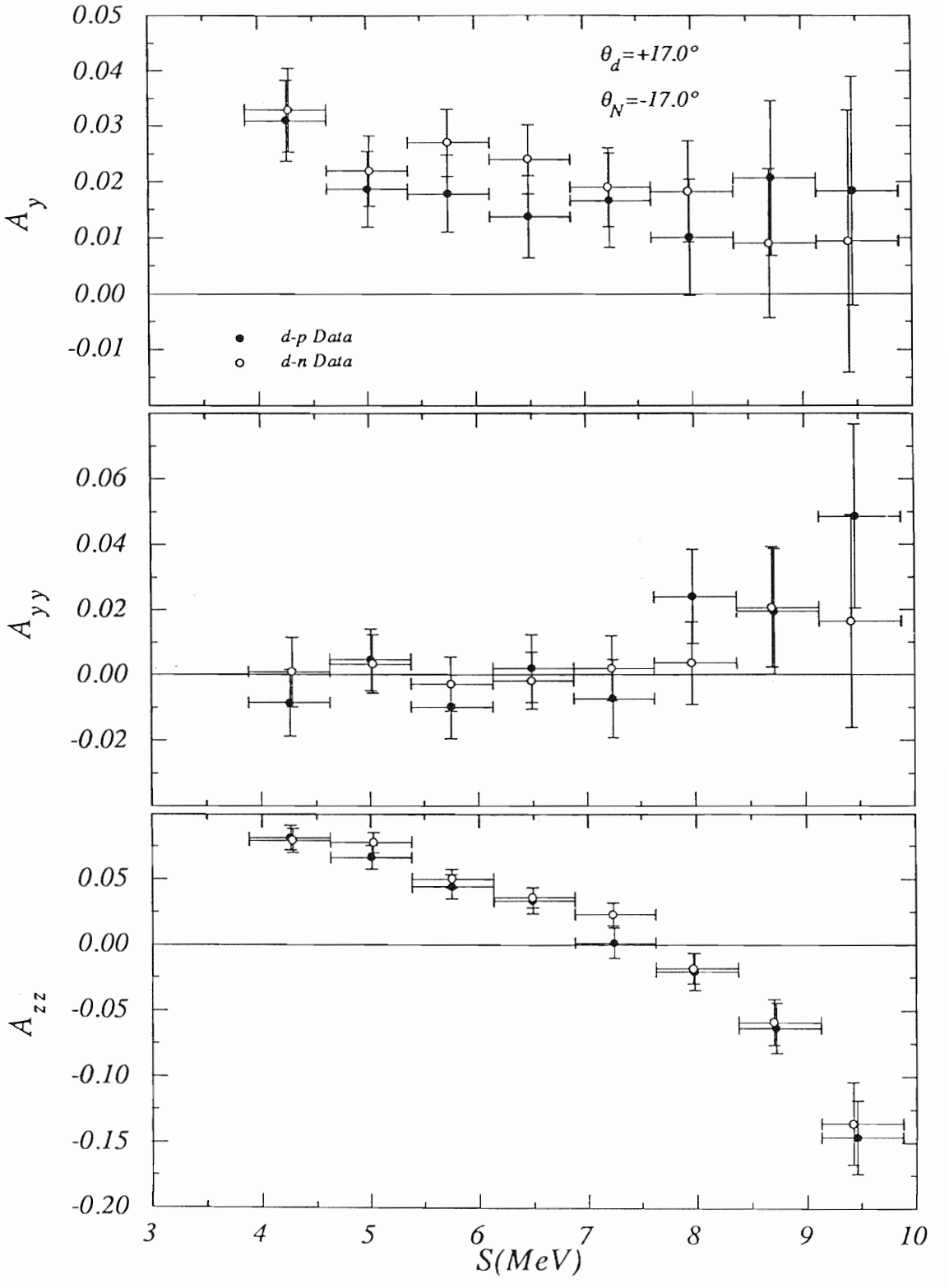

Figure 6.1: Comparison of D($\vec{d}, dp$)n (closed circles) to D($\vec{d}, dn$)^{1}H (open circles) for (θ_d,θ_N)=(+17.0°, −17.0°).

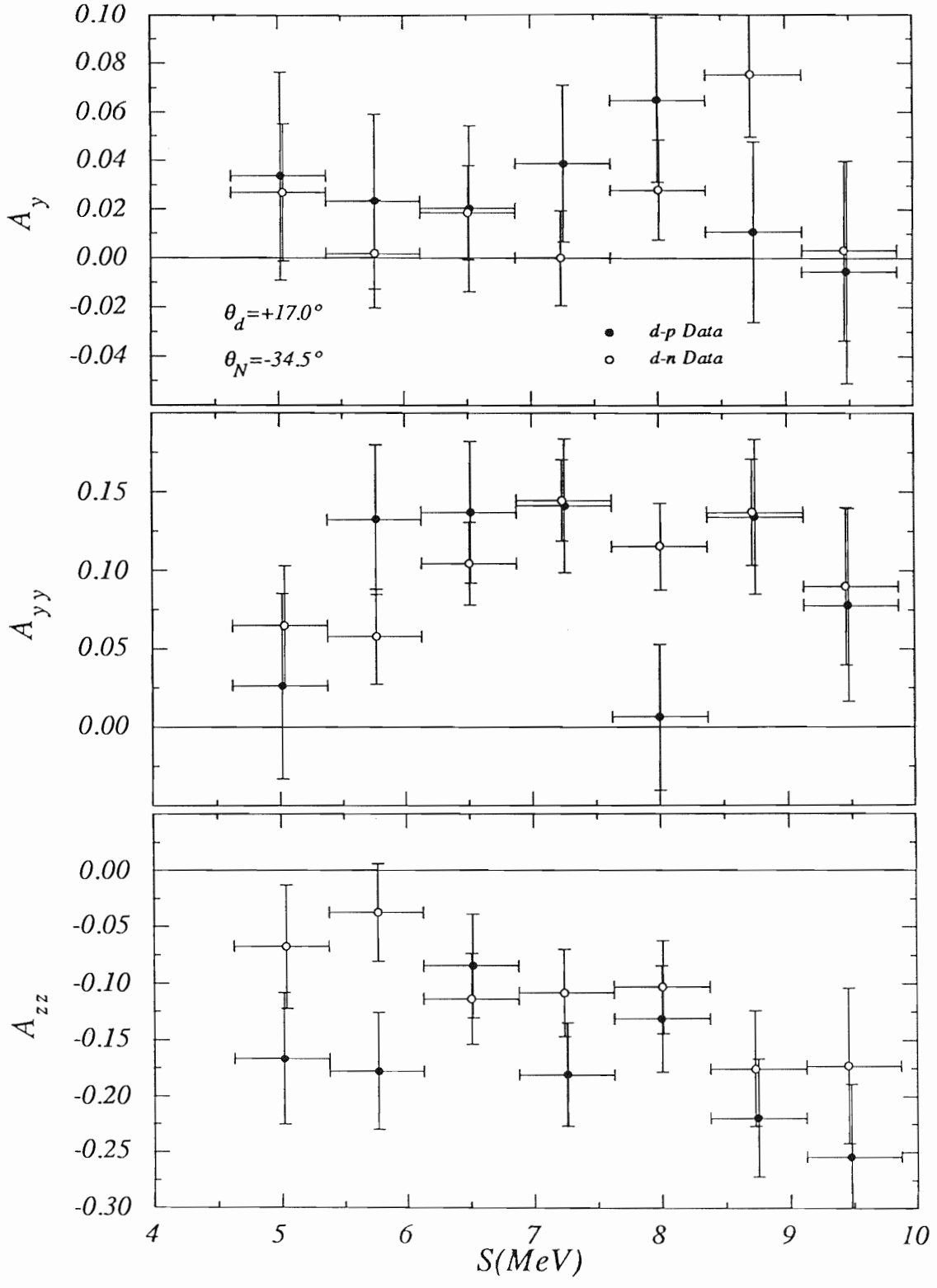

Figure 6.2: Comparison of $D(\vec{d}, dp)n$ (closed circles) to $D(\vec{d}, dn)^1H$ (open circles) for (θ_d, θ_N)=(+17.0°, −34.5°).

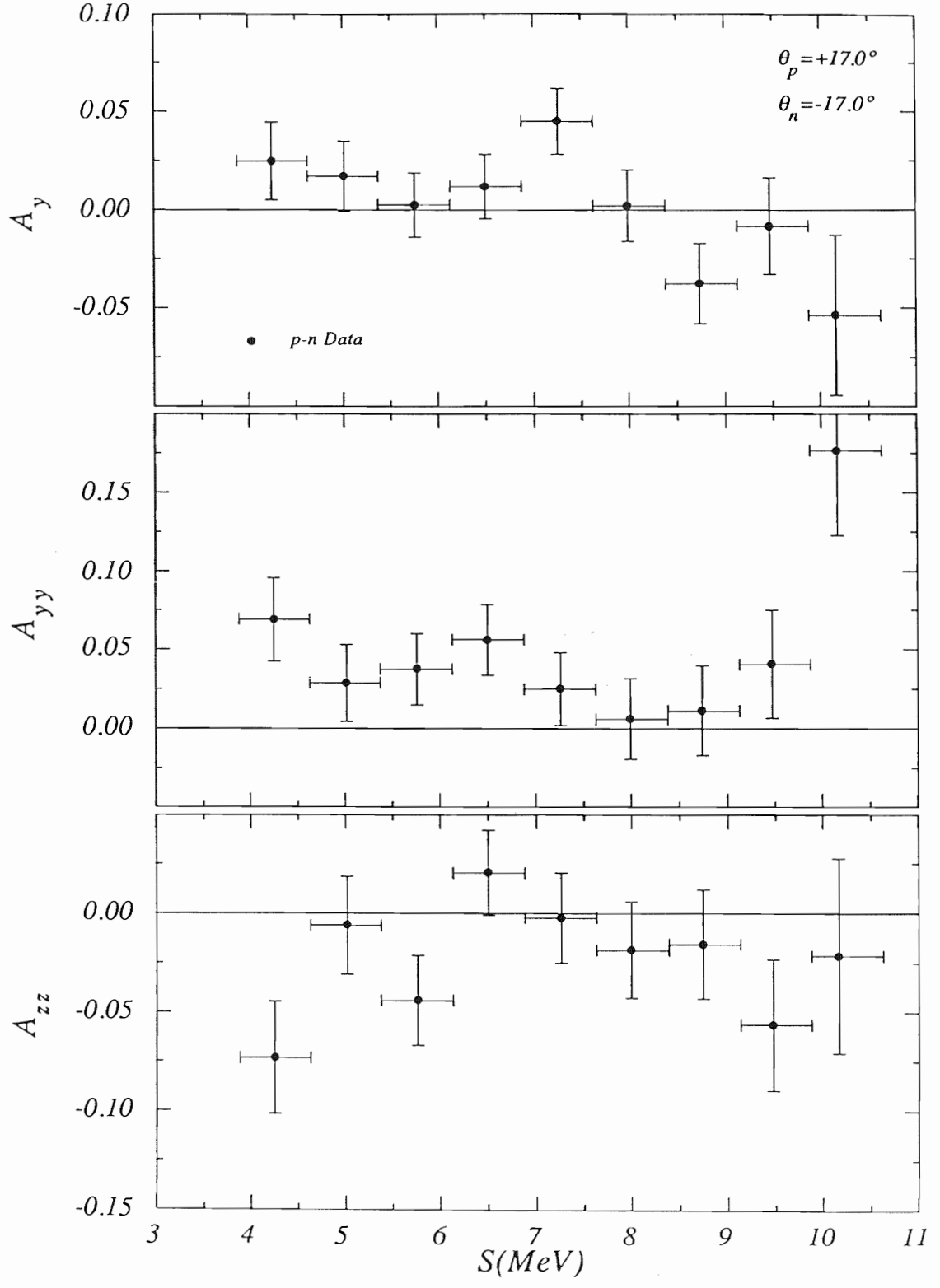

Figure 6.3: D($\vec{d}, pn$)D for (θ_p,θ_n)=(+17.0°, −17.0°).

6.3 Electromagnetic or CSB?

We appreciate that detailed interpretation of our results must wait for rigorous $4N$ calculations, which properly include em forces. However, for the present we will use the Impulse Approximation (IA) (see chapter 4) to gain insight on whether the differences are due to em effects or to CSB. Because of the failure of the IA to accurately predict the analyzing powers (see chapter 5), we will use mainly its kinematic features to interpret our results.

The kinematics of the d+$d \rightarrow d$+p+n reaction for the (θ_p, θ_n)=$(+17.0°, -17.0°)$ coincidence strongly suggest that the differences observed for the A_y data for S=6.4–7.9 MeV are mainly due to the Coulomb force. According to our IA calculations over 95% of the cross section for this pn coincidence is due to the two projectile breakup poles (Pn and Pp poles). The calculation of the relative contributions to the cross section from the two poles is extremely model dependent and depends critically on the treatment of the Coulomb force in the Pn pole. Since our implementation of the IA neglected the Coulomb interaction, we rely solely on the kinematic features of the Pn and Pp poles to gain insight on the cause of the bump in A_y around S=7.3 MeV (see figure 6.3). Along the locus from S=4–10 MeV, the Nd c.m. scattering angles range from 0° to 16° for both the Pn and Pp poles. At these forward angles the Coulomb force dominates elastic pd scattering. Therefore, we conclude that the observed deviation of A_y from antisymmetry about the S=7 MeV point is likely due to the Coulomb force. This conclusion is substantiated by our other pn coincidence data at (θ_p, θ_n)=$(+17.0°, -34.5°)$ (figure 5.11) and (θ_p, θ_n)=$(+19.4°, -28.9°)$ (figure 5.12). In all cases there is a bump in A_y at the position on the locus which corresponds to pd scattering near 0°. Furthermore, a previous study by Kluge *et al.* [Klu78] of the d+$d \rightarrow d$+p+n breakup reaction at 52 MeV, showed a reduction in the measured cross section[3] for dp QFS data compared to dn QFS for dN c.m. scattering angles forward of 60°. They also concluded that the differences between $\mathrm{D}(d, dp)n$ and $\mathrm{D}(d, dn)^1\mathrm{H}$ at forward angles were probably due to the Coulomb interaction.

On the other hand, the observed difference in A_{zz} for the (θ_d, θ_p)=$(+17.0°, -34.5°)$ and (θ_d, θ_n)=$(+17.0°, -34.5°)$ coincidences (see figure 6.2) cannot be easily explained with em effects. Our IA calculations predict that with (θ_d, θ_N)=$(+17.0°, -34.5°)$ the

[3]Measurements of the absolute cross section of the d+$d \rightarrow d$+p+n breakup reaction are susceptible to errors associated with detector alignment and knowledge of neutron-detector efficiencies. Our measurements however, are not sensitive to these potential problems; only relative cross sections are needed to obtain polarization data with our methods.

d+$d \rightarrow d$+p+n breakup is dominated by a single pole, spectator nucleon in the target (Tn pole for D($\vec{d}, dp$)n and Tp pole for D($\vec{d}, dn$)^{1}H). The following pieces of evidence suggest that em effects are not the cause of the dp–dn A_{zz} difference:

1. The dominant pole corresponds to $\vec{d}p$ ($\vec{d}n$) scattering to c.m. angles from 71°–99°. Therefore, the dp coincidence data is free of the large Coulomb effects encountered in forward angle pd elastic scattering.
2. The Coulomb force in the entrance channel is identical for the dp and dn coincidence data.
3. The Coulomb force in the exit channel is the same for the dp and dn data at S=7.2 MeV and the difference between these data sets does not vanish at this point.
4. Statistically there is no difference between the A_y and A_{yy} data for the dp and dn coincidences at the same angle pairs.

It is unlikely that the Coulomb force has such a pronounced effect on A_{zz}, while having such a small effect on A_y and A_{yy}. Therefore, we conclude that the difference between A_{zz} for the dp and dn coincidences for the (θ_d, θ_N)=(+17.0°, −34.5°) angle pairs is not due to em effects, but is probably a signature of CSB.

6.4 Summary

In summary, we have used the $\vec{d}$+$d \rightarrow d$+p+n breakup reaction to search for CSB effects. Of the nine charge-symmetric observables compared in our study, only two were statistically different, A_y for (θ_p, θ_n)=(+17.0°, −17.0°) and A_{zz} for (θ_d, θ_N)=(+17.0°, −34.5°). To gain insight into the cause of the differences in the CS observables, the IA model was used. We conclude that the deviation of the A_y data from antisymmetry about the E_p=E_n point (S=7 MeV) along the locus for (θ_p, θ_n)=(+17.0°, −17.0°) is probably due to em effects, since according to our IA model these data correspond to Nd scattering to forward angles. On the other hand, the difference in the dp and dn A_{zz} for (θ_d, θ_N)=(+17.0°, −34.5°) could not be easily attributed to em effects within our IA model. Therefore, we conclude that the difference in the above A_{zz} data probably is a signature of CSB. However, the interpretation of our observables in terms of CSB in the underlying NN interaction awaits a rigorous $4N$ calculation that includes em forces.

We emphasize that our initial investigation of CSB effects using the $\vec{d}+d \rightarrow d+p+n$ breakup reaction covers only a small portion of the available phase space for this reaction and that future studies (with reduced statistical uncertainties) should be conducted to fully exploit the unique symmetry properties of this reaction.

Chapter 7

Summary and Conclusions

Vector and tensor analyzing powers A_y, A_{yy} and A_{zz} have been measured for the $\vec{d}+d \rightarrow d+p+n$ breakup reaction at an incident energy of 12 MeV in a kinematically complete experimental arrangement. The momenta of two of the three outgoing particles were detected in a coincidence arrangement, thereby overdetermining the kinematics of the reaction. The angle pairs were chosen such that the reaction would be well-suited for observing dp and dn QFS. Since calculations of polarization observables for the $\vec{d}+d \rightarrow d+p+n$ breakup reaction based on a realistic-microscopic approach are not yet available, we have compared our data to the Impulse Approximation (IA). In this approach one of the nucleons is treated simply as a spectator to the two-body (deuteron-nucleon) interaction.

Our calculations of A_y, A_{yy} and A_{zz} using the IA indicate that the simplistic approach of the IA is inadequate for calculating these observables at low energies. Previous attempts to use the phenomenological approach of the IA to calculate the cross section of the $d+d \rightarrow d+p+n$ breakup reaction had been met with limited success. Without modifying the deuteron's wave function, the calculations usually predict a QFS enhancement that is both broader and greater in magnitude (often by a factor of 10 or more) than the measured values. We attribute the need for a scaling factor and our lack of agreement between analyzing power calculations and data to contributions from multiple scattering in the reaction which are absent in our model. The observation of non-zero tensor analyzing powers for projectile-breakup processes reinforces this conclusion. Our calculations do, however, indicate that the analyzing powers show the greatest resemblance to free scattering data when the measurement

is performed when minimum momentum is transferred to the spectator, i.e., the condition for QFS. Furthermore, the relatively large analyzing powers observed in some of our measurements suggest that the breakup process goes through an intermediate state with n-^{3}He or p-^{3}H scattering, since it is well known that these two scattering systems can generate analyzing powers significantly larger than either $\vec{d}d$ or $\vec{d}N$ scattering at low energies. Additionally, we have shown that within the context of the IA the cross section and analyzing powers are sensitive to off-shell effects in the dN subsystem and to P-waves in the NN interaction.

We have also studied the possibility of using the $\vec{d}$+$d \rightarrow d$+p+n breakup reaction as a probe of charge-symmetry breaking (CSB) in the NN interaction. Two methods of using the $\vec{d}$+$d \rightarrow d$+p+n breakup reaction to exploit the inherent symmetry in the system were discussed. The first method is that of comparing D$(\vec{d}, dp)n$ data to D$(\vec{d}, dn)^1$H data at the same point in phase space and the second method is that of comparing the symmetry or antisymmetry of analyzing powers along the locus for D$(\vec{d}, pn)$D with $(\theta_p,\theta_n)=(+\theta, -\theta)$. Both of these methods allow for the matching of interaction energies and Coulomb forces in both the entrance and exit channels. However, in regions of forward angle scattering in the dN subsystem, Coulomb effects can still have a pronounced effect on the observables. To study CSB in the nuclear part of the interaction, care must be taken to avoid these regions of phase space. We have identified one region of phase space that showed a significant difference between D$(\vec{d}, dp)n$ and D$(\vec{d}, dn)^1$H for A_{zz} which we cannot attribute to Coulomb effects, and therefore is a candidate for CSB in the nuclear part of the NN interaction.

The detailed interpretation of our data must wait for rigorous four-nucleon calculations. With this in mind we have formed a collaboration with A.C. Fonseca of Lisbon that should produce the world's first rigorous calculations of the $\vec{d}$+$d \rightarrow d$+p+n breakup reaction. Our current measurements along with the cross section data previously reported in the literature should provide a testing ground for these calculations.

Future measurements are also desirable to further study the possibility of CSB in the NN interaction. These measurements should be performed to obtain errors at least a factor of two smaller than those reported in the present work. This would allow for comparisons between CS observables to be made over smaller regions of the kinematically allowed locus rather than integrating over large portions of the locus. Furthermore, we propose that a careful examination of the reaction kinematics be made before the measurement is designed in order to obtain data that will provide the maximum information.

Appendix A

Analyzing Powers Tabulations

A.1 Analyzing Powers Along S in 250 keV Steps

The analyzing powers for each of our angle pairs were computed as a function of arc length along the kinematically allowed locus as described in chapter 3. The tabulation of these analyzing powers in 250 keV steps along S is presented in the 12 tables in this section. The quantities used in the tables are defined as follows:

S = Centroid of the are segment spanned by the data point along the kinematically allowed curve

S_{min} = Lower end of the arc segment spanned by the data point

S_{max} = Upper end of the arc segment spanned by the data point

E_d = Deuteron laboratory energy in the exit channel to specify the energy coordinates of S_{min} and S_{max}

E_p = Proton laboratory energy in the exit channel to specify the energy coordinates of S_{min} and S_{max}

E_n = Neutron laboratory energy in the exit channel to specify the energy coordinates of S_{min} and S_{max}

A_y = Vector analyzing power for the arc segment S_{min}–S_{max}

A_{yy} = Tensor analyzing power for the arc segment S_{min}–S_{max}

A_{zz} = Tensor analyzing power for the arc segment S_{min}–S_{max}

ΔA_y = Absolute uncertainty in A_y

ΔA_{yy} = Absolute uncertainty in A_{yy}

ΔA_{zz} = Absolute uncertainty in A_{zz}.

Deuteron-Proton coincidence at θ_d= +10.0° and θ_p= −10.0°												
Arc Length			Coordinates				Analyzing Powers					
			S_{min}		S_{max}							
S	S_{min}	S_{max}	E_d	E_p	E_d	E_p	A_y	ΔA_y	A_{yy}	ΔA_{yy}	A_{zz}	ΔA_{zz}
2.75	2.63	2.88	1.19	8.21	1.42	8.12	+0.042	0.089	+0.030	0.123	+0.086	0.120
3.00	2.88	3.13	1.42	8.12	1.64	7.99	+0.007	0.060	−0.003	0.084	−0.004	0.081
3.25	3.13	3.38	1.64	7.99	1.84	7.85	+0.029	0.047	−0.009	0.066	+0.148	0.062
3.50	3.38	3.63	1.84	7.85	2.03	7.69	+0.021	0.039	−0.012	0.054	+0.115	0.051
3.75	3.63	3.88	2.03	7.69	2.22	7.53	+0.005	0.035	+0.037	0.049	+0.082	0.049
4.00	3.88	4.13	2.22	7.53	2.41	7.36	−0.003	0.032	−0.011	0.045	+0.080	0.045
4.25	4.13	4.38	2.41	7.36	2.59	7.18	+0.022	0.031	−0.018	0.043	+0.058	0.043
4.50	4.38	4.63	2.59	7.18	2.76	7.01	+0.023	0.030	+0.014	0.042	+0.042	0.042
4.75	4.63	4.88	2.76	7.01	2.94	6.83	+0.034	0.028	−0.005	0.040	+0.091	0.040
5.00	4.88	5.13	2.94	6.83	3.12	6.65	+0.014	0.029	+0.033	0.040	+0.095	0.039
5.25	5.13	5.38	3.12	6.65	3.29	6.47	−0.011	0.029	+0.006	0.041	+0.070	0.041
5.50	5.38	5.63	3.29	6.47	3.46	6.29	+0.011	0.029	+0.013	0.041	+0.117	0.040
5.75	5.63	5.88	3.46	6.29	3.63	6.11	+0.038	0.029	+0.015	0.041	+0.079	0.041
6.00	5.88	6.13	3.63	6.11	3.80	5.92	+0.018	0.031	+0.032	0.043	+0.020	0.043
6.25	6.13	6.38	3.80	5.92	3.97	5.74	−0.026	0.031	+0.035	0.043	+0.057	0.045
6.50	6.38	6.63	3.97	5.74	4.14	5.56	−0.010	0.032	+0.014	0.045	+0.093	0.045
6.75	6.63	6.88	4.14	5.56	4.31	5.37	+0.009	0.035	−0.043	0.050	+0.014	0.050
7.00	6.88	7.13	4.31	5.37	4.48	5.19	+0.003	0.036	−0.053	0.052	−0.002	0.053
7.25	7.13	7.38	4.48	5.19	4.65	5.01	+0.010	0.039	−0.055	0.056	+0.038	0.056
7.50	7.38	7.63	4.65	5.01	4.82	4.82	−0.025	0.043	+0.016	0.059	+0.094	0.059
7.75	7.63	7.88	4.82	4.82	4.99	4.64	−0.024	0.046	−0.031	0.066	−0.015	0.066
8.00	7.88	8.13	4.99	4.64	5.16	4.46	+0.005	0.050	−0.072	0.072	+0.013	0.070
8.25	8.13	8.38	5.16	4.46	5.33	4.27	−0.018	0.055	+0.024	0.076	+0.019	0.079
8.50	8.38	8.63	5.33	4.27	5.50	4.09	−0.046	0.059	−0.032	0.084	−0.008	0.089
8.75	8.63	8.88	5.50	4.09	5.68	3.91	−0.090	0.071	−0.054	0.100	+0.033	0.094
9.00	8.88	9.13	5.68	3.91	5.85	3.73	+0.031	0.085	+0.047	0.115	+0.015	0.112
9.25	9.13	9.38	5.85	3.73	6.02	3.54	−0.056	0.093	+0.114	0.124	−0.063	0.132
9.50	9.38	9.63	6.02	3.54	6.19	3.36	−0.033	0.125	+0.020	0.171	−0.041	0.151
9.75	9.63	9.88	6.19	3.36	6.36	3.18	−0.050	0.155	+0.123	0.194	−0.047	0.183
10.00	9.88	10.13	6.36	3.18	6.53	3.00	−0.164	0.184	+0.015	0.244	−0.284	0.245

Table A.1: Analyzing powers along the locus S in 250 keV steps for D($\vec{d}, dp$)n with (θ_d,θ_p)=(+10.0°, −10.0°). Arc length and energy ranges given in MeV. The uncertainty in the analyzing powers is understood to be ± everywhere.

Deuteron-Proton coincidence at θ_d= +10.0° and θ_p= −41.2°												
Arc Length			Coordinates				Analyzing Powers					
			S_{min}		S_{max}							
S	S_{min}	S_{max}	E_d	E_p	E_d	E_p	A_y	ΔA_y	A_{yy}	ΔA_{yy}	A_{zz}	ΔA_{zz}
1.25	1.13	1.38	1.14	3.83	1.24	4.06	−0.308	0.232	−0.002	0.278	−0.117	0.257
1.50	1.38	1.63	1.24	4.06	1.35	4.29	−0.200	0.206	+0.117	0.264	−0.074	0.212
1.75	1.63	1.88	1.35	4.29	1.48	4.50	+0.025	0.123	+0.188	0.164	−0.086	0.199
2.00	1.88	2.13	1.48	4.50	1.64	4.69	−0.033	0.107	+0.116	0.146	−0.139	0.172
2.25	2.13	2.38	1.64	4.69	1.83	4.85	−0.139	0.094	−0.025	0.132	−0.016	0.128
2.50	2.38	2.63	1.83	4.85	2.05	4.97	−0.074	0.087	+0.062	0.119	−0.025	0.125
2.75	2.63	2.88	2.05	4.97	2.29	5.04	−0.106	0.082	+0.162	0.107	−0.024	0.122
3.00	2.88	3.13	2.29	5.04	2.53	5.07	−0.088	0.094	+0.079	0.128	−0.110	0.135
3.25	3.13	3.38	2.53	5.07	2.78	5.06	−0.059	0.082	+0.002	0.116	−0.107	0.131
3.50	3.38	3.63	2.78	5.06	3.03	5.02	+0.046	0.079	+0.087	0.109	−0.128	0.125
3.75	3.63	3.88	3.03	5.02	3.27	4.96	+0.003	0.078	+0.044	0.110	−0.151	0.126
4.00	3.88	4.13	3.27	4.96	3.51	4.88	−0.126	0.076	+0.020	0.106	−0.098	0.125
4.25	4.13	4.38	3.51	4.88	3.74	4.79	−0.064	0.077	−0.002	0.109	+0.172	0.107
4.50	4.38	4.63	3.74	4.79	3.97	4.68	−0.027	0.076	+0.028	0.106	+0.144	0.110
4.75	4.63	4.88	3.97	4.68	4.19	4.57	−0.108	0.074	+0.061	0.099	−0.051	0.114
5.00	4.88	5.13	4.19	4.57	4.41	4.45	−0.140	0.075	+0.041	0.100	+0.041	0.112
5.25	5.13	5.38	4.41	4.45	4.63	4.33	−0.062	0.075	−0.006	0.106	−0.034	0.123
5.50	5.38	5.63	4.63	4.33	4.84	4.20	−0.053	0.066	−0.013	0.095	−0.087	0.112
5.75	5.63	5.88	4.84	4.20	5.05	4.06	−0.130	0.068	−0.000	0.095	−0.094	0.107
6.00	5.88	6.13	5.05	4.06	5.26	3.92	−0.060	0.074	+0.062	0.100	−0.234	0.107
6.25	6.13	6.38	5.26	3.92	5.46	3.78	+0.013	0.069	−0.052	0.099	−0.071	0.102
6.50	6.38	6.63	5.46	3.78	5.67	3.63	−0.081	0.063	−0.081	0.091	−0.065	0.099
6.75	6.63	6.88	5.67	3.63	5.87	3.49	−0.122	0.062	+0.007	0.085	−0.117	0.099
7.00	6.88	7.13	5.87	3.49	6.07	3.34	−0.087	0.059	+0.111	0.079	−0.144	0.097
7.25	7.13	7.38	6.07	3.34	6.27	3.19	−0.024	0.057	+0.054	0.079	−0.047	0.083
7.50	7.38	7.63	6.27	3.19	6.47	3.03	−0.025	0.056	+0.013	0.080	+0.004	0.079
7.75	7.63	7.88	6.47	3.03	6.66	2.88	−0.040	0.053	+0.138	0.071	−0.015	0.080
8.00	7.88	8.13	6.66	2.88	6.86	2.72	−0.020	0.051	+0.035	0.071	+0.014	0.076
8.25	8.13	8.38	6.86	2.72	7.05	2.56	+0.020	0.050	+0.058	0.070	+0.003	0.073
8.50	8.38	8.63	7.05	2.56	7.24	2.40	−0.019	0.049	+0.126	0.066	+0.030	0.071
8.75	8.63	8.88	7.24	2.40	7.43	2.24	+0.041	0.049	−0.010	0.070	+0.073	0.068
9.00	8.88	9.13	7.43	2.24	7.62	2.08	−0.020	0.050	−0.015	0.071	−0.040	0.070
9.25	9.13	9.38	7.62	2.08	7.81	1.91	−0.023	0.050	+0.052	0.069	−0.091	0.072
9.50	9.38	9.63	7.81	1.91	8.00	1.75	+0.013	0.049	+0.037	0.068	−0.108	0.071
9.75	9.63	9.88	8.00	1.75	8.18	1.58	−0.022	0.052	+0.092	0.069	−0.050	0.073
10.00	9.88	10.13	8.18	1.58	8.36	1.41	−0.023	0.053	+0.082	0.072	−0.005	0.075
10.25	10.13	10.38	8.36	1.41	8.54	1.23	−0.011	0.057	+0.029	0.079	−0.003	0.081
10.50	10.38	10.63	8.54	1.23	8.72	1.06	+0.032	0.080	+0.028	0.108	−0.011	0.092
10.75	10.63	10.88	8.72	1.06	8.89	0.87	+0.131	0.137	+0.111	0.176	−0.026	0.141

Table A.2: Analyzing powers along the locus S in 250 keV steps for D$(\vec{d}, dp)n$ with (θ_d,θ_p)=(+10.0°, −41.2°). Arc length and energy ranges given in MeV. The uncertainty in the analyzing powers is understood to be ± everywhere.

Deuteron-Proton coincidence at θ_d= +17.0° and θ_p= −17.0°												
Arc Length			Coordinates				Analyzing Powers					
			S_{min}		S_{max}							
S	S_{min}	S_{max}	E_d	E_p	E_d	E_p	A_y	ΔA_y	A_{yy}	ΔA_{yy}	A_{zz}	ΔA_{zz}
2.50	2.38	2.63	1.25	7.90	1.50	7.86	+0.012	0.053	+0.014	0.072	+0.040	0.072
2.75	2.63	2.88	1.50	7.86	1.73	7.76	+0.046	0.032	−0.012	0.045	+0.059	0.044
3.00	2.88	3.13	1.73	7.76	1.94	7.64	+0.050	0.024	−0.012	0.033	+0.106	0.031
3.25	3.13	3.38	1.94	7.64	2.15	7.50	+0.032	0.019	−0.044	0.027	+0.100	0.025
3.50	3.38	3.63	2.15	7.50	2.35	7.35	+0.038	0.016	−0.027	0.023	+0.099	0.021
3.75	3.63	3.88	2.35	7.35	2.54	7.19	+0.045	0.014	−0.004	0.020	+0.100	0.019
4.00	3.88	4.13	2.54	7.19	2.73	7.02	+0.037	0.013	−0.016	0.018	+0.094	0.017
4.25	4.13	4.38	2.73	7.02	2.91	6.85	+0.027	0.012	−0.012	0.017	+0.077	0.016
4.50	4.38	4.63	2.91	6.85	3.09	6.68	+0.030	0.013	+0.002	0.018	+0.075	0.016
4.75	4.63	4.88	3.09	6.68	3.27	6.50	+0.021	0.012	+0.002	0.017	+0.074	0.016
5.00	4.88	5.13	3.27	6.50	3.45	6.33	+0.022	0.012	+0.011	0.016	+0.061	0.015
5.25	5.13	5.38	3.45	6.33	3.62	6.15	+0.013	0.012	+0.000	0.017	+0.066	0.015
5.50	5.38	5.63	3.62	6.15	3.80	5.97	+0.008	0.012	−0.020	0.017	+0.051	0.016
5.75	5.63	5.88	3.80	5.97	3.97	5.78	+0.018	0.012	−0.011	0.017	+0.041	0.016
6.00	5.88	6.13	3.97	5.78	4.14	5.60	+0.028	0.012	+0.002	0.017	+0.040	0.016
6.25	6.13	6.38	4.14	5.60	4.31	5.42	+0.009	0.012	+0.010	0.017	+0.034	0.016
6.50	6.38	6.63	4.31	5.42	4.48	5.23	+0.011	0.013	−0.001	0.018	+0.038	0.017
6.75	6.63	6.88	4.48	5.23	4.64	5.05	+0.022	0.013	−0.005	0.019	+0.029	0.018
7.00	6.88	7.13	4.64	5.05	4.81	4.86	+0.026	0.014	−0.005	0.020	+0.003	0.019
7.25	7.13	7.38	4.81	4.86	4.98	4.68	+0.014	0.015	−0.007	0.021	−0.001	0.020
7.50	7.38	7.63	4.98	4.68	5.15	4.49	+0.008	0.016	−0.011	0.022	+0.004	0.021
7.75	7.63	7.88	5.15	4.49	5.31	4.30	+0.005	0.017	−0.002	0.023	−0.017	0.023
8.00	7.88	8.13	5.31	4.30	5.48	4.12	+0.012	0.018	+0.034	0.025	−0.020	0.024
8.25	8.13	8.38	5.48	4.12	5.64	3.93	+0.015	0.020	+0.047	0.027	−0.026	0.026
8.50	8.38	8.63	5.64	3.93	5.81	3.74	+0.026	0.022	+0.023	0.030	−0.053	0.030
8.75	8.63	8.88	5.81	3.74	5.97	3.55	+0.027	0.024	+0.029	0.033	−0.076	0.033
9.00	8.88	9.13	5.97	3.55	6.14	3.36	+0.003	0.027	+0.002	0.038	−0.063	0.037
9.25	9.13	9.38	6.14	3.36	6.30	3.17	+0.016	0.031	+0.032	0.043	−0.120	0.042
9.50	9.38	9.63	6.30	3.17	6.46	2.98	+0.030	0.035	+0.063	0.048	−0.183	0.049
9.75	9.63	9.88	6.46	2.98	6.62	2.79	+0.006	0.044	+0.058	0.060	−0.142	0.057
10.00	9.88	10.13	6.62	2.79	6.78	2.60	+0.010	0.058	+0.065	0.080	−0.095	0.069
10.25	10.13	10.38	6.78	2.60	6.94	2.40	+0.044	0.074	+0.093	0.099	−0.146	0.092
10.50	10.38	10.63	6.94	2.40	7.10	2.21	+0.002	0.093	+0.089	0.126	−0.232	0.126

Table A.3: Analyzing powers along the locus S in 250 keV steps for $D(\vec{d}, dp)n$ with (θ_d,θ_p)=(+17.0°, −17.0°). Arc length and energy ranges given in MeV. The uncertainty in the analyzing powers is understood to be ± everywhere.

Deuteron-Proton coincidence at θ_d= +17.0° and θ_p= −34.5°												
Arc Length			Coordinates				Analyzing Powers					
			S_{min}		S_{max}							
S	S_{min}	S_{max}	E_d	E_p	E_d	E_p	A_y	ΔA_y	A_{yy}	ΔA_{yy}	A_{zz}	ΔA_{zz}
4.75	4.63	4.88	3.76	5.62	3.96	5.48	−0.034	0.077	−0.018	0.109	−0.134	0.105
5.00	4.88	5.13	3.96	5.48	4.17	5.34	+0.058	0.075	+0.006	0.104	−0.167	0.106
5.25	5.13	5.38	4.17	5.34	4.37	5.19	+0.070	0.072	+0.077	0.096	−0.194	0.095
5.50	5.38	5.63	4.37	5.19	4.57	5.03	−0.012	0.064	+0.063	0.087	−0.155	0.092
5.75	5.63	5.88	4.57	5.03	4.76	4.88	+0.079	0.063	+0.163	0.081	−0.149	0.093
6.00	5.88	6.13	4.76	4.88	4.95	4.72	+0.004	0.061	+0.161	0.079	−0.223	0.086
6.25	6.13	6.38	4.95	4.72	5.14	4.55	−0.055	0.061	+0.159	0.080	−0.203	0.085
6.50	6.38	6.63	5.14	4.55	5.33	4.39	+0.038	0.059	+0.109	0.080	+0.007	0.076
6.75	6.63	6.88	5.33	4.39	5.52	4.22	+0.071	0.057	+0.142	0.075	−0.083	0.079
7.00	6.88	7.13	5.52	4.22	5.70	4.05	+0.098	0.055	+0.095	0.074	−0.208	0.081
7.25	7.13	7.38	5.70	4.05	5.88	3.88	+0.019	0.054	+0.175	0.071	−0.203	0.080
7.50	7.38	7.63	5.88	3.88	6.06	3.71	−0.004	0.058	+0.151	0.076	−0.133	0.079
7.75	7.63	7.88	6.06	3.71	6.24	3.53	+0.049	0.058	+0.034	0.079	−0.143	0.079
8.00	7.88	8.13	6.24	3.53	6.42	3.35	+0.056	0.056	−0.037	0.080	−0.175	0.081
8.25	8.13	8.38	6.42	3.35	6.60	3.18	+0.093	0.061	+0.023	0.084	−0.074	0.083
8.50	8.38	8.63	6.60	3.18	6.77	3.00	+0.007	0.061	+0.120	0.082	−0.168	0.089
8.75	8.63	8.88	6.77	3.00	6.94	2.81	+0.050	0.065	+0.175	0.084	−0.255	0.093
9.00	8.88	9.13	6.94	2.81	7.11	2.63	−0.027	0.068	+0.105	0.090	−0.239	0.093
9.25	9.13	9.38	7.11	2.63	7.28	2.44	+0.003	0.073	+0.064	0.099	−0.278	0.104
9.50	9.38	9.63	7.28	2.44	7.44	2.25	−0.009	0.078	+0.104	0.105	−0.342	0.120
9.75	9.63	9.88	7.44	2.25	7.60	2.06	−0.014	0.088	+0.064	0.121	−0.141	0.116
10.00	9.88	10.13	7.60	2.06	7.76	1.87	+0.013	0.095	+0.063	0.130	−0.120	0.130
10.25	10.13	10.38	7.76	1.87	7.92	1.67	−0.003	0.105	+0.197	0.136	−0.258	0.141
10.50	10.38	10.63	7.92	1.67	8.06	1.47	+0.075	0.117	+0.096	0.154	−0.245	0.164

Table A.4: Analyzing powers along the locus S in 250 keV steps for D($\vec{d}, dp$)n with (θ_d,θ_p)=(+17.0°, −34.5°). Arc length and energy ranges given in MeV. The uncertainty in the analyzing powers is understood to be ± everywhere.

Deuteron-Proton coincidence at θ_d= +19.4° and θ_p= −19.4°												
Arc Length			Coordinates				Analyzing Powers					
			S_{min}		S_{max}							
S	S_{min}	S_{max}	E_d	E_p	E_d	E_p	A_y	ΔA_y	A_{yy}	ΔA_{yy}	A_{zz}	ΔA_{zz}
2.50	2.38	2.63	0.79	7.44	0.96	7.62	−0.251	0.261	+0.230	0.282	−0.209	0.185
2.75	2.63	2.88	0.96	7.62	1.18	7.73	+0.010	0.147	+0.031	0.201	−0.135	0.121
3.00	2.88	3.13	1.18	7.73	1.42	7.75	+0.008	0.135	+0.174	0.168	−0.010	0.116
3.25	3.13	3.38	1.42	7.75	1.66	7.69	+0.104	0.100	+0.107	0.132	+0.125	0.083
3.50	3.38	3.63	1.66	7.69	1.89	7.59	+0.028	0.062	+0.081	0.081	+0.118	0.058
3.75	3.63	3.88	1.89	7.59	2.11	7.47	+0.035	0.046	−0.012	0.065	+0.075	0.046
4.00	3.88	4.13	2.11	7.47	2.31	7.33	+0.058	0.038	+0.003	0.053	+0.088	0.037
4.25	4.13	4.38	2.31	7.33	2.51	7.17	+0.043	0.032	+0.030	0.045	+0.121	0.031
4.50	4.38	4.63	2.51	7.17	2.70	7.02	+0.051	0.028	+0.011	0.040	+0.111	0.028
4.75	4.63	4.88	2.70	7.02	2.89	6.85	+0.030	0.025	−0.020	0.036	+0.085	0.026
5.00	4.88	5.13	2.89	6.85	3.08	6.68	+0.025	0.025	−0.014	0.035	+0.057	0.027
5.25	5.13	5.38	3.08	6.68	3.26	6.51	+0.025	0.024	+0.014	0.034	+0.039	0.025
5.50	5.38	5.63	3.26	6.51	3.44	6.33	+0.023	0.024	−0.006	0.033	+0.012	0.025
5.75	5.63	5.88	3.44	6.33	3.61	6.16	+0.040	0.023	−0.024	0.033	+0.047	0.024
6.00	5.88	6.13	3.61	6.16	3.79	5.98	+0.029	0.023	−0.007	0.032	+0.034	0.024
6.25	6.13	6.38	3.79	5.98	3.96	5.80	+0.021	0.024	+0.016	0.033	+0.065	0.024
6.50	6.38	6.63	3.96	5.80	4.13	5.62	+0.005	0.024	+0.010	0.034	+0.049	0.024
6.75	6.63	6.88	4.13	5.62	4.30	5.43	+0.007	0.025	+0.008	0.034	+0.019	0.025
7.00	6.88	7.13	4.30	5.43	4.47	5.25	+0.008	0.025	−0.010	0.035	+0.021	0.025
7.25	7.13	7.38	4.47	5.25	4.64	5.06	+0.018	0.026	+0.018	0.036	+0.000	0.026
7.50	7.38	7.63	4.64	5.06	4.80	4.87	+0.013	0.026	+0.027	0.037	−0.007	0.028
7.75	7.63	7.88	4.80	4.87	4.97	4.69	+0.019	0.028	+0.014	0.039	+0.020	0.029
8.00	7.88	8.13	4.97	4.69	5.13	4.50	+0.032	0.030	+0.038	0.041	−0.001	0.030
8.25	8.13	8.38	5.13	4.50	5.30	4.31	+0.042	0.032	+0.018	0.044	−0.026	0.033
8.50	8.38	8.63	5.30	4.31	5.46	4.12	+0.041	0.034	+0.026	0.048	−0.040	0.035
8.75	8.63	8.88	5.46	4.12	5.62	3.93	+0.003	0.037	+0.047	0.051	−0.069	0.038
9.00	8.88	9.13	5.62	3.93	5.78	3.74	−0.001	0.040	+0.024	0.056	−0.082	0.042
9.25	9.13	9.38	5.78	3.74	5.94	3.55	+0.001	0.044	+0.019	0.061	−0.055	0.045
9.50	9.38	9.63	5.94	3.55	6.10	3.35	+0.030	0.049	+0.043	0.066	−0.080	0.050
9.75	9.63	9.88	6.10	3.35	6.26	3.16	−0.035	0.055	−0.045	0.077	−0.097	0.056
10.00	9.88	10.13	6.26	3.16	6.42	2.96	−0.036	0.060	+0.006	0.084	−0.140	0.065
10.25	10.13	10.38	6.42	2.96	6.57	2.77	−0.042	0.075	−0.010	0.104	−0.107	0.071

Table A.5: Analyzing powers along the locus S in 250 keV steps for D$(\vec{d}, dp)n$ with (θ_d,θ_p)=(+19.4°, −19.4°). Arc length and energy ranges given in MeV. The uncertainty in the analyzing powers is understood to be ± everywhere.

Deuteron-Proton coincidence at θ_d= +34.5° and θ_p= −17.0°												
Arc Length			Coordinates				Analyzing Powers					
			S_{min}		S_{max}							
S	S_{min}	S_{max}	E_d	E_p	E_d	E_p	A_y	ΔA_y	A_{yy}	ΔA_{yy}	A_{zz}	ΔA_{zz}
2.25	2.13	2.38	4.98	1.61	5.00	1.86	−0.032	0.153	+0.012	0.208	+0.069	0.209
2.50	2.38	2.63	5.00	1.86	4.98	2.11	+0.158	0.136	+0.064	0.187	+0.037	0.176
2.75	2.63	2.88	4.98	2.11	4.94	2.35	−0.037	0.128	+0.095	0.172	+0.135	0.155
3.00	2.88	3.13	4.94	2.35	4.88	2.60	−0.044	0.116	−0.135	0.173	+0.013	0.142
3.25	3.13	3.38	4.88	2.60	4.81	2.83	−0.034	0.096	+0.070	0.132	+0.079	0.118
3.50	3.38	3.63	4.81	2.83	4.72	3.07	+0.050	0.089	+0.037	0.124	+0.086	0.110
3.75	3.63	3.88	4.72	3.07	4.63	3.30	+0.031	0.079	+0.046	0.110	−0.119	0.104
4.00	3.88	4.13	4.63	3.30	4.53	3.53	−0.054	0.074	−0.035	0.106	−0.167	0.097
4.25	4.13	4.38	4.53	3.53	4.42	3.75	−0.020	0.068	−0.034	0.098	−0.003	0.084
4.50	4.38	4.63	4.42	3.75	4.31	3.98	+0.060	0.062	+0.035	0.087	−0.063	0.082
4.75	4.63	4.88	4.31	3.98	4.19	4.20	+0.030	0.057	−0.028	0.081	−0.137	0.077
5.00	4.88	5.13	4.19	4.20	4.07	4.42	−0.022	0.053	−0.044	0.075	−0.068	0.068
5.25	5.13	5.38	4.07	4.42	3.94	4.63	+0.016	0.050	−0.063	0.072	−0.025	0.066
5.50	5.38	5.63	3.94	4.63	3.81	4.85	+0.000	0.048	−0.019	0.068	−0.053	0.064
5.75	5.63	5.88	3.81	4.85	3.68	5.06	−0.017	0.043	+0.060	0.060	−0.111	0.058
6.00	5.88	6.13	3.68	5.06	3.55	5.27	+0.013	0.041	−0.001	0.059	−0.040	0.055
6.25	6.13	6.38	3.55	5.27	3.41	5.48	+0.040	0.038	−0.014	0.055	+0.005	0.051
6.50	6.38	6.63	3.41	5.48	3.27	5.68	+0.032	0.038	−0.033	0.054	−0.032	0.050
6.75	6.63	6.88	3.27	5.68	3.12	5.89	+0.005	0.037	+0.009	0.051	+0.030	0.047
7.00	6.88	7.13	3.12	5.89	2.97	6.09	−0.022	0.034	+0.023	0.048	+0.010	0.045
7.25	7.13	7.38	2.97	6.09	2.82	6.29	−0.018	0.034	−0.029	0.049	+0.004	0.044
7.50	7.38	7.63	2.82	6.29	2.66	6.48	+0.007	0.034	−0.004	0.047	+0.001	0.044
7.75	7.63	7.88	2.66	6.48	2.50	6.67	−0.006	0.033	−0.003	0.047	+0.021	0.043
8.00	7.88	8.13	2.50	6.67	2.33	6.86	−0.026	0.034	+0.033	0.048	+0.031	0.043
8.25	8.13	8.38	2.33	6.86	2.16	7.03	−0.020	0.036	−0.054	0.052	+0.061	0.045
8.50	8.38	8.63	2.16	7.03	1.97	7.20	−0.019	0.037	−0.034	0.054	+0.048	0.046
8.75	8.63	8.88	1.97	7.20	1.78	7.36	−0.025	0.044	+0.049	0.061	−0.048	0.055
9.00	8.88	9.13	1.78	7.36	1.56	7.48	−0.009	0.050	+0.017	0.071	+0.021	0.063
9.25	9.13	9.38	1.56	7.48	1.33	7.56	−0.016	0.068	−0.017	0.096	+0.035	0.086
9.50	9.38	9.63	1.33	7.56	1.09	7.56	+0.025	0.110	+0.199	0.142	+0.019	0.151

Table A.6: Analyzing powers along the locus S in 250 keV steps for D$(\vec{d}, dp)n$ with (θ_d,θ_p)=(+34.5°, −17.0°). Arc length and energy ranges given in MeV. The uncertainty in the analyzing powers is understood to be ± everywhere.

Deuteron-Neutron coincidence at θ_d= +17.0° and θ_n= −17.0°												
Arc Length			Coordinates				Analyzing Powers					
			S_{min}		S_{max}							
S	S_{min}	S_{max}	E_d	E_n	E_d	E_n	A_y	ΔA_y	A_{yy}	ΔA_{yy}	A_{zz}	ΔA_{zz}
4.00	3.88	4.13	2.54	7.19	2.73	7.02	+0.039	0.014	−0.002	0.020	+0.094	0.018
4.25	4.13	4.38	2.73	7.02	2.91	6.85	+0.033	0.013	−0.000	0.019	+0.075	0.016
4.50	4.38	4.63	2.91	6.85	3.09	6.68	+0.029	0.012	+0.003	0.017	+0.073	0.015
4.75	4.63	4.88	3.09	6.68	3.27	6.50	+0.020	0.012	−0.002	0.017	+0.076	0.015
5.00	4.88	5.13	3.27	6.50	3.45	6.33	+0.022	0.011	+0.003	0.015	+0.080	0.013
5.25	5.13	5.38	3.45	6.33	3.62	6.15	+0.023	0.011	+0.007	0.015	+0.077	0.013
5.50	5.38	5.63	3.62	6.15	3.79	5.97	+0.025	0.010	+0.001	0.014	+0.064	0.013
5.75	5.63	5.88	3.79	5.97	3.97	5.79	+0.027	0.010	−0.006	0.015	+0.044	0.013
6.00	5.88	6.13	3.97	5.79	4.14	5.60	+0.030	0.010	−0.004	0.015	+0.042	0.013
6.25	6.13	6.38	4.14	5.60	4.31	5.42	+0.032	0.010	+0.003	0.015	+0.049	0.013
6.50	6.38	6.63	4.31	5.42	4.47	5.24	+0.021	0.011	−0.008	0.015	+0.034	0.013
6.75	6.63	6.88	4.47	5.24	4.64	5.05	+0.019	0.011	−0.000	0.015	+0.023	0.014
7.00	6.88	7.13	4.64	5.05	4.81	4.86	+0.024	0.012	−0.011	0.016	+0.029	0.014
7.25	7.13	7.38	4.81	4.86	4.98	4.68	+0.024	0.013	+0.006	0.018	+0.031	0.015
7.50	7.38	7.63	4.98	4.68	5.14	4.49	+0.008	0.013	+0.013	0.018	+0.007	0.016
7.75	7.63	7.88	5.14	4.49	5.31	4.30	+0.007	0.014	+0.009	0.020	−0.011	0.018
8.00	7.88	8.13	5.31	4.30	5.48	4.12	+0.026	0.016	−0.001	0.022	−0.022	0.020
8.25	8.13	8.38	5.48	4.12	5.64	3.93	+0.025	0.018	+0.001	0.025	−0.025	0.023
8.50	8.38	8.63	5.64	3.93	5.81	3.74	+0.011	0.020	+0.024	0.028	−0.040	0.026
8.75	8.63	8.88	5.81	3.74	5.97	3.55	+0.001	0.023	+0.010	0.033	−0.060	0.031
9.00	8.88	9.13	5.97	3.55	6.13	3.36	+0.017	0.027	+0.028	0.037	−0.095	0.036
9.25	9.13	9.38	6.13	3.36	6.30	3.17	+0.025	0.032	+0.011	0.044	−0.127	0.044
9.50	9.38	9.63	6.30	3.17	6.46	2.98	+0.008	0.043	−0.007	0.060	−0.134	0.056
9.75	9.63	9.88	6.46	2.98	6.62	2.79	−0.044	0.059	+0.077	0.080	−0.163	0.075

Table A.7: Analyzing powers along the locus S in 250 keV steps for $D(\vec{d}, dn)^1H$ with $(\theta_d,\theta_n)=(+17.0°, -17.0°)$. Arc length and energy ranges given in MeV. The uncertainty in the analyzing powers is understood to be ± everywhere.

Deuteron-Neutron coincidence at θ_d= +17.0° and θ_n= −34.5°												
Arc Length			Coordinates				Analyzing Powers					
			S_{min}		S_{max}							
S	S_{min}	S_{max}	E_d	E_n	E_d	E_n	A_y	ΔA_y	A_{yy}	ΔA_{yy}	A_{zz}	ΔA_{zz}
2.50	2.38	2.63	1.67	6.11	1.90	6.20	−0.064	0.061	−0.079	0.087	−0.055	0.113
2.75	2.63	2.88	1.90	6.20	2.14	6.23	−0.097	0.074	−0.018	0.104	−0.047	0.156
3.00	2.88	3.13	2.14	6.23	2.39	6.22	−0.019	0.082	+0.068	0.114	−0.021	0.182
3.25	3.13	3.38	2.39	6.22	2.63	6.17	+0.071	0.104	−0.056	0.149	−0.038	0.180
3.50	3.38	3.63	2.63	6.17	2.87	6.09	+0.221	0.137	−0.123	0.190	+0.041	0.186
3.75	3.63	3.88	2.87	6.09	3.10	5.99	−0.080	0.082	+0.028	0.114	−0.037	0.152
4.00	3.88	4.13	3.10	5.99	3.32	5.88	−0.066	0.061	+0.023	0.086	−0.026	0.120
4.25	4.13	4.38	3.32	5.88	3.54	5.75	+0.009	0.058	−0.008	0.082	−0.008	0.113
4.50	4.38	4.63	3.54	5.75	3.75	5.62	+0.028	0.055	−0.035	0.078	−0.149	0.117
4.75	4.63	4.88	3.75	5.62	3.96	5.48	+0.012	0.054	+0.024	0.074	−0.113	0.106
5.00	4.88	5.13	3.96	5.48	4.16	5.34	+0.051	0.049	+0.062	0.067	−0.029	0.094
5.25	5.13	5.38	4.16	5.34	4.37	5.19	+0.017	0.045	+0.094	0.061	−0.070	0.087
5.50	5.38	5.63	4.37	5.19	4.56	5.04	−0.002	0.040	+0.103	0.055	−0.068	0.078
5.75	5.63	5.88	4.56	5.04	4.76	4.88	+0.004	0.038	+0.049	0.052	−0.032	0.074
6.00	5.88	6.13	4.76	4.88	4.95	4.72	+0.003	0.037	+0.027	0.051	−0.016	0.073
6.25	6.13	6.38	4.95	4.72	5.14	4.56	+0.026	0.034	+0.123	0.046	−0.030	0.070
6.50	6.38	6.63	5.14	4.56	5.33	4.39	+0.016	0.033	+0.094	0.045	−0.123	0.069
6.75	6.63	6.88	5.33	4.39	5.51	4.22	+0.015	0.034	+0.097	0.045	−0.184	0.069
7.00	6.88	7.13	5.51	4.22	5.70	4.05	+0.017	0.033	+0.136	0.045	−0.097	0.064
7.25	7.13	7.38	5.70	4.05	5.88	3.88	−0.008	0.034	+0.153	0.045	−0.092	0.065
7.50	7.38	7.63	5.88	3.88	6.06	3.71	−0.009	0.034	+0.145	0.046	−0.141	0.070
7.75	7.63	7.88	6.06	3.71	6.24	3.53	+0.053	0.035	+0.137	0.047	−0.101	0.072
8.00	7.88	8.13	6.24	3.53	6.42	3.36	+0.038	0.036	+0.104	0.049	−0.059	0.070
8.25	8.13	8.38	6.42	3.36	6.59	3.18	−0.009	0.036	+0.103	0.049	−0.152	0.072
8.50	8.38	8.63	6.59	3.18	6.77	3.00	+0.055	0.040	+0.066	0.055	−0.218	0.085
8.75	8.63	8.88	6.77	3.00	6.94	2.81	+0.105	0.044	+0.173	0.058	−0.156	0.088
9.00	8.88	9.13	6.94	2.81	7.11	2.63	+0.070	0.049	+0.193	0.065	−0.145	0.096
9.25	9.13	9.38	7.11	2.63	7.28	2.45	+0.019	0.057	+0.096	0.077	−0.178	0.106
9.50	9.38	9.63	7.28	2.45	7.44	2.26	+0.000	0.062	+0.131	0.085	−0.121	0.120
9.75	9.63	9.88	7.44	2.26	7.60	2.07	−0.021	0.076	+0.018	0.105	−0.234	0.139

Table A.8: Analyzing powers along the locus S in 250 keV steps for D$(\vec{d}, dn)^1$H with (θ_d,θ_n)=(+17.0°, −34.5°). Arc length and energy ranges given in MeV. The uncertainty in the analyzing powers is understood to be ± everywhere.

Deuteron-Neutron coincidence at θ_d= +19.4° and θ_n= −28.9°												
Arc Length			Coordinates				Analyzing Powers					
			S_{min}		S_{max}							
S	S_{min}	S_{max}	E_d	E_n	E_d	E_n	A_y	ΔA_y	A_{yy}	ΔA_{yy}	A_{zz}	ΔA_{zz}
4.25	4.13	4.38	2.62	6.69	2.84	6.57	+0.050	0.056	+0.052	0.076	+0.087	0.069
4.50	4.38	4.63	2.84	6.57	3.06	6.43	+0.050	0.052	+0.030	0.072	+0.058	0.064
4.75	4.63	4.88	3.06	6.43	3.26	6.29	+0.029	0.042	+0.054	0.059	+0.070	0.053
5.00	4.88	5.13	3.26	6.29	3.46	6.15	+0.055	0.038	+0.044	0.052	+0.081	0.044
5.25	5.13	5.38	3.46	6.15	3.66	5.99	+0.049	0.033	+0.049	0.045	+0.055	0.038
5.50	5.38	5.63	3.66	5.99	3.85	5.83	+0.028	0.030	+0.061	0.041	+0.083	0.034
5.75	5.63	5.88	3.85	5.83	4.04	5.67	+0.049	0.027	+0.055	0.037	+0.083	0.031
6.00	5.88	6.13	4.04	5.67	4.23	5.51	+0.058	0.025	+0.068	0.034	+0.010	0.030
6.25	6.13	6.38	4.23	5.51	4.42	5.34	+0.063	0.025	+0.082	0.033	−0.001	0.029
6.50	6.38	6.63	4.42	5.34	4.60	5.16	+0.073	0.024	+0.104	0.032	+0.009	0.028
6.75	6.63	6.88	4.60	5.16	4.78	4.99	+0.048	0.024	+0.084	0.032	−0.000	0.027
7.00	6.88	7.13	4.78	4.99	4.96	4.82	+0.035	0.023	+0.050	0.032	−0.034	0.028
7.25	7.13	7.38	4.96	4.82	5.14	4.64	+0.040	0.024	+0.066	0.032	−0.060	0.027
7.50	7.38	7.63	5.14	4.64	5.31	4.46	+0.060	0.024	+0.095	0.032	−0.063	0.028
7.75	7.63	7.88	5.31	4.46	5.48	4.28	+0.045	0.026	+0.081	0.035	−0.061	0.030
8.00	7.88	8.13	5.48	4.28	5.66	4.10	+0.060	0.028	+0.119	0.037	−0.074	0.032
8.25	8.13	8.38	5.66	4.10	5.83	3.91	+0.046	0.029	+0.084	0.039	−0.125	0.035
8.50	8.38	8.63	5.83	3.91	5.99	3.73	+0.052	0.033	+0.124	0.043	−0.119	0.038
8.75	8.63	8.88	5.99	3.73	6.16	3.54	+0.033	0.033	+0.105	0.044	−0.104	0.039
9.00	8.88	9.13	6.16	3.54	6.33	3.36	−0.006	0.037	+0.080	0.050	−0.189	0.046
9.25	9.13	9.38	6.33	3.36	6.49	3.17	+0.035	0.043	+0.087	0.057	−0.176	0.051
9.50	9.38	9.63	6.49	3.17	6.65	2.98	+0.058	0.049	+0.183	0.064	−0.283	0.065
9.75	9.63	9.88	6.65	2.98	6.81	2.79	+0.029	0.068	+0.044	0.091	−0.225	0.072
10.00	9.88	10.13	6.81	2.79	6.97	2.59	+0.071	0.073	+0.151	0.096	−0.253	0.094

Table A.9: Analyzing powers along the locus S in 250 keV steps for $D(\vec{d}, dn)^1H$ with (θ_d,θ_n)=(+19.4°, −28.9°). Arc length and energy ranges given in MeV. The uncertainty in the analyzing powers is understood to be ± everywhere.

Proton-Neutron coincidence at $\theta_p = +17.0°$ and $\theta_n = -17.0°$												
Arc Length			Coordinates				Analyzing Powers					
			S_{min}		S_{max}							
S	S_{min}	S_{max}	E_p	E_n	E_p	E_n	A_y	ΔA_y	A_{yy}	ΔA_{yy}	A_{zz}	ΔA_{zz}
4.00	3.88	4.13	2.50	6.83	2.70	6.67	+0.039	0.035	+0.064	0.048	−0.073	0.048
4.25	4.13	4.38	2.70	6.67	2.89	6.51	+0.027	0.034	+0.078	0.045	−0.080	0.051
4.50	4.38	4.63	2.89	6.51	3.07	6.35	+0.010	0.034	+0.064	0.046	−0.066	0.049
4.75	4.63	4.88	3.07	6.35	3.26	6.18	+0.014	0.032	+0.017	0.044	−0.036	0.045
5.00	4.88	5.13	3.26	6.18	3.45	6.01	+0.016	0.030	+0.020	0.042	+0.014	0.043
5.25	5.13	5.38	3.45	6.01	3.63	5.84	+0.021	0.030	+0.047	0.041	+0.001	0.042
5.50	5.38	5.63	3.63	5.84	3.81	5.67	+0.021	0.029	+0.044	0.040	−0.064	0.040
5.75	5.63	5.88	3.81	5.67	3.99	5.50	+0.011	0.029	+0.032	0.040	−0.053	0.040
6.00	5.88	6.13	3.99	5.50	4.17	5.33	−0.023	0.028	+0.036	0.039	−0.017	0.039
6.25	6.13	6.38	4.17	5.33	4.35	5.15	−0.009	0.029	+0.053	0.040	+0.011	0.038
6.50	6.38	6.63	4.35	5.15	4.53	4.98	+0.018	0.028	+0.060	0.039	+0.032	0.036
6.75	6.63	6.88	4.53	4.98	4.71	4.80	+0.025	0.028	+0.055	0.039	+0.018	0.038
7.00	6.88	7.13	4.71	4.80	4.89	4.62	+0.067	0.029	+0.024	0.040	−0.020	0.040
7.25	7.13	7.38	4.89	4.62	5.06	4.45	+0.057	0.028	−0.001	0.039	−0.011	0.040
7.50	7.38	7.63	5.06	4.45	5.24	4.27	+0.010	0.029	+0.053	0.040	+0.024	0.040
7.75	7.63	7.88	5.24	4.27	5.41	4.09	+0.005	0.030	+0.025	0.041	+0.006	0.041
8.00	7.88	8.13	5.41	4.09	5.58	3.91	+0.012	0.033	−0.000	0.045	−0.036	0.042
8.25	8.13	8.38	5.58	3.91	5.75	3.73	−0.011	0.033	−0.011	0.046	−0.028	0.044
8.50	8.38	8.63	5.75	3.73	5.92	3.54	−0.058	0.034	+0.047	0.047	−0.016	0.046
8.75	8.63	8.88	5.92	3.54	6.09	3.36	−0.032	0.036	+0.001	0.050	+0.009	0.047
9.00	8.88	9.13	6.09	3.36	6.26	3.17	−0.020	0.037	−0.021	0.051	−0.043	0.051
9.25	9.13	9.38	6.26	3.17	6.42	2.99	+0.011	0.040	+0.006	0.055	−0.074	0.052
9.50	9.38	9.63	6.42	2.99	6.59	2.80	+0.001	0.043	+0.026	0.060	−0.083	0.059
9.75	9.63	9.88	6.59	2.80	6.75	2.61	−0.045	0.047	+0.102	0.063	+0.004	0.065
10.00	9.88	10.13	6.75	2.61	6.91	2.41	−0.072	0.056	+0.118	0.075	−0.044	0.067
10.25	10.13	10.38	6.91	2.41	7.07	2.22	−0.013	0.075	+0.187	0.100	+0.008	0.089
10.50	10.38	10.63	7.07	2.22	7.22	2.02	−0.069	0.096	+0.321	0.125	−0.003	0.119

Table A.10: Analyzing powers along the locus S in 250 keV steps for D$(\vec{d}, pn)$D with (θ_p,θ_n)=$(+17.0°, -17.0°)$. Arc length and energy ranges given in MeV. The uncertainty in the analyzing powers is understood to be $\pm$ everywhere.

Proton-Neutron coincidence at $\theta_p = +17.0°$ and $\theta_n = -34.5°$												
Arc Length			Coordinates				Analyzing Powers					
			S_{min}		S_{max}							
S	S_{min}	S_{max}	E_p	E_n	E_p	E_n	A_y	ΔA_y	A_{yy}	ΔA_{yy}	A_{zz}	ΔA_{zz}
5.00	4.88	5.13	2.68	5.79	2.89	5.66	−0.038	0.109	+0.144	0.149	−0.006	0.226
5.25	5.13	5.38	2.89	5.66	3.10	5.53	−0.055	0.093	−0.197	0.136	−0.028	0.179
5.50	5.38	5.63	3.10	5.53	3.31	5.38	−0.011	0.066	−0.108	0.094	−0.060	0.137
5.75	5.63	5.88	3.31	5.38	3.51	5.24	−0.002	0.056	−0.017	0.078	−0.053	0.116
6.00	5.88	6.13	3.51	5.24	3.71	5.09	−0.003	0.052	+0.077	0.072	−0.060	0.108
6.25	6.13	6.38	3.71	5.09	3.91	4.94	−0.002	0.046	+0.070	0.063	−0.049	0.099
6.50	6.38	6.63	3.91	4.94	4.11	4.79	+0.023	0.043	+0.040	0.060	−0.003	0.089
6.75	6.63	6.88	4.11	4.79	4.31	4.63	+0.017	0.041	+0.006	0.057	+0.047	0.080
7.00	6.88	7.13	4.31	4.63	4.50	4.47	+0.003	0.039	+0.039	0.054	+0.036	0.081
7.25	7.13	7.38	4.50	4.47	4.69	4.31	+0.016	0.038	+0.063	0.052	−0.013	0.078
7.50	7.38	7.63	4.69	4.31	4.88	4.15	−0.000	0.035	+0.054	0.049	+0.014	0.072
7.75	7.63	7.88	4.88	4.15	5.07	3.99	−0.004	0.034	+0.067	0.046	+0.057	0.068
8.00	7.88	8.13	5.07	3.99	5.26	3.82	+0.022	0.033	+0.101	0.046	+0.042	0.070
8.25	8.13	8.38	5.26	3.82	5.44	3.66	+0.051	0.032	+0.098	0.044	−0.011	0.068
8.50	8.38	8.63	5.44	3.66	5.63	3.49	+0.036	0.032	+0.106	0.044	+0.010	0.063
8.75	8.63	8.88	5.63	3.49	5.81	3.32	+0.002	0.032	+0.077	0.044	+0.034	0.063
9.00	8.88	9.13	5.81	3.32	5.99	3.14	+0.005	0.032	+0.006	0.044	−0.027	0.065
9.25	9.13	9.38	5.99	3.14	6.17	2.97	−0.021	0.032	+0.020	0.044	−0.009	0.063
9.50	9.38	9.63	6.17	2.97	6.35	2.79	−0.001	0.032	+0.014	0.045	−0.039	0.063
9.75	9.63	9.88	6.35	2.79	6.52	2.61	+0.008	0.033	+0.022	0.046	−0.023	0.067
10.00	9.88	10.13	6.52	2.61	6.69	2.43	−0.020	0.034	+0.096	0.047	+0.013	0.067
10.25	10.13	10.38	6.69	2.43	6.86	2.24	+0.018	0.035	+0.068	0.049	−0.008	0.073
10.50	10.38	10.63	6.86	2.24	7.02	2.05	−0.009	0.039	+0.046	0.054	+0.001	0.078
10.75	10.63	10.88	7.02	2.05	7.18	1.86	+0.036	0.046	+0.042	0.063	+0.010	0.085
11.00	10.88	11.13	7.18	1.86	7.33	1.66	+0.021	0.053	+0.014	0.074	+0.032	0.098
11.25	11.13	11.38	7.33	1.66	7.48	1.46	+0.035	0.068	+0.070	0.094	−0.203	0.139
11.50	11.38	11.63	7.48	1.46	7.61	1.25	+0.098	0.111	+0.069	0.153	−0.188	0.218

Table A.11: Analyzing powers along the locus S in 250 keV steps for D$(\vec{d}, pn)$D with (θ_p, θ_n)=(+17.0°, −34.5°). Arc length and energy ranges given in MeV. The uncertainty in the analyzing powers is understood to be ± everywhere.

Proton-Neutron coincidence at θ_p= +19.4° and θ_n= −28.9°												
Arc Length			Coordinates				Analyzing Powers					
			S_{min}		S_{max}							
S	S_{min}	S_{max}	E_p	E_n	E_p	E_n	A_y	ΔA_y	A_{yy}	ΔA_{yy}	A_{zz}	ΔA_{zz}
4.75	4.63	4.88	2.75	6.14	2.95	5.99	+0.014	0.050	+0.027	0.069	+0.033	0.059
5.00	4.88	5.13	2.95	5.99	3.15	5.84	+0.043	0.044	+0.067	0.059	+0.026	0.055
5.25	5.13	5.38	3.15	5.84	3.35	5.69	+0.023	0.040	+0.050	0.055	+0.034	0.050
5.50	5.38	5.63	3.35	5.69	3.55	5.53	−0.001	0.038	+0.047	0.051	+0.033	0.045
5.75	5.63	5.88	3.55	5.53	3.74	5.38	+0.011	0.036	+0.084	0.048	+0.014	0.043
6.00	5.88	6.13	3.74	5.38	3.93	5.22	+0.035	0.033	+0.089	0.045	−0.017	0.041
6.25	6.13	6.38	3.93	5.22	4.12	5.05	+0.021	0.032	+0.057	0.043	−0.039	0.040
6.50	6.38	6.63	4.12	5.05	4.31	4.89	−0.008	0.031	+0.012	0.043	+0.009	0.037
6.75	6.63	6.88	4.31	4.89	4.50	4.72	+0.007	0.031	+0.004	0.042	+0.034	0.036
7.00	6.88	7.13	4.50	4.72	4.68	4.55	+0.047	0.030	+0.022	0.041	+0.017	0.035
7.25	7.13	7.38	4.68	4.55	4.87	4.39	+0.037	0.029	+0.041	0.039	+0.015	0.034
7.50	7.38	7.63	4.87	4.39	5.05	4.21	+0.023	0.028	+0.043	0.038	−0.014	0.035
7.75	7.63	7.88	5.05	4.21	5.23	4.04	+0.017	0.029	+0.031	0.040	−0.018	0.035
8.00	7.88	8.13	5.23	4.04	5.41	3.87	−0.003	0.029	+0.027	0.040	+0.004	0.034
8.25	8.13	8.38	5.41	3.87	5.59	3.69	+0.018	0.029	+0.048	0.039	−0.006	0.034
8.50	8.38	8.63	5.59	3.69	5.76	3.51	+0.007	0.029	+0.001	0.040	+0.005	0.035
8.75	8.63	8.88	5.76	3.51	5.94	3.33	+0.007	0.029	−0.001	0.040	+0.008	0.036
9.00	8.88	9.13	5.94	3.33	6.11	3.15	−0.011	0.030	+0.022	0.041	+0.003	0.036
9.25	9.13	9.38	6.11	3.15	6.28	2.97	−0.006	0.030	+0.042	0.041	+0.017	0.037
9.50	9.38	9.63	6.28	2.97	6.45	2.78	−0.022	0.032	+0.002	0.044	−0.012	0.039
9.75	9.63	9.88	6.45	2.78	6.61	2.59	−0.024	0.033	−0.005	0.046	−0.009	0.042
10.00	9.88	10.13	6.61	2.59	6.78	2.40	−0.004	0.036	+0.049	0.049	+0.013	0.047
10.25	10.13	10.38	6.78	2.40	6.93	2.21	−0.016	0.042	+0.033	0.058	−0.045	0.054
10.50	10.38	10.63	6.93	2.21	7.09	2.01	−0.003	0.050	+0.069	0.068	−0.023	0.065
10.75	10.63	10.88	7.09	2.01	7.24	1.81	+0.023	0.064	+0.059	0.090	−0.019	0.091
11.00	10.88	11.13	7.24	1.81	7.38	1.60	+0.115	0.098	+0.051	0.134	−0.159	0.182
11.25	11.13	11.38	7.38	1.60	7.51	1.38	+0.162	0.202	+0.115	0.267	−0.358	0.720

Table A.12: Analyzing powers along the locus S in 250 keV steps for D($\vec{d}, pn$)D with (θ_p,θ_n)=(+19.4°, −28.9°). Arc length and energy ranges given in MeV. The uncertainty in the analyzing powers is understood to be ± everywhere.

A.2 Analyzing Powers Along S in 750 keV Steps

To reduce the uncertainty in the displayed data, the binning size of the tabulated data was increased to 750 keV from the previous 250 keV bins in section A.1. This was accomplished by the statistical addition of the points from the 250 keV bins in groups of three. The effective centroid for each 750 keV bin was determined by weighting the centroids of the 250 keV bins by the error in A_{zz}. The tabulation of these analyzing powers in 750 keV steps along S is presented in the 12 tables in this section. The quantities used in the tables are defined as follows:

S_{eff} = Effective centroid of the arc segment along the kinematically allowed curve

S_{min} = Lower end of the arc segment spanned by the data point

S_{max} = Upper end of the arc segment spanned by the data point

A_y = Vector analyzing power for the arc segment S_{min}–S_{max}

A_{yy} = Tensor analyzing power for the arc segment S_{min}–S_{max}

A_{zz} = Tensor analyzing power for the arc segment S_{min}–S_{max}

ΔA_y = Absolute uncertainty in A_y

ΔA_{yy} = Absolute uncertainty in A_{yy}

ΔA_{zz} = Absolute uncertainty in A_{zz}.

Deuteron-Proton coincidence at θ_d= +10.0° and θ_p= −10.0°								
Arc Length			Analyzing Powers					
S_{eff}	S_{min}	S_{max}	A_y	ΔA_y	A_{yy}	ΔA_{yy}	A_{zz}	ΔA_{zz}
3.10	2.63	3.38	+0.024	0.034	−0.001	0.048	+0.091	0.045
3.78	3.38	4.13	+0.006	0.020	+0.005	0.028	+0.091	0.028
4.52	4.13	4.88	+0.027	0.017	−0.003	0.024	+0.065	0.024
5.25	4.88	5.63	+0.005	0.017	+0.018	0.023	+0.095	0.023
5.99	5.63	6.38	+0.011	0.018	+0.027	0.024	+0.052	0.025
6.73	6.38	7.13	+0.000	0.020	−0.024	0.028	+0.040	0.028
7.48	7.13	7.88	−0.011	0.024	−0.024	0.035	+0.043	0.034
8.22	7.88	8.63	−0.017	0.031	−0.028	0.044	+0.010	0.045
8.95	8.63	9.38	−0.044	0.047	+0.024	0.065	+0.005	0.063
9.68	9.38	10.13	−0.067	0.086	+0.054	0.113	−0.088	0.105

Table A.13: Analyzing powers along the locus S in 750 keV steps for $^2H(\vec{d}, dp)n$ with (θ_d,θ_p)=(+10.0°, −10.0°). Arc length and energy ranges given in MeV. The uncertainty in the analyzing powers is understood to be ± everywhere. The effective location of S is obtained by weighting the coordinates with the cross sections.

Deuteron-Proton coincidence at θ_d= +10.0° and θ_p= −41.2°								
Arc Length			Analyzing Powers					
S_{eff}	S_{min}	S_{max}	A_y	ΔA_y	A_{yy}	ΔA_{yy}	A_{zz}	ΔA_{zz}
1.55	1.13	1.88	−0.081	0.096	+0.134	0.125	−0.089	0.126
2.30	1.88	2.63	−0.085	0.055	+0.048	0.076	−0.045	0.076
2.99	2.63	3.38	−0.084	0.049	+0.086	0.067	−0.077	0.075
3.76	3.38	4.13	−0.028	0.045	+0.050	0.062	−0.125	0.072
4.49	4.13	4.88	−0.067	0.044	+0.031	0.060	+0.093	0.064
5.26	4.88	5.63	−0.082	0.041	+0.007	0.058	−0.027	0.067
6.01	5.63	6.38	−0.059	0.041	+0.003	0.057	−0.131	0.061
6.76	6.38	7.13	−0.097	0.035	+0.022	0.049	−0.110	0.057
7.51	7.13	7.88	−0.030	0.032	+0.074	0.044	−0.019	0.047
8.27	7.88	8.63	−0.006	0.029	+0.075	0.040	+0.016	0.042
9.00	8.63	9.38	+0.000	0.029	+0.009	0.040	−0.016	0.040
9.75	9.38	10.13	−0.010	0.030	+0.069	0.040	−0.056	0.042
10.43	10.13	10.88	+0.017	0.044	+0.038	0.060	−0.009	0.056

Table A.14: Analyzing powers along the locus S in 750 keV steps for D($\vec{d}, dp$)n with (θ_d,θ_p)=(+10.0°, −41.2°). Arc length and energy ranges given in MeV. The uncertainty in the analyzing powers is understood to be ± everywhere. The effective location of S is obtained by weighting the coordinates with the cross sections.

Deuteron-Proton coincidence at θ_d= +17.0° and θ_p= −17.0°								
Arc Length			Analyzing Powers					
S_{eff}	S_{min}	S_{max}	A_y	ΔA_y	A_{yy}	ΔA_{yy}	A_{zz}	ΔA_{zz}
2.88	2.38	3.13	+0.044	0.018	−0.009	0.025	+0.085	0.024
3.55	3.13	3.88	+0.039	0.009	−0.021	0.013	+0.099	0.012
4.26	3.88	4.63	+0.031	0.007	−0.009	0.010	+0.082	0.010
5.01	4.63	5.38	+0.019	0.007	+0.005	0.010	+0.067	0.009
5.75	5.38	6.13	+0.018	0.007	−0.010	0.010	+0.044	0.009
6.49	6.13	6.88	+0.014	0.007	+0.002	0.010	+0.034	0.010
7.24	6.88	7.63	+0.017	0.008	−0.007	0.012	+0.002	0.011
7.98	7.63	8.38	+0.010	0.010	+0.024	0.014	−0.020	0.014
8.72	8.38	9.13	+0.021	0.014	+0.020	0.019	−0.063	0.019
9.46	9.13	9.88	+0.018	0.021	+0.049	0.028	−0.146	0.028
10.16	9.88	10.63	+0.019	0.041	+0.079	0.056	−0.132	0.051

Table A.15: Analyzing powers along the locus S in 750 keV steps for D$(\vec{d}, dp)n$ with (θ_d,θ_p)=(+17.0°, −17.0°). Arc length and energy ranges given in MeV. The uncertainty in the analyzing powers is understood to be ± everywhere. The effective location of S is obtained by weighting the coordinates with the cross sections.

Deuteron-Proton coincidence at θ_d= +17.0° and θ_p= −34.5°								
Arc Length			Analyzing Powers					
S_{eff}	S_{min}	S_{max}	A_y	ΔA_y	A_{yy}	ΔA_{yy}	A_{zz}	ΔA_{zz}
5.02	4.63	5.38	+0.034	0.043	+0.026	0.059	−0.167	0.059
5.77	5.38	6.13	+0.023	0.036	+0.132	0.048	−0.178	0.052
6.52	6.13	6.88	+0.020	0.034	+0.137	0.045	−0.085	0.046
7.26	6.88	7.63	+0.039	0.032	+0.141	0.042	−0.181	0.046
8.00	7.63	8.38	+0.065	0.034	+0.007	0.047	−0.131	0.047
8.75	8.38	9.13	+0.011	0.037	+0.134	0.049	−0.219	0.053
9.48	9.13	9.88	−0.005	0.046	+0.078	0.062	−0.254	0.065
10.22	9.88	10.63	+0.024	0.060	+0.118	0.080	−0.199	0.083

Table A.16: Analyzing powers along the locus S in 750 keV steps for D$(\vec{d}, dp)n$ with (θ_d,θ_p)=(+17.0°, −34.5°). Arc length and energy ranges given in MeV. The uncertainty in the analyzing powers is understood to be ± everywhere. The effective location of S is obtained by weighting the coordinates with the cross sections.

Deuteron-Proton coincidence at θ_d= +19.4° and θ_p= −19.4°								
Arc Length			Analyzing Powers					
S_{eff}	S_{min}	S_{max}	A_y	ΔA_y	A_{yy}	ΔA_{yy}	A_{zz}	ΔA_{zz}
2.82	2.38	3.13	−0.024	0.093	+0.135	0.117	−0.093	0.076
3.59	3.13	3.88	+0.041	0.035	+0.035	0.047	+0.097	0.033
4.30	3.88	4.63	+0.050	0.019	+0.015	0.026	+0.109	0.018
5.01	4.63	5.38	+0.027	0.014	−0.006	0.020	+0.059	0.015
5.76	5.38	6.13	+0.031	0.013	−0.012	0.019	+0.031	0.014
6.50	6.13	6.88	+0.011	0.014	+0.012	0.019	+0.045	0.014
7.24	6.88	7.63	+0.012	0.015	+0.011	0.021	+0.006	0.015
7.98	7.63	8.38	+0.030	0.017	+0.024	0.024	+0.000	0.018
8.73	8.38	9.13	+0.016	0.021	+0.033	0.030	−0.061	0.022
9.47	9.13	9.88	+0.001	0.028	+0.011	0.039	−0.074	0.029
10.22	9.88	10.63	−0.021	0.040	+0.019	0.056	−0.114	0.041
10.94	9.63	10.38	−0.044	0.069	+0.065	0.092	−0.148	0.076

Table A.17: Analyzing powers along the locus S in 750 keV steps for D($\vec{d}, dp$)n with (θ_d,θ_p)=(+19.4°, −19.4°). Arc length and energy ranges given in MeV. The uncertainty in the analyzing powers is understood to be ± everywhere. The effective location of S is obtained by weighting the coordinates with the cross sections.

Deuteron-Proton coincidence at θ_d= +34.5° and θ_p= −17.0°								
Arc Length			Analyzing Powers					
S_{eff}	S_{min}	S_{max}	A_y	ΔA_y	A_{yy}	ΔA_{yy}	A_{zz}	ΔA_{zz}
2.55	2.13	2.88	+0.031	0.080	+0.063	0.108	+0.087	0.102
3.29	2.88	3.63	−0.002	0.057	+0.012	0.080	+0.065	0.070
4.04	3.63	4.38	−0.017	0.043	−0.010	0.060	−0.086	0.054
4.79	4.38	5.13	+0.018	0.033	−0.016	0.046	−0.088	0.043
5.53	5.13	5.88	−0.002	0.027	+0.001	0.038	−0.067	0.036
6.27	5.88	6.63	+0.029	0.023	−0.017	0.032	−0.021	0.030
7.02	6.63	7.38	−0.012	0.020	+0.001	0.029	+0.014	0.026
7.76	7.38	8.13	−0.008	0.019	+0.008	0.027	+0.018	0.025
8.47	8.13	8.88	−0.021	0.022	−0.019	0.032	+0.029	0.028
9.13	8.88	9.63	−0.007	0.038	+0.032	0.053	+0.025	0.048

Table A.18: Analyzing powers along the locus S in 750 keV steps for D$(\vec{d}, dp)n$ with (θ_d,θ_p)=(+34.5°, −17.0°). Arc length and energy ranges given in MeV. The uncertainty in the analyzing powers is understood to be ± everywhere. The effective location of S is obtained by weighting the coordinates with the cross sections.

Deuteron-Neutron coincidence at θ_d= +17.0° and θ_n= −17.0°								
Arc Length			Analyzing Powers					
S_{eff}	S_{min}	S_{max}	A_y	ΔA_y	A_{yy}	ΔA_{yy}	A_{zz}	ΔA_{zz}
4.28	3.88	4.63	+0.033	0.008	+0.001	0.011	+0.079	0.009
5.03	4.63	5.38	+0.022	0.006	+0.003	0.009	+0.078	0.008
5.75	5.38	6.13	+0.027	0.006	−0.003	0.008	+0.050	0.007
6.49	6.13	6.88	+0.024	0.006	−0.002	0.009	+0.036	0.008
7.23	6.88	7.63	+0.019	0.007	+0.002	0.010	+0.023	0.009
7.97	7.63	8.38	+0.018	0.009	+0.004	0.013	−0.018	0.012
8.70	8.38	9.13	+0.009	0.013	+0.021	0.018	−0.059	0.017
9.42	9.13	9.88	+0.009	0.023	+0.017	0.033	−0.135	0.031

Table A.19: Analyzing powers along the locus S in 750 keV steps for D$(\vec{d}, dn)^1$H with (θ_d,θ_n)=(+17.0°, −17.0°). Arc length and energy ranges given in MeV. The uncertainty in the analyzing powers is understood to be ± everywhere. The effective location of S is obtained by weighting the coordinates with the cross sections.

Deuteron-Neutron coincidence at θ_d= +17.0° and θ_n= −34.5°								
Arc Length			Analyzing Powers					
S_{eff}	S_{min}	S_{max}	A_y	ΔA_y	A_{yy}	ΔA_{yy}	A_{zz}	ΔA_{zz}
2.67	2.38	3.13	−0.063	0.041	−0.022	0.058	−0.046	0.082
3.54	3.13	3.88	+0.022	0.058	−0.025	0.082	−0.016	0.098
4.26	3.88	4.63	−0.006	0.033	−0.008	0.047	−0.060	0.067
5.04	4.63	5.38	+0.027	0.028	+0.065	0.038	−0.068	0.055
5.77	5.38	6.13	+0.002	0.022	+0.058	0.030	−0.037	0.043
6.51	6.13	6.88	+0.019	0.019	+0.105	0.026	−0.114	0.040
7.24	6.88	7.63	+0.000	0.019	+0.145	0.026	−0.108	0.038
8.01	7.63	8.38	+0.028	0.021	+0.115	0.028	−0.103	0.041
8.73	8.38	9.13	+0.075	0.025	+0.137	0.034	−0.175	0.052
9.46	9.13	9.88	+0.003	0.037	+0.090	0.050	−0.173	0.069

Table A.20: Analyzing powers along the locus S in 750 keV steps for D$(\vec{d}, dn)^1$H with (θ_d,θ_n)=(+17.0°, −34.5°). Arc length and energy ranges given in MeV. The uncertainty in the analyzing powers is understood to be ± everywhere. The effective location of S is obtained by weighting the coordinates with the cross sections.

Deuteron-Neutron coincidence at θ_d= +19.4° and θ_n= −28.9°								
Arc Length			Analyzing Powers					
S_{eff}	S_{min}	S_{max}	A_y	ΔA_y	A_{yy}	ΔA_{yy}	A_{zz}	ΔA_{zz}
4.55	4.13	4.88	+0.041	0.028	+0.046	0.039	+0.071	0.035
5.30	4.88	5.63	+0.042	0.019	+0.053	0.026	+0.073	0.022
6.01	5.63	6.38	+0.057	0.015	+0.069	0.020	+0.029	0.017
6.76	6.38	7.13	+0.052	0.014	+0.080	0.018	−0.009	0.016
7.49	7.13	7.88	+0.048	0.014	+0.080	0.019	−0.061	0.017
8.22	7.88	8.63	+0.053	0.017	+0.108	0.023	−0.103	0.020
8.96	8.63	9.38	+0.020	0.021	+0.092	0.029	−0.149	0.026
9.70	9.38	10.13	+0.053	0.035	+0.140	0.046	−0.256	0.043

Table A.21: Analyzing powers along the locus S in 750 keV steps for D$(\vec{d}, dn)^1$H with (θ_d,θ_n)=(+19.4°, −28.9°). Arc length and energy ranges given in MeV. The uncertainty in the analyzing powers is understood to be ± everywhere. The effective location of S is obtained by weighting the coordinates with the cross sections.

Proton-Neutron coincidence at θ_p= +17.0° and θ_n= −17.0°								
Arc Length			Analyzing Powers					
S_{eff}	S_{min}	S_{max}	A_y	ΔA_y	A_{yy}	ΔA_{yy}	A_{zz}	ΔA_{zz}
4.25	3.88	4.63	+0.025	0.020	+0.069	0.027	−0.073	0.028
5.02	4.63	5.38	+0.017	0.018	+0.029	0.024	−0.006	0.025
5.76	5.38	6.13	+0.003	0.016	+0.037	0.023	−0.044	0.023
6.50	6.13	6.88	+0.012	0.016	+0.056	0.023	+0.021	0.022
7.26	6.88	7.63	+0.045	0.017	+0.025	0.023	−0.002	0.023
7.99	7.63	8.38	+0.002	0.018	+0.006	0.025	−0.019	0.024
8.74	8.38	9.13	−0.038	0.021	+0.011	0.028	−0.016	0.028
9.47	9.13	9.88	−0.008	0.025	+0.041	0.034	−0.056	0.033
10.16	9.88	10.63	−0.054	0.041	+0.177	0.054	−0.021	0.049

Table A.22: Analyzing powers along the locus S in 750 keV steps for D$(\vec{d}, pn)$D with (θ_p,θ_n)=(+17.0°, −17.0°). Arc length and energy ranges given in MeV. The uncertainty in the analyzing powers is understood to be ± everywhere. The effective location of S is obtained by weighting the coordinates with the cross sections.

Proton-Neutron coincidence at θ_p= +17.0° and θ_n= −34.5°								
Arc Length			Analyzing Powers					
S_{eff}	S_{min}	S_{max}	A_y	ΔA_y	A_{yy}	ΔA_{yy}	A_{zz}	ΔA_{zz}
5.34	4.88	5.63	−0.028	0.048	−0.077	0.069	−0.040	0.098
6.03	5.63	6.38	−0.002	0.029	+0.049	0.040	−0.054	0.062
6.77	6.38	7.13	+0.014	0.024	+0.029	0.033	+0.028	0.048
7.53	7.13	7.88	+0.003	0.020	+0.062	0.028	+0.022	0.042
8.27	7.88	8.63	+0.037	0.019	+0.102	0.026	+0.013	0.038
9.00	8.63	9.38	−0.005	0.018	+0.034	0.025	+0.000	0.037
9.74	9.38	10.13	−0.004	0.019	+0.043	0.027	−0.017	0.038
10.48	10.13	10.88	+0.013	0.023	+0.054	0.031	+0.000	0.045
11.14	10.88	11.63	+0.035	0.039	+0.040	0.054	−0.062	0.075

Table A.23: Analyzing powers along the locus S in 750 keV steps for D($\vec{d}, pn$)D with (θ_p,θ_n)=(+17.0°, −34.5°). Arc length and energy ranges given in MeV. The uncertainty in the analyzing powers is understood to be ± everywhere. The effective location of S is obtained by weighting the coordinates with the cross sections.

Proton-Neutron coincidence at θ_p= +19.4° and θ_n= −28.9°								
Arc Length			Analyzing Powers					
S_{eff}	S_{min}	S_{max}	A_y	ΔA_y	A_{yy}	ΔA_{yy}	A_{zz}	ΔA_{zz}
5.03	4.63	5.38	+0.028	0.026	+0.050	0.035	+0.031	0.031
5.77	5.38	6.13	+0.016	0.020	+0.075	0.028	+0.008	0.025
6.52	6.13	6.88	+0.006	0.018	+0.024	0.025	+0.004	0.022
7.26	6.88	7.63	+0.035	0.017	+0.036	0.023	+0.006	0.020
8.01	7.63	8.38	+0.011	0.017	+0.035	0.023	−0.007	0.020
8.75	8.38	9.13	+0.001	0.017	+0.007	0.023	+0.006	0.020
9.48	9.13	9.88	−0.016	0.018	+0.015	0.025	+0.000	0.022
10.20	9.88	10.63	−0.008	0.024	+0.049	0.033	−0.015	0.031
10.81	10.63	11.38	+0.058	0.052	+0.060	0.072	−0.051	0.081

Table A.24: Analyzing powers along the locus S in 750 keV steps for D($\vec{d}, pn$)D with (θ_p,θ_n)=(+19.4°, −28.9°). Arc length and energy ranges given in MeV. The uncertainty in the analyzing powers is understood to be ± everywhere. The effective location of S is obtained by weighting the coordinates with the cross sections.

Appendix B

Kinematics Tabulations

Various kinematic quantities of interest (defined below) for the angle pairs studied in this work are presented in the tables B.1-B.12. All calculations were performed for the $d+d \rightarrow d+p+n$ breakup reaction with a deuteron laboratory energy of 12 MeV.

E_d = Deuteron laboratory energy in the exit channel

E_p = Proton laboratory energy in the exit channel

E_n = Neutron laboratory energy in the exit channel

E_{dp} = Relative energy of the deuteron and proton in the exit channel

E_{dn} = Relative energy of the deuteron and neutron in the exit channel

E_{pn} = Relative energy of the proton and neutron in the exit channel

S = Arc length along the kinematically allowed locus

θ_d = Scattering angle of undetected deuteron

θ_p = Scattering angle of undetected proton

θ_n = Scattering angle of undetected neutron

q = Momentum of the spectator particle relative to the c.m. of the breakup deuteron

θ = Scattering angle of the deuteron in the deuteron-nucleon c.m. system.

Both q and θ depend on which pole is being considered and is identified by Tn, Tp, Pn or Pp which represents the origin of the spectator particle as being the target-neutron, target-proton, projectile-neutron or projectile-proton, respectively.

Deuteron-Proton coincidence at θ_d= +10.0° and θ_p= −10.0°																
Laboratory Energy			Relative Energy			Arc	Lab Angle	Pole								
								Tn		Tp		Pn		Pp		
E_d	E_p	E_n	E_{dp}	E_{dn}	E_{pn}	S	θ_n	q	θ	q	θ	q	θ	q	θ
0.25	6.68	2.85	3.39	1.18	0.70	0.4	11	73	162	112	163	37	7	20	1
0.50	7.85	1.43	3.64	0.32	1.61	1.7	15	52	161	121	156	58	9	25	6
0.75	8.18	0.85	3.51	0.07	2.19	2.1	18	40	160	124	141	69	11	27	20
1.00	8.26	0.52	3.29	0.01	2.61	2.4	21	31	159	124	75	78	13	27	86
1.25	8.21	0.32	3.05	0.05	2.91	2.7	23	25	158	124	13	84	14	27	148
1.50	8.08	0.19	2.80	0.14	3.14	3.0	26	19	158	123	0	90	16	26	162
1.75	7.92	0.11	2.56	0.27	3.31	3.3	30	14	157	122	5	94	17	25	167
2.00	7.72	0.06	2.33	0.42	3.43	3.6	35	10	157	120	8	98	19	24	170
2.25	7.50	0.02	2.11	0.59	3.51	3.9	44	7	156	119	10	102	20	23	173
2.50	7.27	0.01	1.90	0.76	3.57	4.3	63	4	155	117	11	105	22	22	174
2.75	7.02	0.00	1.70	0.94	3.59	4.6	112	2	154	115	13	107	24	21	176
3.00	6.77	0.01	1.52	1.12	3.60	5.0	161	3	153	113	13	110	26	20	177
3.25	6.51	0.02	1.35	1.30	3.58	5.3	180	5	152	111	14	112	28	19	179
3.50	6.25	0.03	1.19	1.49	3.54	5.7	-171	7	151	108	15	114	30	19	180
3.75	5.98	0.05	1.04	1.67	3.49	6.0	-166	9	149	106	16	115	33	18	179
4.00	5.71	0.06	0.91	1.85	3.42	6.4	-162	11	147	104	16	117	35	18	178
4.25	5.44	0.08	0.78	2.03	3.34	6.8	-160	12	145	101	17	118	39	19	177
4.50	5.17	0.10	0.67	2.20	3.25	7.1	-157	14	143	99	17	119	42	19	176
4.75	4.90	0.12	0.58	2.36	3.15	7.5	-155	15	139	96	18	120	46	20	175
5.00	4.63	0.14	0.49	2.52	3.03	7.9	-152	16	136	93	18	121	51	22	174
5.25	4.36	0.16	0.42	2.68	2.91	8.3	-150	17	131	90	18	122	57	23	173
5.50	4.09	0.18	0.36	2.83	2.78	8.6	-148	18	125	88	19	122	63	25	172
5.75	3.83	0.20	0.31	2.97	2.64	9.0	-146	19	119	85	19	123	71	27	172
6.00	3.56	0.21	0.28	3.10	2.49	9.3	-144	20	111	82	20	123	79	29	171
6.25	3.30	0.23	0.26	3.22	2.33	9.7	-141	21	103	79	20	123	89	32	170
6.50	3.04	0.24	0.26	3.33	2.17	10.0	-139	21	93	75	21	123	99	34	169
6.75	2.77	0.25	0.27	3.44	2.00	10.4	-136	22	84	72	21	123	109	37	168
7.00	2.51	0.26	0.29	3.53	1.83	10.8	-133	22	75	69	22	122	119	40	167
7.25	2.26	0.27	0.34	3.60	1.65	11.2	-130	22	67	65	22	122	128	44	166
7.50	2.00	0.28	0.40	3.66	1.46	11.5	-126	23	60	61	23	121	136	47	165
7.75	1.74	0.28	0.49	3.70	1.27	11.9	-121	23	54	57	23	120	143	51	164
8.00	1.48	0.29	0.60	3.72	1.07	12.2	-116	23	48	53	24	119	149	55	163
8.25	1.23	0.30	0.75	3.71	0.87	12.6	-111	24	44	48	25	117	155	59	161
8.50	0.96	0.31	0.94	3.65	0.67	13.0	-103	24	40	42	26	114	160	65	160
8.75	0.68	0.34	1.21	3.53	0.46	13.3	-94	25	36	36	27	111	165	71	158

Table B.1: Kinematics for D$(d, dp)n$ with (θ_d,θ_p)=(+10.0°, −10.0°). Arc length and energies given in MeV, angles given in degrees and momenta in MeV/c.

Deuteron-Proton coincidence at θ_d= +10.0° and θ_p= −41.2°																
Laboratory Energy			Relative Energy			Arc	Lab Angle	Pole								
								Tn		Tp		Pn		Pp	
E_d	E_p	E_n	E_{dp}	E_{dn}	E_{pn}	S	θ_n	q	θ	q	θ	q	θ	q	θ
1.00	3.31	5.47	1.46	1.84	2.61	0.6	24	101	105	79	133	44	44	70	11
1.25	4.11	4.42	1.82	1.28	2.91	1.4	30	91	103	88	120	54	44	70	20
1.50	4.54	3.74	1.98	0.96	3.14	1.9	35	84	101	92	109	61	46	71	29
1.75	4.80	3.23	2.07	0.76	3.31	2.3	38	78	98	95	98	66	48	72	39
2.00	4.95	2.82	2.11	0.64	3.43	2.6	42	73	96	96	86	71	50	72	50
2.25	5.04	2.48	2.12	0.57	3.51	2.8	45	68	94	97	75	75	52	72	61
2.50	5.07	2.20	2.11	0.55	3.57	3.1	48	64	92	98	64	79	55	72	72
2.75	5.07	1.96	2.09	0.55	3.59	3.3	50	61	90	98	54	82	57	72	82
3.00	5.03	1.74	2.06	0.58	3.60	3.6	53	57	88	97	44	85	60	72	91
3.25	4.97	1.56	2.02	0.63	3.58	3.9	55	54	86	97	36	88	62	72	100
3.50	4.89	1.39	1.98	0.69	3.54	4.1	58	51	84	96	29	90	65	72	107
3.75	4.79	1.24	1.94	0.77	3.49	4.4	60	48	82	95	23	92	67	71	114
4.00	4.67	1.11	1.89	0.86	3.42	4.7	62	46	80	94	18	94	70	71	119
4.25	4.54	0.98	1.85	0.96	3.34	4.9	65	43	78	92	13	96	73	71	125
4.50	4.40	0.87	1.80	1.07	3.25	5.2	67	41	77	91	9	98	76	71	129
4.75	4.25	0.77	1.76	1.18	3.15	5.5	69	38	75	89	6	99	79	71	133
5.00	4.09	0.68	1.72	1.29	3.03	5.8	72	36	73	88	3	101	82	70	137
5.25	3.93	0.60	1.69	1.41	2.91	6.1	74	34	71	86	0	102	85	70	141
5.50	3.75	0.52	1.65	1.53	2.78	6.4	76	31	69	84	2	103	88	70	144
5.75	3.58	0.45	1.62	1.66	2.64	6.7	78	29	67	82	5	104	91	70	147
6.00	3.39	0.38	1.60	1.78	2.49	7.0	81	27	65	80	7	105	95	70	150
6.25	3.20	0.32	1.58	1.91	2.33	7.4	83	25	62	78	8	106	98	70	153
6.50	3.01	0.27	1.56	2.03	2.17	7.7	85	22	60	75	10	107	102	70	156
6.75	2.81	0.22	1.55	2.15	2.00	8.0	88	20	58	73	12	107	106	70	158
7.00	2.60	0.17	1.55	2.27	1.83	8.3	90	18	56	70	13	108	110	71	161
7.25	2.40	0.13	1.55	2.39	1.65	8.6	93	16	54	67	15	108	114	71	164
7.50	2.18	0.09	1.57	2.50	1.46	9.0	95	13	52	64	16	108	118	72	167
7.75	1.97	0.06	1.59	2.60	1.27	9.3	98	11	49	61	18	108	122	72	169
8.00	1.74	0.03	1.62	2.70	1.07	9.6	101	8	47	57	19	108	127	73	172
8.25	1.51	0.01	1.67	2.78	0.87	10.0	105	5	45	53	20	108	132	75	175
8.50	1.27	0.00	1.74	2.85	0.67	10.3	112	1	42	49	22	107	137	76	179
8.75	1.02	0.00	1.83	2.90	0.46	10.7	-73	3	40	44	23	106	142	79	177
9.00	0.74	0.03	1.97	2.91	0.24	11.1	-67	8	37	37	25	103	149	82	173

Table B.2: Kinematics for D$(d, dp)n$ with (θ_d,θ_p)=(+10.0°, −41.2°). Arc length and energies given in MeV, angles given in degrees and momenta in MeV/c.

Deuteron-Proton coincidence at θ_d= +17.0° and θ_p= −17.0°																
Laboratory Energy			Relative Energy			Arc	Lab Angle	Pole								
								Tn		Tp		Pn		Pp		
E_d	E_p	E_n	E_{dp}	E_{dn}	E_{pn}	S	θ_n	q	θ	q	θ	q	θ	q	θ	
0.50	7.10	2.18	3.43	0.63	1.47	1.2	19	64	149	115	151	51	16	34	2	
0.75	7.66	1.37	3.48	0.21	2.02	1.8	23	51	147	120	142	63	19	36	9	
1.00	7.87	0.91	3.38	0.05	2.41	2.1	25	41	146	121	124	71	21	37	27	
1.25	7.91	0.61	3.23	0.01	2.69	2.4	27	34	145	122	56	78	24	37	95	
1.50	7.86	0.41	3.06	0.05	2.90	2.6	29	28	144	121	3	83	26	37	147	
1.75	7.76	0.27	2.87	0.13	3.05	2.9	31	23	143	121	10	88	28	36	161	
2.00	7.60	0.17	2.69	0.25	3.15	3.2	33	18	142	119	16	92	30	36	167	
2.25	7.42	0.10	2.50	0.39	3.22	3.5	34	14	141	118	19	95	33	35	171	
2.50	7.22	0.05	2.33	0.54	3.26	3.8	35	10	141	116	21	98	35	34	174	
2.75	7.00	0.02	2.15	0.71	3.27	4.2	35	7	140	115	23	101	37	34	176	
3.00	6.77	0.01	1.99	0.88	3.25	4.5	34	4	139	113	25	103	40	33	178	
3.25	6.52	0.00	1.83	1.06	3.22	4.8	6	1	138	111	26	106	42	32	180	
3.50	6.27	0.00	1.69	1.24	3.17	5.2	-124	2	136	108	27	107	45	32	178	
3.75	6.01	0.01	1.55	1.42	3.11	5.6	-128	5	135	106	28	109	48	31	176	
4.00	5.75	0.03	1.42	1.60	3.03	5.9	-128	7	133	104	29	111	51	31	175	
4.25	5.48	0.04	1.30	1.78	2.94	6.3	-128	9	131	101	30	112	55	31	173	
4.50	5.21	0.07	1.19	1.96	2.83	6.7	-126	11	129	99	30	113	58	31	172	
4.75	4.93	0.09	1.09	2.14	2.72	7.0	-125	13	127	96	31	114	62	31	170	
5.00	4.65	0.12	1.00	2.31	2.59	7.4	-123	15	124	93	32	115	67	32	169	
5.25	4.37	0.15	0.92	2.48	2.46	7.8	-121	17	121	91	33	116	71	33	167	
5.50	4.09	0.19	0.85	2.64	2.32	8.2	-119	19	117	88	33	116	76	34	166	
5.75	3.80	0.22	0.80	2.80	2.16	8.5	-116	20	114	84	34	117	82	35	164	
6.00	3.52	0.26	0.75	2.95	2.01	8.9	-114	22	109	81	35	117	88	37	163	
6.25	3.23	0.30	0.72	3.09	1.84	9.3	-112	24	104	78	36	117	94	39	161	
6.50	2.93	0.34	0.71	3.22	1.67	9.7	-109	25	99	74	36	117	101	41	159	
6.75	2.64	0.39	0.71	3.33	1.49	10.1	-106	27	93	70	37	117	108	44	158	
7.00	2.34	0.44	0.73	3.44	1.31	10.5	-102	29	87	66	38	116	116	47	156	
7.25	2.03	0.50	0.77	3.52	1.12	10.9	-99	31	81	62	39	115	123	50	154	
7.50	1.71	0.56	0.84	3.58	0.92	11.3	-94	33	75	57	40	113	131	55	151	
7.75	1.37	0.65	0.95	3.61	0.72	11.7	-89	35	68	51	42	111	139	59	149	
8.00	0.99	0.79	1.13	3.57	0.52	12.2	-82	38	61	43	44	108	148	66	145	

Table B.3: Kinematics for D$(d, dp)n$ with (θ_d,θ_p)=(+17.0°, −17.0°). Arc length and energies given in MeV, angles given in degrees and momenta in MeV/c.

Deuteron-Proton coincidence at θ_d= +17.0° and θ_p= −34.5°																
Laboratory Energy			Relative Energy			Arc	Lab Angle	Pole								
								Tn		Tp		Pn		Pp		
E_d	E_p	E_n	E_{dp}	E_{dn}	E_{pn}	S	θ_n	q	θ	q	θ	q	θ	q	θ
0.75	4.28	4.74	2.05	1.64	2.02	0.2	22	94	119	90	140	40	35	60	4
1.00	5.25	3.52	2.49	0.94	2.41	1.3	28	81	117	99	129	52	36	61	11
1.25	5.73	2.79	2.67	0.58	2.69	1.8	32	72	114	104	118	59	38	62	20
1.50	6.01	2.27	2.74	0.37	2.90	2.2	36	65	112	106	105	66	41	63	32
1.75	6.16	1.87	2.76	0.25	3.05	2.5	39	59	111	108	89	71	43	63	48
2.00	6.23	1.55	2.75	0.19	3.15	2.7	42	54	109	108	70	75	45	64	67
2.25	6.24	1.29	2.71	0.18	3.22	3.0	44	49	107	108	50	79	48	64	86
2.50	6.20	1.07	2.66	0.21	3.26	3.2	47	45	106	108	32	82	50	63	104
2.75	6.13	0.89	2.59	0.27	3.27	3.5	49	41	105	107	19	86	53	63	118
3.00	6.04	0.74	2.53	0.34	3.25	3.8	52	37	103	106	9	88	55	63	128
3.25	5.92	0.61	2.45	0.43	3.22	4.0	54	34	102	105	2	91	58	63	136
3.50	5.78	0.50	2.38	0.54	3.17	4.3	57	31	101	104	4	93	60	62	142
3.75	5.63	0.40	2.30	0.66	3.11	4.6	59	27	99	103	9	95	63	62	147
4.00	5.46	0.32	2.23	0.79	3.03	4.9	62	24	98	101	12	97	66	62	152
4.25	5.28	0.25	2.15	0.93	2.94	5.2	64	22	97	100	16	99	68	61	156
4.50	5.09	0.19	2.08	1.07	2.83	5.5	67	19	95	98	18	100	71	61	159
4.75	4.89	0.14	2.01	1.21	2.72	5.9	70	16	94	96	21	102	74	61	162
5.00	4.68	0.10	1.95	1.36	2.59	6.2	73	14	92	94	23	103	77	60	165
5.25	4.46	0.07	1.88	1.52	2.46	6.5	77	11	91	91	25	104	81	60	168
5.50	4.24	0.04	1.82	1.67	2.32	6.9	81	9	89	89	26	105	84	60	171
5.75	4.00	0.02	1.77	1.82	2.16	7.2	88	6	88	87	28	106	87	60	173
6.00	3.77	0.01	1.72	1.98	2.01	7.5	99	4	86	84	29	107	91	60	176
6.25	3.52	0.00	1.68	2.13	1.84	7.9	135	2	84	81	31	108	95	60	178
6.50	3.27	0.00	1.64	2.28	1.67	8.2	-144	2	82	78	32	108	99	61	179
6.75	3.01	0.01	1.61	2.43	1.49	8.6	-117	4	80	75	33	108	103	61	177
7.00	2.75	0.03	1.59	2.58	1.31	9.0	-107	7	78	72	35	108	108	62	174
7.25	2.47	0.05	1.58	2.71	1.12	9.3	-100	10	75	68	36	108	113	63	171
7.50	2.19	0.09	1.58	2.84	0.92	9.7	-95	13	73	64	37	108	118	65	168
7.75	1.89	0.14	1.60	2.96	0.72	10.1	-90	16	70	59	39	107	123	66	165
8.00	1.56	0.21	1.63	3.06	0.52	10.5	-85	20	66	54	41	106	130	69	161
8.25	1.19	0.34	1.71	3.13	0.31	11.0	-78	25	62	47	43	104	138	72	156

Table B.4: Kinematics for D$(d, dp)n$ with (θ_d,θ_p)=(+17.0°, −34.5°). Arc length and energies given in MeV, angles given in degrees and momenta in MeV/c.

Deuteron-Proton coincidence at θ_d= +19.4° and θ_p= −19.4°																
Laboratory Energy			Relative Energy			Arc	Lab Angle	Pole								
								Tn		Tp		Pn		Pp		
E_d	E_p	E_n	E_{dp}	E_{dn}	E_{pn}	S	θ_n	q	θ	q	θ	q	θ	q	θ	
0.50	6.72	2.56	3.30	0.80	1.41	1.6	19	69	145	112	151	47	19	37	0	
0.75	7.39	1.63	3.45	0.30	1.94	2.3	23	55	143	118	144	59	22	39	5	
1.00	7.67	1.11	3.41	0.08	2.32	2.7	25	46	142	120	133	68	24	40	15	
1.25	7.76	0.77	3.30	0.01	2.59	3.0	27	38	141	121	93	75	27	41	54	
1.50	7.75	0.53	3.16	0.02	2.79	3.2	29	32	140	121	9	80	29	41	139	
1.75	7.66	0.36	3.00	0.09	2.93	3.5	30	26	139	120	12	85	32	40	160	
2.00	7.54	0.24	2.84	0.19	3.02	3.7	30	21	138	119	20	89	34	40	168	
2.25	7.37	0.15	2.67	0.31	3.08	4.0	30	17	137	118	23	92	36	39	172	
2.50	7.19	0.09	2.51	0.45	3.11	4.4	30	13	136	116	26	95	39	39	175	
2.75	6.98	0.05	2.35	0.61	3.12	4.7	27	9	135	114	28	98	41	38	178	
3.00	6.75	0.02	2.19	0.78	3.10	5.0	20	6	134	113	29	100	44	37	180	
3.25	6.52	0.01	2.05	0.95	3.06	5.4	1	4	133	111	31	103	47	37	178	
3.50	6.27	0.00	1.90	1.13	3.00	5.7	-49	3	132	108	32	105	49	36	176	
3.75	6.02	0.01	1.77	1.31	2.93	6.1	-89	4	131	106	33	106	52	36	174	
4.00	5.75	0.02	1.64	1.50	2.85	6.4	-103	6	130	104	34	108	55	35	173	
4.25	5.49	0.04	1.53	1.68	2.75	6.8	-108	9	128	101	35	109	59	35	171	
4.50	5.21	0.06	1.42	1.86	2.64	7.2	-110	11	126	99	35	110	62	35	169	
4.75	4.93	0.09	1.31	2.04	2.52	7.5	-110	13	124	96	36	111	66	35	168	
5.00	4.65	0.13	1.22	2.22	2.39	7.9	-110	15	122	93	37	112	70	36	166	
5.25	4.36	0.16	1.14	2.40	2.25	8.3	-109	17	119	90	38	113	75	37	164	
5.50	4.07	0.20	1.07	2.57	2.10	8.7	-107	20	116	87	39	114	79	37	163	
5.75	3.78	0.25	1.01	2.73	1.95	9.1	-106	22	113	84	40	114	85	39	161	
6.00	3.48	0.30	0.96	2.89	1.78	9.5	-104	24	109	81	40	114	90	40	159	
6.25	3.17	0.35	0.93	3.04	1.61	9.9	-101	26	105	77	41	114	96	42	157	
6.50	2.86	0.41	0.91	3.17	1.44	10.3	-99	28	100	73	42	114	102	44	155	
6.75	2.54	0.48	0.90	3.30	1.26	10.7	-96	30	95	69	43	113	109	47	153	
7.00	2.21	0.56	0.92	3.41	1.07	11.1	-93	32	89	64	45	113	117	50	151	
7.25	1.87	0.66	0.96	3.50	0.87	11.5	-89	35	83	59	46	111	124	54	148	
7.50	1.49	0.78	1.04	3.55	0.67	11.9	-84	38	76	53	48	109	133	59	145	
7.75	1.04	0.99	1.19	3.53	0.47	12.5	-77	43	68	44	50	105	144	66	140	

Table B.5: Kinematics for D$(d, dp)n$ with (θ_d,θ_p)=(+19.4°, −19.4°). Arc length and energies given in MeV, angles given in degrees and momenta in MeV/c.

Deuteron-Proton coincidence at θ_d= +34.5° and θ_p= −17.0°																
Laboratory Energy			Relative Energy			Arc	Lab Angle	Pole								
								Tn		Tp		Pn		Pp		
E_d	E_p	E_n	E_{dp}	E_{dn}	E_{pn}	S	θ_n	q	θ	q	θ	q	θ	q	θ
4.33	0.75	4.70	0.89	3.48	1.00	1.0	41	94	90	38	105	71	133	71	83
4.69	1.00	4.09	0.96	3.57	0.77	1.4	45	88	96	43	99	77	127	66	90
4.87	1.25	3.65	1.01	3.60	0.64	1.7	49	83	101	48	94	81	122	61	96
4.97	1.50	3.31	1.05	3.60	0.57	2.0	52	79	106	53	91	84	117	58	100
5.00	1.75	3.02	1.10	3.58	0.55	2.3	54	75	110	57	89	87	112	54	103
5.00	2.00	2.78	1.14	3.53	0.55	2.5	56	72	114	61	87	89	107	51	106
4.97	2.25	2.56	1.19	3.46	0.57	2.8	57	69	118	65	85	90	103	48	108
4.91	2.50	2.36	1.25	3.38	0.61	3.0	59	67	121	68	84	91	99	45	110
4.84	2.75	2.19	1.31	3.29	0.66	3.3	60	64	124	72	83	92	95	43	112
4.75	3.00	2.02	1.37	3.19	0.72	3.6	60	62	127	75	82	93	91	41	114
4.65	3.25	1.87	1.44	3.08	0.79	3.8	61	59	130	78	81	93	87	39	116
4.54	3.50	1.73	1.51	2.95	0.87	4.1	62	57	132	81	80	94	84	37	117
4.42	3.75	1.60	1.58	2.83	0.94	4.4	62	55	134	84	80	94	81	36	118
4.30	4.00	1.48	1.67	2.69	1.02	4.6	62	53	136	87	79	94	77	34	120
4.16	4.25	1.36	1.75	2.55	1.10	4.9	62	51	138	89	79	94	74	33	121
4.02	4.50	1.25	1.84	2.40	1.19	5.2	62	49	139	92	78	94	72	32	122
3.87	4.75	1.15	1.94	2.25	1.27	5.5	61	47	141	94	78	93	69	32	123
3.72	5.00	1.05	2.04	2.10	1.35	5.8	60	45	142	97	78	93	66	31	124
3.56	5.25	0.96	2.15	1.93	1.43	6.1	59	43	143	99	78	92	63	31	124
3.39	5.50	0.88	2.26	1.77	1.51	6.4	57	41	144	102	78	91	61	31	125
3.22	5.75	0.80	2.38	1.60	1.59	6.7	55	39	145	104	78	90	58	31	125
3.04	6.00	0.74	2.51	1.43	1.66	7.0	52	37	146	106	79	89	56	31	125
2.85	6.25	0.68	2.64	1.25	1.72	7.3	49	36	147	108	80	87	53	32	125
2.65	6.50	0.63	2.78	1.07	1.78	7.7	45	34	147	110	81	85	50	32	125
2.43	6.75	0.59	2.93	0.89	1.82	8.0	39	33	148	113	83	83	48	33	123
2.19	7.00	0.58	3.10	0.71	1.85	8.3	33	33	148	115	86	80	45	34	121
1.92	7.25	0.60	3.28	0.52	1.85	8.7	25	34	149	117	92	77	42	35	115
1.56	7.50	0.72	3.51	0.33	1.79	9.2	14	37	149	119	107	71	37	35	101

Table B.6: Kinematics for D$(d, dp)n$ with (θ_d,θ_p)=(+34.5°, −17.0°). Arc length and energies given in MeV, angles given in degrees and momenta in MeV/c.

Deuteron-Neutron coincidence at θ_d= +17.0° and θ_n= −17.0°																
Laboratory Energy			Relative Energy			Arc	Lab Angle	Pole								
								Tn		Tp		Pn		Pp		
E_d	E_p	E_n	E_{dp}	E_{dn}	E_{pn}	S	θ_p	q	θ	q	θ	q	θ	q	θ	
0.25	4.58	4.94	2.13	2.51	0.60	1.2	12	96	161	93	152	32	2	25	14	
0.50	2.17	7.10	0.63	3.42	1.47	1.8	19	116	151	64	149	34	2	50	16	
0.75	1.37	7.66	0.21	3.48	2.02	2.1	23	120	142	51	147	36	9	63	19	
1.00	0.91	7.87	0.05	3.38	2.41	2.4	25	122	124	41	146	37	27	71	21	
1.25	0.61	7.91	0.01	3.23	2.69	2.6	27	122	55	34	145	37	95	78	24	
1.50	0.41	7.86	0.05	3.06	2.90	2.9	29	122	4	28	144	37	147	83	26	
1.75	0.27	7.76	0.14	2.87	3.05	3.2	31	121	10	22	143	36	161	88	28	
2.00	0.17	7.61	0.25	2.69	3.15	3.5	33	120	16	18	142	36	167	92	30	
2.25	0.10	7.42	0.39	2.50	3.22	3.8	34	118	19	14	141	35	171	95	33	
2.50	0.05	7.22	0.54	2.32	3.26	4.2	35	116	21	10	141	34	174	98	35	
2.75	0.02	7.00	0.71	2.15	3.27	4.5	36	115	23	7	140	34	176	101	37	
3.00	0.01	6.77	0.88	1.99	3.25	4.8	34	113	25	3	139	33	178	103	40	
3.25	0.00	6.52	1.06	1.83	3.22	5.2	7	111	26	1	137	32	180	105	42	
3.50	0.00	6.27	1.24	1.68	3.17	5.6	-125	109	27	2	136	32	178	107	45	
3.75	0.01	6.01	1.42	1.55	3.11	5.9	-129	106	28	5	135	31	176	109	48	
4.00	0.03	5.75	1.60	1.42	3.03	6.3	-129	104	29	7	133	31	175	111	51	
4.25	0.04	5.48	1.78	1.30	2.94	6.7	-128	101	30	9	131	31	173	112	55	
4.50	0.07	5.21	1.96	1.19	2.83	7.0	-126	99	30	11	129	31	172	113	58	
4.75	0.09	4.93	2.14	1.09	2.72	7.4	-125	96	31	13	127	32	170	114	62	
5.00	0.12	4.65	2.31	1.00	2.59	7.8	-123	94	32	15	124	32	169	115	67	
5.25	0.15	4.37	2.48	0.92	2.46	8.2	-121	91	33	17	121	33	167	116	71	
5.50	0.19	4.09	2.64	0.85	2.32	8.5	-119	88	33	19	117	34	166	116	76	
5.75	0.22	3.80	2.80	0.80	2.16	8.9	-117	85	34	20	113	35	164	117	82	
6.00	0.26	3.52	2.95	0.75	2.01	9.3	-114	81	35	22	109	37	163	117	88	
6.25	0.30	3.23	3.09	0.72	1.84	9.7	-112	78	36	24	104	39	161	117	94	
6.50	0.34	2.93	3.22	0.71	1.67	10.1	-109	74	36	25	99	41	159	117	101	
6.75	0.39	2.64	3.33	0.71	1.49	10.5	-106	70	37	27	93	44	158	116	108	
7.00	0.44	2.34	3.44	0.73	1.31	10.9	-102	66	38	29	87	47	156	116	116	
7.25	0.50	2.03	3.52	0.77	1.12	11.3	-99	62	39	31	81	51	154	115	123	
7.50	0.56	1.71	3.58	0.84	0.92	11.7	-94	57	40	33	75	55	151	113	131	
7.75	0.65	1.37	3.61	0.95	0.72	12.2	-89	51	42	35	68	60	149	111	139	

Table B.7: Kinematics for D$(d, dn)^1$H with (θ_d,θ_n)=(+17.0°, −17.0°). Arc length and energies given in MeV, angles given in degrees and momenta in MeV/c.

Deuteron-Neutron coincidence at θ_d= +17.0° and θ_n= −34.5°																
Laboratory Energy			Relative Energy			Arc	Lab Angle	Pole								
								Tn		Tp		Pn		Pp		
E_d	E_p	E_n	E_{dp}	E_{dn}	E_{pn}	S	θ_p	q	θ	q	θ	q	θ	q	θ
0.75	4.75	4.28	1.64	2.05	2.02	0.2	22	90	140	94	119	60	4	40	35
1.00	3.53	5.25	0.95	2.49	2.41	1.3	28	99	129	81	117	61	11	52	36
1.25	2.79	5.73	0.58	2.66	2.69	1.8	32	104	118	72	114	62	20	59	38
1.50	2.27	6.01	0.37	2.74	2.90	2.2	36	106	105	65	112	63	32	66	41
1.75	1.87	6.16	0.25	2.76	3.05	2.5	39	108	89	59	111	63	48	71	43
2.00	1.55	6.23	0.19	2.74	3.15	2.7	42	108	70	54	109	64	67	75	45
2.25	1.29	6.24	0.18	2.71	3.22	3.0	44	108	50	49	107	64	86	79	48
2.50	1.07	6.20	0.21	2.66	3.26	3.2	47	108	32	45	106	64	104	82	50
2.75	0.89	6.13	0.27	2.59	3.27	3.5	49	107	19	41	105	63	117	85	53
3.00	0.74	6.04	0.34	2.53	3.25	3.8	52	107	9	37	103	63	128	88	55
3.25	0.61	5.92	0.44	2.45	3.22	4.0	54	105	2	34	102	63	136	91	58
3.50	0.50	5.78	0.54	2.38	3.17	4.3	57	104	4	31	101	62	142	93	60
3.75	0.40	5.62	0.66	2.30	3.11	4.6	59	103	9	27	99	62	147	95	63
4.00	0.32	5.46	0.79	2.23	3.03	4.9	62	101	12	24	98	62	152	97	66
4.25	0.25	5.28	0.93	2.15	2.94	5.2	64	100	16	22	97	61	155	99	68
4.50	0.19	5.09	1.07	2.08	2.83	5.5	67	98	18	19	95	61	159	100	71
4.75	0.14	4.88	1.21	2.01	2.72	5.9	70	96	21	16	94	61	162	102	74
5.00	0.10	4.68	1.36	1.95	2.59	6.2	73	94	23	14	92	61	165	103	77
5.25	0.07	4.46	1.52	1.88	2.46	6.5	77	92	24	11	91	60	168	104	81
5.50	0.04	4.24	1.67	1.82	2.32	6.8	81	89	26	9	89	60	170	105	84
5.75	0.02	4.00	1.83	1.77	2.16	7.2	88	87	28	6	88	60	173	106	87
6.00	0.01	3.77	1.98	1.72	2.01	7.5	99	84	29	4	86	60	176	107	91
6.25	0.00	3.52	2.13	1.68	1.84	7.9	135	81	31	2	84	61	178	107	95
6.50	0.00	3.27	2.28	1.64	1.67	8.2	-145	78	32	2	82	61	179	108	99
6.75	0.01	3.01	2.43	1.61	1.49	8.6	-117	75	33	4	80	61	177	108	103
7.00	0.03	2.75	2.58	1.59	1.31	9.0	-107	72	35	7	78	62	174	108	108
7.25	0.05	2.47	2.71	1.58	1.12	9.3	-100	68	36	10	75	63	171	108	113
7.50	0.09	2.19	2.84	1.58	0.92	9.7	-95	64	37	13	73	65	168	108	118
7.75	0.14	1.89	2.96	1.60	0.72	10.1	-90	60	39	16	70	66	165	107	123
8.00	0.21	1.56	3.06	1.64	0.52	10.5	-85	54	41	20	66	69	161	106	130
8.25	0.34	1.19	3.13	1.71	0.31	11.0	-79	47	43	25	62	72	156	104	138

Table B.8: Kinematics for D$(d, dn)^1$H with (θ_d,θ_n)=(+17.0°, −34.5°). Arc length and energies given in MeV, angles given in degrees and momenta in MeV/c.

Deuteron-Neutron coincidence at θ_d= +19.4° and θ_n= −28.9°															
Laboratory Energy			Relative Energy			Arc	Lab Angle	Pole							
								Tn		Tp		Pn		Pp	
E_d	E_p	E_n	E_{dp}	E_{dn}	E_{pn}	S	θ_p	q	θ	q	θ	q	θ	q	θ
0.75	3.25	5.77	0.95	2.79	1.94	1.6	25	104	138	78	128	53	5	48	29
1.00	2.39	6.39	0.49	3.00	2.32	2.3	29	110	128	67	126	54	13	58	31
1.25	1.83	6.70	0.25	3.07	2.59	2.6	33	112	115	59	124	55	24	65	34
1.50	1.42	6.86	0.12	3.06	2.79	3.0	35	114	96	52	122	55	43	71	37
1.75	1.11	6.91	0.08	3.01	2.93	3.2	38	114	66	46	121	55	73	76	39
2.00	0.87	6.90	0.09	2.94	3.02	3.5	40	114	35	40	119	55	104	80	42
2.25	0.68	6.84	0.13	2.85	3.08	3.7	43	113	13	36	118	55	126	84	44
2.50	0.53	6.75	0.21	2.75	3.11	4.0	45	113	0	31	117	55	140	87	46
2.75	0.40	6.62	0.31	2.65	3.12	4.3	47	112	8	28	116	55	148	90	49
3.00	0.30	6.47	0.42	2.55	3.10	4.6	49	110	14	24	115	54	155	92	52
3.25	0.22	6.30	0.55	2.45	3.06	4.9	51	109	18	20	114	54	159	95	54
3.50	0.16	6.12	0.69	2.34	3.00	5.2	53	107	21	17	113	53	163	97	57
3.75	0.11	5.92	0.84	2.24	2.93	5.5	55	105	24	14	111	53	167	99	60
4.00	0.07	5.71	1.00	2.14	2.85	5.8	58	104	26	11	110	52	170	101	62
4.25	0.04	5.49	1.16	2.05	2.75	6.2	60	102	28	8	109	52	172	102	65
4.50	0.02	5.26	1.32	1.95	2.64	6.5	62	99	30	6	108	52	175	104	68
4.75	0.00	5.02	1.49	1.87	2.52	6.8	65	97	31	3	106	52	177	105	72
5.00	0.00	4.77	1.66	1.78	2.39	7.2	76	95	33	0	105	51	180	106	75
5.25	0.00	4.52	1.83	1.71	2.25	7.5	-113	92	34	2	103	51	178	107	79
5.50	0.01	4.26	2.00	1.64	2.10	7.9	-110	90	35	5	101	51	176	108	82
5.75	0.03	4.00	2.17	1.57	1.95	8.3	-108	87	37	7	99	52	173	109	86
6.00	0.05	3.72	2.33	1.52	1.78	8.6	-105	84	38	10	97	52	171	109	90
6.25	0.08	3.44	2.49	1.47	1.61	9.0	-103	80	39	12	95	53	169	109	95
6.50	0.12	3.16	2.65	1.43	1.44	9.4	-100	77	40	15	92	54	166	110	100
6.75	0.16	2.86	2.80	1.40	1.26	9.8	-97	73	41	18	89	55	164	110	105
7.00	0.22	2.55	2.94	1.38	1.07	10.2	-94	69	43	20	86	57	161	109	110
7.25	0.29	2.23	3.07	1.38	0.87	10.6	-90	65	44	23	83	59	158	109	116
7.50	0.39	1.89	3.19	1.40	0.67	11.0	-86	60	46	27	78	61	155	108	123
7.75	0.52	1.50	3.28	1.45	0.47	11.5	-81	53	48	31	73	65	151	106	131

Table B.9: Kinematics for D$(d,dn)^1$H with (θ_d,θ_n)=(+19.4°, −28.9°). Arc length and energies given in MeV, angles given in degrees and momenta in MeV/c.

Proton-Neutron coincidence at $\theta_p = +17.0°$ and $\theta_n = -17.0°$																
Laboratory Energy			Relative Energy			Arc	Lab Angle	Pole								
								Tn		Tp		Pn		Pp		
E_d	E_p	E_n	E_{dp}	E_{dn}	E_{pn}	S	θ_d	q	θ	q	θ	q	θ	q	θ
1.76	0.25	7.76	0.13	3.01	2.85	1.2	21	121	34	22	-144	37	175	86	-31
1.36	0.50	7.91	0.01	3.32	2.56	1.5	22	122	58	31	-146	37	152	77	-28
1.11	0.75	7.91	0.01	3.48	2.31	1.8	22	122	176	38	-147	37	33	71	-25
0.94	1.00	7.84	0.07	3.57	2.10	2.1	23	121	166	43	-147	37	15	66	-24
0.80	1.25	7.72	0.16	3.60	1.91	2.3	23	120	161	48	-148	36	10	61	-22
0.70	1.50	7.58	0.27	3.60	1.74	2.6	22	119	159	53	-148	36	7	58	-21
0.61	1.75	7.41	0.40	3.58	1.59	2.9	22	118	157	57	-148	35	6	54	-20
0.54	2.00	7.23	0.53	3.53	1.46	3.2	21	117	156	61	-149	34	4	51	-18
0.48	2.25	7.04	0.68	3.46	1.34	3.5	20	115	156	65	-149	34	3	48	-17
0.44	2.50	6.84	0.83	3.38	1.24	3.9	19	113	155	68	-149	33	2	45	-16
0.40	2.75	6.63	0.98	3.29	1.15	4.2	18	112	154	72	-150	33	0	43	-15
0.36	3.00	6.41	1.14	3.19	1.07	4.5	16	110	154	75	-150	32	1	41	-14
0.33	3.25	6.19	1.30	3.08	1.00	4.9	14	108	154	78	-150	32	2	39	-13
0.31	3.50	5.96	1.45	2.95	0.94	5.2	12	106	153	81	-150	31	3	37	-12
0.29	3.75	5.73	1.61	2.83	0.90	5.5	10	104	153	84	-151	31	4	36	-11
0.28	4.00	5.49	1.77	2.69	0.86	5.9	8	102	153	87	-151	31	5	34	-10
0.27	4.25	5.25	1.93	2.55	0.83	6.2	5	99	152	89	-151	31	6	33	-9
0.27	4.50	5.01	2.09	2.40	0.82	6.6	3	97	152	92	-151	31	7	32	-9
0.26	4.75	4.76	2.24	2.25	0.81	6.9	0	95	152	94	-152	32	7	32	-8
0.27	5.00	4.51	2.40	2.10	0.82	7.3	-3	92	151	97	-152	33	8	31	-7
0.27	5.25	4.25	2.55	1.93	0.83	7.6	-5	89	151	99	-152	33	9	31	-6
0.28	5.50	3.99	2.70	1.77	0.86	8.0	-8	87	151	102	-153	35	10	31	-5
0.30	5.75	3.73	2.84	1.60	0.90	8.4	-10	84	151	104	-153	36	11	31	-4
0.32	6.00	3.46	2.98	1.43	0.95	8.7	-13	81	150	106	-153	38	12	31	-3
0.34	6.25	3.18	3.11	1.25	1.02	9.1	-15	77	150	108	-154	39	13	32	-1
0.38	6.50	2.90	3.23	1.07	1.10	9.5	-17	74	150	110	-154	42	15	32	0
0.42	6.75	2.61	3.35	0.89	1.20	9.9	-18	70	149	113	-155	44	16	33	-1
0.47	7.00	2.30	3.45	0.71	1.32	10.3	-20	66	149	115	-156	47	17	34	-2
0.55	7.25	1.98	3.53	0.52	1.48	10.7	-21	61	149	117	-157	51	18	35	-4
0.65	7.50	1.62	3.59	0.33	1.67	11.1	-22	55	148	119	-158	56	20	35	-6
0.83	7.75	1.20	3.60	0.14	1.95	11.6	-23	47	148	121	-162	63	22	36	-11

Table B.10: Kinematics for D(d, pn)D with (θ_p, θ_n)=$(+17.0°, -17.0°)$. Arc length and energies given in MeV, angles given in degrees and momenta in MeV/c.

Proton-Neutron coincidence at θ_p= +17.0° and θ_n= −34.5°																
Laboratory Energy			Relative Energy			Arc	Lab Angle	Pole								
								Tn		Tp		Pn		Pp		
E_d	E_p	E_n	E_{dp}	E_{dn}	E_{pn}	S	θ_d	q	θ	q	θ	q	θ	q	θ
3.70	0.25	5.83	0.51	3.01	2.29	2.0	27	105	49	22	-108	63	173	86	-67
3.08	0.50	6.20	0.22	3.32	2.25	2.5	29	108	61	31	-112	64	162	77	-62
2.67	0.75	6.35	0.09	3.48	2.19	2.8	31	109	81	38	-114	64	144	71	-58
2.37	1.00	6.40	0.05	3.57	2.12	3.1	32	110	113	43	-115	64	111	66	-56
2.13	1.25	6.39	0.06	3.60	2.06	3.3	32	110	149	48	-116	64	76	61	-54
1.93	1.50	6.34	0.10	3.60	2.00	3.6	33	109	170	53	-117	64	54	58	-52
1.76	1.75	6.26	0.16	3.58	1.94	3.8	33	108	178	57	-118	64	42	54	-50
1.62	2.00	6.16	0.25	3.53	1.89	4.1	34	108	171	61	-118	63	34	51	-49
1.49	2.25	6.04	0.34	3.46	1.85	4.4	34	107	166	65	-118	63	29	48	-48
1.37	2.50	5.90	0.45	3.38	1.81	4.7	33	105	162	68	-119	63	25	45	-47
1.27	2.75	5.75	0.56	3.29	1.77	5.0	33	104	160	72	-119	62	22	43	-46
1.18	3.00	5.59	0.69	3.19	1.75	5.3	33	103	158	75	-120	62	19	41	-45
1.10	3.25	5.43	0.81	3.08	1.72	5.6	32	101	156	78	-120	62	17	39	-44
1.03	3.50	5.25	0.95	2.95	1.71	5.9	32	99	155	81	-120	61	15	37	-43
0.96	3.75	5.07	1.08	2.83	1.69	6.2	31	98	154	84	-120	61	13	36	-42
0.90	4.00	4.87	1.22	2.69	1.69	6.5	30	96	153	87	-120	61	11	34	-41
0.85	4.25	4.68	1.36	2.55	1.69	6.8	29	94	152	89	-120	61	10	33	-40
0.80	4.50	4.47	1.51	2.40	1.69	7.1	27	92	151	92	-121	60	8	32	-39
0.76	4.75	4.27	1.65	2.25	1.71	7.5	26	90	151	94	-121	60	7	32	-39
0.72	5.00	4.05	1.79	2.10	1.72	7.8	24	87	150	97	-121	60	5	31	-38
0.69	5.25	3.83	1.94	1.93	1.75	8.1	22	85	149	99	-121	60	3	31	-37
0.67	5.50	3.61	2.08	1.77	1.78	8.5	20	82	149	102	-120	60	2	31	-37
0.65	5.75	3.37	2.22	1.60	1.82	8.8	17	80	148	104	-120	61	0	31	-36
0.64	6.00	3.13	2.36	1.43	1.87	9.1	15	77	148	106	-120	61	1	31	-36
0.64	6.25	2.89	2.50	1.25	1.92	9.5	12	74	147	108	-120	62	3	32	-36
0.64	6.50	2.63	2.64	1.07	1.99	9.8	9	70	147	110	-119	63	5	32	-36
0.66	6.75	2.36	2.77	0.89	2.07	10.2	6	67	147	113	-118	64	7	33	-36
0.70	7.00	2.08	2.89	0.71	2.17	10.6	2	63	146	115	-117	65	9	34	-36
0.75	7.25	1.78	3.00	0.52	2.28	11.0	-2	58	146	117	-114	67	11	35	-38
0.84	7.50	1.43	3.09	0.33	2.43	11.4	-5	52	145	119	-110	70	14	35	-42
1.03	7.75	1.00	3.14	0.14	2.64	11.9	-10	43	145	121	-96	75	18	36	-55

Table B.11: Kinematics for D(d,pn)D with (θ_p,θ_n)=(+17.0°, −34.5°). Arc length and energies given in MeV, angles given in degrees and momenta in MeV/c.

Proton-Neutron coincidence at $\theta_p = +19.4°$ and $\theta_n = -28.9°$																
Laboratory Energy			Relative Energy			Arc	Lab Angle	Pole								
								Tn		Tp		Pn		Pp		
E_d	E_p	E_n	E_{dp}	E_{dn}	E_{pn}	S	θ_d	q	θ	q	θ	q	θ	q	θ
2.96	0.25	6.57	0.35	2.99	2.56	1.7	26	111	46	22	-120	54	174	86	-55
2.41	0.50	6.87	0.11	3.29	2.45	2.1	28	114	58	31	-122	55	163	78	-50
2.05	0.75	6.97	0.03	3.45	2.34	2.4	29	114	87	38	-124	56	134	72	-47
1.79	1.00	6.98	0.02	3.53	2.23	2.7	30	115	146	43	-125	56	75	67	-45
1.59	1.25	6.94	0.06	3.56	2.13	2.9	30	114	179	48	-126	56	42	63	-43
1.42	1.50	6.86	0.12	3.55	2.04	3.2	31	114	168	53	-126	55	29	59	-41
1.28	1.75	6.75	0.21	3.52	1.96	3.5	31	113	162	57	-127	55	22	55	-40
1.16	2.00	6.62	0.31	3.47	1.89	3.7	31	112	158	61	-127	55	18	52	-38
1.06	2.25	6.47	0.42	3.40	1.82	4.0	30	110	156	65	-128	54	15	50	-37
0.97	2.50	6.31	0.55	3.32	1.76	4.3	30	109	154	68	-128	54	13	47	-36
0.89	2.75	6.14	0.68	3.22	1.71	4.6	29	107	152	72	-128	53	11	45	-34
0.82	3.00	5.96	0.81	3.11	1.67	4.9	28	106	151	75	-129	53	9	43	-33
0.76	3.25	5.77	0.95	3.00	1.63	5.2	27	104	150	78	-129	53	7	42	-32
0.70	3.50	5.57	1.10	2.87	1.60	5.6	26	102	149	81	-129	52	6	40	-31
0.66	3.75	5.37	1.25	2.74	1.57	5.9	25	100	149	84	-129	52	4	39	-30
0.62	4.00	5.16	1.39	2.61	1.56	6.2	23	98	148	87	-130	52	3	38	-29
0.58	4.25	4.94	1.54	2.46	1.55	6.5	21	96	148	89	-130	51	1	37	-28
0.55	4.50	4.72	1.70	2.31	1.54	6.9	19	94	147	92	-130	51	0	36	-27
0.53	4.75	4.49	1.85	2.16	1.55	7.2	17	92	146	94	-130	51	2	36	-26
0.51	5.00	4.26	2.00	2.00	1.56	7.6	15	89	146	97	-130	51	3	35	-26
0.50	5.25	4.02	2.15	1.84	1.58	7.9	12	87	146	99	-130	52	4	35	-25
0.50	5.50	3.78	2.30	1.67	1.61	8.3	9	84	145	102	-130	52	6	35	-24
0.50	5.75	3.53	2.44	1.50	1.64	8.6	6	81	145	104	-130	53	7	35	-23
0.51	6.00	3.27	2.59	1.32	1.69	9.0	3	78	144	106	-130	53	9	36	-22
0.52	6.25	3.00	2.73	1.15	1.75	9.3	0	75	144	108	-130	54	10	36	-22
0.55	6.50	2.73	2.86	0.96	1.81	9.7	-3	72	144	110	-130	56	12	37	-21
0.59	6.75	2.44	2.99	0.78	1.90	10.1	-6	68	143	113	-130	57	14	37	-21
0.65	7.00	2.13	3.11	0.59	2.00	10.5	-9	63	143	115	-129	59	16	38	-21
0.73	7.25	1.79	3.22	0.41	2.12	10.9	-12	58	142	117	-128	62	18	39	-21
0.87	7.50	1.40	3.29	0.21	2.29	11.4	-15	51	142	119	-124	66	21	40	-24

Table B.12: Kinematics for D(d, pn)D with (θ_p, θ_n)=$(+19.4°, -28.9°)$. Arc length and energies given in MeV, angles given in degrees and momenta in MeV/c.

References

[Alt70] E.O. Alt, P. Grassberger, and W. Sandhas. *Treatment of the Three- and Four-Nucleon Systems by a Generalized Separable-Potential Model.* Physical Review C, **1**(1970) 85–98.

[And72] E. Andrade, V. Valković, D. Rendrić, and G.C. Phillips. *Angular Distributions of Quasi-Free Scattering Contributions in Deuteron Break-Up by Protons and Deuterons.* Nuclear Physics, **A183**(1972) 145–160.

[Arv74] J. Arvieux. *Phase-Shift Analysis of Elastic Proton-Deuteron Scattering Cross Sections and ^3He Excited States.* Nuclear Physics, **A221**(1974) 253–268.

[Baj87] Ž. Bajzer. *Coulomb Effects in Quasi-Free Scattering.* Few Body Systems, **2**(1987) 9–18.

[Bar70] H.H. Barschall and W. Haeberli, editors. *Polarization Phenomena in Nuclear Reactions, Third International Symposium*, Madison, Wisconsin, 1970. The University of Wisconsin Press.

[Bon73] D.I. Bonbright, R.G. Allas, R.O. Bondelid, E.L. Petersen, A.G. Pieper, R.B. Theus, and Ivo Šlaus. *$^2H(^2H, dp)n$ Reaction.* Physical Review C, **8**(1973) 114–119.

[Bra88] R.A. Brandenburg, G.S. Chulick, Y.E. Kim, D.J. Klepacki, R. Machleidt, A. Picklesimer, and R.M. Thaler. *Nuclear charge symmetry breaking and the ^3H–^3He binding energy difference.* Physical Review, **C37**(1988) 781–785.

[Bro90] Virginia R. Brown. *The Nucleon-Nucleon Interaction in the Presence of the Electromagnetic Field: Nucleon-Nucleon Bremsstrahlung.* In *Lectures from the Workshop on Nucleon-Nucleon Bremsstrahlung*, B.F. Gibson, M.E.

Schillaci, and S.A. Wender, editors, pages 1–12, Los Alamos, New Mexico, 1990. Los Alamos National Laboratory.

[Bun75] S.N. Bunker, Mahavir Jain, C.A. Miller, J.M. Nelson, and W.T.H. van Oers. *$(p, 2p)$ and (p, pd) Reactions on ^3He at 45.0 MeV.* Physical Review C, **12**(1975) 1396–1406.

[Bur72] J.P. Burq, J.C. Cabrillat, M. Chemarin, B. Ille, and G. Nicolai. *Quasifree Scattering in Deuteron Break-Up by Deuterons.* Nuclear Physics, **A179**(1972) 385–388.

[Cah74] R.T. Cahill. *The Deuteron Dilation Effect in nd Break-Up.* Physics Letters, **49B**(1974) 150–152.

[Car89] J. Carlson. *Green's Function Monte Carlo Calculations of Light Nuclei.* In *Proceedings of the Twelfth International IUPAP Conference on Few Body Problems in Physics (Few Body XII)*, Harold W. Fearing, editor, pages 141c–150c, Netherlands, 1989. North-Holland.

[Che52] Geoffrey F. Chew and Gian Carlo Wick. *The Impulse Approximation.* Physical Review, **85**(1952) 636–642.

[Cle74] T. Clegg, G. Bissinger, and T. Trainor. *A Lamb-Shift Polarized Ion Source for the TUNL Tandem Accelerator.* Nuclear Instruments and Methods, **120**(1974) 445.

[Dja76] A. Djaloeis, J. Bojowald, C. Alderliesten, C. Mayer-Böricke, G. Paić, and Ž. Bajzer. *Study of the $^2H(d, dp)n$ Reaction in the Energy Range Between 50 and 85 MeV.* Nuclear Physics, **A273**(1976) 29–44.

[Duc72] I.M. Duck, V. Valković, and G.C. Phillips. *Off-Shell Effects in Deuteron-Induced Deuteron Breakup.* Physical Review Letters, **29**(1972) 875–877.

[Eps71] M.B. Epstein, I. Šlaus, D. L. Shannon, J.R. Richardson, J.W. Verba, H.H. Forster, C.C. Kim, and D.Y. Park. *The Effects of the Neutron Pickup Process on $^3He(p, pd)p$ Quasi-Free Scattering.* Physics Letters, **36B**(1971) 305–306.

[Fel91] P.D. Felsher, C.R. Howell, I. Šlaus, W. Tornow, M.L. Roberts, J.M. Hanly, G.J. Weisel, M. Al Ohali, R.L. Walter, J.M. Lambert, P.A. Treado,

G. Mertens, and Y. Koike. *Search for Charge Symmetry Breaking in the Deuteron-Induced Deuteron Breakup.* To be submitted to Physical Review Letters, 1991.

[Fon89] A.C. Fonseca. *Four-Body Calculation of $dd \rightarrow dd$ and $dd \rightarrow p^3H$ Tensor Analyzing Powers.* Physical Review Letters, **63**(1989) 2036–2039.

[Fon90] A.C. Fonseca, 1990. Private communication.

[Fri87] J.L. Friar, B.F. Gibson, and R.L. Payne. *Coulomb effects in the ^{3}He ground state.* Physical Review, **C35**(1987) 1502–1507.

[Fuk89] K. Fukunaga, S. Kakigi, T. Ohsawa, A. Okihana, T. Sekioka, H. Nakamarua-Yokota, T. Murayama, and T. Hayashi. *Break-Up of Deuteron by Vector-Polarized Deuterons at 60 MeV.* Few-Body Systems, **7**(1989) 119–126.

[Fur72] M. Furić and H.H. Forster. *Two-Particle Coincidence Measurements of Four Body Break-Up.* Nuclear Instruments and Methods, **98**(1972) 301–307.

[Ger63] David G. Gerke. *$^{12}C(d,p)^{13}C$: Distorted Wave Born Approximation Analysis of Proton Angular Distributions and Proton-Gamma Angular Correlations.* Ph.D. thesis, Duke University, 1963. Unpublished.

[Gle83] Norman K. Glendenning. *Direct Nuclear Reactions*, chapter: Operator Formalism, pages 81–85. Academic Press, 1983.

[Gou81] C.R. Gould, L.G. Holzsweig, S.E. King, Y.C. Lau, R.V. Poore, N.R. Roberson, and S.A. Wender. *The XSYS Data Acquisition System at Triangle Universities Nuclear Laboratory.* IEEE Transactions Nuclear Science, **NS-28, No. 5**(1981) 3708–3714.

[Gra67] P. Grassberger and W. Sandhas. *Systematical Treatment of the Non-Relativistic N-Particle Scattering Problem.* Nuclear Physics, **B2**(1967) 181–206.

[Gru81] W. Grüebler. *Three- and Four-Nucleon Systems (Experiment).* Nuclear Physics, **A353**(1981) 31c–46c. And references therein.

[Gru89] W. Grüebler. *Charge Symmetry Breaking in Few-Nucleon Systems.* In *Proceedings of the Symposium/Workshop on Spin and Symmetries*, W.D. Ramsay and W.T.H. van Oers, editors, pages 225–234, Vancouver, Canada, 1989. TRIUMF.

[Hae67] W. Haeberli. *Sources of Polarized Ions.* Annual Review of Nuclear Science, **17**(1967) 373–426.

[Hae74] W. Haeberli. *Polarization Experiments.* In *Nuclear Spectroscopy and Reactions, Part A*, Joseph Cerny, editor, pages 151–191. Academic Press, New York & London, 1974. Volume 40-A in Pure and Applied Physics.

[Hal87] G.M. Hale, Ronald E. Brown, and Nelson Jarmie. *Pole Structure of the $J^\pi = \frac{3}{2}^+$ Resonance in ^5He.* Physical Review Letters, **59**(1987) 763–766.

[Hen79] E.M. Henley and G.A. Miller. In *Mesons in Nuclei*, M. Rho and D.H. Wilkinson, editors, page 405. North-Holland, Amsterdam, 1979.

[Hof84a] H.M. Hofmann. *Resonating Group Calculations in Nuclear Few Cluster Systems.* Nuclear Physics, **A416**(1984) 363–378.

[Hof84b] H.M. Hofmann and D. Fick. *Fusion of Polarized Deuterons.* Physical Review Letters, **52**(1984) 2038–2040.

[How87] C.R. Howell, W. Tornow, K. Murphy, H.G. Pfützner, M.L. Roberts, Anli Li, P.D. Felsher, R.L. Walter, I. Šlaus, P.A. Treado, and Y. Koike. *Comparisons of Vector Analyzing-Power Data and Calculations for Neutron-Deuteron Elastic Scattering from 10 to 14 MeV.* Few-Body Systems, **2**(1987) 19–32.

[How88] C.R. Howell, W. Tornow, I. Šlaus, P.D. Felsher, M.L. Roberts, H.G. Pfützner, Anli Li, K. Murphy, R.L Walter, J.M. Lambert, P.A. Treado, H. Witała, W. Glöckle, and T. Cornelius. *Rigorous Calculations and Measurements of $A_y(\theta)$ for n+d Elastic-Scattering and Breakup Processes.* Physics Review Letters, **61**(1988) 1565–1568.

[Kan91] H. Kanada, T. Kaneko, and Y.C. Tang. *Reaction Cross Sections in the Four-Nucleon System with the Multiconfiguration Resonating-Group Method.* Physical Review C, **43**(1991) 371–378.

[Kin81] S.E. King, Y.C. Lau, and C.R. Gould. *Data Acquisition with a VAX 11/780 and MBD Branch Driver.* IEEE Transactions Nuclear Science, **NS-28, No. 5**(1981) 3822–3827.

[Klu78] W. Kluge, H. Matthäy, R. Schlüfter, H. Schneider, and K. Wick. *The Deuteron Break-Up in the Reaction dd→dpn at 52 MeV.* Nuclear Physics, **A302**(1978) 93–124.

[Knu91] L.D. Knutson, S.E. Vigdor, W.W. Jacobs, J. Sowinski, P.L. Jolivette, S.W. Wissink, C. Bloch, C. Whiddon, and R.C. Byrd. *Charge-Symmetry Violation in Neutron-Proton Elastic Scattering at E_n=183 MeV.* Physical Review Letters, **66**(1991) 1410–1413.

[Koi86] Y. Koike and Y. Taniguchi. *Three-Body Calculation of Neutron-Deuteron Elastic Scattering in the Energy Region from 2.5 MeV up to 50 MeV.* Few-Body Systems, **1**(1986) 13–36.

[Koi89] Y. Koike, 1989. Private communication.

[Kok81] L.P. Kok and H. van Haeringen. *Importance of Coulomb Effects in Half-Shell Scattering.* Physical Review Letters, **46**(1981) 1257–1260.

[Koo90] S.E. Koonin and M. Mukerjee. *Branching Ratios in Low-Energy Deuteron-Induced Reactions.* Physical Review C, **42**(1990) 1639–1645.

[Lam91] J. Lambert, 1991. Private communication.

[Lem90] S. Lemaître and H. Paetz gen. Schieck. *Determination of the Reaction-Matrix Elements of the $D(d,n)^3He$ and $D(d,p)^3H$ Reactions for $E_d \leq 500$ keV.* Few-Body Systems, **9**(1990) 155–164.

[Mac89] R. Machleidt. *The Meson Theory of Nuclear Forces and Nuclear Structure.* In *Advances in Nuclear Physics*, J.W. Negele and E. Vogt, editors, pages 189–376. Plenum Press, New York and London, 1989. And references therein.

[Mar69] Pierre Marmier and Eric Sheldon. *Physics of Nuclei and Particles*, volume 1, chapter: Passage of Ionizing Radiation through Matter. Academic Press, 1969.

[Mar71] D.J. Margaziotis, J.C. Young, I. Šlaus, G. Anzelon, F.P. Brady, and R.T. Cahill. *The D(p,2p)n Reaction at 14.45 MeV and the Amada Model.* Physics Letters, **37B**(1971) 262–265.

[McC71] I.E. McCarthy and P.C. Tandy. *The Off-Shell Spectator Model for $d(p,2p)n$.* Nuclear Physics, **A178**(1971) 1–8.

[McI72] J.A. McIntyre, P.H. Beatty, J.D. Bronson, R.J. Hastings, J.G. Rogers, and M.S. Shaw. *Investigation of Proton-Proton Quasifree Scattering in the Scattering in the Reaction $^2H(p,2p)n$.* Physical Review C, **5**(1972) 1796–1799.

[Mdl86a] T.E. Mdlalose, H. Fiedeldey, and W. Sandhas. *Deuteron on Deuteron ^2H(d,nd)p Break-Up in the AGS Formalism.* Nuclear Physics, **A457**(1986) 273–284.

[Mdl86b] T.E. Mdlalose, H. Fiedeldey, and W. Sandhas. *Four-Body Calculation of the Breakup Reaction ^3He(p,pd)^1H.* Physical Review C, **33**(1986) 784–789.

[Mil90] G.A. Miller, B.M.K. Nefkens, and Ivo Šlaus. *Charge Symmetry, Quarks and Mesons.* Physics Reports, **194**(1990) 1–116.

[Ohl65] G.G. Ohlsen. *Kinematic Relations in Reactions of the Form $A + B \rightarrow C + D + E$.* Nuclear Instruments and Methods, **37**(1965) 240–248.

[Ohl70] G.G. Ohlsen. *Los Alamos Lamb-Shift Polarized Ion Source: A User's Guide.* Technical Report LA-4451, Los Alamos Scientific Laboratory of the University of California, 1970. UC-28, Particle Accelerators and High-Voltage Machines TID-4500.

[Ohl72] G.G. Ohlsen. *Polarization Transfer and Spin Correlation Experiments in Nuclear Physics.* Reports on Progress in Physics, **35**(1972) 717–801.

[Ohl81] G.G. Ohlsen, R.E. Brown, F.D. Correll, and R.A. Hardekopf. *The Description of Polarization Analyzing Powers for Three-Body Breakup Reactions.* Nuclear Instruments and Methods, **179**(1981) 283–294.

[Opp35] J.R. Oppenheimer and M. Phillips. *Note on the Transmutation Function for Deuterons.* Physical Review, **48**(1935) 500–502.

[Pae88] H. Paetz gen. Schieck. *Experiments on Four-Nucleon Reactions.* Few-Body Systems, **5**(1988) 171–207.

[Pai70] G. Paić, J.C. Young, and D.J. Margaziotis. *A Modified Impulse Approximation Calculation of the N-N Quasi-Free Scattering and the Chew-Low Extrapolation in the D(p,NN)N Reaction.* Physics Letters, **32B**(1970) 437–440.

[Ped86] Ron S. Pedroni. *Cross Sections and Analyzing Powers in the 8- to 17-MeV Range for Neutron Scattering from* $^{54,56}Fe$, $^{58,60}Ni$, ^{93}Nb, *and* ^{120}Sn. Ph.D. thesis, Duke University, 1986. Unpublished.

[Pet70] E.L. Petersen, R.G. Allas, R.O. Bondelid, A.G. Pieper, and R.B. Theus. *Quasi-Free Scattering in the D(p,pn)p Reaction from 15 to 50 MeV.* Physics Letters, **31B**(1970) 209–210.

[Red70] Edward F. Redish, G.J. Stephenson, Jr., and Gerald M. Lerner. *Off-Shell Effects in Knockout Reactions.* Physical Review C, **2**(1970) 1665–1677.

[Rob81] N.R. Roberson and S.E. Edwards. *Interface for the TUNL VAX Data Acquisition Facility.* IEEE Transactions Nuclear Science, **NS-28, No. 5**(1981) 3834–3837.

[Sla71a] Ivo Šlaus, J.W. Sunier, G. Thompson, J.C. Young, J.W. Verba, D.J. Margaziotis, P. Doherty, and R.T. Cahill. *Neutron-Neutron Quasifree Scattering.* Physical Review Letters, **26**(1971) 789–792.

[Sla71b] Ivo Šlaus, M.B. Epstein, G. Paić, J. Reginald Richardson, D.L. Shannon, J.W. Verba, H.H. Forster, C.C. Kim, D.Y. Park, and L.C. Welch. *Anomalies in Quasifree Scattering from* $p + {}^3He$ *Reactions.* Physical Review Letters, **27**(1971) 751–754.

[Sla77] Ivo Šlaus, R.G. Allas, L.A. Beach, R.O. Bondelid, E.L. Petersen, J.M. Lambert, P.A. Treado, and R.A. Moyle. *Quasifree Processes in the* $^2H + ^3He$ *Interaction.* Nuclear Physics, **A286**(1977) 67–88.

[Sla89] Ivo Šlaus, Yoshinori Akaishi, and Hajime Tanaka. *Neutron-Neutron Effective Range Parameters.* Physics Reports, **173**(1989) 257–300.

[Sof85] S.A. Sofianos, H. Fiedeldey, and W. Sandhas. *Four-Nucleon Scattering in the K-Matrix Approach with Improved Treatment of the (2+2) Channels.* Physical Review C, **32**(1985) 400–410.

[Tak85] Toshinori Takemiya. *On the Low Energy n-d Scattering.* Progress of Theoretical Physics, **74**(1985) 301–314.

[Tor91] W. Tornow, C.R. Howell, R.L. Walter, and I. Šlaus. *Coulomb Effects in Three-Nucleon Scattering versus Charge-Symmetry Breaking in the ^3P Nucleon-Nucleon Interactions.* Submitted to Physics Letters, 1991.

[Tra73] T.A. Trainor. *Polarized Ion Source Development and the Lowest $T=\frac{3}{2}$ Level in ^{41}Sc.* Ph.D. thesis, University of North Carolina at Chapel Hill, 1973. Unpublished.

[Val72a] V. Valković, I. Duck, W.E. Sweeney, and G.C. Phillips. *Three-Body Break-Up in the $d+d \rightarrow d+p+n$ Reaction.* Nuclear Physics, **A183**(1972) 126–144.

[Val72b] V. Valković, I.M. Duck, , and G.C. Phillips. *Coulomb Effects in Deuteron-Induced Deuteron Break-Up.* Physics Letters, **42B**(1972) 191–193.

[Val72c] V. Valković, N. Gabitzsch, D. Rendič, I. Duck, and G.C. Phillips. *Coincidence Spectra from $d+d \rightarrow d+p+n$ and $p+d \rightarrow p+p+n$ Reactions with Neutron Detection at Zero Degrees.* Nuclear Physics, **A182**(1972) 225–233.

[Wie71] B.J. Wielinga, A.D. IJpenberg, K. Mulder, R. van Dantzig, and I. Šlaus. *Prominent Two-Body Effects in the Processes $p(^3He, pd)p$ and $d(d, pd)n$.* Physical Review Letters, **27**(1971) 1229–1232.

[Win86] J.S. Winfield, Sam M. Austin, R.P. DeVito, U.E.P. Berg, Ziping Chen, and W. Sterrenburg. *Measurements of elastic neutron scattering from ^{12}C and ^{32}S at 30.3 and 40.3 MeV: Limits on charge symmetry breaking in the nuclear mean field.* Physical Review, **C33**(1986) 1–13.

[Wit72] W. Von Witsch, W. Viefers, H. Mommsen, P. David, and F. Hinterberger. *Test of the Treiman-Yang Criterion in the $^2H(d, pd)n$ Reaction at 20 MeV Bombarding Energy.* Nuclear Physics, **A195**(1972) 617–622.

[Wit88] H. Witała, W. Glöckle, and Th. Cornelius. *Elastic Scattering and Break-Up Processes in the n-d System.* Few-Body Systems, **3**(1988) 123–134.

[Wit89a] H. Witała, W. Glöckle, and Th. Cornelius. *Nucleon-Deuteron Polarization Observables in ND Elastic Scattering at 6.7 MeV c.m. Energy: Predictions of meson based NN interactions.* Nuclear Physics, **A496**(1989) 446–461.

[Wit89b] H. Witała, W. Glöckle, and Th. Cornelius. *Quasi-Free Scattering in the 3-N Continuum.* Few-Body Systems, **6**(1989) 79–95.

[Wit89c] H. Witała, W. Glöckle, and Th. Cornelius. *Rigorous Faddeev Calculations For Elastic Neutron-Deuteron Scattering Around 8 MeV c.m. Energy.* Nuclear Physics, **A491**(1989) 157–172.

[Wu90] Y. Wu, S. Ishikawa, and T. Sasakawa. *Nuclear Charge Asymmetry and Charge Dependence and the ^3H-^3He Binding-Energy Difference.* Physical Review Letters, **64**(1990) 1875–1878.

[Ynd83] F.J. Ynduráin. *Quantum Chromodynamics*, chapter: QCD as a Field Theory. Springer, New York, 1983.

[Zan84] H. Zankel and W. Plessas. *Off-Shell Effects in Nucleon-Deuteron Polarization Observables.* Atoms and Nuclei, **317**(1984) 45–54.

[Zha86] J.S. Zhang and K.F. Liu. *Fusion Reactions of Polarized Deuterons.* Physical Review Letters, **57**(1986) 1410–1413.

Biography

PAUL DANIEL FELSHER

Born

Falls Church, Virginia, May 20, 1961

Education

B.S., University of North Carolina at Wilmington, Wilmington, North Carolina, 1983
A.M., Duke University, Durham, North Carolina, 1985

Positions

Research Assistant, Duke University, 1984–1991
Teaching Assistant, Duke University, 1983–1985
Teaching Assistant, University of North Carolina at Wilmington, 1981–1983
Junior Fellowship in Nuclear Physics, Florida State University, 1982 (summer)

Memberships

American Physical Society, member
Sigma Pi Sigma (National Physics Honor Society)
Pi Mu Epsilon (National Honorary Mathematics Fraternity)
Phi Eta Sigma (Freshman Honor Society)
Phi Kappa Phi (National Honor Society)

Publications

Journal Articles

1. *Measurement of $A_y(\theta)$ for $n+^{208}Pb$ from 6 to 10 MeV and the Neutron-Nucleus Interaction over the Energy Range from Bound-States at -17 MeV up to Scattering at 40 MeV*, M.L. Roberts, P.D. Felsher, G.J. Weisel, Zemin M. Chen, C.R. Howell, W. Tornow, R.L. Walter and D.J. Horen, Submitted to Physical Review C.

2. *The Low-Energy Neutron-Deuteron Analyzing Power and the $^3P_{0,1,2}$ Interactions of Nucleon-Nucleon Potentials*, W. Tornow, C.R. Howell, M. Alohali, Z.P. Chen, P.D. Felsher, J.M. Hanly, R.L. Walter, G. Weisel, G. Mertens, I. Šlaus, H. Witała and W. Glöckle, Physical Review B in press.

3. *Neutron-Proton Analyzing Power Data at 7.6, 12.0, 14.1, 16.0, 18.5 MeV*, G.J. Weisel, W. Tornow, C.R. Howell, M.L. Roberts, P.D. Felsher, M. Al Ohali, Z.P. Chen, J.M. Hanly, R.L. Walter, J.M. Lambert and P.A. Treado, Colloque De Physique, Colloque **C6**, supplément au n°22, Tome 51, (1990)C6-515–C6-518.

4. *Neutron-deuteron elastic scattering and breakup reactions below 20 MeV*, C.R. Howell, W. Tornow, H.G. Pfützner, M.L. Roberts, K. Murphy, P.D. Felsher, G.J. Weisel, G. Mertens, R.L Walter, J.M. Lambert, P.A. Treado and I. Šlaus, Nuclear Instruments and Methods in Physics Research **B56/57**(1991)459–463.

5. *Techniques for Vector Analyzing Power Measurements of the $^2H(\vec{n}, np)n$ Breakup Reaction at Low Energies*, C.R. Howell, W. Tornow, H.G. Pfützner, Anli Li, M.L. Roberts, K. Murphy, P.D. Felsher, G.J. Weisel, A. Naqvi, R.L. Walter, J.M. Lambert, P.A. Treado and I. Šlaus, Nuclear Instruments and Methods in Physics Research **A290**(1990)424.

6. *Analyzing Power for $^{12}C(\vec{n}, n_{0,1})^{12}C$ and Evaluation of n-^{12}C Scattering at 18.2 MeV*, W. Tornow, C.R. Howell, H.G. Pfützner, M.L. Roberts, P.D. Felsher, Z.M. Chen, M. Al Ohali, G.J. Weisel, R.L. Walter and A.A. Naqvi, Journal of Physics G: Nuclear Physics **14**(1988)49.

7. *Low-Energy Neutron-Proton Analyzing Power and the New Bonn Potential and Paris Potential Predictions*, W. Tornow, C.R. Howell, M.L. Roberts, P.D. Felsher, Z.M. Chen, R.L. Walter, G. Mertens and I. Šlaus, Physical Review **C37**(1988) 2326.

8. *Rigorous Calculations and Measurements of $A_y(\theta)$ for n+d Elastic-Scattering and Breakup Processes*, C.R. Howell, W. Tornow, I. Šlaus, P.D. Felsher, M.L. Roberts, H.G. Pfützner, Anli Li, K. Murphy, R.L. Walter, J.M. Lambert, P.A. Treado, H. Witała, W. Glockle and T. Cornelius, Physical Review Letters **61**(1988)1565.

9. *Comparisons of Vector Analyzing-Power Data and Calculations for Neutron-Deuteron Elastic Scattering from 10 to 14 MeV*, C.R. Howell, W. Tornow, K. Murphy, H.G. Pfützner, M.L. Roberts, Anli Li, P.D. Felsher, R.L. Walter, I. Šlaus, P.A. Treado and Y. Koike, Few-Body Systems **2**(1987)19.

10. *Search for a Purported Resonance in ^{13}C at 20 MeV Via Analyzing Power Measurements of $^{12}C(\vec{n},n)$*, W. Tornow, C.R. Howell, H.G. Pfützner, M.L. Roberts, P.D. Felsher, Z.M. Chen and R.L. Walter, Physical Review **C35**(1987)1578.

Conference Abstracts/Talks Presented

1. *Measurements of Vector and Tensor Analyzing Powers for d-p and d-n Quasifree Scattering using the $\vec{d}$+d $\rightarrow$ d+p+n Breakup Reaction at 12 MeV Compared to Plane-Wave-Impulse-Approximation Calculations*, P.D. Felsher, C.R. Howell, W. Tornow, I. Šlaus, J.M. Hanly, M.L. Roberts, G.J. Weisel, M. Al Ohali, R.L. Walter, G. Mertens, J.M. Lambert, P.A. Treado and Y. Koike, Bulletin of the American Physical Society **35**(1990)979.

2. *Analyzing Power Measurements of the $\vec{d}$+d $\rightarrow$ d+p+n Breakup Reaction*, P.D. Felsher, C.R. Howell, W. Tornow, I. Šlaus, J.M. Lambert, P.A. Treado, G. Mertens, J.M. Hanly, M.L. Roberts, G.J. Weisel, M. Al Ohali, R.L. Walter and Y. Koike, Contributed Papers from Few Body XII, 12^{th} International Conference on Few Body Problems in Physics, Vancouver **C29**(1989).

3. *Measurements of Vector and Tensor Analyzing Powers for d-p and d-n Quasifree Scattering Using the $\vec{d}$+d $\rightarrow$ d+p+n Breakup Reaction*, P.D. Felsher, C.R. Howell,

W. Tornow, I. Šlaus, J.M. Hanly, M.L. Roberts, G.J. Weisel, M. Al Ohali, R.L. Walter, G. Mertens, J.M. Lambert, P.A. Treado and Y. Koike, Bulletin of the American Physical Society **34**(1989)1140.

4. *Neutron Detection Efficiency Calculations Compared to Experimental Determinations*, P.D. Felsher, J.M. Hanly, C.R. Howell, W. Tornow, Z.P. Chen, G.J. Weisel, M. Al Ohali, R.L. Walter and G. Dietze, Bulletin of the American Physical Society **33**(1988)2195.

5. *Measurements of the Absolute Detection Efficiency for a Large Volume Neutron Detector*, J.M. Hanly, C.R. Howell, W. Tornow, P.D. Felsher, G. Weisel, M. Al Ohali, R.L. Walter, A. Aksoy and A. Coban, Bulletin of the American Physical Society **33**(1988)1577.

6. *Experimental Techniques for Measuring Polarization Observables in the* $d+d \rightarrow d+p+n$ *Breakup Reaction at Low Energies*, P.D. Felsher, C.R. Howell, W. Tornow, M.L. Roberts, I. Šlaus, R.L. Walter, J.M. Lambert and P.A. Treado, Bulletin of the American Physical Society **33**(1988)1100.

Co-Authored Abstracts

1. *Analyzing Power Measurements of the* $\vec{d}+d \rightarrow d+p+n$ *Breakup Reaction at 12 MeV*, P.D. Felsher, C.R. Howell, W. Tornow, G.J. Weisel, J.M. Hanly, M.L. Roberts, M.A. Al Ohali, R.L. Walter, J.M. Lambert, P.A. Treado, G. Mertens and Y. Koike, Contributed Papers in 7^{th} International Conference on Polarization Phenomena in Nuclear Physics, Paris **12B**(1990).

2. *Analyzing Power Data for* $^{209}Bi(n,n)$ *at 6 and 9 MeV and Corrections for Compound Nucleus Reactions*, G.J. Weisel, W. Tornow, C.R. Howell, M.L. Roberts, P.D. Felsher, M. Al Ohali, J.M. Hanly, R.L. Walter and G. Mertens, Contributed Papers in 7^{th} International Conference on Polarization Phenomena in Nuclear Physics, Paris **84B**(1990).

3. *Neutron-Proton Analyzing Power Data at 7.6, 12.0, 14.1, 16.0, 18.5 MeV*, G.J. Weisel, W. Tornow, C.R. Howell, M.L. Roberts, P.D. Felsher, M. Al Ohali, Z.P. Chen, J.M. Hanly, R.L. Walter, J.M. Lambert and P.A. Treado, Contributed

Papers in 7^{th} International Conference on Polarization Phenomena in Nuclear Physics, Paris **16D**(1990).

4. *Large Discrepancies Between Rigorous Faddeev Calculations and Elastic Neutron-Deuteron Analyzing-Power Data at Low Energies*, W. Tornow, C.R. Howell, M. Al Ohali, Z.P. Chen, P.D. Felsher, J.M. Hanly, R.L. Walter, G.J. Weisel and G. Mertens, Contributed Papers in 7^{th} International Conference on Polarization Phenomena in Nuclear Physics, Paris **28A**(1990).

5. *Analyzing Power Data for $^{209}Bi(\vec{n},n)$ at 6 and 9 MeV*, G.J. Weisel, W. Tornow, C.R. Howell, M.L. Roberts, P.D. Felsher, M. Al Ohali, J.M. Hanly, R.L. Walter and G. Mertens, Bulletin of the American Physical Society **35**(1990)1039.

6. *Elastic Neutron-Deuteron Analyzing Power Data Below 10 MeV*, W. Tornow, P.D. Felsher, C.R. Howell, G. Mertens, M. Al Ohali, Z.P. Chen, J.M. Hanly, G.J. Weisel, I. Šlaus and R.L. Walter, Contributed Papers from Few Body XII, 12^{th} International Conference on Few Body Problems in Physics, Vancouver **C14**(1989).

7. *Neutron-Proton Analyzing Power Data Below 20 MeV*, G.J. Weisel, W. Tornow, C.R. Howell, M. Al Ohali, Z.P. Chen, P.D. Felsher, J.M. Hanly, J.M. Lambert, P.A. Treado and R.L. Walter, Contributed Papers from Few Body XII, 12^{th} International Conference on Few Body Problems in Physics, Vancouver **C13**(1989).

8. *A Consistent Potential for Describing $n+^{208}Pb$ Scattering and Single-Particle Bound States*, M.L. Roberts, R.L. Walter, W. Tornow, C.R. Howell, P.D. Felsher, G.J. Weisel, M. Al Ohali, Z.M. Chen and D.J. Horen, Bulletin of the American Physical Society **34**(1989)1243.

9. *Analyzing Power Data for Neutron Scattering from Protons Between 7.6 and 18.5 MeV*, G.J. Weisel, W. Tornow, C.R. Howell, P.D. Felsher, Z.P. Chen, M. Al Ohali, J.M. Hanly, R.L. Walter, J.M. Lambert and P.A. Treado, Bulletin of the American Physical Society **34**(1989)1140.

10. *Analyzing Power Data for Neutron Scattering from ^{209}Bi at 6 and 9 MeV*, G.J. Weisel, W. Tornow, C.R. Howell, M.L. Roberts, P.D. Felsher, M. Al Ohali, J.M. Hanly, R.L. Walter and G. Mertens, Bulletin of the American Physical Society **33**(1988)2195.

11. *Measurements of Polarization Observables for d-p and d-n Quasifree Scattering in the d+d System*, C.R. Howell, W. Tornow, P.D. Felsher, I. Šlaus, J.M. Hanly, M.L. Roberts, G.J Weisel, M. Al Ohali, R.L. Walter, G. Mertens, J.M. Lambert, P.A. Treado and Y. Koike, Bulletin of the American Physical Society **33**(1988)1101.

12. *Measurements and Rigorous Calculations of $A_y(\theta)$ for n+d Elastic Scattering and Breakup Processes*, W. Tornow, C.R. Howell, I. Šlaus, P.D. Felsher, M.L. Roberts, K. Murphy, H.G. Pfützner, R.L. Walter, H. Witała, W. Glockle, T. Cornelius, J.M. Lambert and P.A. Treado, Bulletin of the American Physical Society **33**(1988)1100.

13. *Neutron Scattering of 6 to 10 MeV Neutrons from ^{208}Pb*, M.L. Roberts, W. Tornow, C.R. Howell, P.D. Felsher, G.J. Weisel, M. Al Ohali, K. Murphy, H.G. Pfützner, Z.M. Chen, R.L. Walter and D.J. Horen, Bulletin of the American Physical Society **33**(1988)1061.

14. *Vector Analyzing Powers for the $\vec{n}$+d Breakup Reactions*, C.R. Howell, I. Šlaus, W. Tornow, P.A. Treado, H.G. Pfützner, Anli Li, M.L. Roberts, K. Murphy, P.D. Felsher and R.L. Walter, Proceedings of the Sixth International Symposium on Polarization Phenomena in Nuclear Physics (1985), Supplement to Japanese Physical Society, Japan **55**(1986)866.

15. *Search for a Narrow Resonance in the n-^{12}C System via Analyzing Power Measurements with 16 MeV Neutrons*, W. Tornow, C.R. Howell, H.G. Pfützner, M.L. Roberts, P.D. Felsher, Z. Chen and R.L. Walter, Bulletin of the American Physical Society **31**(1986)1238.

16. *Comparison Between Predictions and Preliminary Data of 7-MeV Analyzing Power for ^{208}Pb*, D.J. Horen, C.H. Johnson, M.L. Roberts, C.R. Howell, W. Tornow, R.L. Walter, Z. Chen, K. Murphy, H.G. Pfützner and P.D. Felsher, Bulletin of the American Physical Society **31**(1986)1237.

17. *Extension of the Capability of $A_y(\theta)$ Measurements for Neutron Scattering to 19 MeV at TUNL*, C.R. Howell, W. Tornow, M.L. Roberts, P.D. Felsher, H.G. Pfützner, A.A. Naqvi, Z. Chen and R.L. Walter, Bulletin of the American Physical Society **31**(1986)1225.

18. *Vector Analyzing Powers for N-d Elastic Scattering from 10 to 14 MeV*, C.R. Howell, W. Tornow, I. Šlaus, P.A. Treado, K. Murphy, H.G. Pfützner, M.L.

Roberts, P.D. Felsher and R.L. Walter, Bulletin of the American Physical Society **31**(1986)854.

19. *Vector Analyzing Power Data and Calculations for Nucleon-Deuteron Elastic Scattering from 10 to 14.1 MeV*, W. Tornow, C.R. Howell, K. Murphy, H.G. Pfützner, M.L. Roberts, Anli Li, P.D. Felsher, R.L. Walter, I. Šlaus and Y. Koike, Proceedings of the International Symposium on the Three-Body Force in the Three-Nucleon System, Lecture Notes in Physics **260**(1986)251.

20. *A Study of the n-d Breakup Reaction with Polarized Neutrons*, C.R. Howell, I. Šlaus, W. Tornow, P.A. Treado, H.G. Pfützner, Anli Li, M.L. Roberts, K. Murphy, P.D. Felsher, A. Naqvi and R.L. Walter, Bulletin of the American Physical Society **30**(1985) 1267.

21. *Vector Analyzing Powers for the $\vec{n}$+d Breakup Reaction*, C.R. Howell, I. Šlaus, W. Tornow, P.A. Treado, H.G. Pfützner, Anli Li, M.L. Roberts, K. Murphy, P.D. Felsher and R.L. Walter, Bulletin of the American Physical Society **30**(1985)796.